Modeling heat exchanges
at the land-atmosphere interface using
multi-angular thermal infrared measurements

Li Jia

Promotor: **Prof. Dr. R. A. Feddes**

Hoogleraar in de bodemnatuurkunde, agrohydrologie en het grondwaterbeheer

Co-promotor: **Prof. Dr. M. Menenti**

Istituto per i Sistemi Agricoli e Forestali del Mediterraneo (ISAFoM), CNR, Italy

Samenstelling Promotiecommissie:

Prof. Dr. A. J. Dolman, Vrije Universiteit Amsterdam

Prof. Dr. M. E. Schaepman, Wageningen Universiteit

Dr. C. Ottle, Centre d'Etude des Environnements Terrestre et Planétaires (CETP)/CNRS (France)

Dr. W. Verhoef, Nationaal Lucht – en Ruimtevaartlaboratorium (NLR), Emmeloord

Li Jia

Modeling heat exchanges
at the land-atmosphere interface using
multi-angular thermal infrared measurements

Abstract

Jia, L., 2004, Modeling heat exchanges at the land-atmosphere interface using multi-angular thermal infrared measurements. PhD thesis, Wageningen University, Wageningen, The Netherlands.

This thesis describes the use of multi – angular radiometric observations of the terrestrial biosphere to characterize and understand thermal heterogeneity towards better models of heat exchange at the land – atmosphere interface.

The models and algorithms described in this thesis have been evaluated using data collected during field experiments in China, USA and Spain. Radiative and convective processes in the canopy space are described first using a 3D model to deal with realistic canopy architecture. Penetration and interception of direct, diffuse and emitted radiance are treated separately taking into account the spatial organization of canopy elements and the angular distribution of leaves. This model is used to analyze the relation between the anisotropy of exitance and the thermal heterogeneity of vegetation canopies.

Simpler models of Top Of Canopy (TOC) radiance as a linear mixture of radiance emitted by either four or two canopy components are proposed in view of current Top Of Atmosphere (TOA) bi- angular observations of emittance by space – borne radiometers such as Along Track Scanning Radiometer (ATSR)-2 and Advanced ATSR (AATSR). Comparison with multi-angular, multi – temporal measurements of exitance proved that the two – components model does reproduces observed anisotropy.

The initial 3D model is then used to derive analytically four-, dual- and single heat source models to parameterize heat transfer at the land – atmosphere interface. Assumptions necessary to arrive at these parameterizations are identified to document how the parameterizations account for the radiative and convective processes described in detail by the initial 3D model. Field measurements proved that the dual source model agrees with sensible heat flux density better than single source models, independently of the parameterization of the heat transfer resistance. As regards single source models, the best results were obtained with a parameterization of the resistance dependent on the anisotropy of exitance.

A novel algorithm has been developed to retrieve soil and foliage component temperatures from the bi-angular observations provided by the ATSR-2 and AATSR systems. This algorithms makes optimal use of information contained in the four spectral channels in the VISible, Near InfraRed and Short Wave InfraRed regions and in the two spectral channels in the Thermal InfraRed region at two view angles to retrieve simultaneously atmospheric column water vapor, aerosols optical depth, vegetation fractional cover, soil and foliage component temperatures. Values of TOC radiance are obtained after correction of atmospheric effects, then used to invert the simple two – component model to retrieve soil and foliage component temperatures. Agreement with detailed contact and radiometric ground measurements of soil and foliage temperatures was very good. At larger spatial scales the algorithm has been validated in detail with simulated TOA and TOC image data. Direct validation of retrieved soil and foliage temperatures from ATSR-2 observations was less detailed because of the large ATSR footprint, compounded by the large difference between footprint size and shape in the nadir and forward views.

At the regional scale sensible heat flux density was modeled using bi-angular ATSR-2 observations of exitance and compared with measurements by Large Aperture Scintillometers at a spatial scale comparable with the ATSR-2 spatial resolution. Agreement was very good and within the accuracy of the Scintillometers.

Preface

This work was initiated in 1999 when I started my second visit at Alterra Green World Research of Wageningen University and Research Centre (formerly Winand Staring Centre (SC) of DLO). The idea to do Ph.D. research at Wageningen University, however, came up much earlier in 1996 when I had my first visit at SC-DLO undertaking a cooperative project between the Chinese Academy of Science (CAS) and the Netherlands Royal Academy of Sciences (KNAW).

My first experience in remote sensing research dates back to 1993 when I was involved in the Sino-Japan cooperative project 'Hei He International Field Experiments (HEIFE)' at Lanzhou Institute of Plateau Atmospheric Physics (LIPAP) of (CAS). The focus was on boundary layer physics and land surface processes. Dr. Massimo Menenti came to LIPAP with the idea to apply remote sensing to the energy and water balance study over the Gobi-desert area in Gansu, NW China, where HEIFE was carried out over several years since 1989. A cooperative project between CAS and KNAW was initiated in 1994 and I had the opportunity to visit SC-DLO and to contribute to the project.

My special appreciation goes to my co-promotor Prof. Dr. Massimo Menenti. I have been impressed by his tremendous ideas over a wide range of research subjects and by his solid physics background. What I have learnt from him is far beyond the contents of this thesis. First of all, I thank him for spending time and patience in explaining theories, discussing problems and correcting my English writing in the many versions of the draft. Discussions with him have been of great benefit not only to this study but also to my research career. I thank him for bringing me to the research field of multi-angular remote sensing. I have to say it has been a very intense period in my life in the past five years – I had to keep running between working on my thesis and working for projects, especially those projects related to the preparation of the ESA SPECTRA mission organized by Massimo. There has been work waiting for me all the time, to be done quickly but precisely. This all required moving often from one place to another, partly because of Massimo's 'Zipped'-life schedule. The ups-, downs- and emerging issues in the preparation of SPECTRA mission had a significant impact on the contents and progress of my thesis and in my own perception of it.

I am very grateful to my promotor Prof. Dr. Reinder Feddes. Without his critical comments and detailed discussions, there could have been no guarantee of the academic quality of this dissertation. He suggested me to structure my thesis as a book instead of a set of papers by developing a logical path from theories to applications.

I enjoyed the valuable opportunity to spend some time at the LSIIT of Université Louis Pasteur of France which is one of the famous places one can get solid theoretical and experimental knowledge about thermal infrared remote sensing. I am deeply grateful to Dr. Zhao-Liang Li for his expert supports on the work related to the 'thermal infrared' aspects in this thesis, it would not have been possible to have this part of work well done without his scientific contribution. I thank Prof. Marc-Philip Stoll for detailed discussions and comments about surface temperature and emissivity which helped me efficiently with improving my understanding of thermal infrared research both in the past and nowadays. I also thank him and other members in the LSIIT for the offer of facilities when I was visiting LSIIT. Dr. Françoise Nerry is especially acknowledged, through her I got in touch and eventually familiar with techniques of thermal infrared measurements.

I am very indebted to Dr. Zhongbo (Bob) Su of Alterra Green World Research, WUR. Discussions with him have greatly contributed to this study and beyond it. His wide interest in various scientific issues impressed me. I thank him a lot for showing his confidence in me by having me involved in many projects at Alterra during my Ph.D. research period.

CONTENTS

Abbreviations and acronyms

AATSR	Advanced Along-Track Scanning Radiometer
ABL	Atmospheric Boundary Layer
ASL	Atmospheric Surface Layer
ATSR	Along-Track Scanning Radiometer
BAS	Bulk Atmospheric boundary layer Similarity theory
BOA	Bottom of Atmosphere
BRDF	Bidirectional Reflectance Distribution Function
CBL	Convective Boundary Layer
ENVISAT	ENVIronmental SATellite
ERS	European Remote Sensing Satellites
EWBMS	Energy and Water Balance Monitoring System
FOV	Field-Of-View
IFOV	Instantaneous Field-Of-View
GBT	Gridded Brightness Temperature/reflectance
HAPEX-Sahel	Hydrologic Atmospheric Pilot Experiment in the Sahel
HEIFE	Hei He International Field Experiment
IMGRASS	Inner Mongolia Grassland-Atmosphere Surface Study
IOP	Intensive Observation Period
LAI	Leaf Area Index
LAS	Large Aperture Scintillometer
LES	Large Eddy Simulation
LID	Leaf Inclination Distribution Function
LIDF	Leaf Inclination Distribution Function
LUT	Look-Up-Table
MODTRAN	MODerate resolution TRANSsmittance
MOS	Monin-Obukhov Similarity theory
NIR	Near Infra-Red
OSCAR	Optical Soil Canopy Atmosphere Radiative transfer model
QRSLSP	Quantitative Remote Sensing theory and application for Land Surface Parameters
RACMO	Regional Atmospheric Climate Model
RMSE	Root Mean Square Error
SADIST	Synthesis of ATSR Data Into Sea-surface Temperatures
SAIL	Scattering by Arbitrarily Inclined Leaves
SAILH	Scattering by Arbitrarily Inclined Leaves with Hot spot effect
SEB	Surface Energy Balance
SEBI	Surface Energy Balance Index

SEBS	Surface Energy Balance System
SGP'97	The Southern Great Plains 1997 Hydrology Experiment
SPECTRA	Surface Processes and Ecosystem Changes Through Response Analysis
SW	Split Window
SWCVR	Split-Window channel Covariance and Variance Ratio
SWIR	Short-Wave Infra-Red
TIR	Thermal Infra-Red
TIROS	Television InfraRed Observation Satellite
TOA	Top of Atmosphere
TOC	Top Of Canopy
VIS	Visible
VISCAL	VISible CALibration system
WMO	World Meteorological Organization
1D	One-dimension (dimensional)
3D	Three-dimension (dimensional)
6S (model)	Second Simulation of Satellite Signal in the Solar Spectrum

List of symbols

Symbol	Meaning	Unit
a_f	ratio between G_0 and R_n for fully covered vegetation surface	-
a_s	ratio between G_0 and R_n for the bare soil	-
a_u	extinction factor for wind-speed inside the canopy	-
a_{u0}	extinction factor for wind-speed inside the canopy under neutral atmosphere condition	-
A	area occupied by a canopy	m^2
B	Planck function	$W\,m^{-2}\,sr^{-1}$
B_w	bulk stability functions for momentum transfer in Atmospheric Boundary Layer	-
c_{df}	foliage drag coefficient	-
c_p	heat capacity of the air	$J\,kg^{-1}\,K^{-1}$
c_s	volumetric heat capacity of soil	$J\,m^{-3}\,K^{-1}$
C	concentration of a scalar, i.e. temperature, moisture, CO_2, etc.	
C_t	heat transfer coefficient of the leaf	-
C_t^*	heat transfer coefficient of the soil, given by $C_t^* = Pr^{-2/3} Re_*^{-1/2}$	-
C_w	bulk stability functions for heat transfer in Atmospheric Boundary Layer	-
D	path length that a ray of radiation passes through the canopy	m
D_i	incident diffuse fraction of irradiance	-
$D_{ij}(\vec{r}, \mathbf{\Omega})$	distance the ray travels through the jth sub-canopy in the ith box	m
e_a	water vapor pressure of air	Pa
$e_{ac}(\vec{r})$	actual water vapor pressure in the air surrounding the leaves in leaf angle class $\mathbf{\Omega_L}$ at point-grid $\vec{r}$	Pa
e_s	water vapor pressure near soil surface	Pa
e_0	saturation water vapor pressure at reference height z_{0e} in a canopy, so-called 'surface water vapor pressure' in single-source models	Pa
$e_{0f}(\vec{r}, \mathbf{\Omega_L})$	saturation water vapor pressure of leaf surface boundary at $T_f(\vec{r}, \mathbf{\Omega_L})$ at point-grid $\vec{r}$	Pa
E	sphere area index which is defined as the fraction of the unit area that is covered by the sphere above the soil surface	-

Symbol	Meaning	Unit
f_{Dr}	fraction of R_{s0} that is direct beam	-
f_f	fractional foliage cover	-
$f_f(\theta_v)$	fractional foliage cover at zenith view angle θ_v	-
f_{fw}	fractional cover of foliage in the forward zenith view	-
$f_k(\theta_v, \varphi_v)$	fraction of the linear dimension of the volume δV of a grid point seen by the radiometer within the IFOV	-
f_{nd}	fractional cover of foliage in the nadir zenith view	-
$f_s(\theta_v)$	fractional cover of soil at zenith view angle θ_v	-
$f_{s\_f}(\theta_v)$	fractional cover of sunlit foliage at zenith view angle θ_v	-
$f_{s\_s}(\theta_v)$	fractional cover of sunlit soil at zenith view angle θ_v	-
$f_{sh\_f}(\theta_v)$	fractional cover of shaded foliage at zenith view angle θ_v	-
$f_{sh\_s}(\theta_v)$	fractional cover of shaded soil at zenith view angle θ_v	-
F	flux density of a scalar between points in a canopy	W m^{-2}
$F(\vec{\mathbf{r}}, \mathbf{\Omega_L})$	fraction of leaves area in leaf angle class $\mathbf{\Omega_L}$ at point-grid $\vec{\mathbf{r}}$	-
g	acceleration due to gravity	m s^{-2}
Gr	Grashof number	-
$G(\vec{\mathbf{r}}, \mathbf{\Omega})$	fraction of leaf area that is projected towards the source of radiation in the direction $\mathbf{\Omega}$ and is referred to as *extinction coefficient*	-
$G_{ij}(\vec{\mathbf{r}}, \mathbf{\Omega})$	extinction coefficient in the jth sub-canopy in the ith box, determined by leaf inclination/orientation distribution	-
G_0	soil heat flux density at soil surface	W m^{-2}
$G_0(\vec{\mathbf{r}})$	soil heat flux density at soil surface	W m^{-2}
h_b	blending height of boundary layer	m
h_c	canopy height	m
h_s	roughness height of the soil	m
h_{st}	height of Atmospheric Surface Layer	m
H	sensible heat flux density	W m^{-2}
H_d	Sensible heat flux density under dry-limit condition (dry-bound)	W m^{-2}
H_f	sensible heat flux density from foliage	W m^{-2}
$H_f(\vec{\mathbf{r}})$	foliage sensible heat flux density over all leaf angle classes at grid-point $\vec{\mathbf{r}}$	W m^{-2}
$H_f(\vec{\mathbf{r}}, \mathbf{\Omega_L})$	foliage sensible heat flux density in leaf angle class $\mathbf{\Omega_L}$ at grid-point $\vec{\mathbf{r}}$	W m^{-2}

Symbol	Meaning	Unit
H_s	sensible heat flux density from the soil	W m^{-2}
$H_s(\vec{r})$	soil sensible heat flux density at grid-point $\vec{r}$	W m^{-2}
H_w	Sensible heat flux density under wet-limit condition (wet-bound)	W m^{-2}
i_w	relative turbulence intensity	-
$Irrad_{ij}$	irradiance on the small plane normal to the midvector of the sector i in the hemispherical band j at grid point $\vec{r}$	W m^{-2}
k	von Karman constant (= 0.40)	-
k_a	extinction coefficient of a ray penetrating the canopy	-
kB^{-1}	non-dimensional parameter, equal to $\ln(z_{0m}/z_{0h})$ by the original definition, representing $(kB^{-1})'$ when T_{rad} is used	-
kB_s^{-1}	the value of kB^{-1} for bare soil surface	-
$(kB^{-1})'$	*aerodynamic-radiometric* non-dimensional parameter, written as kB^{-1} after introduced for the sake of simplicity	-
$K_D(z)$	soil thermal conductivity at depth z in the soil	W m^{-1} K^{-1}
K_h	turbulent exchange coefficient for heat	J m^{-1} s^{-1} K^{-1}
$K_w(z)$	capillary conductivity	kg s m^{-3}
LAI	leaf area index	m^2 m^{-2}
LAI_{s_f}	sunlit leaf area index	m^2 m^{-2}
LAI_{sh_f}	shadowed leaf area index	m^2 m^{-2}
l_L	characteristic dimension of leaves	m
l_m	mean mixing length within a canopy	m
L	Monin-Obukhov length	m
L_d	Monin-Obukhov length under dry-limit condition (dry-bound)	m
L_w	Monin-Obukhov length under wet-limit condition (wet-bound)	m
l_s	characteristic dimension of soil surface	m
n	windspeed extinction coefficient within the canopy in Massman (1997) model	-
N_b	number of replicated boxes through which the ray of radiation passes	-
N_c	number of grid-points that would be seen by the sensor	-
N_{hor}	number of grid-points in the horizontal direction of a canopy	

Symbol	Meaning	Unit
N_k	number of grid-points for each type of component within the IFOV	-
$N_{k,ij}$	number of grid points in direction (i,j) at grid point k	-
N_{layer}	number of layers in a 1D model, i.e. total leaf area index LAI divided by the thickness of one layer in LAI units: $LAI / \delta L$	-
N_s	number of sub-canopies in a box	-
N_{s_f}	number of grid-points with sunlit foliage	-
N_{sh_f}	number of grid-points with shaded foliage	-
N_{s_s}	number of grid-points with sunlit soil	-
N_{sh_s}	number of grid-points with shaded soil	-
N_z	number of grid-points in the vertical direction of a canopy	-
Nu	non-dimensional conductance Nusselt number	-
p	ambient air pressure	Pa
$P(\theta_v)$	angle-dependent "gap fraction" or "gap frequency"	-
$P(\theta_{s0}, \theta_v, \Delta\varphi)$	geometric parameter dependent only on view and illumination directions	-
P_{B1}	(or $P_{B1}(\theta)$) non-interceptance of direct radiation in a 1D model	-
P_{D1}	(or $P_{D1}(\theta)$) non-interceptance of diffuse radiation in a 1D model	-
$P_{D1,U}(Z_1)$	non-interceptance of diffuse radiation at position Z_1 from upper hemisphere in a 1D canopy	-
$P_{D1,L}(Z_2)$	non-interceptance of diffuse radiation at position Z_2 from lower hemisphere in a 1D canopy	-
$P_{Df}(\bar{\mathbf{r}})$	non-interceptance for diffuse radiation at grid-point $\bar{\mathbf{r}}$	-
$P_{Df,L}$	diffuse penetration probability for the lower hemisphere in 1D model	-
$P_{Df,U}$	diffuse penetration probability for the upper hemisphere in 1D model	-
$P_{Dr}(\bar{\mathbf{r}}, \boldsymbol{\Omega})$	non-interceptance for direct radiation at grid-point $\bar{\mathbf{r}}$ in the direction $\boldsymbol{\Omega}$	-
P_h	hemispheric gap frequency	-
$Phit_{ij}(\theta,\phi)$ (or $Phit_{ij}(\bar{\mathbf{r}})$)	hit-probability in the direction (θ,φ), i.e. in the sector i in the hemispheric band j (or at grid-point $\bar{\mathbf{r}}$)	-
Pr	Prandtl number	-

Symbol	Meaning	Unit
q	ratio of the horizontal correlation length of leaf projection and the height of the canopy layer	-
q_a	specific humidity of air	kg kg^{-1}
q_{ra}	relative humidity of air	-
$\bar{\mathbf{r}} = (x, y, z)$	coordinates of grid-points x: towards the east; y: towards the north z: upwards and being zero at the ground surface	-
r_{ae}	aerodynamic resistance for water vapor transfer	s m^{-1}
r_{ah}	aerodynamic resistance for heat transfer	s m^{-1}
r_{ah}'	aerodynamic-radiometric resistance because of the use of T_{rad} in a single-source model	s m^{-1}
$r_{ah, f}$	leaf boundary layer resistance	s m^{-1}
$r_{ah, f}(\bar{\mathbf{r}})$	leaf boundary layer resistance at grid-point $\bar{\mathbf{r}}$	s m^{-1}
r_{ah, s_f}	sunlit leaf boundary layer resistance	s m^{-1}
r_{ah, sh_f}	shadowed leaf boundary layer resistance	s m^{-1}
$r_{ah, s}$	soil surface boundary layer resistance	s m^{-1}
r_{ah, s_s}	sunlit soil surface boundary layer resistance	s m^{-1}
r_{ah, s_sh}	shadowed surface boundary layer resistance	s m^{-1}
r_{am}	aerodynamic resistance for momentum transfer	s m^{-1}
r_f	reflectance of leaf	-
r_{er}	excess resistance, accounts for the difference between T_{rad} and T_{aero}	s m^{-1}
r_{e0}	excess resistance, identifies the difference between aerodynamic resistance for momentum transfer r_{am} and aerodynamic resistance for heat transfer r_{ah}	s m^{-1}
r_{e0}'	aerodynamic-radiometric excess resistance	s m^{-1}
r_i	bulk internal resistance	s m^{-1}
r_k	reflectance of element k	-
r_s	soil reflectance	-
$r_{st}(\bar{\mathbf{r}}, \mathbf{\Omega_L})$	stomatal resistance of leaves in leaf angle class $\mathbf{\Omega_L}$ at grid-point $\bar{\mathbf{r}}$	s m^{-1}

Symbol	Meaning	Unit
$R_{atm}^{\downarrow}$	down-welling hemispheric atmospheric long-wave radiation flux density divided by π	W m^{-2} sr^{-1}
$R_{atm}^{\downarrow}\uparrow$	reflected down-welling atmospheric TIR radiation by the components at all the grid points in the IFOV	W m^{-2} sr^{-1}
$R_{atm,i}^{\uparrow}(\theta_v)$	upwelling atmospheric radiance at θ_v in channel i	W m^{-2} sr^{-1}
$R_{atm,i}^{\downarrow}$	downwelling hemispheric atmospheric radiance in channel i divided by π.	W m^{-2} sr^{-1}
$R_{atm}^{\downarrow}\uparrow'$	A radiance related to multiple scattering by canopy components of the down-welling atmospheric longwave radiation.	W m^{-2} sr^{-1}
R_{atm}^{fw}	reflection of the down-welling atmospheric radiance by the foliage and the soil components in the forward zenith view angle	W m^{-2}
R_{atm}^{nd}	reflection of the down-welling atmospheric radiance by the foliage and the soil components in the nadir zenith view angle	W m^{-2}
$R_{Df}^{U}(\vec{r},\Omega_L)$	diffuse flux density arrived at the upper side of the leaves with angle class Ω_L at grid-point $\vec{r}$	W m^{-2}
$R_{Df}^{L}(\vec{r},\Omega_L)$	diffuse flux density arrived by the lower side of leaves with angle class Ω_L at grid-point $\vec{r}$	W m^{-2}
$R_{Df}^{uh}(\vec{r})$	downward diffuse flux density from the upper hemisphere of a small plane at grid-point $\vec{r}$	W m^{-2}
$R_{Df}^{lh}(\vec{r})$	upward diffuse flux density from the lower hemisphere of a small plane at grid-point $\vec{r}$	W m^{-2}
$R_{Dr}^{U}(\vec{r},\Omega_L)$	direct radiation flux density arrived at the upper side of leaves with leaf angle Ω_L at grid-point $\vec{r}$	W m^{-2}
R_f	radiance from foliage	W m^{-2}
R_{fw}	radiance from the canopy in the forward zenith view angle	W m^{-2}
$R_{k,atm}^{\downarrow}\uparrow$	atmospheric long-wave radiance reflected by each point k is	W m^{-2} sr^{-1}
$R_k(\lambda,T_k)$	radiance emitted by the components at the kth grid point	W m^{-2} sr^{-1}
$R_k'(\lambda)$	radiance reflected by the components in the kth grid point, i.e. a fraction of the emittance by the components in the surrounding grid points	W m^{-2} sr^{-1}
$R_{k,scat}$	radiance emitted from surrounding grid-points and arrived at the surfaces of all leaves at the point k	W m^{-2} sr^{-1}
$R_L^{\downarrow}$	incoming long-wave radiation flux density	W m^{-2}
$R_L^{\uparrow}$	outgoing long-wave radiation flux density	W m^{-2}
R_n	net radiation flux density above canopy	W m^{-2}

Symbol	Meaning	Unit
$R_n(\vec{r})$	net radiation flux density integrated over all the leaf inclinations and orientations at a grid-point $\vec{r}$	W m^{-2}
$R_n(\vec{r}, \mathbf{\Omega_L})$	net radiation flux density in leaf angle class $\mathbf{\Omega_L}$ at a grid point $\vec{r}$	W m^{-2}
R_{nd}	radiance from the canopy in the nadir zenith view angle	W m^{-2}
$R_{n,f}$	net radiation flux density absorbed by foliage	W m^{-2}
$R_{n,s}$	net radiation flux density absorbed by soil surface	W m^{-2}
R_s	radiance from foliage	W m^{-2}
$R_s^{\downarrow}$	incoming solar radiation flux density	W m^{-2}
$R_s^{\uparrow}$	outgoing solar radiation flux density	W m^{-2}
R_{s0}	global solar radiation flux density on the horizontal surface above TOC	W m^{-2}
$R_{TIR}^{U}(\vec{r}, \mathbf{\Omega_L})$	absorbed TIR irradiance by the upper side of leaves with leaf angle $\mathbf{\Omega_L}$ at grid-point $\vec{r}$	W m^{-2}
$R_{TIR}^{L}(\vec{r}, \mathbf{\Omega_L})$	absorbed thermal irradiance by the lower side of leaves with leaf angle $\mathbf{\Omega_L}$ at grid-point $\vec{r}$	W m^{-2}
$R_{TIR}^{U}(\vec{r})$	absorbed TIR flux density by the soil grid-point $\vec{r}$	W m^{-2}
$R_{TIR,ij}^{U}(\vec{r}, \mathbf{\Omega_L})$	absorbed TIR irradiance from source sector i in the hemispherical band j	W m^{-2}
Rad	(or $Rad(\theta, \varphi)$) emitted radiance from a point $\vec{r}$ (or in the direction (θ, φ))	Wm^{-2}sr^{-1}
Re	Reynolds number	-
Re_*	roughness Reynolds number $Re_* = h_s u_* / v$	-
Ri	Richardson's number	-
R_λ	radiance measured by the radiometer at wavelength λ	W m^{-2} sr^{-1}
S	source or sink density of a scalar	nonspecific
$S_E(\vec{r})$	source/sink distribution for water vapor at grid-point $\vec{r}$	kg m^{-3} s^{-1}
$S_H(\vec{r})$	source/sink distribution for heat at grid-point $\vec{r}$	W m^{-3}
S_{H,s_f}	mean heat source term from sunlit foliage	W m^{-3}
S_{H,sh_f}	mean heat source term from shadowed foliage	W m^{-3}
S_{H,s_s}	mean heat source term from sunlit soil	W m^{-3}
S_{H,sh_s}	mean heat source term from shadowed soil	W m^{-3}
S_i	spherical albedo of atmosphere in channel i,	-

Symbol	Meaning	Unit
$S_{SH}(z)$	source/sink for heat at depth z in the soil	W m^{-3}
$S_{SW}(z)$	source/sink of water content at depth z in the soil	kg m^{-3} s^{-1}
S_{s0}	solar constant = 1367	W m^{-2}
t_{relax}	relaxation time of turbulent dispersion	s
tg_i	total gaseous transmittance in channel i associated with gaseous absorption along the sun-target-sensor atmospheric path	-
$T(\vec{r})$	mean temperature of components at grid-point $\vec{r}$	K
T_a	air temperature	K
T_{abs}	absolute temperature (equal to the thermal expansion coefficient for ideal gases	K
$T_{ac}(\vec{r})$	air temperature at grid-point $\vec{r}$	K
$T_{ac}(z_0)$	air temperature at reference height z_0 inside canopy	K
T_{aero}	aerodynamic temperature	K
T_{ap}	potential temperature of air	K
$T_b(\theta_v, \varphi_v)$	directional brightness temperature at TOA at zenith view angle θ_v and azimuth view angle φ_v	K
T_{bi} (or T_{bj})	TOA brightness temperature in channel i (or j)	K
$T_{bi,k}$ (or $T_{bj,k}$)	TOA brightness temperature in channel i (or j) in pixel k	K
$\overline{T_{bi}}$ (or $\overline{T_{bj}}$)	mean (or the median) TOA brightness temperature over N neighboring pixels of pixel k in channel i (or j)	K
T_{b0}	brightness temperature at BOA (or TOC)	K
$T_{b0}(\theta_v, \varphi_v)$	directional brightness temperature at BOA (or TOC) at zenith view angle θ_v and azimuth view angle φ_v	K
T_f	(mean) foliage temperature	K
$T_f(\vec{r})$	mean temperature of foliage at grid-point $\vec{r}$	K
$T_f(\vec{r}, \Omega_L)$	temperature of foliage in leaf angle class Ω_L at grid-point $\vec{r}$	K
T_{fw}	TOC brightness temperature in the forward zenith view angle	K
T_{ij}	mean temperature of a grid point that is located in the direction (θ, φ) (in sector i in band j)	K
T_k	temperature of element k	K
T_{nd}	TOC brightness temperature in the nadir zenith view angle	K
T_{rad}	TOC radiometric temperature	K

Symbol	Meaning	Unit
$T_{\text{rad}}(\theta_{\text{v}},\varphi_{\text{v}})$	TOC radiometric temperature at zenith view angle θ_{v} and azimuth view angle φ_{v}	K
T_{s}	(mean) soil temperature	K
$T_{\text{s}}(\vec{\mathbf{r}})$	(effective) soil surface temperature at the grid-point $\vec{\mathbf{r}}$	K
$T_{\text{s\_f}}$	mean sunlit foliage temperature	K
$T_{\text{sh\_f}}$	mean shaded foliage temperature	K
$T_{\text{s\_s}}$	mean sunlit soil temperature	K
$T_{\text{sh\_s}}$	mean shaded soil temperature	K
T_0	surface (aerodynamic or radiometric) temperature	K
$\overline{T_0}$	mean (or the median) TOC temperature over N neighboring pixels of pixel k	K
T_{11} (or T_{12})	brightness temperature at TOA in channel centered at 11 (or 12) μm	K
u	horizontal mean wind speed	m s^{-1}
$u(h_{\text{c}})$	windspeed at top of canopy	m s^{-1}
$u_{\text{ac}}(z_0)$	windspeed at reference height z_0 in the canopy	m s^{-1}
u_*	friction velocity	m s^{-1}
U	wind speed along x directions	m s^{-1}
V	wind speed along y directions	m s^{-1}
$\mathbf{V}_{\text{ij}}$	unit vector in the direction (θ,φ)	-
w	volumetric soil water content	kg m^{-3}
W	atmospheric water vapor content	kg m^{-2}
WD	wind direction	$^{\text{o}}$
z_{ref}	reference height above canopy	m
z_0	reference height in a canopy	m
z_{0e}	roughness length for water vapor transfer	m
$z_{0\text{h}}$	roughness length for heat transfer	m
$z_{0\text{m}}$	roughness length for momentum transfer	m
α	TOC albedo	-
α_{G}	coefficient of soil surface heat flux density as proportion of net radiation at the soil	-
α_{s}	albedo of soil surface	-
$\alpha_{\text{s\_f}}$	hemispherical fraction of sunlit foliage	-

Symbol	Meaning	Unit
α_{s_s}	hemispherical fraction of sunlit soil	-
α_{sh_f}	hemispherical fraction of shaded foliage	-
α_{sh_s}	hemispherical fraction of shaded soil	-
β	coefficient of thermal expansion of air	K^{-1}
δL	thickness of one canopy layer in LAI units	$m^2\,m^{-2}$
δV	a small volume centered at grid-point $\bar{\mathbf{r}}$	m^3
$\delta T(\bar{\mathbf{r}},\mathbf{\Omega_L})$	$= T_f(\bar{\mathbf{r}},\mathbf{\Omega_L}) - T_{ac}(\bar{\mathbf{r}})$	K
δz	thickness of grid-point in a canopy	m
$\delta \Omega$	solid angle for each pair of band and sector	sr
$\delta \varphi$	interval of azimuth angle	°
$\delta \theta$	interval of zenith angle	°
δ_0	$= 0.622$	-
Δ	rate of change of saturation vapor pressure with temperature	$Pa\,K^{-1}$
$\Delta T_{rad}/\Delta f$	$[T_{rad}(0) - T_{rad}(53)]\,/\,[f_f(53) - f_f(0)]$	-
ε	emissivity	-
$\varepsilon(\bar{\mathbf{r}})$	emissivity at grid-point $\bar{\mathbf{r}}$ which is either leaf or soil depending on the location of the grid-point	-
ε_a	effective atmospheric emissivity	-
ε_c	TOC emissivity at nadir view and in the broad band 8-14µm	-
$\varepsilon_c(\lambda,\theta_v,\varphi_v)$	effective directional emissivity of the foliage-soil mixture as observed at zenith view angle θ_v, azimuth angle φ_v and at wavelength λ	-
ε_f	emissivity of foliage	-
$\varepsilon_f^{'}(\theta_v)$	effective emissivity of foliage at zenith view angle θ_v	-
ε_k	emissivity of element k	-
$\varepsilon_k(\lambda)$	emissivity at wavelength λ and at grid point k which is either leaf or soil depending on the location of the grid-point	-
$\varepsilon_k(\lambda,\theta_v,\varphi_v)$	directional emissivity at wavelength λ and at grid-point k which is either leaf or soil depending on the location of the grid-point	-
ε_i (or $\varepsilon_i(\theta_v)$)	directional TOC emissivity in channel i (at zenith angle θ_v)	-
ε_{ij}	emissivity at grid-point in sector i and in band j (either leaf or soil depending on the location of the grid-point)	-

Symbol	Meaning	Unit
ε_{j}	(or $\varepsilon_{j}(\theta_{v})$)directional TOC emissivity in channel j (at θ_{v})	-
ε_{s}	emissivity of soil	-
$\varepsilon_{s\_f}{}'(\theta_{v})$	effective emissivity of sunlit foliage	-
$\varepsilon_{s}{}'(\theta_{v})$	effective emissivity of soil at zenith view angle θ_{v}	-
$\varepsilon_{s\_s}{}'(\theta_{v})$	effective emissivity of sunlit soil	-
$\varepsilon_{sh\_f}{}'(\theta_{v})$	effective emissivity of shaded foliage	-
$\varepsilon_{sh\_s}{}'(\theta_{v})$	effective emissivity of shaded soil	-
ε_{0}	land surface emissivity	-
ε_{11} (or ε_{12})	TOC emissivity in channel centered at 11 μm (or 11 μm)	
γ	psychrometric constant	Pa K^{-1}
γ	mean hemispherically integrated probability of escape of light without further interaction, after a scattering event at the land surface	-
λ	wavelength	μm
λ	latent heat for vaporization of water	J kg^{-1}
λ_{a}	thermal conductivity of air	W m^{-1} K^{-1}
λE	latent heat flux density	W m^{-2}
λE_{d}	latent heat flux density under dry-limit condition (dry-bound)	W m^{-2}
λE_{f}	latent heat flux density from foliage	W m^{-2}
$\lambda E_{f}(\bar{r},\Omega_{L})$	foliage latent heat flux density in leaf angle class Ω_{L} at grid-point $\bar{r}$	W m^{-2}
$\lambda E_{f}(\bar{r})$	foliage latent heat flux density over all leaf angle classes at grid-point $\bar{r}$	W m^{-2}
λE_{p}	potential evaporation flux density	W m^{-2}
λE_{s}	latent heat flux density from soil	W m^{-2}
$\lambda E_{s}(\bar{r})$	soil latent heat flux density at grid-point $\bar{r}$	W m^{-2}
Λ	evaporative fraction, defined as $\Lambda = \dfrac{\lambda E}{R_{n}-G}$	-
Λ_{r}	relative evaporation, $\Lambda_{r} = \dfrac{\lambda E}{\lambda E_{p}}$	-
Φ_{m}	stability correction function for heat transfer inside a canopy	-
ρ_{a}	air density	kg m^{-3}

Symbol	Meaning	Unit
ρ_f	foliage area density (foliage area per canopy volume)	$m^2\,m^{-3}$
$\rho_f(\vec{r})$	foliage area density (leaf area per canopy volume)	$m^2\,m^{-3}$
$\rho_{f,ij}(\vec{r})$	foliage area density in the jth sub-canopy in the ith box	$m^2\,m^{-3}$
ρ_i	reflectance in channel i at BOA	-
ρ_i^*	reflectance measured in channel i at TOA	-
$\rho_i^a(\theta_s,\theta_v,\Delta\varphi)$	atmospheric reflectance	-
$\rho_i^m(\theta_s,\theta_v,\Delta\varphi)$	land reflectance in channel i predicted by the parametric reflectance model	-
$\rho_{s\_f}(\vec{r})$	sunlit foliage area density (foliage area per canopy volume)	$m^2\,m^{-3}$
$\rho_{s\_s}(\vec{r})$	sunlit soil area density (soil area per canopy volume)	$m^2\,m^{-3}$
$\rho_{sh\_f}(\vec{r})$	shadowed foliage area density (foliage area per canopy volume)	$m^2\,m^{-3}$
$\rho_{sh\_s}(\vec{r})$	shadowed soil area density (soil area per canopy volume)	$m^2\,m^{-3}$
$\rho_s(\theta_v,\varphi_v-\varphi_{s0})$	soil bidirectional reflectance distribution function	-
φ	azimuth angle	o
φ_L	leaf orientation angle	o
φ_{s0}	solar azimuth angle	o
φ_v	azimuth view angle	o
θ	zenith angle	o
θ_{av}	virtual potential temperature of air	K
θ_{ij1}, θ_{ij2}	zenith limits of sector i in the hemispheric band j	o
θ_L	leaf inclination angle	o
θ_{s0}	solar zenith angle	o
θ_v	zenith view angle	o
Ψ_e	correction function for atmospheric stability for water vapor transfer	-
Ψ_h	correction function for atmospheric stability for heat transfer	-
Ψ_m	correction function for atmospheric stability for momentum transfer	-
ψ_s	soil matric potential	$J\,kg^{-1}$
Ω	solid angle of radiance	sr
Ω_{IFOV}	instantaneous field-of-view (IFOV) of radiometer	m

Symbol	Meaning	Unit
$\boldsymbol{\Omega}$	unit vector of the direction identified by θ and ϕ	-
$\boldsymbol{\Omega}_{\mathrm{L}}$	unit vector normal to a leaf with inclination θ_{L} and orientation φ_{L}	-
$\boldsymbol{\Omega}_{\mathrm{s0}}$	unit vector of the solar direction defined by solar zenith θ_{s} and solar azimuth φ_{s}	-
σ	Stefan-Boltzman's constant ($=5.678\times10^{-8}$)	W m^{-2} K^{-4}
τ_{a}	atmospheric transmittance in the visible- near-infrared spectrum	-
τ_{i} (or $\tau_{\mathrm{i}}(\theta_{\mathrm{v}})$)	directional total atmospheric transmittance along the target-sensor atmospheric paths in channel i (at θ_{v})	-
$\tau_{\mathrm{i}}(\theta_{\mathrm{s0}})$	total atmospheric transmittance along the sun-target atmospheric paths	-
τ_{j} (or $\tau_{\mathrm{j}}(\theta_{\mathrm{v}})$)	directional total atmospheric transmittance along the target-sensor atmospheric paths in channel j (at θ_{v})	-
τ_{0}	surface shear stress	kg m^{-2} s^{-1}
τ_{11} (or τ_{12})	transmittance of atmosphere in channel centered at 11 (or 12) μm	-
τ_{550}^{a}	aerosol optical depth at 550 nm (or aerosol loading)	-
υ	kinematic viscosity of air	m^{2} s^{-1}
ν_{e}	mean velocity of eddies	m s^{-1}
ω_{i}	Lambertian reflectance ω_{i} of surface component i	-

Chapter 1

Introduction

1.1   General description of the problems

The exchange of energy between the land surface and the atmosphere and within terrestrial vegetation canopies is a significant determinant of processes in the atmospheric boundary layer and in terrestrial ecosystems. In these processes, it is crucial to determine accurately the partitioning of available energy into sensible heat flux density H (heating or cooling of the surface) and latent heat flux density λE (evaporation from surface) over a wide range of spatial and temporal scales. Observation and modeling of turbulent heat fluxes at the land surface has been a very active area of research at least since the work of Bowen (1926) on the relative magnitude of heat transfer over dry and wet surfaces (Monteith, 1965 ; Feddes, 1971; Verma et al., 1976; Hall et al., 1979; Price, 1982; De Bruin and Jacobs, 1989; Beljaars and Holtslag, 1991; Lhomme et al, 1994; Sellers et al., 1995). Most conventional techniques that employ point measurements to estimate the components of energy balance are representative only of local scales and cannot be extended to large areas because of the heterogeneity of the land surface, of the dynamic nature and of the spatial distribution of heat transfer. Remote sensing is one of the few techniques which can provide representative measurements, e.g. surface temperature and albedo, at regional and global scales.

Methods using remote sensing techniques to estimate heat exchange at the land-atmosphere interface fall into two main categories: 1) use *surface radiometric temperature* T_{rad} to calculate H then obtain λE as the residual of the energy balance equation (Blad and Rosenberg, 1976; Seguin et al., 1989; Hatfield et al., 1984); 2) use T_{rad} to estimate the Crop Water Stress Index or the evaporative fraction (the ratio of evapotranspiration to the available energy) (Jackson et al., 1981; Menenti and Choudhury, 1993). The former category can be further subdivided into single-source, dual-source and multi-source models corresponding with a single-, dual- or multi-layer schematization of the surface respectively. Successful estimations of heat fluxes have been achieved over horizontal homogeneous surfaces, such as a surface fully covered by vegetation, open water and bare soil (Jackson, 1985; Huband and Monteith, 1986; Choudhury et al., 1986). Large deviations from these conditions occur at partial canopies which are geometrically and thermally heterogeneous. Recent years have seen increasing evidence of specific difficulties inherent to the heterogeneous nature of terrestrial vegetation. For instance, in many semi-arid environments where the surfaces are partially covered by vegetation, both the soil surface and cooler foliage determine the heat

exchanges. This leads to the challenge of relating the separate contributions from these elements to the turbulent transport of heat across the land-atmosphere interface.

1.2   Modeling heat exchanges using radiometric temperature

1.2.1   Three-dimensional nature of land surfaces and multi / dual-source model

The architecture of most vegetation canopies leads to a complex three-dimensional distribution of absorbed radiant energy and, therefore, of the local balance of energy within the canopy space (Fig. 1.1). On the one hand, within the canopy space the surface temperature of foliage and soil varies significantly. On the other hand, the vertical distribution of foliage temperature is also variable with the solar elevation, the density of leaves and the angle distribution of leaves. These thermal heterogeneity within a vegetation canopy leads to the fact that T_{rad} measured by thermal infrared (TIR) sensors is a function of canopy geometry, vertical distribution of foliage temperature distribution T_f, soil temperature T_s, sensor view angle (θ_v, φ_v) and incoming radiation (Kimes, 1980; Francois et al., 1997) (Fig. 1.2).

As discussed by Anderson et al. (1997) the resistance to heat transfer from the soil fraction of the observed soil-foliage mixture is often significantly larger than the resistance above the canopy. This is also proved by experimental results showing that the difference between T_{rad} and air temperature increased during morning and early afternoon relatively faster than H (Kustas, et al., 1989). It implies that the variation of resistance should also be taken into account accordingly to the shift of heat source from the cooler foliage to the warmer soil. From the theoretical point of view a dual-source model has been considered more realistic than a single-source model, since it apportions the net surface flux among the sources from which it emanates (Kustas, 1990). The sensible heat flux from the vegetated surface H comprises the sensible heat flux from the foliage (H_f) and from the soil (H_s).

Several dual- or multi-source models of heat transfer, have been developed to estimate the component heat fluxes from elements of the canopy, then the total flux from the canopy system (Shuttleworth and Wallace, 1985; Choudhury and Monteith, 1988; Smith et al., 1988).

Among current dual-source models, one of them makes use of a composite radiometric surface temperature, with the help of a relationship between the difference of two components temperatures and the difference between T_{rad} and T_{aero} (see §1.2.2 for the definition), the coefficients of which are site (or surface type) specific (Lhomme et al., 1994a,b) and highly sensitive to canopy properties and architecture.
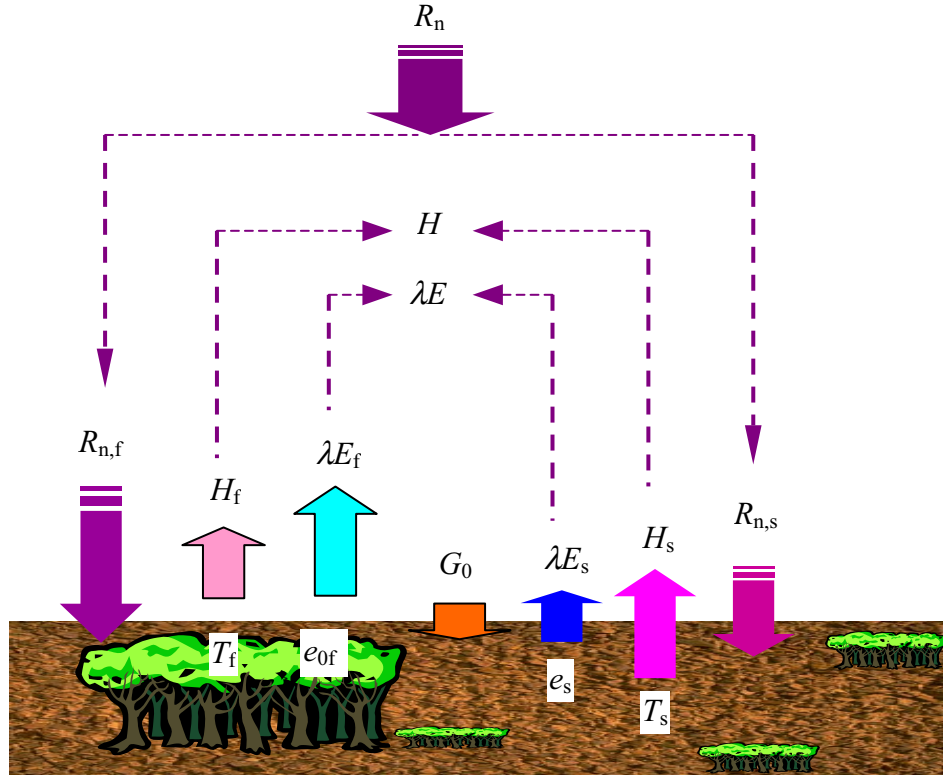
Figure 1.1 Schematic illustration of local energy balance in a dual-source model which represents heat transfer of a 3-D canopy.
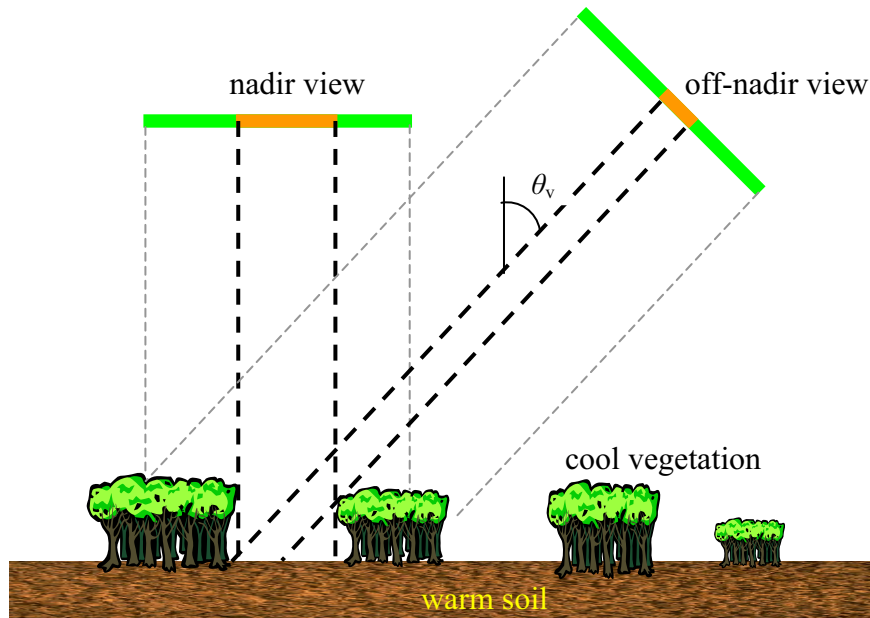
Figure 1.2 Illustration of observed TIR radiance as a function of canopy geometry, foliage and soil component temperatures and the zenith view angle θ_v. The green bar indicates the fraction of foliage in the instantaneous field of view (IFOV) of the sensor, the orange bar indicates the fraction of soil in the IFOV.

In recent studies, Norman et al. (1995) have developed a different dual-source model using component temperatures of soil and foliage, improved later by Anderson et al. (1997). In their earlier dual-source model framework, component temperatures were estimated by including an additional equation, i.e. a Priestley-Taylor approximation (Priestley and Taylor, 1972) because they were considered not available from thermal infrared measurements at a single viewing angle only. The performance of this dual-source model was evaluated later by Zhan et al. (1996). Compared with single-source models (Kustas et al., 1989; Troufleau et al., 1995) and the dual-source model by Lhomme et al. (1994a), the Norman et al (1995) dual-source model gave the best agreement with the measurements.

When component temperatures of soil and foliage can be measured or derived with acceptable accuracy, a challenge in a dual-source model (Kustas et al. 1996) is specifying the separate resistances to the heat transport from the soil and from vegetation to the surrounding atmosphere within the canopy (within-canopy resistances). Different researchers have used different resistance schemes to describe the heat exchanges between the within-canopy sources of heat and the air above the canopy in their dual-source model (Lhomme et al., 1994a; Norman et al., 1995), and achieved fair results over partial canopies. However, as shown by Ham and Heilman (1991), within-canopy resistance may not be described adequately using standard meteorological data. A more appropriate parameterization for within-canopy resistance needs to be developed that is applicable to large scale.

1.2.2   One-dimensional system and single-source models

In single-source models, the surface is treated as a single source of heat exchanged with the overlying atmosphere (see Fig. 1.3 for the schematic illustration). Sensible heat flux is related to the difference between the air temperature at a source height for heat transfer (so-called *aerodynamic surface temperature*, T_{aero}) and air temperature at a reference height within the surface layer, T_a. The exchange coefficient or traditional *aerodynamic resistance* (between source height and the reference height) for a single-source model is usually estimated on the basis of similarity theory. The source height is the fictive level at which the air temperature should take its 'surface' value. For homogeneous land surfaces, such as a dense canopy and bare soil, the single source concept is a suitable approximation because the portion of the surface dominating heat exchanges is thermally homogeneous. When using remote sensing TIR measurements in such a traditional single-source formulation, the assumption is generally made that the *surface radiometric temperature* (T_{rad}) measured by a radiometer is equivalent to T_{aero}. In reality, T_{aero} is mathematically computed from the extrapolation of a logarithmic profile to the effective source height, i.e. the roughness length

4

for heat transfer, z_{0h}, and is usually not measurable directly. For closed canopies, most of the incident solar radiation is intercepted and partitioned by the vegetation. In this case T_{rad} as measured by a thermal infrared sensor corresponds fairly well with T_{aero} and errors in heat flux estimation with a single-source model are small. Such approaches have been moderately successful for applications to surfaces with near complete canopy cover using ground-, aircraft- and space-based remotely sensed measurements (Verma et al., 1976; Hatfield et al., 1984; Reginato et al., 1985; Choudhury et al., 1986; Jackson et al., 1987; Kustas et al, 1994).
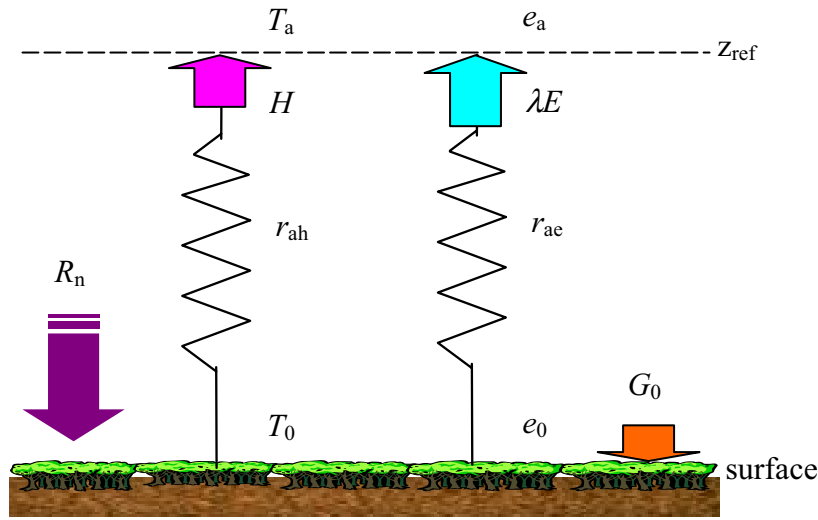
Figure 1.3 Schematic illustration of a single-source model to describe heat exchange between land-surface and the atmosphere. z_{ref} is the reference height in the overlaying atmosphere, T_0 is the surface temperature which is either T_{aero} or estimated by T_{rad}.

When using a single-source model in a vegetation canopy with thermal heterogeneity, the major problem arises from the substitution of T_{rad} for T_{aero}. Strictly speaking, considering the complex thermal heterogeneity in vegetation canopies, T_{rad} is generally not equivalent to T_{aero}.

T_{rad} is usually measured at nadir view, and in partial canopies may differ significantly from T_{aero}. Large differences between T_{rad} and T_{aero}, ranging up to 10°, have been observed (Choudhury et al., 1986; Huband and Monteith, 1986; Kustas et al., 1989) for partial canopies. Under unstable conditions, T_{rad} is higher than T_{aero}, particularly over a surface with only sparse vegetation. This can be attributed to the fact that a nadir viewing sensor would see more warmer soil surface which is heating rapidly with increasing incident radiation (**Fig. 1.2**). This implies that a single-source model overestimates the sensible heat flux. Different approaches have been developed to improve the accuracy of single-source models when they

are applied to thermally heterogeneous surfaces:

Using off-nadir T_{rad} measurements

To decrease the soil contribution, i.e. to increase the vegetation contribution to the signal captured by the sensor, so that observed T_{rad} is closer to T_{aero}, some authors suggested to use measurements at off-nadir zenith view angle in a single-source model so that estimated heat flux density is closer to observations (Nielsen et al., 1984). In the Huband and Monteith (1986) study, an optimum view zenith angle of 55°, depending on the position of the sun, was found with a 1°C difference between measured T_{rad} at this angle and the bulk surface temperature. Vinning and Blad (1992) concluded that this optimum viewing angle depends on the windspeed. By means of numerical experiments combined with field measurements, Matsushima and Kondo (1997) proposed that T_{rad} observations measured at a viewing angle of 50° to 70° from nadir were suitable to predict reliable H values using a single-source approach over a horizontally homogeneous rice paddy.

It seems that such an optimal angle, however, is unpredictable for operational use over various terrestrial surfaces at large scale. The only available space-borne TIR measurements at off-nadir view angle are currently provided by the Along-Track Scanning Radiometers (ATSR-1, ATSR-2) and Advanced ATSR (AATSR) on board the European Remote Sensing Satellites (ERS-1, ERS-2) and ENVIronmental SATellite (ENVISAT) at a 55° forward view angle besides the at-nadir measurements. However, there is no evidence showing this off-nadir view angle is the optimum one for all land surfaces.

Formulating the relationship between T_{rad} and T_{aero}

The equivalence of T_{rad} with T_{aero} has often been assumed in single-source models, there is no theoretical evidence, however, that supports this assumption. The other possible way to estimate H from T_{rad} using a single-source models is to establish a relationship between T_{rad} and T_{aero}.

The correction to T_{rad} through an empirical relationship between T_{rad} and T_{aero} leads to a more complex kB^{-1} formulation than a single value obtained by model calibration (Troufleau et al., 1997). Therefore, it may be more appropriate to account for the physical processes involved when H has to be inferred from T_{rad}. Chehbouni et al. (1996) have analyzed the relationship between the difference of T_{rad} and T_{aero} and the surface-air temperature gradient by coupling a hydrologic model with a vegetation growth model. Their results showed that the ratio between T_{rad-T_a} and T_{aero-T_a} is intimately related to LAI which should be

accounted for in any form of relationship between radiometric surface temperature and aerodynamic surface temperature, particularly for sparsely vegetated surfaces. This implies that the empirical coefficients involved in the approach of Chehbouni et al. (1996) need to be adjusted a priori and may be difficult to implement in practice.

The relationship between T_{rad} and T_{aero} has been studied by many researchers in the past decade, but this relationship is still empirical and needs to be adjusted according to vegetation type and structure. To use it as an operational approach over large areas is still a challenge. The relationship between T_{rad} and T_{aero} depends on the aerodynamic resistances (total, soil and vegetation resistances, i.e. r_{ah}, $r_{ah,s}$ and $r_{ah,f}$), fractional vegetation cover f_f, and the difference between the foliage temperature T_f and T_{aero} (Kalma and Jupp, 1990).

Since the change of T_{rad} with view angle reflects the thermal heterogeneity of partial canopies, it may provide additional information to parameterize heat exchanges within the canopy and between the canopy and the atmosphere. For instance, the relationship between T_{rad} and T_{aero} may be very complex so that it seems there is no hope to develop a simple and usable parameterization without using additional and relevant information such as the one provided by directional observations of T_{rad}.

Excess resistance method

The term '*excess resistance*', r_{e0}, has been commonly used to identify the difference between aerodynamic resistance for momentum transfer r_{am} and aerodynamic resistance for heat transfer r_{ah}:

$$r_{ah} = r_{am} + r_{e0} \qquad (1.1)$$

This *traditional 'excess resistance'* r_{e0} is commonly expressed as a function of a non-dimensional parameter kB^{-1} as:

$$r_{e0} = \frac{1}{k\,u_*} kB^{-1} \qquad (1.2)$$

with

$$kB^{-1} = \ln(z_{0m}/z_{0h}) \qquad (1.3)$$

where z_{0m} is the roughness length for momentum transfer, z_{0h} is the roughness length for heat transfer (Owen and Thompson, 1963; Chamberlain, 1968). The definition of kB^{-1} (Eq. 1.3) provides a measure of the difference in the mechanisms determining heat and momentum transfer (Thom, 1972): heat transfer near the surface is mainly controlled by

molecular diffusion, while momentum transfer is not only due to viscous shear but also due to pressure gradient (Brutsaert, 1982). Moreover, the airflow exchanges momentum with the upper canopy, whereas heat exchange is most intense in the canopy layer between leaves in the lower part of the canopy, soil and air. Heat in the canopy space is then dispersed through exchanges with the surface layer. As a consequence, the source height for heat transfer is lower than the sink height for momentum transfer. This is equivalent to say that the aerodynamic resistance for heat transfer is larger than aerodynamic resistance for momentum transfer. Therefore, the theoretical basis of the kB^{-1} parameter is strictly *aerodynamic*, i.e. related to the aerodynamic surface temperature. When using T_{rad} in a classic single-source model, the difference between T_{rad} and T_{aero} can be adjusted by adding an additional term r_{er} to the traditional aerodynamic resistance r_{ah} (Eq. 1.1):

$$r_{ah}' = r_{ah} + r_{er} \tag{1.4}$$

where r_{er} is the resistance to account for the difference between T_{rad} and T_{aero}. Substituting Eq. 1.1 to Eq. 1.4, r_{ah}' is

$$\begin{aligned} r_{ah}' &= r_{am} + r_{e0} + r_{er} \\ &= r_{am} + r_{e0}' \end{aligned} \tag{1.5}$$

where r_{e0}' is referred to as '*aerodynamic-radiometric excess resistance*', and r_{ah}' is the *aerodynamic-radiometric resistance* for heat transfer. By analog of with Eq. 1.2, this additional resistance r_{e0}' may be expressed as a supplementary correction for kB^{-1} (Eq. 1.3):

$$r_{e0}' = \frac{1}{k\,u_*}\,(kB^{-1})' \tag{1.6}$$

Thus, the term $(kB^{-1})'$, referred to as '*aerodynamic-radiometric kB^{-1}*, is a parameter to determine the *aerodynamic-radiometric excess resistance* r_{e0}', which relates H to T_{rad} and differs from its theoretical definition (Eq. 1.3) due to the use of T_{rad} instead of T_{aero} (see §4.4.2). For sake of simplicity, the symbols kB^{-1} and r_{ah} will be retained in this thesis, but one should note their meaning, i.e. aerodynamic and radiometric, if T_{rad} is used in a single-source model to estimate sensible heat flux.

If an appropriate value of kB^{-1} is determined, H can be estimated accurately by using T_{rad}. This is more efficient for dense and homogeneous crops ('permeable-rough' surfaces), where a kB^{-1} value of about 2~3, based on experimental data and physically based models, gives estimates of H in agreement with measurements (Garratt, 1978; Brutsaert, 1982;

Kalma and Jupp, 1990). However, there is no agreement on the value of kB^{-1} for partial canopies. A wide range of kB^{-1} values have been found, e.g. from 1 to 12 (Kustas et al., 1989; Beljaars and Holtslag, 1991; Stewart, 1994; Troufleau et al. 1997) over heterogeneous surfaces with various types and fractions of vegetation cover (see Table 1.1). Instantaneous values between 0 and 30 were even observed (Stewart, 1994; Troufleau et al. 1997). Troufleau et al. (1997) concluded that the mean value of kB^{-1} for each specific surface is not representative of the observed instantaneous variations.

Kustas et al. (1989) proposed to parameterize kB^{-1} as a function of both the difference of surface and air temperature and wind speed. Their semi-empirical relationship appears valid only within a limited range of the H value (Troufleau et al. 1997).

Table 1.1 Values of kB^{-1} at various (sparse) surfaces

Project(or site)	Surface type	kB^{-1} (avg)	kB^{-1} (std)	Reference author(s)
	Homogeneous, fully vegetated canopy	2 or 3		Brutsaert (1982)
Cabauw	Grassland	8.8	0.24	Beljaars & Holtslag (1991)
SEBEX	Savanna	5.8	2.9	Stewart et al. (1994)
SEBEX	Open forest	8.3	3.3	Stewart et al. (1994)
MONSOON 90	Grass	3.8	2.8	Stewart et al. (1994)
MONSOON 90	Shrubs	5.6	2.8	Stewart et al. (1994)
Owens Valley	Shrubs	8.0	3.8	Stewart et al. (1994)
Smith Creek Valley	Shrubs	12.4	5.9	Stewart et al. (1994)
Smoke Creek Desert	Shrubs	8.4	4.9	Stewart et al. (1994)
La Crau	Grass/Stones	4.5	2.1	Stewart et al. (1994)
HAPEX-Sahel	Fallow savannah	8.8	5.6	Troufleou et al. (1997)
HAPEX-Sahel	Millet	4	4.4	Troufleou et al. (1997)
HAPEX-Sahel	Millet	6.7	5.1	Troufleou et al. (1997)
HEIFE Gobi	Gobi with Shrubs	5.5	4.1	Jia et al. (2000)
AECMP'95 (HEIFE)	Desert with shrubs	12.3	6.0	Jia et al. (2000)

1.3   Potential utility of multi-angular thermal infrared measurements

1.3.1   Separation of component temperatures

From the above discussion, it seems very desirable to be able to measure the foliage and soil surface temperatures. In principle, such information can be obtained at very high spatial resolution (10^{-3} - 10^{-2} m) by measuring individual leaves and soil elements. This

observational approach, however, does not help to improve understanding and modeling heat transfer at larger spatial scales, as needed for example in advanced atmospheric models. It has been considered a difficult task to separate vegetation and soil temperatures based on the measurements of surface temperature from high-altitude sensors such as satellites, and therefore, this may restrict the applicability of a dual-source model to estimate sensible heat flux density H (Lhomme et al., 1994b). Some authors suggested to extract these temperatures from a relationship between surface temperature and vegetation index (Carlson, et al., 1994).

After the pioneering work of Kimes and Kirchner (1983), the existence and significance of anisotropy in the exitance of vegetation canopies has been studied as a potential source of information to quantify the thermal heterogeneity of vegetation canopies. There are several existing models for quantifying directional effects in the thermal infrared (see for instance Smith et al., 1981; Kimes, 1983; Hope et al., 1988; Sobrino and Caselles, 1990; Brunet et al., 1991; Paw U, 1992; Prévot et al., 1994).

Although the robust physics relating the anisotropy of exitance with the heterogeneity of surface temperature and, therefore, of radiation and heat transfer within the canopy space is beyond doubt, the problem remains of actually using this directional signal to improve models of heat transfer. There are two main elements in such a problem: 1) angular changes in exitance are relatively small, so only observations at very different angles give a signal significantly larger than the accuracy of observations; 2) the magnitude and the direction of angular changes depend on both canopy architecture and radiative forcing.

These problem elements lead to conflicting solutions: the second element should be addressed by using relatively complex models of radiative processes in the canopy space, while the first element limits to very few the number of significant and independent angular measurements of exitance. The latter implies that only very simple models (i.e. with very few unknowns) can be used to interpret the observations and to obtain estimates of the component temperatures of vegetation canopies. In principle one should consider at least four component temperatures: 1) sunlit foliage, 2) shadowed foliage, 3) sunlit soil, 4) shadowed soil. Additional unknowns are related to surface structure parameters, such as Leaf Inclination Distribution Function (LIDF), fractional cover of vegetation or Leaf Area Index (LAI), soil spectral emissivity, and foliage spectral emissivity, etc.

Recent work by Menenti et al. (2001) showed that a simplified linear model of directional exitance involving four unknowns only, i.e. the foliage and soil temperature, LAI and the difference in emissivity between 11 μm and 12 μm can be used to estimate the foliage and soil temperatures. Li et al., (2001) and Jia, et al. (2003b) used a similar simplified linear model of directional exitance but retrieved fractional vegetation cover $f_f(\theta_v)$ in different ways. These results show that the simplified approach is very promising, although several

10

aspects remain to be clarified. The latter relates especially to understand the relation of radiative and boundary layer forcing with the extent and direction of the directional signal and to evaluate in more detail the feasibility of using multi-angular (i.e. more than two view angles) observations.

1.3.2   Parameterization of aerodynamic-radiometric excess resistance

A number of parameterizations of kB^{-1} have been proposed by different researchers (see the detailed review by Verhoef et al., 1997; Massman, 1999; Blümel, 1999). These models are mainly aerodynamically based without considering the effects of thermal heterogeneity of the canopy on kB^{-1} except the empirical formulation of Kustas et al. (1989). The source height, i.e. the value of z_{0h}, will vary significantly with irradiance in partial canopies. Moreover, the parameterization of kB^{-1}, as discussed in §1.2.2, will become complex when relating it to the measured T_{rad} and is an *aerodynamic-radiometric* parameter. Previous studies (e.g. McNaughton and van den Hurk, 1995; Prévot, 1994 among others) have shown the strong dependence of kB^{-1} on aerodynamic and thermodynamic properties of the surface (McNaughton and van den Hurk, 1995; Prévot, 1994). Any proper parameterization of kB^{-1} must therefore consider the effects of the thermal heterogeneity of the vegetation canopy, in relation with the anisotropy of exitance. It may then be possible to deduce kB^{-1} from multi-angular observations of T_{rad} and then use a potentially accurate single-source heat transfer model.

1.4   Objectives of the thesis

The main objective of this thesis is to understand the relation of the thermal heterogeneity of the land surface with the dependence of exitance on view angle. Furthermore, to model exchanges of water and heat at heterogeneous land surfaces using a measure of thermal heterogeneity of the land surfaces, based on multi-angular measurements of emitted radiance obtained with ground and space sensors. Literature documents extensively the difficulty of modeling heat transfer at the land-atmosphere interface , without any characterization of the thermal heterogeneity of canopy space. This study aims at filling this gap.

To accomplish this task, radiative and convective processes in the canopy space will be described using a three-dimensional (3D) model to deal with a realistic canopy architecture. This complete model allows to *evaluate the relation between the anisotropy of exitance and the thermal heterogeneity of vegetation canopies in response to radiative forcing and boundary layer conditions*. Furthermore, it makes it possible to interpret *the effects of*

heterogeneous properties of vegetation canopies on the signal observed by a remote radiometer at a given view angle (Fig.1.2).

Based on the improved understanding of the anisotropy of exitance in the canopy*, simple linear mixture models of directional exitance* will be developed to reproduce observed anisotropy in exitance. The need for simpler radiative transfer models is that they involve fewer canopy variables and they are invertible to estimate the component temperatures of land targets. Complex models cannot be easily inverted to determine properties of heterogeneous land surfaces using measurements available at present.

The complete model will also be used to derive analytically *simpler heat transfer models*, i.e. *multi-source models and single-source model*, by reducing the number of sources (or sinks). *Multi-source models*, which *have better physical basis compared to single-source models*, requires a measure of the thermal heterogeneity of foliage-soil canopies in terms of component temperatures which may be determined by inverting a simple linear mixture model of directional exitance using radiance measurements at different view angles. To make single-source model still usable, a parameterization of resistance for heat transfer will be developed using directional thermal infrared measurements. *The accuracy of a single-source model is therefore improved by using this parameterization of resistance for heat transfer.*

A flowchart (Fig. 1.4) describes briefly the technical procedures from a complete model of radiative and convective transfer to simpler models. As a specific case, Fig. 1.5 shows the overview of approaches involved in developments of a dual-source and a single-source model for heat transfer.

Data required in this thesis are basically of two types: ground-based and satellite measurements. Field data were collected at different experimental areas with diverse surface conditions of homogeneity and heterogeneity. Bi-angular and multi-spectral observations from space were obtained with the ATSR-2 sensor systems onboard ERS-2.

1.5   Organization of the thesis

Chapter 2 reviews studies on the directionality of TIR radiance in soil-vegetation canopies. Canopy processes such as radiation, convection and conduction in a 3D canopy are then described in detail to characterize the energy exchanges with special reference to heterogeneous biomes with sparse vegetation cover.

Chapter 3 describes simplified models of TIR transfer in a soil-vegetation canopy based on the complete model presented in Chapter 2. Various degrees of simplification including four components, two components and the classic one component concept can be obtained to represent the canopy TIR properties. Such simple models can be inverted to determine component temperatures by using multi-angular TIR measurements.
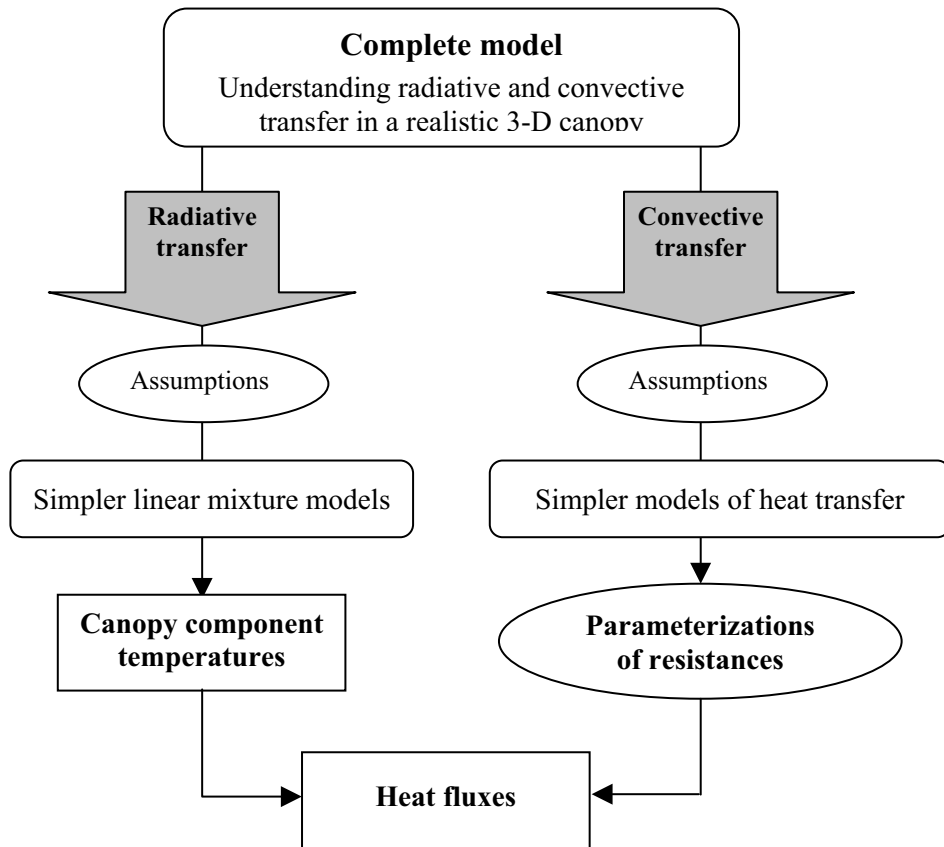
Figure 1.4 Illustration of procedures from a complete model for radiative and convective transfer in a canopy to simpler models of radiation and heat exchanges.
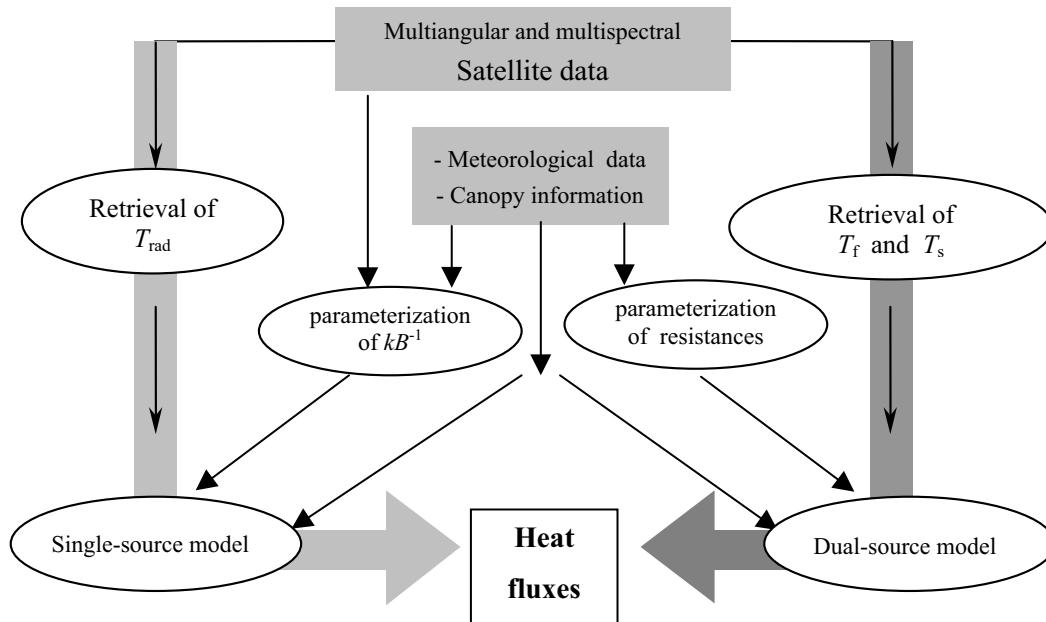
Figure 1.5 Overview of approaches developed in this thesis to model land – atmosphere sensible heat exchanges (H) using directionally thermal infrared (TIR) measurements.

Chapter 4 addresses the simplified model for heat and water vapor transfer in a soil-vegetation canopy based on the complete description given in chapter 2. Generic forms of the simplified model with four components, two components and the classic one component heat and water vapor transfer model are addressed first. Accordingly, specific dual- and single-source models are introduced to estimate heat and water vapor flux densities using the component temperatures derived by the simple TIR transfer models. A dual-source model for heat transfer between the land surface and the atmosphere is developed, which uses the component temperatures of soil and vegetation. A parameterization of the excess resistance for heat transfer in terms of kB^{-1} using bi-angular measurements of radiance in TIR and visible / near infrared (VIS/NIR) domain is proposed. This new parameterization will improve an existing single-source model by taking into account the anisotropy in the canopy exitance.

Chapter 5 describes the experiments and data used in this thesis. The data are basically put into two categories: local and regional scale measurements. The latter one includes satellite remote sensing observations.

In Chapter 6, the validation of the inversion of the simple linear TIR transfer model developed in Chapter 3 is done using directional surface temperature measurements made in field experiments with different land surface conditions. The sensitivity of the model inversion is also investigated for various canopy conditions.

Chapter 7 shows the application of the simple linear TIR transfer model to the bi-angular measurements of reflectances and emittance of the land surface made by ATSR-2 to derive component temperatures at the regional scale. A practical algorithm to invert the simple linear TIR transfer model with ATSR-2 data is developed, including the data pre-processing procedures associated with the atmospheric corrections both in the VIS/NIR channels and in TIR channels.

In Chapter 8, both the single- and dual-source models developed in Chapter 4 are first evaluated with field measurements of sensible heat flux density and then used to estimate the sensible heat flux density at the land-atmosphere interface at the regional scale by using the component temperatures (Chapter 7) retrieved by the inversion of the simple linear TIR transfer model in Chapter 3.

Chapter 2

Modeling thermodynamically heterogeneous soil-vegetation systems

2.1   Introduction

As reviewed in Chapter 1 the land surface-atmosphere interactions for complete vegetation canopies may be represented by a single-source model. For sparse canopies, however, a frequent case in nature, the interaction between the canopy and the atmosphere becomes complex due to the canopy geometry in terms of the size and spacing between plants, the leaf density and the leaf angle distributions. The complex canopy geometry determines the distribution of absorbed solar radiation in the canopy, thereafter inducing spatial variability of sources and sinks of heat and water vapor in the canopy space. A large spacing between plants or lower leaf density, for instance, makes the exposed soil to play an important role in the land-atmosphere interaction. Canopy geometry has also influence on the airflow in the canopy space and the boundary layer resistance of leaves and soil, thus changing the source/sink strength. The interaction between thermodynamic and dynamic processes will lead to thermal heterogeneity, which will in turn give rise to the anisotropy in the exitance of canopy.

The anisotropy in canopy exitance implies that *brightness temperature (T_{b0}) at the Top Of the Canopy (TOC) changes with view zenith angle θ_v and azimuth angle φ_v* as shown by many field measurements over a range of canopies, especially over sparse canopies. A number of models have been proposed and developed to describe radiation transfer in the canopy and the anisotropy of exitance. These modeling studies on the directionality properties in TIR domain can be grouped in the three categories described below.

Simple geometric model of the system

This approach applies to structured vegetation such as row crops, tree lines, and patches. As long as the geometry is known, the system can be simplified and described with a small number of known parameters, for example, height, width and spacing of elements, soil emissivity, and vegetation emissivity [Sutherland and Bartholic, 1977; Kimes et al., 1981; Kimes, 1983; Sobrino et al., 1990; Sobrino and Caselles, 1990; Caselles et al., 1992]. Attempts to incorporate a coupling with the down-welling atmospheric radiation have been scarce [Colton, 1996].

This modeling approach is quite useful for sensitivity studies. Except when the geometry is accurately known or can be inferred from other measurements (also from satellite), the

usefulness of this type of model, however, is limited since it cannot deal with the physical processes within the system, and model inversion is very sensitive to uncertainties in system properties.

Radiative transfer within the canopy

This approach applies to systems that can be described statistically using generic biome characteristics. Models in this domain try to solve radiative transfer in the canopy with atmosphere and soil state as boundary conditions, assuming plant type and distribution, plant architecture, LAI (total, horizontally / vertically projected), Leaf Inclination Distribution Function (LIDF), etc.). Examples of this approach were presented by Kimes (1981), Balick et al. (1987), McGuire et al. (1989), Norman and Chen (1990), Ottermann et al. (1992, 1995), Smith and Goltz (1995), Smith et al. (1996) and Ottermann et al. (1999). Soil temperature, leaf temperature, and temperature gradient within the canopy may either be assumed or be solved simultaneously. Observed TIR anisotropy may reveal whether there exists a temperature gradient within the canopy. However, interpretation of observed directional radiance implies that all properties of the system are known or can be accurately retrieved from other measurements, for example, from concurrent multi-spectral measurements in the visible (VIS), near infrared (NIR) and short-wave infrared (SWIR) domains.

Since the fluxes *within* the canopy are coupled to the fluxes *above* the canopy, the micrometeorological conditions have to be known. It turns out that the anisotropy of exitance is quite sensitive to ambient conditions (Stoll et al., 1998). For a given biome, the TIR-emitted radiance may reverse the sign of its angular variation with zenith angle (i.e. decrease or increase), or even show no variation at all (Jia et al, 2002).

This category of models may not lead directly to efficient algorithms to retrieve land surface properties. Nevertheless, radiative transfer models are extremely useful for (1) evaluating the order of magnitude of the angular effect that can be expected and (2) comparing what is observed with outputs of models. It is worth noting that the anisotropy in T_{b0} is in no case more than a few Kelvins, even if radiance is observed at large (> 60°) zenith angles in addition to nadir viewing.

Radiative transfer in an inhomogeneous thick vegetation layer

This approach can be statistically described by an angle-dependent "gap fraction" or "gap frequency" $P(\theta_v)$ (Nilson, 1971). This approach represents an intermediate situation between the two categories mentioned above. It allows the directional TIR radiance to be described as a weighted (by $P(\theta_v)$) contribution of foliage radiance and soil radiance. A detailed and comprehensive discussion of direct and inverse modeling is found in the work of François and Ottlé (1997). François et al. (1997) and François (2002) have investigated, in a very detailed stepwise manner, the performance of such linear mixture radiative model both

in forward and inverse mode using simulated datasets. Only the influences from the canopy structure rather than from the environmental factors were considered, however, and a one-dimensional, horizontal homogeneous canopy was assumed.

Hitherto, *most of the models to describe TIR directionality are built up on the basis of radiative transfer theory*. Although some of these models can be used to investigate radiative transfer in a canopy in relatively detailed manner, including a three-dimensional (3D) canopy structure, *the environmental dependence of TIR angular variation is usually not considered.* The exception is the one by Smith et al (1995). Their model did not include, however, heat and water transfer in the soil, while the latter is crucial in controlling the water supply for foliage transpiration and soil evaporation, which affects foliage and soil temperature. One existing model dealing with all important processes occurring in a canopy with respect to the directionality of thermal radiation is a one-dimensional (1D) model proposed by Norman (1979). The limitation of this model is that it treats the canopy as a horizontally homogeneous one, and it may not be sufficient to investigate the relation of thermal heterogeneity with the anisotropy of exitance for a sparse canopy.

As a matter of fact, radiative and thermal properties of a soil-vegetation canopy system are strongly dependent on its geometric structure (radiative transfer) and on its environmental situation (convection and conduction processes). Fig. 2.1 illustrates how the elements in a sparse canopy are interacting with their environment. The interactions between the land surface and the atmosphere consist of the interactions between foliage and soil surface, foliage and air in the canopy space, soil surface and air in the canopy space, and between the soil surface and deeper soil layers, i.e. root zone. A realistic model requires describing the processes involved at each spatial point. However, it may not be possible or necessary to do so. Adequate simplification is necessary to redefine the canopy, which should retain the dominant aspects of 3D radiative, heat and mass transfer.

A comprehensive 3D soil-vegetation-atmosphere model therefore is developed first based on some previous work to describe the radiative, convective and conductive transfer in a partial canopy. *This model allows to simulate the directional variability in TIR radiance under various soil, vegetation and atmospheric conditions, based on the energy balance of the soil-vegetation canopy.*

In this chapter, the canopy constructions used in the 3D model are first set up. Working assumptions and equations are then given for all processes involved.
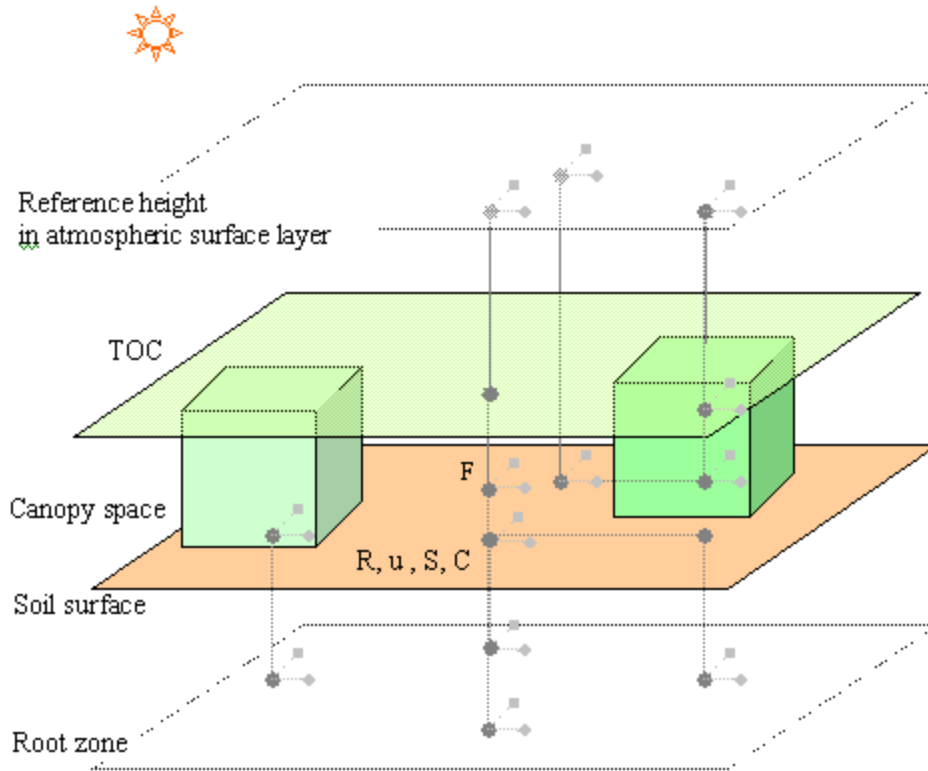
Figure 2.1 Simplified schematic illustration of interactions between points (either containing foliage or soil) in a three-dimensional canopy (soil + vegetation) and in the atmosphere just above the TOC, with all possible physical, chemical and biophysical processes included. TOC is represented by 'green plane' while soil surface is represented by 'orange plane'. The green blocks represent sub-canopies. Points are symbolized by symbol '•', interaction between points are represented by 'lines'. The symbol ⟋• implies that the interactions are 3D (vertical and horizontal exchanges). Each point is characterized by absorbed radiation flux density R, windspeed u, concentration C of a scalar (i.e. temperature, moisture, CO_2, etc), source/sink S of a scalar. F represents the flux density of a scalar between points.

2.2   Canopy geometry construction

2.2.1   Introduction

The basic construction of the canopy is 3D and it will be applied to describe radiation penetration to any point in a canopy. The direct radiation flux at each point (considering a small surface at that point) is simply a fraction of solar radiation at the top of the canopy multiplied by the penetration probability, while all the possible sources for diffuse radiation to a point must be taken into account. A multiple scattering theory (Norman and Jarvis, 1975) for a 1D layered canopy will be used to compute the diffuse radiation fluxes at any point in the canopy. To make such model applicable in a 3D canopy, an equivalent one-dimensional

canopy is necessary. In this section, both 3D and 1D canopy constructions used in this chapter are described below.

The 1D scheme will be utilized to describe heat and water vapor transfer throughout the canopy from above the canopy to the soil. Though points (either leaves or soil surface; see Fig.2.1) absorb different amounts of net radiation depending on their locations in the canopy, heat and water vapor transfer inside the canopy is controlled solely by the vertical variability of wind speed, air temperature and vapor pressure. These ambient variables inside the canopy space are assumed to be horizontally homogeneous (see the discussion in the following §2.5.1).

2.2.2   Three-dimensional canopy construction

In this study, following Welles and Norman (1991), *a canopy is defined by means of sub-canopies whose outer envelope has an ellipsoidal shape*. Sub-canopies can be individual trees or crops, even entire rows. Foliage within the ellipsoidal envelops of sub-canopies is assumed randomly distributed as an arbitrary function of zenith angle and random azimuthal distribution. A fraction of the top and/or bottom of each ellipsoidal sub-canopy can be chopped off so that a larger range of sub-canopy shapes can be dealt with.

An arbitrary box may be used to encompass the sub-canopies as shown in Fig. 2.2 for three different canopies: a row crop canopy, an orchard canopy, and a deciduous forest canopy. The box is then replicated along the horizontal extent of canopy allowing a canopy of large extent to be specified without necessarily specifying the location and size of each sub-canopy.

Each box volume is described by a set of grid-points equally spaced in the vertical and horizontal directions throughout the box. Grid-points are defined by their coordinates $\bar{\mathbf{r}} = (x, y, z)$ with x towards the east, y towards the north, and z upwards and being zero at the ground surface. The term 'grid-point', therefore, represents a *small volume δV centered at $\bar{\mathbf{r}}$*. The number and spacing of grid-points within the box is somewhat arbitrary; they should be sufficiently dense to represent the smallest sub-canopies without making the computational time prohibitive. A grid-point within the sub-canopies is assumed to have a certain amount of foliage. The grid-points are the basic units in the 3D model to compute the radiation, heat and water vapor flux densities. Direct beam radiation from the sun, the diffuse radiation from the sky and soil, and the diffuse radiation scattered by foliage are calculated at each grid-point. This description of geometry may also be used to model convection of heat and water vapor.
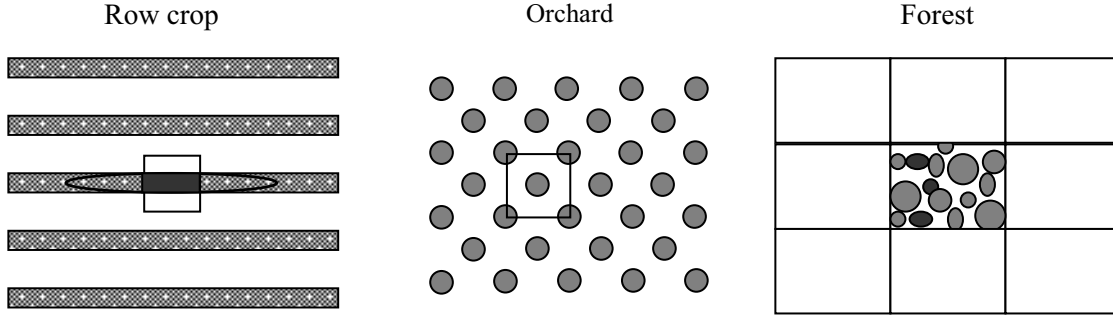
Figure 2.2 The 2-D top-view representations of three types of canopies: row crop, orchard and mixed hard wood forest. The square frames denote the 'box' as defined in the text. (Reproduced from Welles and Norman, 1991).

For the radiative transfer calculation, the spherical coordinate system used in Kimes (1981) is applied to deal with the irradiance and the associated emitting source directions at each grid-point. Taking a small flat element at the center of each grid-point, the upper and lower hemisphere of this small element (referred to as mid-plane) are discretized into 9 zenith angle θ classes (referred to as hemispherical bands) between 0° and 90° and 18 azimuth angle φ classes (referred to sectors) between 0° and 360° with intervals of 10° for $\delta\theta$ and $\delta\varphi$, i.e. $\theta_2 - \theta_1 = \theta_3 - \theta_2 = ... = \theta_9 - \theta_8 = 10^{\circ}$ and $\varphi_2 - \varphi_1 = \varphi_3 - \varphi_2 = ... = \varphi_{18} - \varphi_{17} = 10^{\circ}$ (Fig. 2.3). The radiation flux density applies to a direction (θ, φ) determined by the band and the sector. The solid angle for each pair of bands and sectors, $\delta\Omega$, is

$$\delta\Omega = \sin\theta \; \delta\theta \; \delta\varphi \tag{2.1}$$
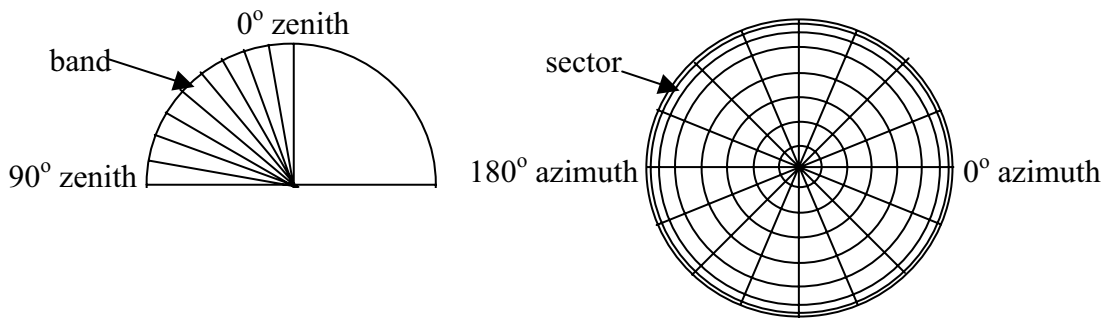
Figure 2.3 The hemisphere of a small plane at grid-point is discretized into 9 zenith angles (bands $\delta\theta$) and 18 azimuth angles (sectors $\delta\varphi$).

20

2.2.3 One-dimensional canopy construction

The one-dimensional canopy construction is applied to: (1) calculate diffuse radiation fluxes for each grid-point; (2) model convection of heat and water vapor within the canopy and in the atmosphere immediately above TOC and (3) model conduction of heat and water content in the soil.

For the first aspect, an equivalent 1D canopy will be introduced. This infinite, horizontally homogeneous canopy is divided into layers along the vertical direction. The number of layers is calculated in the model and is dependent on the total leaf area index: $N_{\text{layer}} = LAI\big/\Delta L$, ΔL is the thickness of one layer in LAI units.

For the second and the third aspect, the atmosphere above TOC and the soil is also divided in layers. Physical variables in the atmosphere and in the soil used in the model are layer dependent rather than point dependent. The zero plane reference is set at the ground surface, Z is positive away from the reference plane.

2.3 Heterogeneity of radiative transfer within a 3D canopy

2.3.1 Non-interceptances of radiation in a 3D canopy

The radiance incident onto a canopy will be attenuated due to the absorption and scattering of the leaves inside the canopy.

In any canopy, the probability of a ray of direct radiation passing through the canopy and reaching a grid-point at $\vec{r}$ along the path length D (m) through the canopy without being intercepted, $P_{\text{Dr}}(\vec{r}, \mathbf{\Omega})$, is given by

$$P_{\text{Dr}}(\vec{r}, \mathbf{\Omega}) = \exp\left[-\int_0^D G(\vec{r},\mathbf{\Omega})\,\rho_{\text{f}}(\vec{r})\,\mathrm{d}\vec{r}\right] \tag{2.2}$$

where $G(\vec{r},\mathbf{\Omega})$ (-) is the fraction of leaf area that is projected towards the source of radiation in the direction $\mathbf{\Omega}$ and is referred to as *extinction coefficient* ($\mathbf{\Omega}$ is the unit vector of the direction identified by θ and φ.), $\rho_{\text{f}}(\vec{r})$ $(\text{m}^2\,\text{m}^{-3})$ is the foliage area density (the leaf area per canopy volume). $P_{\text{Dr}}(\vec{r},\mathbf{\Omega})$ is referred to as the *non-interceptance of direct radiation* (e.g. Welles and Norman, 1991).

For a given grid-point $\vec{r}$ within the box of a canopy (see §2.2.2), $P_{\text{Dr}}(\vec{r},\mathbf{\Omega})$ is expressed as

$$P_{\text{Dr}}(\vec{r}, \mathbf{\Omega}) = \exp\left[-\sum_{i=1}^{N_{\text{b}}}\sum_{j=1}^{N_{\text{s}}} G_{\text{ij}}(\vec{r},\mathbf{\Omega})\,\rho_{\text{f,ij}}(\vec{r})\,D_{\text{ij}}(\vec{r},\mathbf{\Omega})\right] \tag{2.3}$$

The symbols used in Eq. 2.3 have the following meaning, respectively,

N_b — the number of replicated boxes through which the ray passes

N_s — the number of sub-canopies in any box

$G_{ij}(\vec{r}, \mathbf{\Omega})$ — the extinction coefficient in the jth sub-canopy in the ith box, determined by the leaf inclination/orientation distribution

$\rho_{f,ij}(\vec{r})$ — the foliage area density in the jth sub-canopy in the ith box

$D_{ij}(\vec{r}, \mathbf{\Omega})$ — the distance the ray travels through the jth sub-canopy in the ith box

with $i=1,2,3\cdots\cdots N_b$ and $j=1,2,3\cdots\cdots N_s$.

Once the canopy geometry has been defined and $\rho_{f,ij}(\vec{r})$ is known from measurements, the major task is to compute $D_{ij}(\vec{r}, \mathbf{\Omega})$ in Eq.2.3. $D_{ij}(\vec{r}, \mathbf{\Omega})$ can be determined according to the geometry knowing the shapes and sizes of the sub-canopies, the spacing between the sub-canopies and the direction of the ray of radiation. Norman and Welles (1983) and Welles and Norman (1991) gave the general expression of computing $D_{ij}(\vec{r}, \mathbf{\Omega})$ for nonrandom array canopies with ellipsoidal sub-canopies (Fig. 2.4). A ray enters the box at point $\vec{r}_1$ then goes out from it at point $\vec{r}_2$ after passing a distance within the sub-canopy between points $\vec{r}_3$ and $\vec{r}_4$. The distance between points $\vec{r}_3$ and $\vec{r}_4$ is calculated from their coordinates (Norman and Welles, 1983; Welles and Norman, 1991).

The probability of penetration of diffuse radiation to the point $\vec{r}$ from the upper hemisphere, $P_{Df}(\vec{r}, \mathbf{\Omega})$, which is referred to as the *non-interceptance of diffuse radiation*, is derived by integrating $P_{Dr}(\vec{r}, \mathbf{\Omega})$ over the upper hemisphere (Norman and Welles, 1983):

$$P_{Df}(\vec{r}, \mathbf{\Omega}) = \frac{\int_0^{2\pi} \int_0^{\pi/2} P_{Dr}(\vec{r}, \mathbf{\Omega}) \sin\theta \cos\theta \, d\theta d\varphi}{\pi} \tag{2.4}$$

The $P_{Df}(\vec{r}, \mathbf{\Omega})$ from the lower hemisphere at point $\vec{r}$ is obtained by a similar expression except that the zenith angles of integration are negative i.e. $[-\pi/2, 0]$.

The probability of penetration of thermal infrared radiation emitted from leaves in the upper (lower) hemisphere to the point $\vec{r}$ inside canopy is treated in the same way as diffuse radiation.
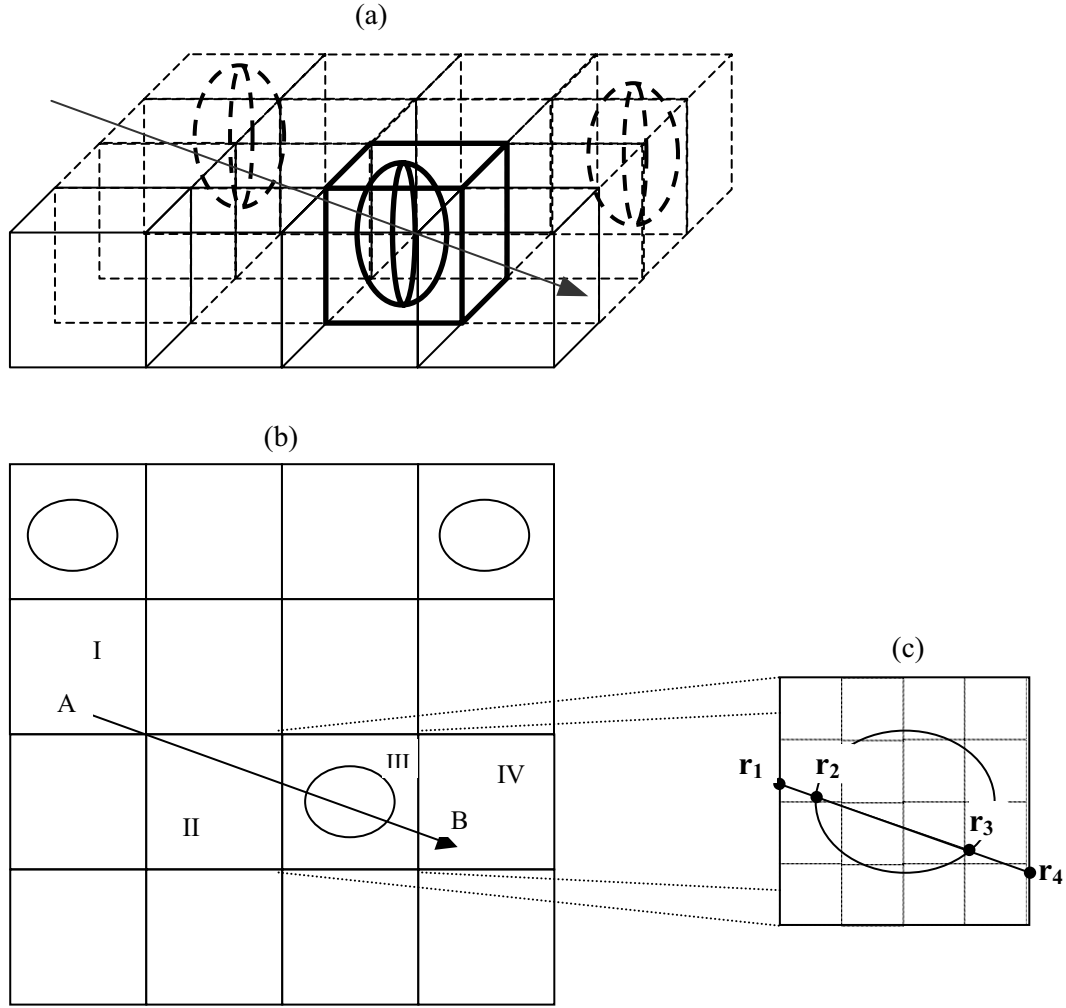
Figure 2.4 An illustration of a ray traveling into a canopy box: (a) The ensemble of boxes is the array canopy. (b) The top view of the boxes. (c) Details of a ray traveling in one box containing a sub-canopy. The boxes are divided by grid-points. A ray enters the canopy at point A, and travels to the point B, going through parts of four replicated boxes numbered I, II, III, and IV respectively.

2.3.2   Radiation budget at any point in a 3D canopy

Direct radiation flux density

Knowing the *non-interceptance of direct radiation* $P_{\text{Dr}}(\vec{\mathbf{r}}, \boldsymbol{\Omega}_{s0})$, the direct radiation flux density arriving at the upper side of leaves in the leaf angle class $\boldsymbol{\Omega}_{\mathbf{L}}$ (unit vector normal to a leaf with inclination $\theta_{\mathbf{L}}$ and orientation $\varphi_{\mathbf{L}}$) at any grid-point $\vec{\mathbf{r}}$, $R_{\text{Dr}}^{\text{U}}(\vec{\mathbf{r}}, \boldsymbol{\Omega}_{\mathbf{L}})$, is

$$R_{\mathrm{Dr}}^{\mathrm{U}}(\vec{\mathbf{r}},\mathbf{\Omega}_{\mathbf{L}}) \;=\; P_{\mathrm{Dr}}(\vec{\mathbf{r}},\mathbf{\Omega}_{s0})\frac{R_{s0}f_{\mathrm{Dr}}}{\cos\theta_{\mathrm{s}}}\big|\mathbf{\Omega}_{s0}\cdot\mathbf{\Omega}_{\mathbf{L}}\big| \tag{2.5}$$

where R_{s0} is the total solar radiation flux density on the horizontal surface above TOC, f_{Dr} is the fraction of R_{s0} that is direct beam, $\mathbf{\Omega}_{s0}$ is the unit vector of the sun direction (defined by solar zenith θ_{s0} and azimuth φ_{s0}).

Diffuse radiation flux density

Assuming diffuse irradiance is isotropic, the diffuse flux density arrived at the upper side of the leaves with angle class $\mathbf{\Omega}_{\mathbf{L}}$ at grid-point $\vec{\mathbf{r}}$, $R_{\mathrm{Df}}^{\mathrm{U}}(\vec{\mathbf{r}},\mathbf{\Omega}_{\mathbf{L}})$, is proportional to the downward diffuse flux density from the upper hemisphere $R_{\mathrm{Df}}^{\mathrm{uh}}(\vec{\mathbf{r}})$ and upward diffuse flux density from the lower hemisphere $R_{\mathrm{Df}}^{\mathrm{lh}}(\vec{\mathbf{r}})$ at the horizontal surface at $\vec{\mathbf{r}}$ as $\dfrac{1+\cos\theta_{\mathrm{L}}}{2}$ and $\dfrac{1-\cos\theta_{\mathrm{L}}}{2}$ (Ross, 1981), respectively,

$$R_{\mathrm{Df}}^{\mathrm{U}}(\vec{\mathbf{r}},\mathbf{\Omega}_{\mathbf{L}}) \;=\; \frac{1+\cos\theta_{\mathrm{L}}}{2}R_{\mathrm{Df}}^{\mathrm{uh}}(\vec{\mathbf{r}}) \;+\; \frac{1-\cos\theta_{\mathrm{L}}}{2}R_{\mathrm{Df}}^{\mathrm{lh}}(\vec{\mathbf{r}}) \tag{2.6}$$

The diffuse flux density arrived at the lower side of leaves with angle class $\mathbf{\Omega}_{\mathbf{L}}$ at $\vec{\mathbf{r}}$, $R_{\mathrm{Df}}^{\mathrm{L}}(\vec{\mathbf{r}},\mathbf{\Omega}_{\mathbf{L}})$, is

$$R_{\mathrm{Df}}^{\mathrm{L}}(\vec{\mathbf{r}},\mathbf{\Omega}_{\mathbf{L}}) \;=\; \frac{1+\cos\theta_{\mathrm{L}}}{2}R_{\mathrm{Df}}^{\mathrm{lh}}(\vec{\mathbf{r}}) \;+\; \frac{1-\cos\theta_{\mathrm{L}}}{2}R_{\mathrm{Df}}^{\mathrm{uh}}(\vec{\mathbf{r}}) \tag{2.7}$$

In Eqs. 2.6 and 2.7, to calculate $R_{\mathrm{Df}}^{\mathrm{uh}}(\vec{\mathbf{r}})$ and $R_{\mathrm{Df}}^{\mathrm{lh}}(\vec{\mathbf{r}})$ in a 3D canopy, all the possible diffuse sources must be taken into account which is difficult to deal with. In this study, $R_{\mathrm{Df}}^{\mathrm{uh}}(\vec{\mathbf{r}})$ and $R_{\mathrm{Df}}^{\mathrm{lh}}(\vec{\mathbf{r}})$ are calculated by using a multiple scattering theory for a 1D layered canopy as developed by Norman and Jarvis (1975), and the detailed calculation is given in Appendix I.

Thermal irradiance

The flux density in the thermal infrared region arriving at the surface of leaves at any grid-point $\vec{\mathbf{r}}$ in the canopy (denoted with subscript 'TIR') originates from the emissions of leaves in the grid-points surrounding $\vec{\mathbf{r}}$.

The absorbed thermal irradiance by the upper side of leaves with leaf angle $\mathbf{\Omega_L}$ at grid-point $\vec{r}$, $R_{TIR}^U(\vec{r},\mathbf{\Omega_L})$, is expressed (see Appendix II for details) in terms of the temperature of emitting elements by Stefan-Boltzman law:

$$R_{TIR}^U(\vec{r},\mathbf{\Omega_L}) = \varepsilon(\vec{r})\sigma\sum_{i=1}^{18}\sum_{j=1}^{9}\varepsilon_{ij}\,T_{ij}^4\,Phit_{ij}(\theta_{ij},\varphi_{ij})\frac{(\sin\theta_{ij2}-\sin\theta_{ij1})}{9}\mathbf{V}_{ij}\cdot\mathbf{\Omega_L} \qquad (2.8)$$

where $Phit_{ij}(\theta,\phi)$ is the hit-probability in the direction (θ,φ), i.e. in sector i in band j, θ_{ij1} and θ_{ij2} are the zenith limits of sector i in the hemispherical band j, $\mathbf{V}_{ij}$ is the unit vector in the direction (θ,φ). In Eq. 2.8 the use of symbol $\varepsilon(\vec{r})$ (and ε_{ij}) for emissivity indicates that the value of emissivity is either taken as the one for foliage, ε_f, or the one for soil, ε_s, depending on the location specified by $\vec{r}$ (and the location of sector i in band j).

In Eq. 2.8, T_{ij} is the mean temperature of a grid-point that is located in the direction (θ,φ). For a grid-point at $\vec{r}$ containing foliage, the mean temperature at this grid-point, $T_f(\vec{r})$, is defined by averaging the temperature of leaves in leaf angle class $\mathbf{\Omega_L}$ at the grid-point $\vec{r}$, $T_f(\vec{r},\mathbf{\Omega_L})$, over all the leaf angle class $\mathbf{\Omega_L}$ weighted by the respective fraction of leaf area $F(\vec{r},\mathbf{\Omega_L})$ in each $\mathbf{\Omega_L}$:

$$T_f(\vec{r}) = \sum_{\mathbf{\Omega_L}} F(\vec{r},\mathbf{\Omega_L})T_f(\vec{r},\mathbf{\Omega_L}) \qquad (2.9)$$

The same formula applies to T_{ij}.

The calculation of the absorbed thermal irradiance by the lower side of leaves with leaf angle $\mathbf{\Omega_L}$ at grid-point $\vec{r}$, $R_{TIR}^L(\vec{r},\mathbf{\Omega_L})$, is similar to Eq. 2.8 except the emitting sources are in the lower hemisphere.

Radiation budget of a grid-point

Assuming the leaf is a Lambertian scatterer and isotropic emitter, the net radiation flux density in leaf angle class $\mathbf{\Omega_L}$ at a grid-point $\vec{r}$, $R_n(\vec{r},\mathbf{\Omega_L})$, is expressed as:

$$\begin{aligned}R_n(\vec{r},\mathbf{\Omega_L}) = {}&(1-r_f)\,R_{Dr}^U(\vec{r},\mathbf{\Omega_L})\\&+(1-r_f)\,R_{Df}^U(\vec{r},\mathbf{\Omega_L})+(1-r_f)\,R_{Df}^L(\vec{r},\mathbf{\Omega_L})\\&+R_{TIR}^U(\vec{r},\mathbf{\Omega_L})+R_{TIR}^L(\vec{r},\mathbf{\Omega_L})-2\varepsilon_f\sigma[T_f(\vec{r},\mathbf{\Omega_L})]^4\end{aligned} \qquad (2.10)$$

where r_f is the reflectance of leaf. Thus, the last term on the right hand side of Eq. 2.10 is the emission from the leaves at the grid-point $\vec{r}$ and double sides of each leaf are considered.

The net radiation integrated over all leaf inclinations and orientations at a grid-point $\vec{r}$, $R_n(\vec{r})$, can be expressed as,

$$R_n(\vec{r}) = (1-r_f)\int_{2\pi} R_{Dr}^U(\vec{r},\mathbf{\Omega_L})\,d\mathbf{\Omega_L}$$
$$+ (1-r_f)\int_{2\pi} R_{Df}^U(\vec{r},\mathbf{\Omega_L})\,d\mathbf{\Omega_L} + (1-r_f)\int_{2\pi} R_{Df}^L(\vec{r},\mathbf{\Omega_L})\,d\mathbf{\Omega_L} \qquad (2.11)$$
$$+ \int_{2\pi} R_{TIR}^U(\vec{r},\mathbf{\Omega_L})\,d\mathbf{\Omega_L} + \int_{2\pi} R_{TIR}^L(\vec{r},\mathbf{\Omega_L})\,d\mathbf{\Omega_L} - 2\int_{2\pi} \varepsilon_f \sigma[T_f(\vec{r},\mathbf{\Omega_L})]^4\,d\mathbf{\Omega_L}$$

If the grid-point $\vec{r}$ is on the soil surface, $R_n(\vec{r})$ is calculated by assuming Lambertian scattering of diffuse radiation and non-Lambertian scattering of direct radiation:

$$R_n(\vec{r}) = R_{s0}f_{Dr}P_{Dr}(\vec{r},\mathbf{\Omega}_{s0})$$
$$- \alpha_s\left[R_{s0}f_{Dr}P_{Dr}(\vec{r},\mathbf{\Omega}_{s0})\int_0^{2\pi}\int_0^{\pi/2}\frac{\rho_s(\theta_{s0},\theta_v,\varphi_v-\varphi_{s0})}{\rho_s(0,0)}\sin\theta_v\,d\theta_v\,d\varphi_v\right] + (1-\alpha_s)R_{Df}^{uh}(\vec{r}) \quad (2.12)$$
$$+ R_{TIR}^U(\vec{r}) - \varepsilon_s\sigma[T_s(\vec{r})]^4$$

where α_s is the albedo of the soil, $R_{TIR}^U(\vec{r})$ is the absorbed TIR flux density by the soil grid-point, $T_s(\vec{r})$ is soil surface temperature, $\rho_s(\theta_{s0},\theta_v,\varphi_v-\varphi_{s0})$ is the soil bidirectional reflectance distribution function (BRDF) and can be calculated using different BRDF models as discussed in Appendix III.

2.4 Energy balance at a grid-point

2.4.1 Introduction

In §2.3.2, the net radiation flux density absorbed by leaves or by soil at any grid-point was obtained. The energy balance of leaves and soil determines the distribution of the heat/water sources and sinks in the canopy, and it affects the transport of heat and vapor from the individual leaf throughout the canopy. The radiation budget needs the leaf (or soil) temperature at each grid-point $T_f(\vec{r})$ (see Eqs. 2.11 and 2.12). Therefore, the leaf (or soil) temperature must be determined first from the leaf energy balance equation.

Heat and water vapor transfer inside the canopy combines two processes: (1) exchange of heat and water vapor of leaf and soil with the surrounding air, which is mainly controlled by molecular diffusion and conduction processes, (2) exchange of heat and water vapor between the canopy air space and the overlying atmosphere, which is controlled by turbulent eddy movement and referred to as convection process. This section will deal with the first issue, while convection will be discussed in §2.5.

26

2.4.2 Energy balance at a grid-point containing leaves

As described in §2.3.2, the net radiation flux density absorbed by leaves depends on the leaf angle so that leaf processes that depend on incident radiation must be stratified by leaf angle class. Neglecting the effect of photosynthesis and heat storage in the leaf, the energy balance for leaves at grid-point $\vec{r}$ and leaf angle class $\mathbf{\Omega_L}$ can be written as

$$R_n(\vec{r},\mathbf{\Omega_L}) = H_f(\vec{r},\mathbf{\Omega_L}) + \lambda E_f(\vec{r},\mathbf{\Omega_L}) \tag{2.13}$$

where $H_f(\vec{r},\mathbf{\Omega_L})$ is the foliage sensible heat flux density, $\lambda E_f(\vec{r},\mathbf{\Omega_L})$ is the foliage latent heat flux density. $H_f(\vec{r},\mathbf{\Omega_L})$ and $\lambda E_f(\vec{r},\mathbf{\Omega_L})$ are expressed as, respectively

$$H_f(\vec{r},\mathbf{\Omega_L}) = \frac{2\rho_a c_p}{r_{ah,f}(\vec{r})}\left[T_f(\vec{r},\mathbf{\Omega_L}) - T_{ac}(\vec{r})\right] \tag{2.14}$$

$$\lambda E_f(\vec{r},\mathbf{\Omega_L}) = \frac{2\rho_a \lambda \delta_0}{p}\frac{\left[e_{0f}(\vec{r},\mathbf{\Omega_L}) - e_{ac}(\vec{r})\right]}{r_{st}(\vec{r},\mathbf{\Omega_L}) + r_{ah,f}(\vec{r})} \tag{2.15}$$

where ρ_a is the air density (kg m^{-3}), c_p is the heat capacity of the air (J kg^{-1} K^{-1}), λ is the latent heat for vaporization of water (J kg^{-1}), $\delta_0 = 0.622$, $r_{ah,f}(\vec{r})$ is the leaf boundary layer resistance (s m^{-1}), $r_{st}(\vec{r},\mathbf{\Omega_L})$ is the stomatal resistance (s m^{-1}), $T_{ac}(\vec{r})$ is the temperature of air at grid-point $\vec{r}$ (K), p is ambient air pressure (Pa), $e_{0f}(\vec{r},\mathbf{\Omega_L})$(Pa) is the saturation water vapor pressure of leaf surface boundary at $T_f(\vec{r},\mathbf{\Omega_L})$, $e_{ac}(\vec{r})$ (Pa) is the actual water vapor pressure in the air surrounding the leaves at grid-point $\vec{r}$. In Eqs.2.14 and 2.15, the coefficient ''2'' indicates that both sides of a leaf contribute to heat transfer.

Sensible and latent heat flux densities at the $H_f(\vec{r})$ and $\lambda E_f(\vec{r})$, are the sum over all leaf angle classes $\mathbf{\Omega_L}$ weighted by the respective fractions of leaf area density and given respectively by

$$H_f(\vec{r}) = \sum_{\mathbf{\Omega_L}} F(\vec{r},\mathbf{\Omega_L}) H_f(\vec{r},\mathbf{\Omega_L}) \tag{2.16}$$

$$\lambda E_f(\vec{r}) = \sum_{\mathbf{\Omega_L}} F(\vec{r},\mathbf{\Omega_L}) \lambda E_f(\vec{r},\mathbf{\Omega_L}) \tag{2.17}$$

Substituting Eqs. 2.14 and 2.15 into Eqs. 2.16 and 2.17 and taking into account Eq. 2.9, one can get

$$H_f(\mathbf{\vec{r}}) = \frac{2\rho_a c_p}{r_{ah,f}(\mathbf{\vec{r}})}\left[T_f(\mathbf{\vec{r}})-T_{ac}(\mathbf{\vec{r}})\right] \tag{2.18}$$

$$\lambda E_f(\mathbf{\vec{r}}) = \frac{2\rho_a\lambda\delta_0}{p}\sum_{\mathbf{\Omega_L}}\left\{F(\mathbf{\vec{r}},\mathbf{\Omega_L})\frac{[e_{0f}(\mathbf{\vec{r}},\mathbf{\Omega_L})-e_{ac}(\mathbf{\vec{r}})]}{r_{st}(\mathbf{\vec{r}},\mathbf{\Omega_L})+r_{ah,f}(\mathbf{\vec{r}})}\right\} \tag{2.19}$$

The energy balance at the grid-point $\mathbf{\vec{r}}$ containing leaves is then given by

$$R_n(\mathbf{\vec{r}}) = H_f(\mathbf{\vec{r}})+\lambda E_f(\mathbf{\vec{r}}) \tag{2.20}$$

Since $R_n(\mathbf{\vec{r}},\mathbf{\Omega_L})$ (Eq.2.10) depends on both the temperature of leaves at grid-point $\mathbf{\vec{r}}$ and of surrounding leaves from which thermal radiation originates, initial $R_n(\mathbf{\vec{r}},\mathbf{\Omega_L})$ must be calculated. This is done either with initial leaves temperatures or excluding thermal emission from other leaves as a first estimation of $R_n(\mathbf{\vec{r}},\mathbf{\Omega_L})$. The leaf energy balance equation (Eq.2.13) is solved to obtain $\delta T(\mathbf{\vec{r}},\mathbf{\Omega_L})$ ($\delta T(\mathbf{\vec{r}},\mathbf{\Omega_L})=T_f(\mathbf{\vec{r}},\mathbf{\Omega_L})-T_{ac}(\mathbf{\vec{r}})$). The new value of $T_f(\mathbf{\vec{r}},\mathbf{\Omega_L})$ is then used to adjust $R_n(\mathbf{\vec{r}},\mathbf{\Omega_L})$ and a new $\Delta T(\mathbf{\vec{r}},\mathbf{\Omega_L})$ is calculated. Moreover, one should note that to solve Eq.2.13, the profiles of windspeed, temperature and water vapor pressure of air in the canopy are needed, this implies that Eq.2.13 needs to be solved by using the convective transfer equations (see §2.5).

2.4.3 Energy balance of a grid-point at the soil surface

The energy balance of a grid-point at the soil surface is

$$R_n(\mathbf{\vec{r}}) = H_s(\mathbf{\vec{r}})+\lambda E_s(\mathbf{\vec{r}})+G_0(\mathbf{\vec{r}}) \tag{2.21}$$

where $H_s(\mathbf{\vec{r}})$ is soil sensible heat flux density at grid-point $\mathbf{\vec{r}}$, $\lambda E_s(\mathbf{\vec{r}})$ is soil latent heat flux density at grid-point $\mathbf{\vec{r}}$, $G_0(\mathbf{\vec{r}})$ is the soil heat flux density at soil surface.

The equations to compute $H_s(\mathbf{\vec{r}})$ and $\lambda E_s(\mathbf{\vec{r}})$ at the soil surface are similar to Eqs.2.14 and 2.15, except there is no stomatal resistance for soil surface evaporation.

$$H_s(\mathbf{\vec{r}}) = \frac{2\rho_a c_p}{r_{ah,s}(\mathbf{\vec{r}})}\left[T_s(\mathbf{\vec{r}})-T_{ac}(\mathbf{\vec{r}})\right] \tag{2.22}$$

$$\lambda E_s(\mathbf{\vec{r}}) = \frac{2\rho_a\lambda\delta_0}{p}\frac{[e_{0s}(\mathbf{\vec{r}})-e_{ac}(\mathbf{\vec{r}})]}{r_{ah,s}(\mathbf{\vec{r}})} \tag{2.23}$$

2.5   Convective and conductive transfer within and above a canopy

2.5.1   Introduction

In §2.4, the distribution and the intensity of sources and sinks for heat and water vapor were determined. To model exchanges inside the canopy the profiles of windspeed u, air temperature T_a and water vapor pressure e_a through the canopy are needed.

A number of plant-environmental models utilized the gradient-diffusion relationship (i.e. the K-theory) to estimate the turbulent flux of any scalar such as heat, water vapor and carbon dioxide as the product of the scalar concentration gradient times the eddy diffusivity. Such examples can be found, for instance, in Thom (1972), Goudriaan (1977), Norman (1979). However, several studies have shown that scalar transfer in canopies does not always obey the K-theory, and counter-gradient fluxes have been observed within canopies (Legg and Monteith, 1975; Denmead and Bradley, 1985, 1987; Finnigan and Raupach, 1987; Raupach, 1988). One of the realistic alternatives to K-theory with limited complication is to use a Lagrangian formulation to describe canopy turbulent transfer (Raupach, 1989). However, Van den Hurk and McNaughton (1995) and McNaughton and Van den Hurk (1995) have found no significant advantage of using Raupach's L-theory over the K-theory to estimate bulk soil-canopy evaporation when applying the Raupach L-theory to a two-layer canopy-resistance model. The use of the Lagrangian formulation instead of the K-theory in a comprehensive vegetation-soil-atmosphere model as done by Wilson et al (2002) showed that the fluxes estimations were similar between these two methods, while large differences occurred in the simulated radiometric surface temperature of the canopy when the Lagrangian formulation was implemented in the model used.

As discussed in the previous sections, the three-dimensional geometry of a realistic canopy results in the heterogeneity of net radiation inside the canopy and of surface radiometric temperature. This implies, in principle, spatial heterogeneity in turbulent fluxes.

Albertson et al. (2001) investigated the vertical latent heat fluxes at the top of canopy (i.e. reflecting total canopy contribution) by using Large Eddy Simulation (LES) technique. They concluded: 'Although the difference of LAI between the maximum and the minimum over the interested area is large, the impact on the simulation of heat fluxes from the canopy doesn't seem significant. This implies that the LAI distribution does not affect significantly the vertical profile of air temperature inside the canopy so that the one-dimensional parameterization is still applicable to describe the heat transfer in 3D canopy'. Such results are supported by the measurements made in corn and potato canopies (both are row crops) by Jacobs et al (1995). Their experimental data showed that the air temperature inside the canopy did not change significantly with the location within the inter-row, while it is affected by the vertical distribution of leaf area density.

The relaxation time of turbulent dispersion, t_{relax}, is defined as

$$t_{relax} = \frac{l_m}{v_e} = \frac{l_m^2}{K_h} \qquad (2.24)$$

where l_m is the mean mixing length within a canopy, v_e is the mean velocity of eddies, K_h is the turbulent exchange coefficient for heat (J m^{-1} s^{-1} K^{-1}). The value of l_m within the canopy is taken as the free space between the leaves (if only leaves are considered) which can be determined by the dimension of leaves l_L and the leaf area density ρ_f given the shape of leaves (Goudriaan, 1977). For moderately sparse canopies, relaxation time of turbulence inside the canopy is very short, e.g. a few seconds for maize according to the order of magnitudes of l_m and K_h given by Goudriaan (1977), so that any gradient in air temperature within the canopy space will disappear quickly. One can assume that the horizontal variation can be neglected under such time scale of dispersion although the canopy is heterogeneous geometrically. A unique vertical profile of air temperature can be applied to the entire canopy under this assumption. The measurements of Jacobs et al. (1995) showed that this hypothesis is acceptable. This implies that the horizontal exchange of heat and water vapor in the canopy air space is negligible as compared with vertical transfer.

After reviewing the studies relevant to the scalar transfer within the canopy, we consider that the one-dimensional K-theory can still be used with acceptable accuracy in determining total fluxes from 3D heterogeneous canopies. Under the geometry schematization described in §2.2, we assumed that there is no horizontal variability in windspeed, air temperature, and water vapor pressure inside sub-canopies, while these variables will only change in the vertical direction. These variables will be referred to as 'layer-dependent variables', i.e. only the 'z' coordinate is considered. Other variables, such as radiation flux density, heat flux density, water vapor flux density and leaf temperature, are still 'point-dependent variables' retaining the 3D character.

2.5.2   Heat and water exchange throughout a canopy

The equations describing heat and mass exchange should include storage terms and not be limited to steady state, i.e. by using the following scalar (heat, water and carbon dioxide) conservation equation

$$\frac{\partial C}{\partial t} + U\frac{\partial C}{\partial x} + V\frac{\partial C}{\partial y} + \frac{\partial F}{\partial z} = S \qquad (2.25)$$

where C is the mean scalar concentration field, F is the vertical scalar flux density, U and V are the wind speed along x and y directions respectively, with $u^2 = U^2 + V^2$, where u is the mean horizontal wind speed. The coordinates x and z lie in the mean stream and vertical directions, respectively. S is the source density of the concerned scalar. For unsteady conditions in an extensive, horizontally homogeneous canopy in which horizontal variations in gradients of air temperature and water vapor pressure are ignored, Eq.2.25 is dominated by the vertical flux divergence and source terms, and reduces to

$$\frac{\partial C(x,y,z)}{\partial t} + \frac{\partial F(x,y,z)}{\partial z} = S(x,y,z) \qquad (2.26)$$

Such equation may describe heat and water movement from below the root zone to the atmosphere above the canopy by substituting the appropriate scalar variables and the associated capacitances, conductivities and sources. The source or sink distributions are derived by the local heat and water balance in each point.

Heat and water vapor transfer within vegetation part in the canopy

Under the defined canopy construction described before, sensible and latent fluxes H and λE at each grid-point (determined in §2.4.2) are related to the gradients of air temperature and water vapor pressure inside the canopy by applying the K-theory to Eq.2.26:

$$\rho_a c_p \frac{\partial T_{ac}(z)}{\partial t} = \frac{\partial}{\partial z}\left(K_h(z)\frac{\partial T_{ac}(z)}{\partial z}\right) + S_H(\bar{r}) \qquad (2.27)$$

$$\frac{\rho_a \delta_0}{p} \frac{\partial e_{ac}(z)}{\partial t} = \frac{\partial}{\partial z}\left(\frac{\delta_0 K_h(z)}{c_p p}\frac{\partial e_{ac}(z)}{\partial z}\right) + S_E(\bar{r}) \qquad (2.28)$$

where $\delta K_h(z)/(c_p p)$ is the eddy diffusivity for water vapor (kg m^{-1} s^{-1} Pa^{-1}), $S_H(\bar{r})$ is the source/sink distribution for heat (W m^{-3}), $S_E(\bar{r})$ is the source/sink distribution for water vapor (kg m^{-3} s^{-1}). $S_H(\bar{r})$ and $S_E(\bar{r})$ are determined by the energy balance of leaves at each grid-point in §2.4.2. The turbulent exchange coefficient for heat, K_h (J m^{-1} s^{-1} K^{-1}), inside the canopy can be expressed as a function of a mean mixing length l_m and a mean velocity of eddies v_e (Goudriaan, 1977) and its parameterization will be discussed in Chapter 4.

Heat and water transfer in the soil

Transport of heat and water in the soil is described by the same form of conservation equations (Eq.2.26) but using the appropriate conductivities, heat capacity, etc. The

convection equations for heat and water content in the soil are expressed as (Norman and Campbell, 1983)

$$c_s \frac{\partial T_s(z)}{\partial t} = \frac{\partial}{\partial z}\left(K_D(z)\frac{\partial T_s(z)}{\partial z}\right) + S_{SH}(z) \qquad (2.29)$$

$$\frac{\partial w(z)}{\partial t} = \frac{\partial}{\partial z}\left(K_w(z)\frac{\partial \psi_s(z)}{\partial z} - K_w(z)g\right) + S_{Sw}(z) \qquad (2.30)$$

where c_s is volumetric heat capacity of soil (J m^{-3} K^{-1}), $K_D(z)$ is soil thermal conductivity (W m^{-1} K^{-1}), $S_{SH}(z)$ is the source/sink for heat (W m^{-3}) in the soil, w is the volumetric water content (kg m^{-3}), $K_w(z)$ is the capillary conductivity (kg s m^{-3}), $\psi_s(z)$ is the soil matric potential (J kg^{-1}), $S_{Sw}(z)$ (kg m^{-3} s^{-1}) is a source/sink including root uptake, thermally induced vapor flow or, in the surface layer, the difference between infiltration and soil evaporation.

The heat sources in the soil are zero except at the soil surface where the heat source is the residual between net radiation just above the soil surface and the soil surface latent heat flux due to evaporation. In the soil, $K_D(z)$ is a function of soil type and water content (Baver et al., 1972), c_s is mainly a function of water content. Norman and Campbell (1983) have given a detailed description about the water movement and the associated parameters in the soil.

Heat and water transfer in the atmosphere above the canopy

Besides the lower boundary conditions in the soil described in last section, solving Eqs.2.27 and 2.28 requires the upper boundary conditions, i.e. the associated quantities such as windspeed, air temperature, water vapor pressure at the canopy height. In the atmospheric surface layer, the conservation equation for heat and water vapor are

$$\rho_a c_p \frac{\partial T_a(z)}{\partial t} = \frac{\partial}{\partial z}\left(K_h(z)\frac{\partial T_a(z)}{\partial z}\right) \qquad (2.31)$$

$$\frac{\rho_a \delta_0}{p}\frac{\partial e_a(z)}{\partial t} = \frac{\partial}{\partial z}\left(\frac{\delta_0 K_h(z)}{c_p p}\frac{\partial e_a(z)}{\partial z}\right) \qquad (2.32)$$

where $K_h(z)$ in the atmosphere above the canopy is a function of friction velocity in the near surface layer, the measurement height and the stability of the atmosphere; its parameterization is given in Chapter 4.

2.6   Summary and conclusions

The 3D model of radiative and convective processes in the canopy space describes how the architecture of vegetation canopies determines the heterogeneous distribution of radiance absorbed by leaves and soil. The latter in turn determines the thermal anisotropy of the canopy space and, therefore, of convective heat fluxes. The equations given in the previous sections may be grouped as

-   Eqs. 2.11 and 2.12 give the estimation of energy sources and sinks;
-   Eq. 2.20 together with Eqs. 2.11, 2.18 and 2.19 are the energy balance equations for foliage grid-points; Eqs. 2.21 together with Eq. 2.12, 2.22 and 2.23 are the energy balance equations for the soil grid-points.
-   Eqs. 2.27 and 2.28 describe heat and water vapor transfer in the air space inside the canopy;
-   Eqs. 2.29 and 2.30 describe heat and water transport in the soil;
-   Eqs. 2.31, and 2.32 give exchange of heat and vapor in the atmospheric surface layer just above the canopy.

The theoretical analysis (Eq. 2.24) and experimental evidence given in literature (§2.5.1), lead to the conclusion that horizontal variations of air temperature T_a, windspeed u and water vapor pressure e_a inside a canopy may be neglected and these variables will only change in the vertical direction. It is therefore assumed that a unique vertical profile of T_a, u and e_a can be applied to the entire canopy. These variables are characterized as one-dimensional variables and referred to as '*layer-dependent variables*'. On the other hand, radiation, sensible and latent heat flux densities and leaf temperature, are still '*point-dependent variables*' retaining the 3D character.

When the boundary conditions both at the root zone in the soil and in the atmospheric surface layer just above the canopy are defined, these equations are solved to give sensible and latent heat flux densities above the canopy, air temperature and water vapor pressure profiles inside the canopy, leaf temperature at each grid-point, and source/sink distributions of heat and water vapor within the canopy space. The model results can be used to investigate the relationship between the thermal heterogeneity of vegetation canopies and anisotropy of exitance at TOC (Chapter 3). Further, such a comprehensive vegetation-soil-atmosphere process model can be used to develop and evaluate simpler models that are applicable at larger spatial scale with easily obtained input variables directly provided or derived by remote sensing observations (Chapter 3 and Chapter 6).

Chapter 3

Modeling directional observations of the anisotropic emittance of soil-vegetation canopies

3.1   Introduction

In Chapter 2, foliage (or soil) temperatures in each grid-point have been determined by solving the energy balance equation in each grid-point of a soil-vegetation canopy. The objective of this chapter is to exploit the dependence of observed Top Of Canopy (TOC) brightness temperature $T_{b0}(\theta_v, \varphi_v)$ on the view angle, and thereafter to establish an invertible model to retrieve foliage and soil component temperatures from the directional observations of $T_{b0}(\theta_v, \varphi_v)$.

$T_{b0}(\theta_v, \varphi_v)$ is the temperature measured by a radiometer at zenith angle θ_v and azimuth angle φ_v and is simply derived from the measured radiance R_λ by a radiometer by inverting the Planck's function. Therefore, the observation of $T_{b0}(\theta_v, \varphi_v)$ and the observation of TIR radiance are equivalent. In this chapter, for simplification the symbol 'R' denotes only TIR radiance and the subscript TIR will be neglected. TIR radiance of a target is usually referred to as 'exitance', i.e. the sum of emitted and reflected TIR radiance by the target concerned. Nielsen et al., (1984) have shown that it is common to have large (up to 20K or more) differences between sun-lit soil and shadowed leaf surfaces, particularly when the top soil is dry. Jackson and Idso (1975) found differences between bare soil and air temperature as large as 27°C. For a soybean canopy with 35% ground cover, the soil temperature exceeded the canopy temperature by 11°C and was 15°C higher than air temperature (Kimes, 1980). Usually, $T_{b0}(\theta_v, \varphi_v)$ is measured by a radiometer in a specific spectral range (centered at some wavelength) and in a particular direction (θ_v, φ_v), within an instantaneous field-of-view (IFOV) Ω_{IFOV}. The portions of canopy components with different surface temperatures in the IFOV will change with the view angle (Fig. 3.1). As a consequence, strong anisotropy in exitance, i.e. significant variation in $T_{b0}(\theta_v, \varphi_v)$ with the direction of observation, can be observed over thermally heterogeneous systems like sparse canopies. For instance, Kimes and Kirchner (1983) observed in a cotton field that the difference in $T_{b0}(\theta_v, \varphi_v)$ between the 0° (mixture of vegetation and soil) and the 80° (vegetation only) zenith view angles was 16.2°C at noon, while the difference was only 0.9°C in the early morning. Lagouarde et al. (1995) observed a difference of up to 3.5 K for a corn canopy and 1.5 K for grass (20 cm high) with a view zenith angle between 0° and 60° around solar noon.
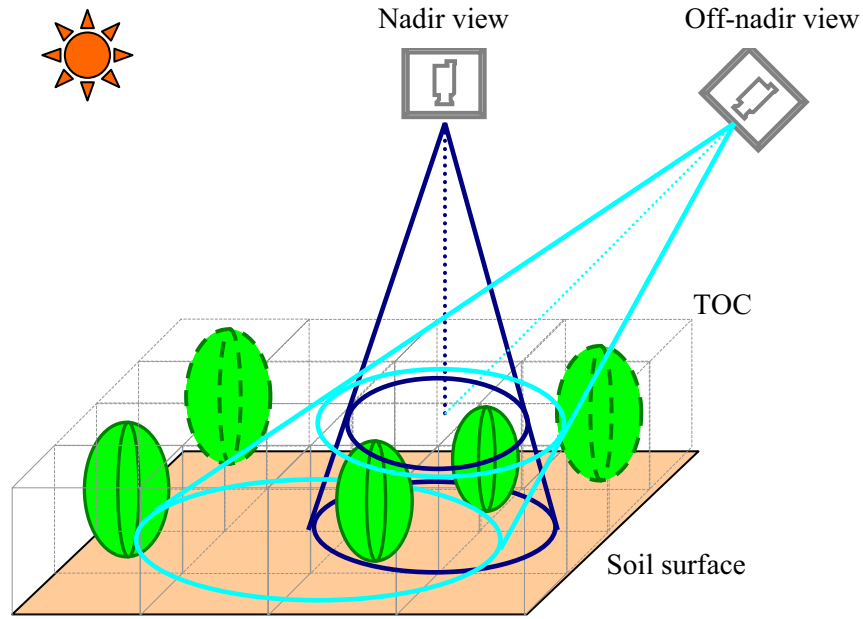
Figure 3.1 Observation of TOC brightness temperature T_{b0} at different view angles. The circles represent the footprints of IFOV at the Top Of Canopy (TOC) and at the bottom of the canopy for different view angles. The components in the volume between TOC and the bottom are observed by a radiometer located above the canopy.

Directional measurements of T_{b0} have been tentatively used to help model the energy fluxes in the soil–vegetation–atmosphere system (Kimes, 1980; Kimes et al., 1980; Kimes and Kirchner, 1983; Paw U, 1991; Lagouarde et al., 1995; Smith et al., 1996).

To investigate the directional properties of observed T_{b0} and its relation with the thermodynamic heterogeneity of canopy components, it is necessary to describe the radiometric observation by a radiometer in a precise manner. This is dealt with in section 3.2 based on the canopy structure constructed in Chapter 2. However, direct or inverse detailed deterministic modeling is virtually impossible, since the system must be characterized in an extremely detailed manner as shown in Chapter 2. Some degree of spatial integration is needed, in which case inverting TIR directional radiance relies on simpler models of the system. Therefore, two types of simpler models are introduced in §3.3 and §3.4 to describe the relationship between the observed T_{b0} and the surface temperatures of canopy components.

3.2 Relationship between thermal heterogeneity of a vegetation canopy and anisotropy of exitance

When a TIR radiometer with domain wavelength centered at λ and a IFOV Ω_{IFOV} is used to observe the soil-vegetation canopy described in Chapter 2 (Fig. 2.4a), the radiance received by the radiometer consists of the following contributions: (1) the emission from canopy components in all grid-points in the IFOV, (2) the reflection by the components in a grid-point of the radiance emitted by the components in the surrounding grid-points, (3) the atmospheric TIR radiation reflected by the components of the grid-points within the IFOV; (4) the multiple-scattering of the atmospheric TIR radiation within the canopy (see Fig. 3.2 for the illustration). Following the canopy construction described in Chapter 2, the observed directional TIR radiance is expressed as a function of canopy geometry and the component temperatures of grid-points seen by the radiometer at the associated view angle,

$$B\left[\lambda, T_{\text{b0}}(\theta_{\text{v}}, \varphi_{\text{v}})\right] = \sum_{k=1}^{N_c}\left[f_{\text{k}}(\theta_{\text{v}}, \varphi_{\text{v}})R_{\text{k}}(\lambda, T_{\text{k}})\right] + \sum_{k=1}^{N_c}\left[f_{\text{k}}(\theta_{\text{v}}, \varphi_{\text{v}})R'_{\text{k}}(\lambda)\right] + R_{\text{atm}}^{\downarrow}\uparrow + R_{\text{atm}}^{\downarrow}\uparrow' \quad (3.1)$$

where B is the Planck's function which relates T_{b0} to the TIR radiance, N_c is the number of grid-points k ($k=1,2,3......N_c$) that would be seen by the sensor, $f_{\text{k}}(\theta_{\text{v}}, \varphi_{\text{v}})$ is the fraction of the linear dimension of the volume δV of a grid-point seen by the radiometer within the IFOV; $R_{\text{k}}(\lambda, T_{\text{k}})$ is the radiance emitted by the components at the kth grid-point; $R'_{\text{k}}(\lambda)$ is the radiance reflected by the components in the kth grid-point, i.e. a fraction of the emittance by the components in the surrounding grid-points; $R_{\text{atm}}^{\downarrow}\uparrow$ is the down-welling atmospheric TIR radiance reflected by the components at all grid-points in the IFOV and $R_{\text{atm}}^{\downarrow}\uparrow'$ is a term related to multiple scattering by canopy components of the down-welling atmospheric TIR radiance.

From Eq. 3.1, it is obvious that the directionality of exitance above a canopy is a complex function of the radiance from components (a function of component temperatures and emissivities), the thermal radiation exchange between the components inside the IFOV and between the components inside the IFOV and those in the surroundings of the IFOV, and the canopy structure. These factors play their roles in the relationship between the heterogeneity in component temperatures and the anisotropy of exitance. Considering that TIR reflectivities ($r_{\text{k}} = 1 - \varepsilon_{\text{k}}$) of soil and foliage are small, only single scattering between grid-points is taken into account and multiple scattering is negligible, which implies that the term $R_{\text{atm}}^{\downarrow}\uparrow'$ in Eq. 3.1 will be neglected from now on.
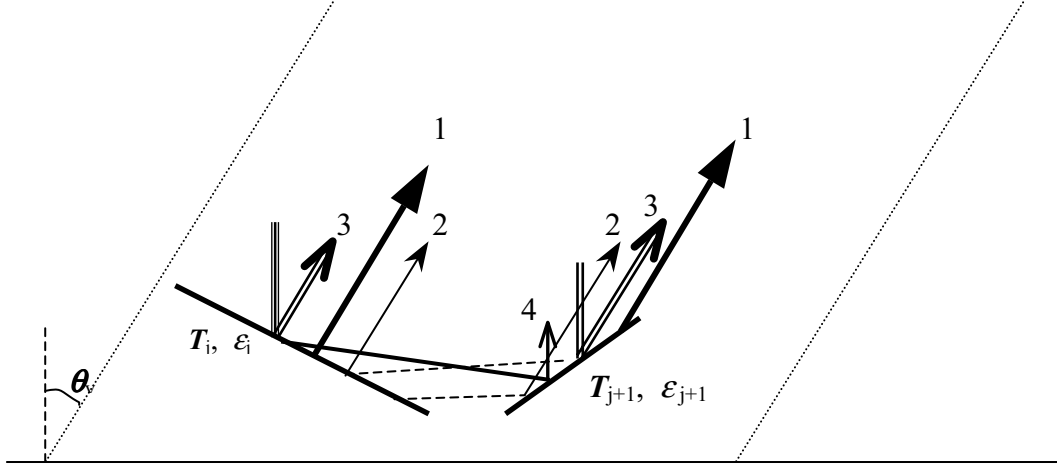
Figure 3.2 Schematic illustration of TIR exitance contributed by two components, j and $j + 1$, to the radiance in the IFOV of a radiometer. The numbers represent: **1**: the emission from canopy components, **2**: the reflection by the components in a grid-point in the IFOV of the radiance emitted by the components in the surrounding grid-points, **3**: the reflected down-welling atmospheric TIR radiation by the components at the grid-points in the IFOV, **4**: the multiple scattering by canopy components in the IFOV of the down-welling atmospheric long-wave radiation.

Direct emission to the sensor

The first term in Eq. 3.1 represents the direct emissions from the components in all grid-points viewed by the sensor and is a function of component emissivity and temperatures according to Planck's law

$$\sum_{k=1}^{N_c} \left[f_k(\theta_v, \varphi_v) R_k(\lambda, T_k) \right] = \sum_{k=1}^{N_c} \left[f_k(\theta_v, \varphi_v) \varepsilon_k(\lambda, \theta_v, \varphi_v) B(\lambda, T_k) \right] \tag{3.2}$$

where $\varepsilon_k(\lambda, \theta_v, \varphi_v)$ is the component directional emissivity at each grid-point which is either leaf or soil depending on the position of the grid-point and at wavelength λ.

The leaf surface can be considered as an isotropic radiator as discussed in Chapter 2. As regards soil, it might be isotropic or anisotropic depending on the degree of soil roughness. If the angular variation of soil emissivity is known it can be taken into account. In this study, both leaf and soil are considered as isotropic emitters, so the symbols of direction (θ_v, φ_v) will not appear further in the emissivity of canopy components, i.e. $\varepsilon_k(\lambda, \theta_v, \varphi_v) = \varepsilon_k(\lambda)$, with $\varepsilon_k(\lambda)$ equal to either ε_s or ε_f in the given wavelength λ.

38

The variations in temperature of grid-points at different positions in the canopy within the IFOV (the first term on the right hand side of Eq. 3.2) are the most important contributors to the anisotropy of exitance. If all the components in the canopy seen by the radiometer would have similar surface temperature, e.g. such as in a dense canopy, a small angular dependence of exitance is expected. However, this is usually not the case for a sparse canopy, since the variability in component temperatures both in horizontal and in vertical directions is significant (Chapter 2).

Scattered emitted radiance

Apart from the direct emission from the canopy components, reflection by other scatterers within the IFOV must be taken into account (the second term in Eq. 3.1). This term is formulated following the procedures below.

For any grid-point k, the radiance emitted from the surrounding grid-points in the upper (lower) hemisphere and arrived at the surfaces of all leaves at this point is calculated by weighing the radiance according to the fraction of leaves in each leaf angle class:

$$R_{k,scat} = \sum_{\mathbf{\Omega_L}} F_k(\mathbf{\Omega_L}) \left\{ \sum_{i=1}^{18} \sum_{j=1}^{9} \left[\mathbf{V}_{ij} \cdot \mathbf{\Omega_L} \sum_{l=1}^{N_{k,ij}} \varepsilon_{ij,l}(\lambda) B(\lambda, T_{ij,l}) Phit_{ij,l}(\theta, \varphi) \right] \right\} \tag{3.3}$$

The radiance reflected by point k to the sensor then is

$$R_k'(\lambda) = [1 - \varepsilon_k(\lambda)] \sum_{\mathbf{\Omega_L}} F_k(\mathbf{\Omega_L}) \left\{ \sum_{i=1}^{18} \sum_{j=1}^{18} \left[\mathbf{V}_{ij} \cdot \mathbf{\Omega_L} \sum_{l=1}^{N_{k,ij}} \varepsilon_{ij,l}(\lambda) B(\lambda, T_{ij,l}) Phit_{ij,l}(\theta, \varphi) \right] \right\} \tag{3.4}$$

where $N_{k,ij}$ is number of grid-points in direction (i, j) at grid-point k, Other terms are the same as defined in Chapter 2. Because both upper and lower hemispheres are considered in Eq. 3.4, there are 18 hemispherical bands.

Reflected down-welling atmospheric TIR radiation

The third term in Eq. 3.1 is the radiative interaction between the components of the canopy and the atmosphere, which depends on the geometry of the canopy through $f_k(\theta_v, \varphi_v)$. Assuming the atmosphere is emitting TIR radiance in an isotropic manner, the radiance from the atmosphere is $R_{atm}^{\downarrow}$ (down-welling hemispheric atmospheric long-wave radiation flux density divided by π), the atmospheric long-wave radiance reflected by each point k, $R_{k,atm}^{\downarrow}\uparrow$, is

$$R_{k,atm}^{\downarrow} \uparrow = R_{atm}^{\downarrow}\left(1-\varepsilon_k(\lambda)\right) \tag{3.5}$$

Then the reflected atmospheric long-wave radiance by all the grid-points in the IFOV to the sensor is

$$R_{atm}^{\downarrow} \uparrow = R_{atm}^{\downarrow} \sum_{k=1}^{N_c}\left[f_k(\theta_v,\varphi_v)\left(1-\varepsilon_k(\lambda)\right)\right] \tag{3.6}$$

Combining Eq. 3.2, 3.4 and 3.6 with Eq. 3.1, one can obtain the modeled radiometer observation of T_{b0} in terms of TIR radiance as

$$
\begin{aligned}
B[\lambda,T_{b0}(\theta_v,\varphi_v)] &= \sum_{k=1}^{N_c}\left[f_k(\theta_v,\varphi_v)\varepsilon_k(\lambda)B(\lambda,T_k)\right]\\
&+\sum_{k=1}^{N_c}\left[f_k(\theta_v,\varphi_v)[1-\varepsilon_k(\lambda)]\sum_{\Omega_L}F_k(\Omega_L)\left\{\sum_{i=1}^{18}\sum_{j=1}^{18}\left[V_{ij}\cdot\Omega_L\sum_{l=1}^{N_{k,ij}}\varepsilon_{ij,l}(\lambda)B(\lambda,T_{ij,l})Phit_{ij,l}(\theta,\varphi)\right]\right\}\right]\\
&+R_{atm}^{\downarrow}\sum_{k=1}^{N_c}\left[f_k(\theta_v,\varphi_v)\left(1-\varepsilon_k(\lambda)\right)\right]
\end{aligned}
$$

$$\tag{3.7}$$

As one can see immediately from Eq.3.7, even if the individual components of canopy are assumed to be isotropic emitters, the behavior of the canopy may be anisotropic due to canopy geometry and the spatial variation of the component surface temperatures.

Eq. 3.7 gives a rather detailed description of the observation of $T_{b0}(\theta_v,\varphi_v)$ by a radiometer for a thermally heterogeneous canopy, which may be too complicated for the purpose of retrieving component temperatures, because 1) the detailed canopy geometry must be known; 2) too many unknowns, e.g. surface temperature of components at each grid-point, are involved. In principle, T_{b0} can be measured in any desired number of directions over a canopy. However, angular changes in exitance may be relatively small when view angles are close to each other, so only observations at very different angles give a signal significantly larger than the accuracy of observations. This limits to very few the number of significant and independent angular measurements of T_{b0}, which implies that only very simple models (i.e. with very few unknowns) can be used to interpret the observations and to obtain estimates of the component temperatures of vegetation canopies. Besides, simplification is also necessary to make the retrieval of component temperatures possible by using currently existing remote sensing observations such as the ones made by ATSR-2 onboard the ERS-2. Therefore, the investigation of simpler models and their capability of representing the same angular signature as described by the complete model (Eq. 3.7) will be the major issue in the following sections of this Chapter.

40

3.3 Simple linear mixture model of thermal infrared radiance for foliage-soil canopy: four components system

To reduce the number of unknowns involved in the model describing the angular variation of observed T_{b0} in terms of emittance, the canopy grid-points considered in the complete model (Eq. 3.7) should be grouped in fewer and simpler categories. Since the difference in temperatures between sunlit and shaded foliage (/soil) can be very large, they have to be treated as separate components. Therefore, the first option is to consider four components: 1) sunlit foliage, 2) shadowed foliage, 3) sunlit soil, 4) shadowed soil. As a simple case, we assume that:

1) The soil and foliage surfaces are Lambertian. The sunlit and shadowed foliage have identical emissivity ε_f, and the sunlit and shadowed soil have identical emissivity ε_s;

2) Sunlit foliage, shadowed foliage, sunlit soil and shadowed soil have the mean temperatures T_{s_f}, T_{sh_f}, T_{s_s} and T_{sh_s}. The mean temperature for each component is defined as the ensemble mean temperature of all grid-points of each type of component within the IFOV according to Planck law:

$$B(T_k) = \frac{1}{N_k} \sum_{i=1}^{N_k} B(T_i)$$
(3.8)

where $T_k = T_{s\_f}$, T_{sh_f}, T_{s_s} or T_{sh_s}. Foliage in a grid-point i is assumed consisting of finite facets with surface temperature T_i. N_k is the number of grid-points for each type of component within the IFOV.

3) The canopy geometry is characterized by the fractional area occupied by each component in the IFOV – the component fractional cover, which changes only with zenith view angle (the azimuth angle φ_v will be ignored in the following content).

Considering the radiative interactions between the four components, the observed surface brightness temperature in terms of TIR radiance of the canopy is:

$$
\begin{aligned}
B[T_{b0}(\theta_v)] =\ & f_{s\_s}(\theta_v)\varepsilon_s B(T_{s\_s}) + f_{sh\_s}(\theta_v)\varepsilon_s B(T_{sh\_s}) \\
& + f_{s\_f}(\theta_v)\varepsilon_f B(T_{s\_f}) + f_{sh\_f}(\theta_v)\varepsilon_f B(T_{sh\_f}) \\
& + f_s(\theta_v)(1-\varepsilon_s)\,\alpha_{s\_f}(1-P_h)\,\varepsilon_f B(T_{s\_f}) + f_s(\theta_v)(1-\varepsilon_s)\,\alpha_{sh\_f}(1-P_h)\,\varepsilon_f B(T_{sh\_f}) \\
& + f_f(\theta_v)(1-\varepsilon_f)\,\alpha_{s\_s}(1-P_h)\,\varepsilon_s B(T_{s\_s}) + f_f(\theta_v)(1-\varepsilon_f)\,\alpha_{sh\_s}(1-P_h)\,\varepsilon_s B(T_{sh\_s}) \\
& + f_{s\_s}(\theta_v)[1-\varepsilon_s]R_{atm}^{\downarrow} + f_{sh\_s}(\theta_v)[1-\varepsilon_s]R_{atm}^{\downarrow} \\
& + f_{s\_f}(\theta_v)[1-\varepsilon_f]R_{atm}^{\downarrow} + f_{sh\_f}(\theta_v)[1-\varepsilon_f]R_{atm}^{\downarrow}
\end{aligned}
$$

(3.9)

where $f_s(\theta_v)$ and $f_f(\theta_v)$ are respectively the fractional cover of soil and foliage, $f_{s\_s}(\theta_v)$, $f_{sh\_s}(\theta_v)$, $f_{s\_f}(\theta_v)$ and $f_{sh\_f}(\theta_v)$ are, respectively, the fractional cover of sunlit soil, shadowed soil, sunlit foliage and shadowed foliage, α_{s_s}, α_{sh_s}, α_{s_f} and α_{sh_f} are, respectively, the hemispherical fractions of sunlit soil, shadowed soil, sunlit foliage and shadowed foliage respectively. P_h is the hemispherical gap frequency defined as the ratio of the radiation traveling through the canopy and reaching the soil to the incident radiation into the canopy over the hemisphere and is defined as

$$P_h = \frac{1}{\pi}\int_{\frac{\pi}{2}}^{\frac{\pi}{2}} f_s(\theta)\,d\theta \qquad (3.10)$$

One can rewrite Eq. 3.9 as:

$$
\begin{aligned}
B[T_{b0}(\theta_v)] &= \left\{1 + (1-\varepsilon_f)\alpha_{s\_s}(1-P_h)f_f(\theta_v)\left[f_{s\_s}(\theta_v)\right]^{-1}\right\} f_{s\_s}(\theta_v)\varepsilon_s B(T_{s\_s}) \\
&+ \left\{1 + (1-\varepsilon_f)\alpha_{sh\_s}(1-P_h)f_f(\theta_v)\left[f_{sh\_s}(\theta_v)\right]^{-1}\right\} f_{sh\_s}(\theta_v)\varepsilon_s B(T_{sh\_s}) \\
&+ \left\{1 + (1-\varepsilon_s)\alpha_{s\_f}(1-P_h)f_s(\theta_v)\left[f_{s\_f}(\theta_v)\right]^{-1}\right\} f_{s\_f}(\theta_v)\varepsilon_f B(T_{s\_f}) \\
&+ \left\{1 + (1-\varepsilon_s)\alpha_{sh\_f}(1-P_h)f_s(\theta_v)\left[f_{sh\_f}(\theta_v)\right]^{-1}\right\} f_{sh\_f}(\theta_v)\varepsilon_f B(T_{sh\_f}) \\
&+ f_{s\_s}(\theta_v)[1-\varepsilon_s]R_{atm}^{\downarrow} + f_{sh\_s}(\theta_v)[1-\varepsilon_s]R_{atm}^{\downarrow} \\
&+ f_{s\_f}(\theta_v)[1-\varepsilon_f]R_{atm}^{\downarrow} + f_{sh\_f}(\theta_v)[1-\varepsilon_f]R_{atm}^{\downarrow}
\end{aligned}
\qquad (3.11)
$$

We define the effective emissivity for each component as:

$$\varepsilon_{s\_s}'(\theta_v) = \left\{1 + (1-\varepsilon_f)\alpha_{s\_s}(1-P_h)f_f(\theta_v)\left[f_{s\_s}(\theta_v)\right]^{-1}\right\}\varepsilon_s \qquad (3.12a)$$

$$\varepsilon_{s\_sh}'(\theta_v) = \left\{1 + (1-\varepsilon_f)\alpha_{sh\_s}(1-P_h)f_f(\theta_v)\left[f_{sh\_s}(\theta_v)\right]^{-1}\right\}\varepsilon_s \qquad (3.12b)$$

$$\varepsilon_{f\_s}'(\theta_v) = \left\{1 + (1-\varepsilon_s)\alpha_{s\_f}(1-P_h)f_s(\theta_v)\left[f_{s\_f}(\theta_v)\right]^{-1}\right\}\varepsilon_f \qquad (3.12c)$$

$$\varepsilon_{f\_sh}'(\theta_v) = \left\{1 + (1-\varepsilon_s)\alpha_{sh\_f}(1-P_h)f_s(\theta_v)\left[f_{sh\_f}(\theta_v)\right]^{-1}\right\}\varepsilon_f \qquad (3.12d)$$

Substituting $\varepsilon_{s\_s}'(\theta_v)$, $\varepsilon_{sh\_s}'(\theta_v)$, $\varepsilon_{s\_f}'(\theta_v)$ and $\varepsilon_{sh\_f}'(\theta_v)$ in Eq. 3.11 and rearranging it leads to:

42

$$B[T_{b0}(\theta_v)] = f_{s\_s}(\theta_v)\,\varepsilon_{s\_s}{}'\,B(T_{s\_s}) + f_{sh\_s}(\theta_v)\,\varepsilon_{sh\_s}{}'\,B(T_{s\_sh})$$

$$+ f_{s\_f}(\theta_v)\,\varepsilon_{s\_f}{}'\,B(T_{s\_f}) + f_{sh\_f}(\theta_v)\,\varepsilon_{sh\_f}{}'\,B(T_{sh\_f}) \qquad (3.13)$$

$$+ R_{atm}^{\downarrow}\left\{1 - \left[f_{s\_s}(\theta_v)\varepsilon_s + f_{sh\_s}(\theta_v)\varepsilon_s + f_{s\_f}(\theta_v)\varepsilon_f + f_{sh\_f}(\theta_v)\varepsilon_f\right]\right\}$$

To estimate the component fractional cover in the IFOV, the ratio of the height of the canopy and the distance between plants in the canopy is needed, which is easier to obtain as compared to the detailed canopy geometry structure required by Eq. 3.7 (Kimes and Kirchner, 1983).

When the interactions between components are neglected, the radiance from the canopy received by the sensor is simplified to

$$B[T_{b0}(\theta_v)] = f_{s\_s}(\theta_v)\,\varepsilon_s B(T_{s\_s}) + f_{sh\_s}(\theta_v)\varepsilon_s B(T_{sh\_s})$$

$$+ f_f(\theta_v)\varepsilon_f B(T_{s\_f}) + f_{sh\_f}(\theta_v)\,\varepsilon_f B(T_{sh\_f})$$

$$+ R_{atm}^{\downarrow}\left\{1 - \left[f_{s\_s}(\theta_v)\varepsilon_s + f_{sh\_s}(\theta_v)\varepsilon_s + f_{s\_f}(\theta_v)\varepsilon_f + f_{sh\_f}(\theta_v)\varepsilon_f\right]\right\}$$

$$\qquad (3.14)$$

$$= \varepsilon_s\left[f_{s\_s}(\theta_v)B(T_{s\_s}) + f_{sh\_s}(\theta_v)B(T_{sh\_s})\right]$$

$$+ \varepsilon_f\left[f_f(\theta_v)B(T_{s\_sh}) + f_{sh\_f}(\theta_v)B(T_{sh\_f})\right]$$

$$+ R_{atm}^{\downarrow}\left\{1 - \left[f_s(\theta_v)\varepsilon_s + f_f(\theta_v)\varepsilon_f\right]\right\}$$

Such equations system are invertible to obtain the component temperatures when the TIR radiance measurements are made at least at four zenith view angles, provided that the component emissivities are known and the component fractional covers can be derived based on e.g. multi-angular VIS/NIR radiance measurements.

3.4 Simple linear mixture model of thermal infrared radiance for foliage-soil canopy: two components system

To consider four components radiance contributions to the sensor response, one still need to know the ratio of the height of the canopy and the distance between plants, besides leaf area index LAI and leaf area density ρ_f, to retrieve the fractional cover of each component. Moreover, multi-angular radiance measurements (at least at four view angles) are needed which are not provided from current airborne and satellite observations. As a consequence, the simplest case with only two canopy components, soil and foliage, needs to be derived. For such a simple canopy system, we assume that: 1) the canopy geometry is characterized by the fraction of each component area occupied in the IFOV – the component

fractional cover. The component fractional covers in the IFOV change only with zenith view angles; 2) the vegetation forms a uniform layer covering the soil surface, this vegetation layer has an mean temperature T_f and the underlying soil has mean temperature T_s; 3) the soil and foliage surfaces are Lambertian.

Taking into account single scattering between foliage and soil, the observed T_{b0} now becomes (here we neglect the symbol for wavelength),

$$
\begin{aligned}
B[T_{b0}(\theta_v)] = \ & f_s(\theta_v)\varepsilon_s B(T_s) + f_f(\theta_v)\varepsilon_f B(T_f) \\
& + f_s(\theta_v)(1-\varepsilon_s)(1-P_h)\,\varepsilon_f B(T_f) + f_f(\theta_v)(1-\varepsilon_f)(1-P_h)\varepsilon_s\,B(T_s) \quad (3.15) \\
& + f_s(\theta_v)[1-\varepsilon_s]R^{\downarrow}_{atm} + f_f(\theta_v)[1-\varepsilon_f]R^{\downarrow}_{atm}
\end{aligned}
$$

The first two terms on the right hand side in Eq. 3.15 are the proportions of the soil radiation that reaches the top of the canopy, respectively the upward emitted radiation from the foliage in the direction θ_v. The third term represents the downward radiation emitted by the foliage and reflected by the soil and is subsequently travelling upwards through the foliage in the view direction θ_v (foliage-soil interaction). The fourth term is the contribution of the radiation emitted by soil towards the foliage and reflected by the foliage towards the sensor outside the canopy in the view direction θ_v (soil-foliage interaction). The last two terms are reflected atmospheric long-wave radiance by soil respectively foliage.

Eq. 3.15 can be rewritten as

$$
\begin{aligned}
B[T_{b0}(\theta_v)] = \ & \left\{ 1 + (1-\varepsilon_f)(1-P_h)f_f(\theta_v)[f_s(\theta_v)]^{-1} \right\} f_s(\theta_v)\varepsilon_s\,B(T_s) \\
& + \left\{ 1 + (1-\varepsilon_s)(1-P_h)f_s(\theta_v)[f_f(\theta_v)]^{-1} \right\} f_f(\theta_v)\varepsilon_f B(T_f) \quad (3.16) \\
& + f_s(\theta_v)[1-\varepsilon_s]R^{\downarrow}_{atm} + f_f(\theta_v)[1-\varepsilon_f]R^{\downarrow}_{atm}
\end{aligned}
$$

In Eq. 3.16, the effective emissivity of soil and foliage, $\varepsilon_s'(\theta_v)$ and $\varepsilon_f'(\theta_v)$, are defined as

$$
\varepsilon_s'(\theta_v) = \left\{ 1 + (1-\varepsilon_f)(1-P_h)f_f(\theta_v)[f_s(\theta_v)]^{-1} \right\}\varepsilon_s \quad (3.17a)
$$

$$
\varepsilon_f'(\theta_v) = \left\{ 1 + (1-\varepsilon_s)(1-P_h)f_s(\theta_v)[f_f(\theta_v)]^{-1} \right\}\varepsilon_f \quad (3.17b)
$$

Soil emissivity has a large potential variation and ranges commonly from 0.90 to 0.98 (Salisbury and Aria, 1992), but the effective value, $\varepsilon_s'(\theta_v)$, is higher due to the cavity effect.

44

Leaf emissivity is generally high and ranges from 0.96 to 0.99 (Salisbury and Aria, 1992), the corresponding value of $\varepsilon_f^{'}(\theta_v)$ is therefore very close to unity.

Combining Eq. 3.17a,b with Eq. 3.16, the observed T_{b0} in terms of TIR radiance of the canopy reads:

$$B[T_{b0}(\theta_v)] = f_s(\theta_v)\varepsilon_s^{'}(\theta_v)B(T_s) + f_f(\theta_v)\varepsilon_f^{'}(\theta_v)B(T_f)$$
$$+ f_s(\theta_v)[1-\varepsilon_s]R_{atm}^{\downarrow} + f_f(\theta_v)[1-\varepsilon_f]R_{atm}^{\downarrow} \tag{3.18}$$

Eq. 3.18 implies that the observed T_{b0} can be represented as a linear composition of radiance from soil and foliage components. With radiance measurements at two zenith view angles θ_1 and θ_2, Eq. 3.18 can be written as two equations

$$B[T_{b0}(\theta_{v1})] = f_s(\theta_{v1})\varepsilon_s^{'}(\theta_{v1})B(T_s) + f_f(\theta_{v1})\varepsilon_f^{'}(\theta_{v1})B(T_f)$$
$$+ [1-\varepsilon_s]R_{atm}^{\downarrow} + [1-\varepsilon_f]R_{atm}^{\downarrow} \tag{3.19a}$$

$$B[T_{b0}(\theta_{v2})] = f_s(\theta_{v2})\varepsilon_s^{'}(\theta_{v2})B(T_s) + f_f(\theta_{v2})\varepsilon_f^{'}(\theta_{v2})B(T_f)$$
$$+ [1-\varepsilon_s]R_{atm}^{\downarrow} + [1-\varepsilon_f]R_{atm}^{\downarrow} \tag{3.19b}$$

Knowing the fractional cover of each component at each zenith view angle and soil and leaf emissivity, Eq. 3.19a,b can be inverted to determine the component temperatures T_s and T_f.

When the reflections of thermal emission between components can be neglected, which implies that the vegetation is assumed to be flat and no cavity effect will be taken into account, the radiance from such simplified canopy system is just a linear composition of the contributions of radiance from foliage and soil components weighted by their respective fractional cover. Hence Eq. 3.18 is reduced to

$$B[T_b(\theta_v)] = f_s(\theta_v)\varepsilon_s B(T_s) + f_f(\theta_v)\varepsilon_f B(T_f)$$
$$+ f_s(\theta_v)[1-\varepsilon_s]R_{atm}^{\downarrow} + [1-\varepsilon_f]f_f(\theta_v)R_{atm}^{\downarrow} \tag{3.20}$$

This is the most simplified form of the dependence of observed brightness temperature on the radiometer view direction due to the thermal heterogeneity and architecture of a canopy.

3.5   Effective Top Of Canopy radiometric temperature

The simplest case of Eq. 3.7 is to consider the foliage-soil canopy as one mixture system in which soil and foliage components are not distinguished and only a single radiometric temperature T_{rad} applies to the observation at TOC. As such, Eq. 3.7 becomes

$$B\left[\lambda, T_{b0}(\theta_v, \varphi_v)\right] = \varepsilon_c(\lambda, \theta_v, \varphi_v) B(\lambda, T_{rad}(\theta_v, \varphi_v)) + R_{atm}^{\downarrow}\left[1 - \varepsilon_c(\lambda, \theta_v, \varphi_v)\right] \tag{3.21}$$

where $\varepsilon_c(\lambda, \theta_v, \varphi_v)$ is the effective directional emissivity of the foliage-soil mixture as observed at zenith view angle θ_v, azimuth angle φ_v and at wavelength λ. $\varepsilon_c(\lambda, \theta_v, \varphi_v)$ is a complex function of thermal properties of canopy components, the canopy geometry and view angle. Apparently, $\varepsilon_c(\lambda, \theta_v, \varphi_v)$ is the key variable to determine the radiometric temperature T_{rad} of a foliage-soil system from the observation of $T_{b0}(\theta_v, \varphi_v)$ by a radiometer. Significant attention has been paid to the retrieval of TOC radiometric temperature from field and space measurements of TIR radiance during the past decades (Norman and Becker, 1995; Becker and Li, 1995; François and Ottlé, 1997; Li et al, 1999). Both the definition of the effective directional emissivity of a non-isothermal system and the definition of the radiometric temperature of such a system, however, are still open to question. Some authors have used the definition for the isothermal system and assumed it can also be applied to a non-isothermal system, such as foliage-soil system (see Chapter 6). Moreover, measurements of radiometric temperature at a single zenith view angle can hardly be representative of the physical temperature of a canopy system (see §3.2). Thus, the estimate of the directional emissivity of the canopy is a crucial issue to determine precisely TOC radiometric temperature $T_{rad}(\theta_v, \varphi_v)$. Moreover, care must be taken when applying $T_{rad}(\theta_v, \varphi_v)$ to estimate heat exchange (see Chapter 4 and 8).

3.6   Summary and conclusions

In this chapter, a complete radiative transfer model to describe the dependence of observed TOC brightness temperature on the view angle is introduced in detail together with the canopy geometry. Although the complete model is useful to describe and understand the angular variability of observed T_{b0}, it can not be inverted to obtain the canopy component temperatures since 1) the canopy geometry must be known; 2) too many unknowns are involved which leads to the need of observations at multiple view angles. Neither requirement can be met in practice by current remote sensing measurements (either space or airborne).

Simpler mixture models with four components and two components, therefore, were derived based on the complete radiative transfer model to reproduce the view angle dependence of exitance of a foliage-soil canopy under the following assumptions:

- The (sunlit/shadowed) soil and (sunlit/shadowed) leaf surface are Lambertian. The (sunlit/shadowed) foliage have identical emissivity ε_f, and the (sunlit/shadowed) soil have identical emissivity ε_s;

- In the four components case, sunlit foliage, shadowed foliage, sunlit soil and shadowed soil have the mean temperatures T_{s_f}, T_{sh_f}, T_{s_s} and T_{sh_s}; while in the two component case, foliage and soil have the mean temperatures T_f, T_s. The mean temperature for each component is defined as the ensemble mean temperature of all grid-points of each type of component according to Planck law:

$$B(T_k) = \frac{1}{N_k}\sum_{i=1}^{N_k} B(T_i) \tag{3.8}$$

where $T_k = T_{s\_f}$, T_{sh_f}, T_{s_s} or T_{sh_s} in the four component model, while $T_k = T_f$, T_s in the two component model. N_k is the number of grid-points for each type of component within the IFOV. Foliage in a grid-point i is assumed consisting of N_k finite facets with surface temperature T_k.

- The canopy geometry is characterized by the fractional area occupied by each component in the IFOV - the component fractional cover, which changes only with view zenith angle.

- Single scattering is taken into account to include the cavity effect in the simple linear mixture model.

Compared to the model with four components, the linear mixture model with two components is easier to invert when using observations of directional T_{b0} at two zenith view angles which are currently available from space. The outputs from such model are estimates of the mean component temperatures of soil and foliage in a canopy. As regards to the four component model, it is also invertible providing that the fractional cover for the four components can be estimated which needs significantly more information on the canopy geometry.

When the foliage-soil canopy is considered as a single emitter or reflector, only an effective radiometric temperature applies to the canopy system and the directional canopy emissivity needs to be determined to give an accurate estimate of the directional radiometric temperature of the canopy. However, radiometric temperature is not equivalent to the

physical temperature of a canopy, because no actual 'surface' exists in a foliage-soil canopy system.

Chapter 4

Approaches to parameterize heat exchanges using bi-angular radiance measurements

4.1   Introduction

The detailed radiative, heat and water vapor transfer model of the soil-vegetation-atmosphere system described in Chapter 2 is too complicated to apply in practice because too many unknowns are involved. Simplifications are necessary to derive a simpler model applicable with meteorological and remote sensing measurements. In Chapter 3 it was shown that directional observations of surface brightness temperatures $T_{b0}(\theta_v, \varphi_v)$ of a 3D soil vegetation canopy system can be represented by simple models. Heat transfer in a 3D canopy system may be parameterized at decreasing levels of complexity in each one of the cases considered in Chapter 3 to model radiative transfer. The complete model, the four-, two- and one components give the surface temperatures of different types of canopy elements, which lead to four-source, dual-source and single-source parameterizations of heat transfer.

A four-source model is closest to the reality. The dual-source parameterization, however, may be more practical, as compared to the four-source model, because the soil and foliage component temperatures can be estimated by inverting a simple linear mixture model (Eqs.3.19a and b) using bi-angular measurements of T_{b0}. On the other hand, soil and foliage component temperatures are more meaningful than the effective TOC radiometric temperature, i.e. a dual-source model is better than a single-source model. The latter is particularly relevant for a sparse canopy due to the strong thermal heterogeneity in such canopies. However, the investigation for the use of single-source models is still important considering that most remote sensing system can only provide measurements of T_{b0} at a single view angle.

In this chapter, the four-source, dual-source and single-source concepts to model heat transfer will be described. A practical dual-source model is proposed to estimate heat and water vapor exchanges between the land surface and the atmosphere above. A parameterization of resistance for heat transfer using bi-angular measurements is proposed and then used in an existing single-source model.

4.2 Derivation of generic simple models for heat transfer in a canopy

4.2.1 Four-source model

Eq. 2.27 is the energy balance equation at a particular grid-point. To infer a simpler model from the complete model (Eq. 2.27) we need to derive first the total instantaneous change in canopy heat content. This is obtained by integrating Eq. 2.27 over all grid-points, considering that T_{ac} is only dependent on the height z:

$$\sum_{j=1}^{N_c}\left[\rho_a c_p \frac{\partial T_{ac}(z_j)}{\partial t}\delta A \delta z\right]=-\sum_{j=1}^{N_c}\left[\frac{\partial}{\partial z}\left(K_h(\mathbf{r})\frac{\partial T_{ac}(z_j)}{\partial z}\right)\delta A \delta z\right]+\sum_{N_c}\left[S_H(\mathbf{r})\delta A \delta z\right] \quad (4.1)$$

where $\delta A \delta z = \delta V$ is the volume element associated with a grid-point, N_c is the total number of grid-points in the canopy. Grouping canopy grid-points into four categories, i.e. sunlit foliage, shaded foliage, sunlit soil and shaded soil, with the number of grid-points in each category being N_{s_f}, N_{sh_f}, N_{s_s} and N_{sh_s} with $N_c = N_{s\_f}+N_{sh\_f}+N_{s\_s}+N_{sh\_s}$, the source term in Eq.4.1 can be written as four explicit terms originating from the four component groups and Eq.4.1 becomes

$$\begin{aligned}
\sum_{j=1}^{N_c}\rho_a c_p \frac{\partial T_{ac}(z_j)}{\partial t}\delta A \delta z &= \sum_{j=1}^{N_c}\left[\frac{\partial}{\partial z}\left(K_h(\mathbf{r})\frac{\partial T_{ac}(z_j)}{\partial z}\right)\delta A \delta z\right]\\
&+\left[\begin{array}{l}\sum_{N_{s\_f}}\left(S_{H,s\_f}(\mathbf{r})\delta A \delta z\right)+\sum_{N_{sh\_f}}\left(S_{H,sh\_f}(\mathbf{r})\delta A \delta z\right)\\
+\sum_{N_{s\_s}}\left(S_{H,s\_s}(\mathbf{r})\delta A \delta z\right)+\sum_{N_{sh\_s}}\left(S_{H,sh\_s}(\mathbf{r})\delta A \delta z\right)\end{array}\right]
\end{aligned} \quad (4.2)$$

Assuming $K_h(\mathbf{r})$ does not change with (x,y) but only change with the height z (i.e. $K_h(\mathbf{r})=K_h(z)$), the first term on the right hand side of Eq.4.2 (and the term on the left hand side of Eq.4.2) can be replaced by a summation over z_j, taking into account that there are N_{hor} identical terms in the summation for each slab of thickness δz and that there are N_z points in the vertical direction ($N_c = N_{hor}\times N_z$):

$$\begin{aligned}
A\sum_{j=1}^{N_z}\left[\rho_a c_p \frac{\partial T_{ac}(z_j)}{\partial t}\delta z\right] &= A\sum_{j=1}^{N_z}\left[\frac{\partial}{\partial z}\left(K_h(z_j)\frac{\partial T_{ac}(z_j)}{\partial z}\right)\delta z\right]\\
&+\left[\begin{array}{l}\sum_{N_{s\_f}}\left(S_{H,s\_f}(\mathbf{r})\delta A \delta z\right)+\sum_{N_{sh\_f}}\left(S_{H,sh\_f}(\mathbf{r})\delta A \delta z\right)\\
+\sum_{N_{s\_s}}\left(S_{H,s\_s}(\mathbf{r})\delta A \delta z\right)+\sum_{N_{sh\_s}}\left(S_{H,sh\_s}(\mathbf{r})\delta A \delta z\right)\end{array}\right]
\end{aligned} \quad (4.3)$$

where A is the area occupied by the canopy, $A = N_{hor}\times \delta A$.

Further, introducing mean source (or sink) terms associated with the four categories, i.e. the mean heat source term from sunlit foliage $S_{\mathrm{H,s\_f}}$, the mean heat source term from shadowed foliage $S_{\mathrm{H,sh\_f}}$, the mean heat source term from sunlit soil $S_{\mathrm{H,s\_s}}$, and the mean heat source term from shadowed soil $S_{\mathrm{H,sh\_s}}$; and meanwhile introducing area density for the four categories, i.e. $\rho_{\mathrm{s\_f}}(\vec{r})$, $\rho_{\mathrm{sh\_f}}(\vec{r})$, $\rho_{\mathrm{s\_s}}(\vec{r})$ and $\rho_{\mathrm{sh\_s}}(\vec{r})$, Eq. 4.3 becomes:

$$
\begin{aligned}
A\sum_{j=1}^{N_z}\left[\rho_{\mathrm{a}}c_{\mathrm{p}}\frac{\partial T_{\mathrm{ac}}(z_j)}{\partial t}\delta z\right] &= A\sum_{j=1}^{N_z}\left[\frac{\partial}{\partial z}\left(K_{\mathrm{h}}(z_j)\frac{\partial T_{\mathrm{ac}}(z_j)}{\partial z}\right)\delta z\right] \\
&+ \begin{bmatrix}
S_{\mathrm{H,s\_f}}\sum_{j=1}^{N_z}\left(\rho_{\mathrm{s\_f}}(\vec{r})\,\delta A\,\delta z\right) + S_{\mathrm{H,sh\_f}}\sum_{j=1}^{N_z}\left(\rho_{\mathrm{sh\_f}}(\vec{r})\,\delta A\,\delta z\right) \\
+ S_{\mathrm{H,s\_s}}\sum_{j=1}^{N_z}\left(\rho_{\mathrm{s\_s}}(\vec{r})\,\delta A\,\delta z\right) + S_{\mathrm{H,sh\_s}}\sum_{j=1}^{N_z}\left(\rho_{\mathrm{sh\_s}}(\vec{r})\,\delta A\,\delta z\right)
\end{bmatrix}
\end{aligned}
\tag{4.4}
$$

Assuming leaf area densities, $\rho_{\mathrm{s\_f}}(\vec{r})$, $\rho_{\mathrm{sh\_f}}(\vec{r})$, $\rho_{\mathrm{s\_s}}(\vec{r})$ and $\rho_{\mathrm{sh\_s}}(\vec{r})$, do not change with (x,y) but only change with the height z, i.e. $\rho_{\mathrm{s\_f}}(\vec{r})=\rho_{\mathrm{s\_f}}(z)$, $\rho_{\mathrm{sh\_f}}(\vec{r})=\rho_{\mathrm{sh\_f}}(z)$, $\rho_{\mathrm{s\_s}}(\vec{r})=\rho_{\mathrm{s\_s}}(z)$, and $\rho_{\mathrm{sh\_s}}(\vec{r})=\rho_{\mathrm{sh\_s}}(z)$, Eq. 4.4 reads

$$
\begin{aligned}
A\sum_{j=1}^{N_z}\left[\rho_{\mathrm{a}}c_{\mathrm{p}}\frac{\partial T_{\mathrm{ac}}(z_j)}{\partial t}\delta z\right] &= A\sum_{j=1}^{N_z}\left[\frac{\partial}{\partial z}\left(K_{\mathrm{h}}(z_j)\frac{\partial T_{\mathrm{ac}}(z_j)}{\partial z}\right)\delta z\right] \\
&+ \begin{bmatrix}
S_{\mathrm{H,s\_f}}N_{\mathrm{hor}}\delta A\sum_{j=1}^{N_z}\left(\rho_{\mathrm{s\_f}}(z_j)\,\delta z\right) + S_{\mathrm{H,sh\_f}}N_{\mathrm{hor}}\delta A\sum_{j=1}^{N_z}\left(\rho_{\mathrm{sh\_f}}(z_j)\,\delta z\right) \\
+ S_{\mathrm{H,s\_s}}N_{\mathrm{hor}}\delta A\sum_{j=1}^{N_z}\left(\rho_{\mathrm{s\_s}}(z_j)\,\delta z\right) + S_{\mathrm{H,sh\_s}}N_{\mathrm{hor}}\delta A\sum_{j=1}^{N_z}\left(\rho_{\mathrm{sh\_s}}(z_j)\,\delta z\right)
\end{bmatrix}
\end{aligned}
\tag{4.5}
$$

The summations of leaf area density $\rho_{\mathrm{s\_f}}(z)$ and $\rho_{\mathrm{sh\_f}}(z)$ over the height z give the leaf area per unit area for each foliage group which are referred to as sunlit leaf area index $LAI_{\mathrm{s\_f}}$ and shadowed leaf area index $LAI_{\mathrm{sh\_f}}$. Since there is only one soil grid-point in each canopy column, the summations of $\rho_{\mathrm{s\_s}}(z)$ and $\rho_{\mathrm{sh\_s}}(z)$ over z give the fraction of sunlit soil area $f_{\mathrm{s\_s}}$ and shadowed soil area $f_{\mathrm{sh\_s}}$ occupying the canopy area A. Considering $A=N_{\mathrm{hor}}\times\delta A$, Eq. 4.5 then reduces to:

$$\sum_{j=1}^{N_z} \left[\rho_a c_p \frac{\partial T_{ac}(z_j)}{\partial t} \delta z \right] = \sum_{j=1}^{N_z} \left[\frac{\partial}{\partial z} \left(K_h(z_j) \frac{\partial T_{ac}(z_j)}{\partial z} \right) \delta z \right]$$
$$+ \left[S_{H,s\_f} LAI_{s\_f} + S_{H,sh\_f} LAI_{sh\_f} + S_{H,s\_s} f_{s\_s} + S_{H,sh\_s} \rho_{sh\_s} \right]$$

(4.6)

Taking into account that under steady stable condition the term on the left hand side in Eq. 4.6 is zero, the total change in canopy heat content per unit area becomes:

$$\sum_{j=1}^{N_z} \left[\frac{\partial}{\partial z} \left(K_h(z_j) \frac{\partial T_{ac}(z_j)}{\partial z} \right) \delta z \right] = - \left[S_{H,s\_f} LAI_{s\_f} + S_{H,sh\_f} LAI_{sh\_f} + S_{H,s\_s} f_{s\_s} + S_{H,sh\_s} \rho_{sh\_s} \right]$$

(4.7)

The term on the left hand side of Eq. 4.7 is the sensible heat flux density, H (Wm^{-2}), positive when away from the TOC:

$$\sum_{j=1}^{N_z} \frac{\partial}{\partial z} \left(K_h(z_j) \frac{\partial T_{ac}(z_j)}{\partial z} \right) \delta z = - \sum_{j=1}^{N_z} \frac{\partial H(z_j)}{\partial z} = - \sum_{j=1}^{N_z} \left[H(z_{j+1}) - H(z_j) \right] = -H \qquad (4.8)$$

The source or sink of heat was determined in §2.4 (Eq.2.18 for grid-point containing leaves, the one for soil was not given but similar to Eq.2.18 with proper resistance and temperature for the soil). The mean heat source terms associated with the four groups in Eq. 4.7 can be defined by the mean temperature (Eq. 3.8) and by introducing a reference height for heat exchange in the canopy z_0 and the aerodynamic resistances for the four groups. The total sensible heat flux density from the canopy is then written

$$H = LAI_{s\_f} \frac{2\rho_a c_p}{r_{ah,s\_f}} \left[T_{s\_f} - T_{ac}(z_0) \right] + LAI_{sh\_f} \frac{2\rho_a c_p}{r_{ah,sh\_f}} \left[T_{sh\_f} - T_{ac}(z_0) \right]$$
$$+ f_{s\_s} \frac{\rho_a c_p}{r_{ah,s\_s}} \left[T_{s\_s} - T_{ac}(z_0) \right] + f_{sh\_s} \frac{\rho_a c_p}{r_{ah,s\_sh}} \left[T_{sh\_f} - T_{ac}(z_0) \right]$$

(4.9)

where $T_{ac}(z_0)$ is air temperature at the reference height z_0 in the canopy, r_{ah,s_f}, r_{ah,sh_f}, r_{ah,s_s} and r_{ah,s_sh} are the aerodynamic resistances for the four groups respectively. The terms of T_{s_f}, T_{sh_f}, T_{s_s}, T_{sh_s}, f_{s_s} and f_{sh_s} are all defined in Chapter 3.

Introducing $r_{ah}(z_0, z)$ as the aerodynamic resistance for heat transfer between z_0 and a reference height above the canopy z_{ref}, the integration of Eq.4.8 also gives

$$H = \rho_a c_p \frac{T_{ac}(z_0) - T_a(z_{ref})}{r_{ah}(z_0, z_{ref})}$$

(4.10)

where $r_{ah}(z_0, z) = \dfrac{\rho_a c_p}{K_h(z)}$.

We have assumed here that the four component groups interact independently with the air flow inside the canopy and the air flow inside the canopy interacts with the overlying atmosphere and the interactions between these components are neglected. Such assumption imply there are five aerodynamic resistances which control the heat transfer between the canopy, consisting of the four components, and the atmosphere above: (1) surface aerodynamic resistance of sunlit soil, r_{ah,s_s}, controlling the heat transfer between the sunlit soil surface and the air at a reference height z_0 inside the canopy; (2) surface aerodynamic resistance of shaded soil, r_{ah,s_sh}, controlling the heat transfer between the shaded soil surface and the air at z_0 inside the canopy; (3) foliage boundary layer resistance of sunlit foliage, r_{ah,f_s}, controlling the heat transfer between the sunlit foliage and the air at a reference height z_0 inside the canopy; (4) foliage boundary layer resistance of shaded foliage, r_{ah,f_sh}, controlling the heat transfer between the shaded foliage and the air at a reference height z_0 inside the canopy; and (5) the canopy aerodynamic resistance, $r_{ah}(z_0, z_{ref})$, which links the canopy air at height to z_0 the mean flow at reference height z_{ref} in the atmosphere above the canopy. The four component resistances together with the differences between component temperatures and in-canopy air temperature determine the distribution of heat sources and sinks within the canopy, which in turn determine the quantity of sensible heat from the canopy along with $r_{ah}(z_0, z_{ref})$ and $[T_{ac}(z_0) - T_a(z_{ref})]$.

4.2.2   Dual-source model

If the soil-foliage system is further simplified under the similar scheme as used in deriving the four-source model and only two components, i.e. soil and foliage, are considered, the sensible heat flux density from such canopy system can be expressed by reducing Eq. 4.9 to

$$H \;=\; LAI \frac{2\rho_a c_p}{r_{ah,f}} \big[T_f - T_{ac}(z_0) \big] + f_s \frac{\rho_a c_p}{r_{ah,s}} \big[T_s - T_{ac}(z_0) \big] \tag{4.11}$$

where the contributions from foliage and from the soil component are:

$$H_f \;=\; LAI \frac{2\rho_a c_p}{r_{ah,f}} \big[T_f - T_{ac}(z_0) \big] \tag{4.12}$$

$$H_s = f_s \frac{\rho_a c_p}{r_{ah,s}} [T_s - T_{ac}(z_0)] \tag{4.13}$$

Eq.10 also applies in the dual-source model to describe the interaction between the air flow within the canopy and the overlaying atmosphere. Eqs.4.10 and 4.11 indicate that, in the dual-source concept (Fig. 4.1), the heat exchange between the canopy and the overlying atmosphere is controlled by the three aerodynamic resistances for heat transfer which are (1) the leaf boundary layer resistance, $r_{ah,f}$, controlling the heat transfer between the foliage surface and the canopy air; (2) the boundary layer resistance of the soil surface, $r_{ah,s}$, controlling the heat transfer between the soil surface and the canopy air; (3) the aerodynamic resistance $r_{ah}(z_0, z_{ref})$ controlling the heat exchange between z_0 and z_{ref}. The parameterization of $r_{ah,f}$, $r_{ah,s}$ and $r_{ah}(z_0, z_{ref})$ will be given in §4.3.3.
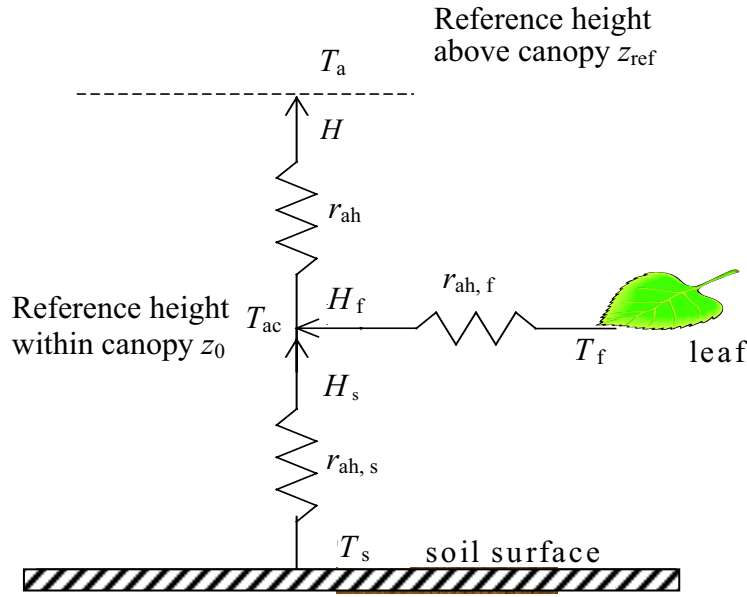
Figure 4.1 Schematic description of the *dual-source* model for heat transfer.

4.2.3   Single-source model

When the canopy is considered as only one single source/sink of heat and water vapor (Fig.4.2), the energy balance equation Eq.4.7 reads:

$$H = \frac{\rho_a c_p}{r_{ah}(z_{0h}, z_{ref})} [T_0(z_{0h}) - T_a(z_{ref})] \tag{4.14}$$

where z_{0h} is the roughness height for heat transfer, $T_0(z_{0h})$ is the temperature at z_{0h}. Eq.4.14 is the classical form of heat transfer description in most single-source models. As one can see there is only one resistance linking the canopy to the atmosphere above - the resistance $r_{ah}(z_{0h}, z_{ref})$ between z_{0h} and z_{ref}. In such a single-source model, the canopy is considered as a homogeneous thin layer exchanging heat and water vapor from the single source/sink height z_{0h}.
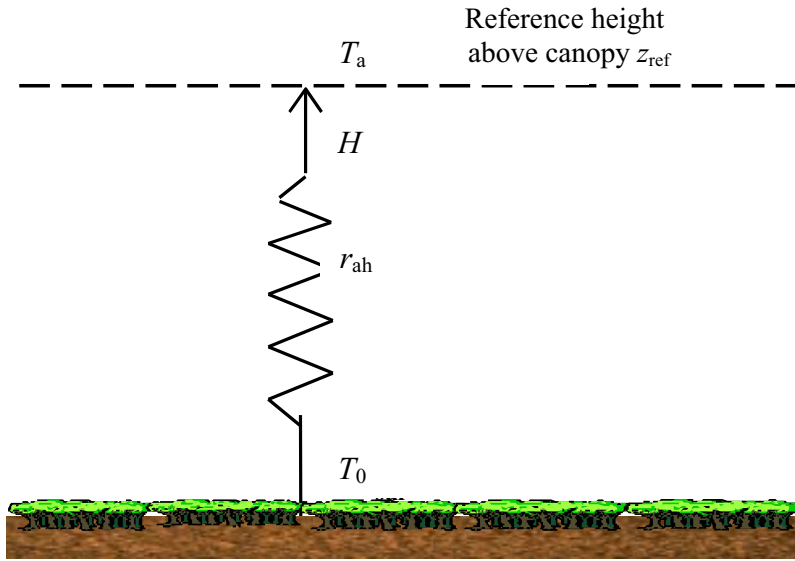
Figure 4.2 Schematic description of the *single-source* model for heat transfer.

4.3 Example of dual-source model for heat transfer using bi-angular thermal infrared measurements

4.3.1 Introduction

As discussed in Chapter 3, it may not be practical at the current stage to measure all the four component temperatures, while observation of T_f and T_s is easier (see Chapter 3). Moreover, four heat transfer resistances need to be parameterized and this may require knowledge of additional canopy properties. On the contrary, many previous works contribute to the parameterization of resistances of soil and foliage. All these facts suggest that the dual-source model may be more applicable. Detailed observation of the distribution of component temperatures will be used later (see Chapter 5 and 6) to document these statements.

The simplest formulation is a single-source model as used in many land surface processes models and NWP models. As discussed in Chapter 1, the problem with a single-source model is *how to define the 'surface'* and *how to measure the associated surface temperature*. The first issue relates to the 3D structure of a soil-vegetation canopy, i.e. it is difficult to define a reference 'surface' in it. The second issue relates to the directionality of measured T_{b0} due to the thermal heterogeneity of the canopy. However, it might be possible to make the single-source model still useful if an adequate parameterization of r_{ah} can be established.

4.3.2　Energy balance in a dual-source model

In the dual-source concept, each component of the canopy system, i.e. foliage and soil interacts individually with the atmosphere above and fulfils the respective energy balance:

$$R_{n,f} \ = \ H_f + \lambda E_f \tag{4.15}$$

$$R_{n,s} \ = \ H_s + \lambda E_s + G_0 \tag{4.16}$$

where $R_{n,f}$ (W m^{-2}) is the net radiation flux density absorbed by foliage, $R_{n,s}$ (W m^{-2}) is the net radiation flux density absorbed by the soil surface, λE_f (W m^{-2}) and λE_s (W m^{-2})are the latent heat flux densities from foliage and soil respectively, and G_0 (W m^{-2}) is the soil heat flux density.

The instantaneous heat balance of the soil-foliage system is obtained by adding the r.h.s. and the l.h.s. of Eqs. 4.15 and 4.16:

$$R_n \ = \ R_{n,f} + R_{n,s} \tag{4.17}$$

$$H \ = \ H_f + H_s \tag{4.18}$$

$$\lambda E \ = \ \lambda E_f + \lambda E_s \tag{4.19}$$

where R_n (W m^{-2}) is the net radiation flux density above the TOC.

Neglecting advection, photosynthesis and heat storage in the canopy, the energy balance equation of a vegetated canopy is the integral throughout the canopy (Eqs.2.20 and 2.21) and equivalent to:

$$R_n \ = \ H + \lambda E + G_0 \tag{4.20}$$

Estimation of $R_{n,f}$ and $R_{n,s}$

Assuming that the extinction of R_n inside the canopy layer follows approximately Beer's Law (Ross, 1981; Schmugge, 1998), $R_{n,f}$ can be described as a function of LAI ,

$$R_{n,f} = R_n \left(1 - e^{-k_a LAI}\right) \tag{4.21}$$

where k_a is the extinction coefficient, in the range $0.3-0.6$ according to observations. Then, $R_{n,s}$ can be estimated as

$$R_{n,s} = R_n - R_{n,f} \tag{4.22}$$

Estimation of G_0

A direct remote sensing technique for estimating G_0 is not available. A practical method used by many authors is to relate G_0 to net radiation arriving at the soil surface with consideration of surface cover conditions in terms of leaf area index, vegetation index or fractional vegetation cover (Choudhury, 1987; Clothier et al, 1986; Kustas and Daughtry, 1990).

In the dual-source model concept, surface, G_0 is simply estimated by taking a proportion of the net radiation at the soil as

$$G_0 = \alpha_G \left(R_n - R_{n,f}\right) \tag{4.23}$$

where the constant α_G has the range of $0.2-0.5$ for bare soil.

Estimation of H_f and H_s

To estimate H_f and H_s by Eqs.4.12 and 4.13, one must know $r_{ah,f}$, $r_{ah,s}$ and $T_{ac}(z_0)$ besides T_f and T_s which can be derived by inverting Eq.3.19 using bi-angular TIR radiance measurements (see Chapter 6). The parameterization of $r_{ah,f}$ and $r_{ah,s}$ will be given in §4.3.3. Combining Eqs. 4.10, 4.12 and 4.13, $T_{ac}(z_0)$ is expressed as

$$T_{ac}(z_0) = \frac{\dfrac{T_a(z_{ref})}{r_{ah}(z_0, z_{ref})} + 2LAI\dfrac{T_f}{r_{ah,f}} + f_s\dfrac{T_s}{r_{ah,s}}}{\dfrac{1}{r_{ah}(z_0, z_{ref})} + \dfrac{2LAI}{r_{ah,f}} + \dfrac{f_s}{r_{ah,s}}} \tag{4.24}$$

Eq.4.24 shows that $T_{ac}(z_0)$ is treated as an ancillary variable and can be expressed as a function of other variables. This implies that precise knowledge of the apparent heat source height z_0 in the dual-source model is not as critical as in a single-source model and can be taken as an arbitrary height inside the canopy. The roughness length for momentum z_{0m} is taken because it can be estimated from canopy height.

Since $T_{ac}(z_0)$ is also involved in $r_{ah,f}$ and $r_{ah,s}$ as will be shown in § 4.3.3, iterations are necessary to determine the values of $T_{ac}(z_0)$ firstly, and then H_f, H_s and H.

Estimation of λE_f and λE_s

In our dual-source model, the emphasis has been put on estimating H while λE_f and λE_s are determined as the residuals of Eq.4.15 and Eq.4.16 respectively.

4.3.3 Parameterization of resistances for heat transfer in the dual-source model

As shown in the previous section, there are basically two types of resistance: bulk aerodynamic resistance between canopy surface and the atmosphere (r_{ah}), and leaf (soil) boundary layer resistance ($r_{ah,f}$ and $r_{ah,s}$). In this section, these two categories of resistance will be discussed separately.

Boundary layer resistances of leaf/soil

Depending on the state of the canopy-air system, heat transfer may be determined by either forced or free convection. In theory, several criteria have been established to recognize the prevailing regime for a given system (Stanghellini, 1987). However, in reality, a region may occur which is neither forced or free convection and is referred to as the transition between these two. In this chapter, the transition region of convection is also taken into account to parameterize $r_{ah,f}$ and $r_{ah,s}$.

The foliage boundary resistance for sensible heat transfer $r_{ah,f}$ is related to the non-dimensional convection Nusselt number Nu, the thermal conductivity of air λ_a (W m^{-1} K^{-1}), and a characteristic leaf dimension l_L (usually taken as the mean leaf width) as

$$r_{ah,f} = \frac{\rho_a \, c_p \, l_L}{\lambda_a \, Nu} \tag{4.25}$$

Nu can be written as a function of either the Reynolds (*Re*) or the Grashof number (*Gr*) depending on whether forced or free convection is dominating the heat transfer. Taking into account the transition between forced and free convection, a mixed convection Nusselt number was introduced (Stanghellini, 1987)

$$Nu = 0.37 [Gr + 6.92 Re^2]^{0.25} \tag{4.26}$$

where *Gr* is the Grashof number given by:

$$Gr = \frac{g \beta l_L^3}{v^2} [T_f - T_{ac}(z_0)] \tag{4.27}$$

and the Reynolds number *Re* is

$$Re = \frac{u_{ac}(z_0) l_L}{v} \tag{4.28}$$

where v is the kinematic viscosity of air (m^2 s^{-1}), g is the acceleration due to gravity (m s^{-2}), β is the coefficient of thermal expansion of air (K^{-1}) [$\beta = 1/T_{ac}(z_0)$], $u_{ac}(z_0)$ (m s^{-1}) is windspeed at reference height z_0 in the canopy .

After substituting Eqs. 4.26, 4.27 and 4.28 into Eq. 4.25, $r_{ah,f}$ can be written as

$$r_{ah,\,f} = \frac{C_1 l_L^{0.5}}{\left(l_L |T_f - T_{ac}| + C_2 u_{ac}^2 \right)^{0.25}} \tag{4.29}$$

where C_1 and C_2 are the coefficients corresponding to the air properties (see Table A.1) ,

$$C_1 = \frac{\rho_a c_p}{0.37 \lambda_a} \left(\frac{v^2}{g \beta} \right)^{0.25} \tag{4.30a}$$

$$C_2 = \frac{6.92}{g \beta} \tag{4.30b}$$

Under either large wind speeds or small leaf size, Eq.4.29 is reduced to forced convection.

To parameterize soil resistance in a similar way in the dual-source model, a suitable linear dimension of the soil surface for the vegetation/soil system must be identified and estimated. Goudriaan's mean mixing length, l_m, within a canopy based on the free space between leaves and stems (Goudriaan, 1977) is considered as an appropriate characteristic dimension for soil area in-between the plants (Sauer and Norman, 1995). The value of l_m

within the canopy is taken by Goudriaan as the free space between the leaves (if only leaves are considered) which can be determined by the dimension of leaves l_L and the leaf area density ρ_f given the shape of leaves:

$$l_m = 2\left(\frac{3l_L^2}{4\pi\rho_f}\right)^{1/3}, \text{ for square leaves} \qquad (4.31a)$$

$$l_m = \left(\frac{4l_L}{\pi\rho_f}\right)^{1/2}, \text{ for long and narrow leaves} \qquad (4.31b)$$

The typical dimension of the soil surface, l_s, is taken as l_m. The parameterization for the soil resistance is then given by

$$r_{ah,s} = \frac{C_1 l_s^{0.5}}{\left(l_s \left|T_s - T_{ac}\right| + C_2 u_{ac}^2\right)^{0.25}} \qquad (4.32)$$

To estimate $r_{ah,f}$ and $r_{ah,s}$ by Eq.4.29 and 4.32, the windspeed inside the canopy must to be known. Assuming that l_m, ρ_f, the relative turbulence intensity i_w, and the drag coefficient of foliage c_{df} are constant with the height inside the canopy, the windspeed inside the canopy is given by Goudriaan (1977),

$$u_{ac}(z) = u(h) \exp\left[-a_u\left(1-\frac{z}{h}\right)\right] \qquad (4.33)$$

where $u(h_c)$ is the windspeed at TOC, i.e. $z = h_c$, the extinction factor for windspeed inside the canopy a_u is expressed as

$$a_u = a\Phi_m^{0.5} \qquad (4.34)$$

with a_{u0} being the extinction factor under neutral atmosphere conditions:

$$a_{u0} = \left(\frac{c_{df} LAI h}{2l_m i_w(z)}\right)^{0.5} \qquad (4.35)$$

The function Φ_m in Eq.4.34 is the stability correction function for heat transfer inside the canopy and is given in Appendix V.

Bulk aerodynamic resistances

In the dual-source model, the heat source is located at some reference height inside the canopy, e.g. the roughness length for momentum. The classical form (Monteith, 1973; Brutsaert, 1999) of r_{ah} is therefore adopted

$$r_{ah} = \frac{1}{ku_*}\left[\ln\left(\frac{z-d}{z_0}\right) - \Psi_h\left(\frac{z-d}{L}\right) + \Psi_h\left(\frac{z_0}{L}\right)\right] \tag{4.36}$$

where k is the von Karman constant (= 0.40), u_* is the friction velocity (m s^{-1}) in the Atmospheric Surface Layer (ASL) (defined as $= \left(\tau_0 \middle/ \rho_a\right)^{\frac{1}{2}}$ with τ_0 the surface shear stress) and is estimated by

$$u_* = \frac{ku(z)}{\ln\left(\frac{z-d}{z_{0m}}\right) - \Psi_m\left(\frac{z-d}{L}\right)} \tag{4.37}$$

where L is the Monin-Obukhov length and given as

$$L = -\frac{\rho_a c_p u_*^3 \theta_{av}}{kgH} \tag{4.38}$$

where θ_{av} is the virtual potential temperature of air (K).

The functions Ψ_h in Eq.4.36 and Ψ_m in Eq.4.37 are the correction function for atmospheric stability which will be given in Appendix V on the basis of either the Monin-Obukhove Similarity (MOS) theory in the Atmospheric Surface Layer (ASL) or the Bulk Atmospheric Boundary Layer (ABL) Similarity (BAS) theory, depending on whether the reference height is in the ASL or in the outer region of the ABL according to Brutsaert (1999). Such treatment will allow to apply the dual-source model at both local (satellite pixel) scale and regional scale, because the reference height is correlated to the footprint of turbulent heat fluxes (see the application and discussion in Chapter 6).

4.4 Example of single-source model for heat transfer using bi-angular thermal infrared measurements

4.4.1 Energy balance in a single-source model

The basic law of Surface Energy Balance (SEB) described by Eq.4.20 is also applied in the single-source model but the canopy is assumed to be a flat, thin layer and radiative, heat and water vapor exchanges with the atmosphere above are occurring at a single source/sink height.

Estimation of R_n

R_n is estimated from the radiation balance

$$R_n = R_s^{\downarrow} - R_s^{\uparrow} + R_L^{\downarrow} - R_L^{\uparrow}$$
$$= (1-\alpha)R_{s0} + R_L^{\downarrow} - R_L^{\uparrow} \tag{4.39}$$

where $R_s^{\downarrow}$ and $R_s^{\uparrow}$ ($R_L^{\downarrow}$ and $R_L^{\uparrow}$) are the incoming and outgoing solar (long-wave) radiation flux density, R_{s0} is the global short-wave radiation flux density above the canopy, α is the albedo of TOC.

R_{s0} can be derived as

$$R_{s0} = S_{s0}\,\tau_a \cos\theta_s \tag{4.40}$$

where S_{s0} is the solar constant (1367 Wm^{-2}), τ_a is the atmospheric transmittance in the VIS/NIR spectrum which is typically 0.75 (Xue et al, 2000).

$R_L^{\downarrow}$ can be estimated as a function of mean air temperature in the atmospheric boundary layer,

$$R_L^{\downarrow} = \varepsilon_a\,\sigma T_a^{\,4} \tag{4.41}$$

where σ ($=5.678\times10^{-8}$) is Stefan-Boltzman's constant. According to Brutsaert (1982), the effective atmospheric emissivity ε_a is a function of water vapor pressure and temperature of air,

$$\varepsilon_a = 1.72\left(\frac{e_a}{T_a}\right)^{1/7} \tag{4.42}$$

$R_L^{\uparrow}$ is estimated as

$$R_L{}^\uparrow = \varepsilon_c \, \sigma \, T_{rad}{}^4 \qquad (4.43)$$

where ε_c and T_{rad} were defined in Eq. 3.21 but the values at nadir view and in the broad band (8-14μm) are used here.

Estimation of G_0

Assuming a linear correlation exists between G_0 and R_n both for the bare soil and the fully covered surface, such relationship can be expressed empirically as

$$G_0 = R_n[a_f + (a_s - a_f)(1 - f_f)] \qquad (4.44)$$

where a_s and a_f are the ratios between G_0 and R_n for the bare soil and the fully covered vegetation surface respectively. The values of a_s were found between 0.3 to 0.5 (Idso et al, 1975; Brutsaert, 1982), while a_f between 0.05 to 0.1 (Monteith, 1973; De Bruin and Holtslag, 1982).

Estimation of H *and* λE *- Surface Energy Balance Index (SEBI) method*

Integrating Eqs.2.18 and 2.19 between z_{0h} and z_{ref}, one can obtain the bulk transfer equation for H (Eq.4.14), while λE is given by:

$$\lambda E = \frac{\rho_a c_p}{\gamma} \frac{e_0(z_{0e}) - e_a(z_{ref})}{r_{ae}(z_{0e}, z_{ref})} \qquad (4.45)$$

where γ (Pa K^{-1}) is the psychrometric constant, $e_0(z_{0e})$ (Pa) is the vapor pressure at the height of the source/sink of water vapor transfer, i.e. roughness length for water vapor z_{0e}, $e_a(z_{ref})$ (Pa) is air vapor pressure at z_{ref} in the atmosphere. The term $e_0(z_{0e})$ has been often referred to as 'surface water vapor pressure' in single-source models.

The aerodynamic resistances for heat $r_{ah}(z_{0h}, z_{ref})$ in Eq. 4.14 and for vapor transfer $r_{ae}(z_{0e}, z_{ref})$ in Eq. 4.45 are expressed respectively as

$$r_{ah}(z_{0h}, z_{ref}) = \frac{1}{ku_*}\left[\ln\left(\frac{z-d}{z_{0h}}\right) - \Psi_h\left(\frac{z-d}{L}\right) + \Psi_h\left(\frac{z_{0h}}{L}\right)\right] \qquad (4.46)$$

$$r_{ae}(z_{0e}, z_{ref}) = \frac{1}{ku_*}\left[\ln\left(\frac{z-d}{z_{0e}}\right) - \Psi_e\left(\frac{z-d}{L}\right) + \Psi_e\left(\frac{z_{0e}}{L}\right)\right] \qquad (4.47)$$

where Ψ_{e} is the stability function for water vapor transfer. It is assumed that $z_{0\mathrm{e}}$ equals to $z_{0\mathrm{h}}$ and Ψ_{e} equals to Ψ_{h} which means that $r_{\mathrm{ae}}(z_{0\mathrm{e}}, z_{\mathrm{ref}})$ and $r_{\mathrm{ah}}(z_{0\mathrm{h}}, z_{\mathrm{ref}})$ are equal.

As the extension of Penman's equation for open water evaporation (Penman, 1948), Monteith (1965) has developed the Penman-Monteith equation for vegetation by introducing the surface resistance based on Eq.4.43. By grouping the resistance terms into the bulk internal resistance (r_{i}) (or surface, or stomatal) and external resistances (e.g. the aerodynamic resistance $r_{\mathrm{ah}}(z_{0\mathrm{h}}, z_{\mathrm{ref}})$), Menenti (1984) proposed another combination equation for evaporation which can also be applied to a soil surface with properly defined internal bulk resistance r_{i},

$$\lambda E = \frac{\Delta\, r_{\mathrm{ah}}(z_{0\mathrm{h}}, z_{\mathrm{ref}})\,(R_{\mathrm{n}} - G_0) + \rho_{\mathrm{a}} c_{\mathrm{p}}[e_0(z_{0\mathrm{h}}) - e_{\mathrm{a}}(z_{\mathrm{ref}})]}{r_{\mathrm{ah}}(z_{0\mathrm{h}}, z_{\mathrm{ref}})\,(\gamma + \Delta) + \gamma\, r_{\mathrm{i}}} \tag{4.48}$$

where $e_0(z_{0\mathrm{h}})$ (Pa) is a function of the temperature $T_0(z_{0\mathrm{h}})$: $e_0(z_{0\mathrm{h}}) = e[T_0(z_{0\mathrm{h}})]$, Δ (Pa K^{-1}) is the rate of change of saturation vapor pressure with temperature.

The difficulty of using Eq.4.48, especially at the regional scale, is the estimation of r_{i} which is regulated by soil water availability as discussed by Su (2002). To avoid using r_{i}, a Surface Energy Balance Index (SEBI) was proposed by Menenti and Choudhury (1993)

$$SEBI = 1 - \frac{\lambda E}{\lambda E_p} = \frac{\dfrac{T(z_{0\mathrm{h}}) - T_{\mathrm{a}}}{r_{\mathrm{ah}}(z_{0\mathrm{h}}, z_{\mathrm{ref}})} - \dfrac{[T(z_{0\mathrm{h}}) - T_{\mathrm{a}}]_{\mathrm{w}}}{r_{\mathrm{ah}}(z_{0\mathrm{h}}, z_{\mathrm{ref}})_{\mathrm{w}}}}{\dfrac{[T(z_{0\mathrm{h}}) - T_{\mathrm{a}}]_{\mathrm{d}}}{r_{\mathrm{ah}}(z_{0\mathrm{h}}, z_{\mathrm{ref}})_{\mathrm{d}}} - \dfrac{[T(z_{0\mathrm{h}}) - T_{\mathrm{a}}]_{\mathrm{w}}}{r_{\mathrm{ah}}(z_{0\mathrm{h}}, z_{\mathrm{ref}})_{\mathrm{w}}}} \tag{4.49}$$

where $\dfrac{\lambda E}{\lambda E_{\mathrm{p}}} = \Lambda_{\mathrm{r}}$ is the relative evaporation, λE_{p} is the potential evaporation of the surface and defined according to Penman (1948) as

$$\lambda E_{\mathrm{p}} = \frac{\Delta(R_{\mathrm{n}} - G) + \dfrac{\rho_{\mathrm{a}} c_p [e_0(z_{0\mathrm{h}}) - e_{\mathrm{a}}(z_{\mathrm{ref}})]}{r_{\mathrm{ah}}(z_{0\mathrm{h}}, z_{\mathrm{ref}})}}{\gamma + \Delta} \tag{4.50}$$

By substitution of Eqs.4.14 and 4.48 into Eq. 4.20, the surface-air temperature difference is obtained as

$$T(z_{0h}) - T_a(z_{ref}) = \cfrac{\cfrac{r_i + r_{ah}(z_{0h}, z_{ref})}{\rho_a c_p}(R_n - G_0) - \cfrac{e_0(z_{0h}) - e_a(z_{ref})}{\gamma}}{1 + \cfrac{\Delta}{\gamma} + \cfrac{r_i}{r_{ah}(z_{0h}, z_{ref})}} \tag{4.51}$$

In Eq.4.49, the subscript w denotes the wet-limit condition (wet-bound) where evaporation takes its potential value and the energy balance equation can be written as

$$\lambda E_w = R_n - G_0 - H_w \tag{4.52}$$

This is the case for $r_i \to 0$ in Eq.4.51 and the wet bound of surface-air temperature difference is therefore

$$[T(z_{0h}) - T_a(z_{ref})]_w = \cfrac{\cfrac{r_{ah}(z_{0h}, z_{ref})_w}{\rho_a c_p}(R_n - G_0) - \cfrac{e_0(z_{0h}) - e_a(z_{ref})}{\gamma}}{\left(1 + \cfrac{\Delta}{\gamma}\right)} \tag{4.53}$$

The subscript d in Eq.4.51 denotes the dry-limit condition (dry-bound) when evaporation becomes zero and the sensible heat flux density takes its maximum value, i.e.

$$H_d = R_n - G_0 \tag{4.54}$$

This corresponds with the case for $r_i \to \infty$ in Eq.4.51 and the dry bound of the surface-air temperature difference is

$$[T(z_{0h}) - T_a(z_{ref})]_d = \frac{r_{ah}(z_{0h}, z_{ref})_d}{\rho_a c_p}(R_n - G_0) \tag{4.55}$$

By analogy with Eq.4.46, aerodynamic resistances in wet and dry conditions are defined as

$$r_{ah}(z_{0h}, z_{ref})_w = \frac{1}{ku_*}\left[\ln\left(\frac{z-d}{z_{0h}}\right) - \Psi_h\left(\frac{z-d}{L_w}\right) + \Psi_h\left(\frac{z_{0h}}{L_w}\right)\right] \tag{4.56}$$

$$r_{ah}(z_{0h}, z_{ref})_d = \frac{1}{ku_*}\left[\ln\left(\frac{z-d}{z_{0h}}\right) - \Psi_h\left(\frac{z-d}{L_d}\right) + \Psi_h\left(\frac{z_{0h}}{L_d}\right)\right] \tag{4.57}$$

assuming that the surface architecture does not change under these two limits. The Monin-Obukhov length for these two limits are expressed respectively as

$$L_{\text{w}} = -\frac{\rho_a u_*^3}{kg\left(\dfrac{H_{\text{w}}}{T(z_{0\text{h}})c_{\text{p}}} + 0.61\dfrac{R_{\text{n}} - G_0}{\lambda}\right)} \tag{4.58}$$

and

$$L_{\text{d}} = -\frac{\rho_a u_*^3}{kg\left(\dfrac{R_{\text{n}} - G_0}{T(z_{0\text{h}})c_{\text{p}}}\right)} \tag{4.59}$$

The evaporative fraction $\varLambda$ is defined as the ratio of actual evaporation to the available energy $R_{\text{n}} - G_0$,

$$\varLambda = \frac{\lambda E}{R_{\text{n}} - G_0} \tag{4.60}$$

and can be written as a function of $SEBI$,

$$\varLambda = \varLambda_{\text{r}} \frac{\lambda E_{\text{p}}}{R_{\text{n}} - G_0} = \left(1 - SEBI\right)\frac{\lambda E_{\text{p}}}{R_{\text{n}} - G_0} \tag{4.61}$$

Combining Eqs. 4.60 and 4.61, λE can be expressed as a function of $SEBI$ and λE_{p}

$$\lambda E = \left(1 - SEBI\right)\lambda E_{\text{p}} \tag{4.62}$$

And H is written as a function of $R_{\text{n}} - G_0$, λE_{p} and $SEBI$

$$H = R_{\text{n}} - G_0 - SEBI\ \lambda E_{\text{p}} \tag{4.63}$$

4.4.2 Parameterization of excess resistance for heat transfer in the single-source model

As discussed in Chapter 1, the essential parameter to estimate H and λE in a single-source model is $z_{0\text{h}}$, or kB^{-1}. A recently developed kB^{-1} model will be introduced firstly,

while a new parameterization of kB^{-1} will be proposed on the basis of the dual-source concept of heat transfer in a soil-vegetation canopy.

Massman's (1999) kB^{-1} model

A new physically based model for roughness length for heat transfer has been developed by Su et al (2001) on the basis of Massman's model (1999). In their model, z_{0h}, in terms of $kB^{-1} = \ln(z_{0h}/z_{0m})$, is expressed as a function of surface conditions and of aerodynamic parameters

$$kB^{-1} = \frac{kc_{df}}{4C_t \frac{u_*}{u(h_c)}\left(1-e^{-n/2}\right)} f_f(0)^2 + \frac{k\frac{u_*}{u(h_c)}\frac{z_{0m}}{h_c}}{C_t^*} f_f(0)^2 f_s(0)^2 + kB_s^{-1} f_s(0)^2 \qquad (4.64)$$

where C_t is the heat transfer coefficient of the leaf ranging in $0.005N \leq C_t \leq 0.075N$ (N is number of sides of a leaf to participate in heat exchange), n is the windspeed extinction coefficient within the canopy, C_t^* the heat transfer coefficient of the soil and is given by $C_t^* = Pr^{-2/3}Re_*^{-1/2}$, where Pr is the Prandtl number (0.71, Massman, 1999) and the roughness Reynolds number $Re_* = h_s u_*/v$, with h_s the roughness height of the soil, kB_s^{-1} is the value of kB^{-1} for bare soil surface and is calculated according to Brutsaert (1982) as

$$kB_s^{-1} = 2.46(Re_*)^{1/4} - \ln(7.4) \qquad (4.65)$$

The three terms on the right hand side of Eq. 4.64 represent the contributions of canopy only, canopy-soil interaction and soil only, respectively. Eq.4.64 reduces to limiting cases of canopy only for $f_f = 1$ and soil surface only for $f_s = 1$.

A new kB^{-1} model derived based on dual-source of heat and their interaction

The equation to determine kB^{-1} is obtained by combining Eqs.4.14 and 4.46 and substituting $T_{rad}(0)$ for $T_a(z_{0h})$ as

$$kB^{-1} = \frac{ku_*[T_{rad}(0) - T_a(z_{ref})]}{H/(\rho_a c_p)} - \left[\ln\left(\frac{z-d}{z_{0m}}\right) - \Psi_h\left(\frac{z-d}{L}\right) + \Psi_h\left(\frac{z_{0m}}{L}\right)\right] \qquad (4.66)$$

Actually, both the structure and the conditions of the canopy may affect the thermodynamic properties of the composite surface. This is the reason why in the

parameterization of kB^{-1} surface properties such as fractional foliage cover, leaf area index and the height of the canopy must be taken into account. Moreover, kB^{-1} is an effective parameter accounting for the distribution of heat sources in a 3D canopy, and the thermal heterogeneity of the canopy has an influence on it. Prévot et al (1994) found that the kB^{-1} values from Eq.4.66 were strongly related to LAI and the difference of temperature between soil and foliage. It is tempting to estimate kB^{-1} from directional radiometric temperature measurements because component temperatures are related to the directional signature as discussed in chapter 2 and 3. Prévot et al. (1994) proposed an empirical parameterization of kB^{-1} by fitting the kB^{-1} from Eq.4.66 and directional radiometric temperature measurements as

$$kB^{-1} = C_1\left[T_{\text{rad}}(\theta_{\text{v}}) - T_{\text{rad}}(0)\right] + C_2\,e^{-LAI} + C_3 \tag{4.67}$$

where $C_1 = 0.655$, $C_2 = 3.82$, $C_3 = -1.34$, and the zenith view angle θ_{v} is taken as 80° in their study.

Even though Eq.4.67 is still empirical, it leads to the consideration of using angular thermal infrared measurement to parameterize kB^{-1}. Such parameterization can be performed by combining single-source model and the complete model. Actually, H in Eq.4.14 can be estimated by the complete model (Chapter 2) which in turn is used in Eq. 4.66 to calculate kB^{-1}. Then, a relationship between the kB^{-1} values from Eq.4.66 and the simulated $T_{\text{rad}}(\theta_{\text{v}})$ (or component temperatures T_{f} and T_{s}) by the complete model can be established by considering that $H_{\text{single-source}} = H_{\text{complet-model}}$ and take into account the foliage and soil fractional cover at different view zenith angles,

$$kB^{-1} = \text{F}\left[T_{\text{rad}}(\theta_{\text{v1}}),\ T_{\text{rad}}(\theta_{\text{v2}}),\ f_{\text{f}}(\theta_{\text{v1}}),\ f_{\text{f}}(\theta_{\text{v2}})\right] \tag{4.68}$$

or

$$kB^{-1} = \text{F}\left[T_{\text{f}},\ T_{\text{s}},\ f_{\text{f}}(\theta_{\text{v}})\right] \tag{4.69}$$

4.5   Summary and conclusions

Just as the directional observations of exitance of a three-dimensional foliage-soil canopy can be represented by simpler models, heat transfer in a 3D canopy can also be parameterized at decreasing levels of complexity in each one of the cases considered in Chapter 3 for radiative transfer modeling. Thus, a four-source, a dual-source and a single-

source model were derived based on the complete model for heat and water vapor transfer following the procedures and assumptions as:

- In the four-source model of heat transfer, the canopy is represented by four components: sunlit foliage, shadowed foliage, sunlit soil and shadowed soil. Each component interacts independently with air in the canopy space. A bulk aerodynamic resistance then links the canopy space to the overlying atmosphere. As for the retrieval of the four component temperatures, parameterizations of the four resistances may need more information on the canopy properties, which is not easy to derive using current remote sensing observations (see Chapter 3).

- The 3D foliage-soil canopy was further simplified to a dual-source model in which only foliage and soil were taken into account. Such model is more practical compared to the complete model and the four-component model. On the one hand, the parameterizations of the boundary layer resistances for the two components can be well characterized using fewer canopy properties, such as LAI, roughness length for momentum which can be observed or retrieved using remote sensing measurements. On the other hand, the foliage and soil component temperature required in the dual-source model can be retrieved using bi-angular measurements of canopy radiance both in the field and at the larger spatial scale of satellite observations.

- The single-source model developed in this chapter is the most simplified way to represent heat transfer of a foliage-soil canopy. Only a single TOC radiometric temperature is considered in the single-source model. The use of the TOC radiometric temperature in a single-source model, however, can bring large errors in the estimation of heat flux, because a) radiometric temperature is not equivalent to the aerodynamic surface temperature which is actually needed in the single-source model and b) it depends on the observation angle. A single-source model may still be useful, however, if an appropriate parameterization of the canopy resistance can be established to represent the thermal heterogeneity of soil-vegetation canopies. The latter can be accomplished by using bi-angular measurements of surface brightness temperatures with the help of the dual-source model.

As a conclusion, *the dual-source model has a better physical basis compared to the single-source model and is easier to apply than the four-source model.* The soil and vegetation component temperatures needed in the dual-source model, which have a clearer physical meaning compared to the single 'surface' temperature of the canopy, can be obtained by the inversion of the simple linear mixture model proposed in Chapter 3 using bi-angular (or multi-angular) measurements of TOC brightness temperature $T_{b0}(\theta_v)$.

Chapter 5

Descriptions of field experiments and satellite data

5.1   Introduction

Theory and methods need to be validated and this requires observations at both local and regional scale. In this thesis, the validation of methods and algorithms presented is done in two steps: first at the local scale where all relevant variables can be measured in the field; second at regional scale where measurements over a larger area, e.g. satellite observations of surface parameters and Large Aperture Scintillometer (LAS) measurements of heat flux density, are used. The data from local and larger scale field measurements were collected from several different experiments and the respective study areas listed in Table 5.1.

The reason of selecting the IMGRASS and QRSLSP experiments is that, in addition to heat flux measurements, observations of directional surface brightness temperature were made during these two field campaigns. As regards EWBMS, it is chosen as a regional scale experiment because surface sensible heat flux over up to 5 kilometers was measured using LAS. Satellite observations by the Along-Track Scanning Radiometer (ATSR)-2 were collected over IMGRASS, EWBMS and SGP'97 study areas.

Table 5.1 List of experiments and locations used in this thesis.

Experiments	Site names	Location	Month/Year
IMGRASS (China)	Baiyinsumu	$44°16.725'$ N, $115°56.539'$ E	July 1988
QRSLSP (China)	Shunyi	$116°26'$ E - $117°$ E, $40°$ N - $40°21'$ N	April 2001
SGP'97 (USA)	CF01ARM CF02ARM	$36°36.3'$ N, $97°29.1'$ W $36°36.36'$ N, $97°29.28'$ W	July 1997
EWBMS (Spain)	Tomelloso Lleida Badajoz	$39°07.357'$ N, $2°55.314'$ W $41°32.644'$ N, $0°51.644'$ E $38°55.697'$ N, $6°36.590'$ W	April- September 1999

5.2   Local scale field measurements

5.2.1   IMGRASS Experimental site 4

General

The field campaign of 'The Inner Mongolia Grassland-Atmosphere Surface Study (IMGRASS)' was carried out between May and August in 1998 over the Inner Mongolia grassland plateau. The overall objective of the experiment was to study the effects of changes

in vegetation cover on the hydrologic and heat cycle of the land surface and of surface-cloud interactions to improve current understanding of soil-vegetation-atmosphere interactions in temperate semi-arid grassland (Lu, 1997).

The study area is located in the north-east of China. It is mainly a C3-grass ecosystem with several species being present. There is a significant variability in fractional vegetation cover spatially and seasonally. More specific observational objectives were to provide flux measurements of water, heat, and trace gases over various scales and to develop validated remote sensing algorithms.

Data collected at site 4, located at about 970 m above sea level, have been used in this thesis. The land cover is sparse short grass, approximately 10 cm high with clumped higher grass about 40 cm high dispersed in July 1998, a so-called degraded prairie. A leaf area index (LAI) of 0.5 was determined by counting grass leaf area in a square meter area.

The data from IMGRASS that will be used in this thesis are directional surface brightness temperatures, radiation balance including upward and downward short-wave and long-wave radiation flux densities, sensible and latent heat flux densities, soil heat flux densities, the profiles of windspeed u, air temperature T_a and relative humidity q_{ra}, and canopy properties such as canopy height and LAI. Table 5.2 gives a summary of these measurements and the associated instruments. The details of the observations are given in the following sections.

Table 5.2 Measurements and instruments at the site 4 of the IMGRASS field experiment.

Measurements	Height	Instruments
Directional surface brightness temperature $T_{b0}(\theta_v, \varphi_v)$	1.5m	Portable digital thermometer (IR-AHT)
Upward/downward short-wave radiation flux densities $R_s^{\downarrow}$ and $R_s^{\uparrow}$	1.5m	Pyranometer (Eko MS-42)
Upward/downward long-wave radiation flux densities $R_L^{\downarrow}$ and $R_L^{\uparrow}$		Pyrgeometer (Eppley PIR)
Sensible heat flux density H	4.9m	3-D sonic anemometer-thermometer (Kaijo Denki DAT-300)
Latent heat flux density λE	4.9m	Infrared hygrometer (Kaijo-Denki AH-300) and the associated Humicap sensor(VAISALA)
Soil heat flux G_0	0.01m	Heat flux plate (EKO CN-81)
Windspeed u, air temperature T_a and humidity q_{ra} profiles	0.5-8m	VAISALA Belfort 1022S, Thermafilm 100W30, and HMP-35A
Canopy height h_c LAI	-	Direct measure Destructive sampling

Directional surface brightness temperature

$T_{b0}(\theta_v, \varphi_v)$ During the period of 26-31 of July 1998, directional surface brightness temperature was measured at site 4 in IMGRASS using a portable digital thermometer (IR-AHT, Chino, Korea) which operates in the spectral window 8-13 μm. The radiometer can measure temperatures ranging from –50 °C to 1000 °C, and the absolute accuracy is ±2 °C when temperature is below 200 °C. The response time of the thermometer is 1 second. The footprint diameter of the radiometer equals to the distance to object divided by 50. The emissivity was set to 1. Observations at nadir, 23° and 52° zenith view angle and at 0°, 90°, 180° and 270° azimuth angles (0° was set in the north, e.g. radiometer was looking at the target from the north of the target) were designed to obtain directional surface brightness temperature. The measurement height at nadir was 1.5 m, corresponding to a footprint diameter of about 3 cm. Because of the small field of view the sensor was mounted to observe bare soil only when at nadir [Su et al., 1999].

Radiation balance measurements

The upward and downward short-wave radiation flux densities, $R_s^{\downarrow}$ and $R_s^{\uparrow}$, were measured by a pyranometer (EKO MS-42, Japan) mounted at 1.5 m height on a mast. Two sets of pyrgeometers (Eppley PIR, USA) with spectral range 4-50 μm were used to measure upward and downward long-wave flux densities, $R_L^{\downarrow}$ and $R_L^{\uparrow}$. The net radiation then is calculated from these four components of the radiation balance.

Sensible and latent heat flux densities

Measurements of H and λE were made at 4.9 m height by means of an eddy correlation system which consists of a 3-D sonic anemometer- thermometer (SAT; Kaijo DAT-300 with TR-61A Probe, Japan), a infrared hygrometer (Kaijo AH-300, Japan), a clinometer (Kaijo CM-100, Japan) and a rotator (Kaijo 502MSA, Japan). The components of wind velocity u and air temperature T_a were measured by the 3-D sonic anemometer-thermometer and the specific humidity q_a was measured with the infrared hygrometer. The rotator was used to adjust the cross angle of 120-degree between the horizontal components against the prevailing wind direction. The clinometer signals were used to correct the inclinations of the wind probe. The digital data sampling frequency was 10Hz and the data were collected every 30 minutes. The sensible and latent heat fluxes were computed by the eddy-correlation method over a 30 minutes averaging period starting from ($hr - 15\,\text{min}$) to ($hr + 15\,\text{min}$). For instance, the heat flux densities at 13:00h were calculated from signals sampled over the 12:45h to 13:15h period.

Soil heat flux G_0

The measurements of soil heat flux density G_0 were made using three heat flux plates (Eko CN-81, Japan) placed at 120º angle between each other at the depth 0.01 m under the ground surface. Also soil heat flux density measurements were averaged over 30 minutes.

u, T_a and q_{ra}

A 10 m high tower was set up to measure profiles of wind speed u, air temperature T_a and relative humidity q_{ra} with 5 levels at 0.5 m, 1 m, 2 m, 4 m and 8 m height above the ground respectively. The instruments used were three-cup anemometers (Belfort 1022S, Vaisala) for wind-speed, the platinum resistance detectors (Thermafilm 100W30) for air temperature T_a, and humidity sensors (Vaisala HMP-35A) for RH measurements respectively.

5.2.2   Shunyi campaign in Beijing

General

The program 'Quantitative Remote Sensing theory and application for Land Surface Parameters (QRSLSP)' funded by Chinese Special Funds for Major State Basic Research Project was designed to evaluate and improve the retrieval accuracy of land surface properties from remote sensing data, as well as to assimilate remote sensing data into land surface models at various scales. The experimental area, located in Shunyi, the plain of Northern China, is dominated by agricultural fields with bare soil, grass land, trees (windbreak) and orchards. The first field campaign was carried out from October 2000 to June 2001. For details of the QRSLSP study, readers are referred to Liu et al. (2001).

An Intensive Observation Period (IOP) was performed from 5th to 25th of April in 2001 in the Shunyi county, Beijing, China. Three IOP experimental sites were covered by winter wheat, a row crop canopy in the early growth stage with different plant densities and irrigation conditions. The three sites were flat and adjacent at the location 116°26′ E-117° E and 40° N - 40°21′ N. During the IOP, the winter wheat went through growing stages of three leaves, jointing, earing, milking and riping.

These field measurements have been used to evaluate, at the field scale, the algorithm to determine component temperatures and afterwards the single- and dual-source heat transfer models (Chapters 3 and 4). These data are listed in Table 5.3. The methods of measurements will be described in the following sections.

Table 5.3 The measurements and the instruments at Shunyi site of QRSLSP field experiment.

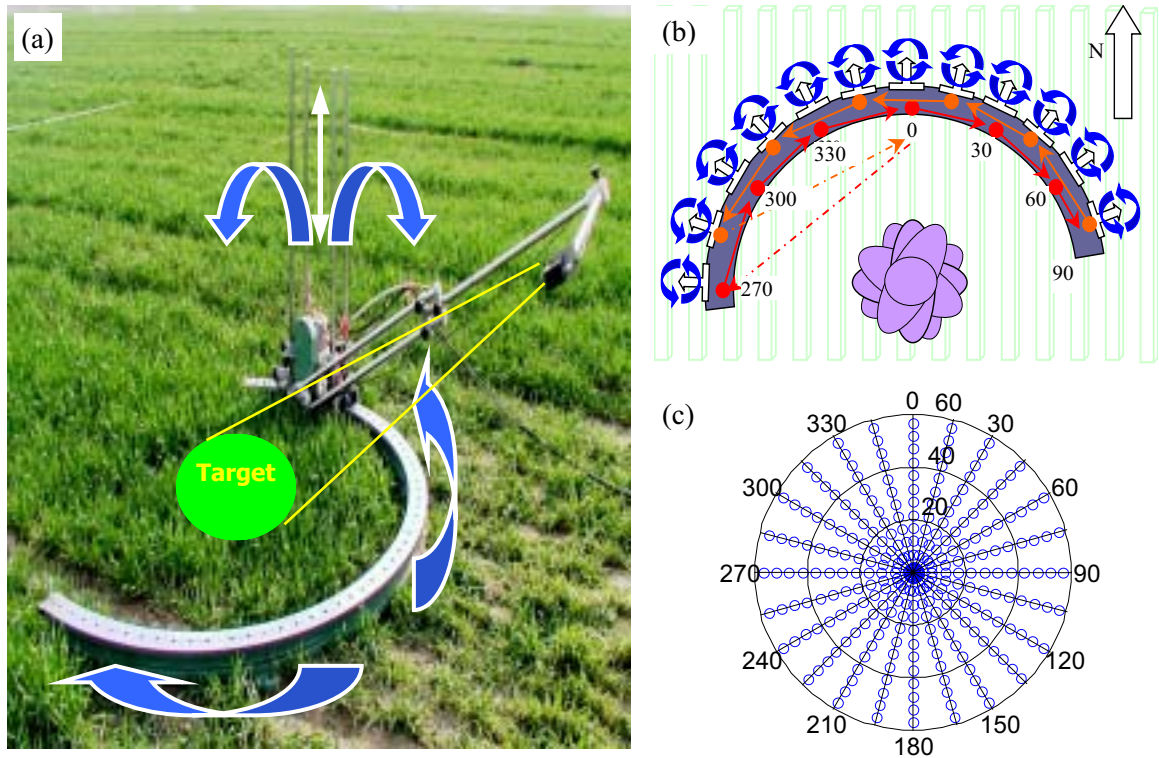| Measurements	Instruments
Directional surface brightness temperatures $T_{b0}(\theta_v, \varphi_v)$	- Radiometers + goniometers - AGEMA THV 900 LW thermo-camera + goniometer
Component temperatures T_f and T_s	- AGA Thermopoint 80 thermometer - JM424 digital thermometer
Downward/upward short-wave radiation flux densities $R_s^{\downarrow}$ and $R_s^{\uparrow}$	Pyranometer (Eko MS-42)
Downward/upward long-wave radiation flux densities $R_L^{\downarrow}$ and $R_L^{\uparrow}$	Pyrgeometer (Eppley PIR)
Sensible heat flux density H Latent heat flux density λE	Bowen ratio system + eddy-correlation system
Soil heat flux density G_0	Soil heat flux plates
Canopy height h_c LAI	Direct measure Destructive sampling

Figure 5.1 Demonstration of directional $T_{b0}(\theta_v, \varphi_v)$ measurements in the field campaign of QRSLSP.

Directional surface brightness temperature $T_{b0}(\theta_v, \varphi_v)$

A goniometer (Fig.5.1a) was designed specifically for canopy directional $T_{b0}(\theta_v, \varphi_v)$ measurements. Two arms are connected perpendicularly to each other with the longer one being fixed onto a circular track, which is set up on the ground, and the shorter one is kept horizontal on top of which radiometers can be mounted. The longer arm can move along the track to change the azimuth position. At each specific azimuth position φ_v the longer arm sways over a range of zenith angles θ_v (maximum 60º). Such movements are designed and performed to measure the TIR radiance of the same target on the ground (Fig. 5.1b) within a desired range of azimuth and zenith angles. The diameter of the footprint, however, increases with increasing θ_v because of slant viewing. A 10º interval was taken for the zenith angle change, and 15º interval for azimuth angle change (Fig. 5.1c).

Two radiometers were used to measure $T_{b0}(\theta_v, \varphi_v)$. One radiometer was set up on the top of the short horizontal arm to measure the radiance of the canopy at each azimuth and zenith angle. Distance to the target was the same at any position of the arm so that the radiometer footprint included the same target at all positions as shown in Fig. 5.1b. The other radiometer was mounted on a mast observing continuously the canopy at nadir. The second radiometer provided the continuous measurements needed to correct for the temporal change in the measurements of $T_{b0}(\theta_v, \varphi_v)$ during a complete goniometer scan. The latter usually took about 20 minutes during which the surface temperature may change significantly due to the variation of the solar radiation and windspeed. Due to technical problems, different radiometers were used during the experiment (Table 5.4).

Table 5.4 The properties of radiometers used to measure $T_{b0}(\theta_v, \varphi_v)$ during the field campaign of QRSLSP.

Instrument	Wavelength (µm)	FOV (º)
Radiometer 1	8 - 11, 10.4 - 14	4.7
Radiometer 2	8 - 11, 10.4 - 14	8.6
Radiometer 3	8 - 11, 10.4 - 14	8.6
Radiometer (single channel)	8 - 14	15
Raytek radiometer	8 - 14	7

A thermal camera (AGEMA THV 900 LW), mounted on top of another goniometer, was used to obtain images of surface temperature of the wheat crop $T_{b0}(\theta_v, \varphi_v)$ for prescribed azimuth and zenith directions. The AGEMA thermal camera has a scanning HgCdTe detector and a Stirling cooler with the single channel covering the spectral range between 8-12 µm,

76

the frame rate is 15Hz for 136×272 pixels, and the nominal sensitivity is 80 mK at 30 °C. The camera was equipped with a lens having a FOV of $5 \times 10°$.

Component temperatures measurements

The component temperatures of sunlit and shaded leaves, T_{s_f} and T_{sh_f}, and of sunlit and shaded soil, T_{s_s} and T_{sh_s}, were measured using a hand-held infrared thermometer (AGA Thermopoint 80 thermometer) and a thermocouple thermometer (JM424 digital thermometer). The AGA thermometer has a measurement resolution of 0.1 °C, and the emissivity was set to 1.0. The sensor of the JM424 digital thermometer is a K-type thermocouple (contact type) and has the nominal sensitivity 0.1°C. The samplings were made simultaneously and randomly in the same wheat field but at different points from those where $T_{b0}(\theta_v, \varphi_v)$ was measured.

Radiation balance

Downward and upward short-wave radiation flux densities $R_s^\downarrow$ and $R_s^\uparrow$, downward/upward long-wave radiation flux densities $R_L^\downarrow$ and $R_L^\uparrow$ were measured from which the net radiation flux density was calculated based on the radiation balance.

Heat flux densities

A Bowen ratio system was used to measure wind speed u, dry and wet bulb temperatures T_a at two reference levels (0.5m above the canopy height and 2m above the ground, respectively), the soil temperature profile and the soil heat flux density G_0. The sensible and latent heat flux densities, H and λE, were obtained from these measurements. An eddy-correlation system was also used to measure H and λE together with the CO_2 flux density.

Canopy variables

Leaf area was determined by measuring the width and length of each leaf. Leaf area index (*LAI*) was obtained by multiplying the leaf area of each stalk by plant density in the field. The height of the canopy h_c was also measured throughout the campaign period.

5.2.3 Ground data from SGP'97

The Southern Great Plains 1997 (SGP'97) Hydrology Experiment took place in Oklahoma over the period of June 18 - July 17 in 1997. The land cover over SGP''97 experimental area is a mixture of grass and wheat which is relatively dense and homogeneous as compared to the land cover in IMGRASS and EWBMS. Data from two SGP'97 sites are

used in this study. These two experimental sites were located at the Department of Energy's Atmosphere and Radiation Measurement Cloud and Radiation Testbed (ARM-CART) Central Facility (CF) named as CF01ARM (36.605ºN, 97.485ºW, 318 m altitude) and CF02ARM (36.606ºN, 97.488ºW, 317 m altitude), respectively. The CF01Arm is a grass site with height of 22 ± 8 cm and LAI of 2.0 ± 0.6 $m^2\,m^{-2}$, while the CF02Arm is covered by a wheat crop with height 24 ± 5 cm and LAI of 1.3 ± 0.3 $m^2\,m^{-2}$ (Hollinger and Daughtry, 1999). Data used in this thesis are energy balance measurements, wind-speed, and air temperature and humidity close to the ATSR-2 overpass time in CF01ARM and CF02 ARM. Table 5.5 gives an overview of the data from these two SGP'97 sites.

Table 5.5 Overview of in-situ measurements in two SGP'97 sites

Variable	Measurement heights (m)	
	CF01ARM	CF02ARM
Net radiation R_n	2.3	-
Sensible heat flux density H	0.96, 1.96	3.0
Latent heat flux density λE	0.96, 1.96	3.0
Soil heat flux density G_0	-0.05 (depth)	-
Friction velocity u_*	0.96, 1.96	3.0
Average wind speed u	2.5	3.0
Air temperature T_a	0.96, 1.96	3.0
Vapor pressure of air e_a	0.96, 1.96	3.0

5.3   Regional scale field and satellite measurements

5.3.1   General

Two types of data at larger spatial scale area are used in this thesis: (1) directional surface brightness temperatures observed by ATSR-2 which can provide (bi-angular) surface brightness temperatures over a $500km\times500km$ area with pixel size at nadir of $1km\times1km$; (2) Sensible heat flux measurements were made by LAS system.

5.3.2   Ground data from EWBMS study area in Spain

Background

In the framework of the large scale Energy and Water Balance Monitoring System (EWBMS) project, field campaigns were carried out at three experimental sites, Lleida,

Tomelloso and Badajoz, in Spain in 1999 (see Fig. 5.2 for their locations). Land cover at the three experimental sites is rather different ranging from dryland vegetation to irrigated crops. Sensible heat flux measurements were made simultaneously and continuously using Large Aperture Scintillometer (LAS) at the three sites. The data used in this thesis were from the period between March and September 1999. The LAS instruments used in the campaigns were manufactured by the Meteorology and Air Quality Group of Wageningen University. For details of the LAS instruments and the theory of calculating sensible heat flux density from the LAS signal, the reader is referred to, for instance, De Bruin et al. (1995), De Bruin (2002), Moene and De Bruin (2001), Moene (2001), and Meijninger et al. (2002). A summary of measurements and surface characteristics is given in Table 5.6. The brief description of the surface characteristics of each site and the measurement set-up are given in the following sections.

Figure 5.2 Locations of LAS measurements sites of EWBMS in Spain.

Table 5.6 Summary of characteristics of Large Aperture Scintillometer (LAS) experimental sites in Spain.

Site	Transmitter Location	Receiver Location	Mean height of LAS beam above ground	Path length	Surface Characteristics
Tomelloso	39°07.357'N 2°55.314'W	39°07.653'N 2°55.951'W	4.35 m	1070 m	Dry vineyard
Lleida	41°32.644'N 0°51.644'E	41°34.962'N 0°52.444'E	41.2 m	4440 m	Irrigation area with fruit trees, alfalfa
Badajoz	38°55.697'N 6°36.590'W	38°56.298'N 6°40.141'W	51.3 m	5250 m	Irrigation area with wheat, corn, alfalfa, lettuce, olives, beans, tomatoes

Tomelloso

The LAS was installed in a dry vineyard area. Both the transmitter and receiver were mounted on steel masts at a distance of about 1070m ± 40m (GPS estimation). The height of the path was 4.35m.

Additional data, e.g. the mean values over 10 minutes of wind speed u, wind direction WD, temperature T_a and relative humidity q_{ra} at two heights (2m and 10m respectively), long-wave and short-wave radiation flux densities $R_s^\downarrow$, $R_s^\uparrow$, $R_L^\downarrow$ and $R_L^\uparrow$, soil temperatures T_s, soil heat flux density G_0, atmospheric pressure p and precipitation were obtained from a meteorological station near Tomelloso, located at 39°10.487'N 3°00.036'W. The land cover at the site is bare soil and grass, land cover of the surrounding area is crops and vineyards. The meteorological station was operated by the University of Castilla-La Mancha.

Lleida

The LAS was set up in a region with small-scale irrigation. The main crops in this site were: fruit trees (peaches) and alfalfa. Both the transmitter and the receiver (the co-ordinates are given in Table 5.5) were installed on hills. The distance between transmitter and receiver was 4690m ± 50m (distance estimated from the map). The effective height of the LAS beam (taking into account the shape of the weighting function) was 41.2m.

The additional data needed to process the LAS-data come from two sources: 1) A mast was set up at the approximate location 41°35.5'N and 0°47.5'E to obtain temperature T_a and temperature difference ΔT between two levels (2m and 10m), water vapor pressure e_a at the two heights, wind speed u (mean and standard deviation), wind direction WD, and precipitation over a 10 minute averaging period. This mast was operational between April 1 and mid September 1999. 2) The meteorological station near Juneda (approximate location 41°33'N and 0°49.5'E) provided mean values of air temperature T_a, relative humidity q_{ra}, wind speed u, wind direction WD, precipitation and solar radiation R_{s0} every half-hour.

Badajoz

The LAS was installed in a region with large-scale irrigation (sprinkler irrigation). Crops grown in this region were wheat, corn, alfalfa, lettuce, olives, beans and tomatoes. The receiver of the LAS was installed on the top of a hill, whereas the transmitter was installed on a water tower (used for irrigation). The distance between transmitter and receiver was 5250m ± 200m. The height of the path was 62 m.

Additional data such as air temperature T_a, relative humidity q_{ra}, wind speed, wind direction, global radiation, net radiation, soil heat flux, soil temperature, and precipitation were available from a station operated by Servicio de Investigacion y Desarrollo Tecnologico which was located some 7 kilometres from the LAS receiver. The surface cover of the meteorological station is short grass.

5.3.3 Satellite bi-angular radiance measurements - ATSR-2 data

Channel properties of ATSR-2 instruments

The Along-Track Scanning Radiometer (ATSR) instruments are imaging radiometers which are currently the only observing system from space able to provide quasi-simultaneous radiance measurements of the earth's surface in the TIR and SWIR spectrum regions (in addition to VIS/NIR channels) at two view angles. ATSR-1 onboard the first European Remote Sensing satellite (ERS-1) was launched in July 1991 and operated until June 1996. ATSR-1 had four channels – one short wave infrared (SWIR) channel located at 1.6μm and three TIR channels centred at 3.7μm, 11μm and 12μm. ATSR-1 was designed particularly for providing data over the sea. ATSR-2 onboard the ERS-2 satellite was launched in April 1995 and is currently providing the data both over land and over sea. In addition to one SWIR channel and three TIR channels as on ATSR-1, ATSR-2 has three narrow-band visible-near infrared channels in the blue, green and red spectrum located at 0.55μm, 0.67μm and 0.87μm respectively for vegetation monitoring. The data used in this thesis were provided by ATSR-2. Table 5.7 gives information on channel spectral characteristics. Further details of this instrument can be found on the World Wide Web site at http://www.atsr.rl.ac.uk/.

Table 5.7 Central wavelength and bandwidth of ATSR-2 spectral channels

Channel No.	Central wavelength (μm)	Full width at half maximum (μm)
1	12.0	11.60 - 12.50
2	11.0	10.52 - 11.33
3	3.7	3.47 - 3.90
4	1.6	1.575 - 1.642
5	0.87	0.853 - 0.875
6	0.65	0.647 - 0.669
7	0.55	0.543 - 0.565

The Orbit and geometric properties of ATSR-2 observation

The ERS-2 has a mean orbit height of approximately 780 km and operates with a south-bound equator crossing (descending node) of around 10:30 local solar time and a north-bound equator crossing (ascending node) of 22:30 local solar time. The orbit tracks do not repeat on a daily basis due to the non-integer number of orbits per day. The 3, 25 and 168-day repeats have been employed by ATSR-2 so that images over a specific region can be obtained al least every 3 days.

Besides the spectral features described above, ATSR-2 has the unique capability of measuring TOA radiance at two view angles, i.e. nadir and forward. The use of the along track scanning technique makes it possible to observe the same point on the earth's surface at two view angles through two different atmospheric path within a short period of time. The first view is at a view angle of 55° (approximately 53° at the earth surface) along the direction of the orbit track when the satellite is flying toward the target point, which is referred to as *forward observation* in this thesis. Within 2 and half minutes the nadir (0°) view observation is made over the same point, which will be referred to as *nadir observation* later on. Fig 5.3 shows the viewing geometry of ATSR-2 observations.

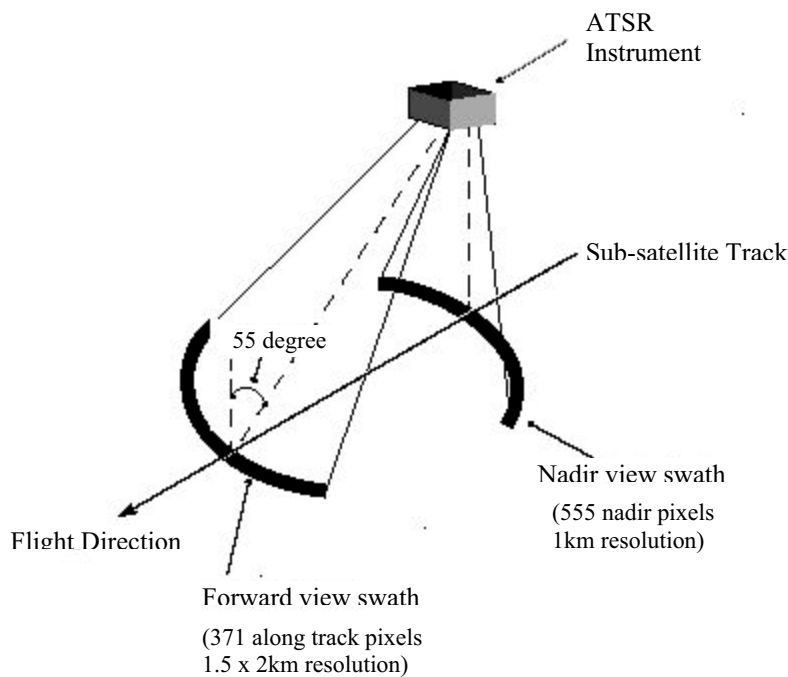**Figure 5.3** Illustration of Along Track Scanning Radiometer (ATSR) observation (adapted from Mutlow, et al, 1999).

The swath width of ATSR-2 is 500km, which provides 555 pixels across the nadir (0° zenith angle) swath and 371 pixels across the forward (55° zenith angle) swath. The nominal pixel size of ATSR-2 is $1km \times 1km$ at the center of the nadir swath and $1.5\ km \times 2\ km$ at

the center of the forward swath. The data used in the study are the GBT (gridded brightness temperature/reflectance) products processed by the SADIST (Synthesis of ATSR Data Into Sea-surface Temperatures) system, which include the calibrated brightness temperature or reflectance images ($512 \text{ km} \times 512 \text{ km}$) geolocated and regridded onto $1 \text{ km} \times 1 \text{ km}$ spatial resolution for both view angle observations (Bailey, 1995).

Calibration of visible channels of ATSR-2

Since no routine calibration is performed on the VIS/NIR image data products provided by SADIST-2, the calibration must be done for these channels using the calibration Look-Up-Table (LUT) provided on the ATSR Project Web site (http://www.atsr.rl.ac.uk) to convert these data from counts to top-of-atmosphere fractional-reflectance. These conversion factors given in the LUT were derived using data from the on-board visible calibration system (VISCAL) which is described in detail in Smith et al. (1997).

ATSR-2 data-sets

ATSR-2 data sets collected over EWBMS and SGP study areas were used in this study to derive the component temperatures of soil and foliage (Table 5.8). These images of the component temperatures are in turn applied as the input of the dual-source model in Chapter 4 to estimate heat flux densities H and λE. As regards the calculation of heat flux density using single-source model, the surface temperature T_0 provided by ATSR-2 is used.

Table 5.8 List of ATSR images used in this study. Image alias is for the convenience in the latter text.

Study Area	Dates of Images	DOY	Overpass (UTC) (hh:mm)	Image Central Coordinates	Covered site	Image Alias
EWBMS	13-04-1999	103	10:33	37.884°N, 4.149°W	Tomelloso	SP990413
(Spain)	06-06-1999	157	10:36	37.891°N, 4.865°W	Tomelloso	SP990606
	19-06-1999	170	10:28	37.890°N, 2.701°W	Tomelloso	SP990619
	15-07-1999	196	10:10	42.281°N, 2.974°E	Lleida	SP990715
	21-07-1999	202	10:22	42.281°N, 0.096°E	Lleida	SP990721
	30-07-1999	211	10:39	37.859°N, 5.661°W	Badajoz	SP990730
	15-08-1999	227	10:36	37.859°N, 4.952°W	Badajoz	SP990815
	21-08-1999	233	10:48	37.859°N, 7.826°W	Badajoz	SP990821
	28-08-1999	240	10:27	37.886°N, 2.691°W	Tomelloso	SP990828
	16-09-1999	259	10:30	37.885°N, 3.481°W	Tomelloso	SP990916
	29-09-1999	272	10:22	42.275°N, 0.096°E	Lleida	SP990929
SGP'97 (USA)	01-07-1997	182	18:16	37.882°N, 94.681°W	CF01ARM CF02ARM	SGP970701

5.4   Synthetic image data

At-surface observations need to be linked very precisely with at-satellite radiance measurements to evaluate some of the methods described in this thesis to determine vegetation properties. To a limited extent this is feasible using real field measurements concurrent with measurements from space. Field measurements can explore a limited range of variability, however, and the detail of sampling may not be adequate to evaluate the results obtained with the measurements from space. Synthetic TOC and TOA radiometric data generated by detailed modelling of radiative transfer in the soil – vegetation – atmosphere system can be used for the evaluation of algorithms. In this case the properties of soil and vegetation need to be defined a priori for the required (large) number of different situations. Spectro-directional radiance is then calculated by detailed models both at TOC and TOA. The latter, i.e. the TOA radiometric data that a sensor in space would measure, can then be used to estimate vegetation properties with the algorithms to be evaluated. Statistics of the deviations of retrievals from the values of vegetation properties used in the accurate forward calculation provide a measure of accuracy of the algorithms.

Synthetic multi-angular, hyperspectral images, covering the visible, near-infrared and thermal infrared spectral regions, were generated for a realistic landscape. Only a brief description of simulated TOC and TOA brightness temperature and spectral reflectance in relation with necessary input data is given here. The modelling approach and results have been described in detail by Verhoef and Bach (2003) for the VIS, NIR and SWIR regions and by Jia e al. (2001) for the TIR region.

Table 5.9 The vegetation properties used in the simulation of $T_{b0}(\theta_v, \varphi_v)$.

	Corn	Barley	Alfalfa	Dry crops
Canopy height (m)	0.90	0.80	0.50	0.40
Leaf width (m)	0.05	0.02	0.01	0.02
Reflectance (VIS)	0.0892	0.0826	0.0889	0.0826
(NIR)	0.3125	0.3547	0.3629	0.3406
Transmittance (VIS)	0.0680	0.0348	0.0299	0.0348
(NIR)	0.3859	0.3424	0.3044	0.3268
LIDF parameters a	-0.65	-0.85	0.00	0.00
b	-0.15	-0.15	-0.15	0.00
Average leaf angle (˚)	68.7	76.0	45.0	45.0
Std. leaf angle (˚)	18.5	13.7	23.6	25.9

The synthetic image data set was generated over a $10\,\text{km}\times10\,\text{km}$ area of the region of Barrax, Spain (see also previous section). The area is covered by agricultural crops. The data used as the input in the brightness surface temperature and reflectance simulation are listed as the following:

- Land use classification map with $25\,\text{m}\times25\,\text{m}$ pixel resolution
- LAI map
- Soil moisture
- Meteorological measurements of windspeed, air temperature and humidity

Land use classifications are merged into four dominant types: maize, barley, alfalfa and dry crops. The model variables and parameters required for each crop are listed in Table 5.9.

For the TIR region, the detailed model described in Chapter 2 was used to simulate heat and water transfer inside the canopy over each pixel and gives the temperature for each canopy layer. Following the procedures described in Chapter 2, the mean soil temperature T_s, mean foliage temperature T_f and brightness temperature $T_\text{b0}(\theta_\text{v},\varphi_\text{v})$ at $0°$ and $53°$ along/across track were obtained. The brightness temperature $T_\text{b0}(\theta_\text{v},\varphi_\text{v})$ will be taken as the input to invert the linear mixture model (Eq.3.19), while the values of the two component temperatures T_f and T_s, used in the forward calculation with the complete model, will be used as reference component temperatures to evaluate the inversion of the simple linear mixture model.

The simulated reflectances in VIS/NIR spectral channels will be used to train and evaluate the algorithm used to estimate the fractional vegetation cover which is needed in Eq.3.19.

Chapter 6

Retrieval of component temperatures of the land surface using bi-angular measurements of thermal infrared radiance: sensitivity and validation

6.1 Introduction

Although the robust physics relating the anisotropy of exitance with the heterogeneity of surface temperature and, therefore, of radiation and heat transfer within the canopy space is beyond doubt (Chapters 2 and 3), the problem remains of actually using this directional signal to improve models of heat transfer. There are two main elements of such problem: 1) angular changes in exitance are relatively small, so only observations at very different angles give a signal significantly larger than the accuracy of observations; 2) the magnitude and the direction of angular changes depend on both canopy architecture and radiative forcing.

These problem elements lead to conflicting solutions: the second element should be addressed by using relatively complex models of radiative processes in the canopy space, while the first element limits the number of significant and independent angular measurements of exitance. The latter implies that only simple models i.e. with very few unknowns, can be used to interpret the observations and to obtain estimates of the component temperatures of vegetation canopies. In principle one should consider at least four component temperatures are: 1) sunlit foliage, 2) shadowed foliage, 3) sunlit soil, 4) shadowed soil. Additional unknowns: 5) Leaf Area Index (LAI); 6) Leaf Inclination Distribution Function LIDF, 7) soil spectral emissivity ε_s, and 8) foliage spectral emissivity ε_f.

For measurements of spectral exitance to be of any use, spectral emissivity has to be known a-priori, at least at a subset of wavelengths covered by the observations. If for example, we consider two wavelengths, say 11 μm and 12 μm and we assume to know the emissivities of foliage and soil at 11 μm, the emissivities at 12 μm may be considered unknown and we are still left with the eight unknowns listed above. Assuming again that measurements at 11 μm and 12 μm are independent and that the directional signal is significant at all angles, we need four different view angles to determine the component temperatures. This complex situation suggested to evaluate very simple models (see Chapter 3).

Moreover, the choice of the simplest model (i.e. the simple linear mixture model of TIR radiance for a two components foliage-soil canopy system described in §3.4) is also a consequence of the limited number of directional TIR observations provided by current

sensors such as ATSR-2 and AATSR: just two view angles and two wavelengths. This leads to that the model used should not have more than four unknown variables. Moreover, the information provided by the two wavelengths is limited because it depends on the spectral emissivities of foliage and soil which have to be known a priori. More realistic models and algorithms require a better directional sampling, such as proposed for the ESA Surface Processes and Ecosystem Changes Through Response Analysis (SPECTRA) Mission (Menenti et al. 2003) which would provide observations at seven view angles.

As discussed in Chapter 2 and Chapter 3, the dependence of directional TIR radiance on canopy conditions is complex. The investigation of the sensitivity of directional TIR signatures and of the sensitivity of the inversion model for component temperatures to canopy conditions will help to understand the characteristics of the directional TIR signal and to improve the accuracy of the retrieval of the component temperatures. In this Chapter, firstly the observations of $T_{b0}(\theta_v, \varphi_v)$ made in the IMGRASS and QRSLSP experiments are analyzed taking into account the canopy structure and the soil moisture. A sensitivity study of directional brightness temperature is carried out by means of the complete soil-vegetation-atmospheric model described in Chapter 2.

Second, the soil and foliage component temperatures are retrieved by applying the simple two-component model (Eq.3.19 in §3.4) to these measurements and the results are compared with the field measurements.

6.2   Sensitivity study

6.2.1   Observations of directional thermal infrared signature

IMGRASS case study

The IMGRASS case - study is relatively simple due to the homogeneity of the land surface covered by a mixture of different species of short grasses as described in Chapter 5. Fig.6.1 shows the change of brightness temperature T_{b0} with the observation zenith angles θ_v, i.e. 0, 23° and 52° respectively. Due to the small FOV the radiometer actually saw only the bare soil in-between plants at the 0° zenith angle. Thus, the value of T_{b0} measured at nadir was the surface brightness temperature of bare soil. The maximum difference of T_{b0} between 0° and 52° is about 6 °C, while 1.5 °C was observed between 23° and 52°. The dependence of T_{b0} on θ_v was observed, independently of the time of observations.
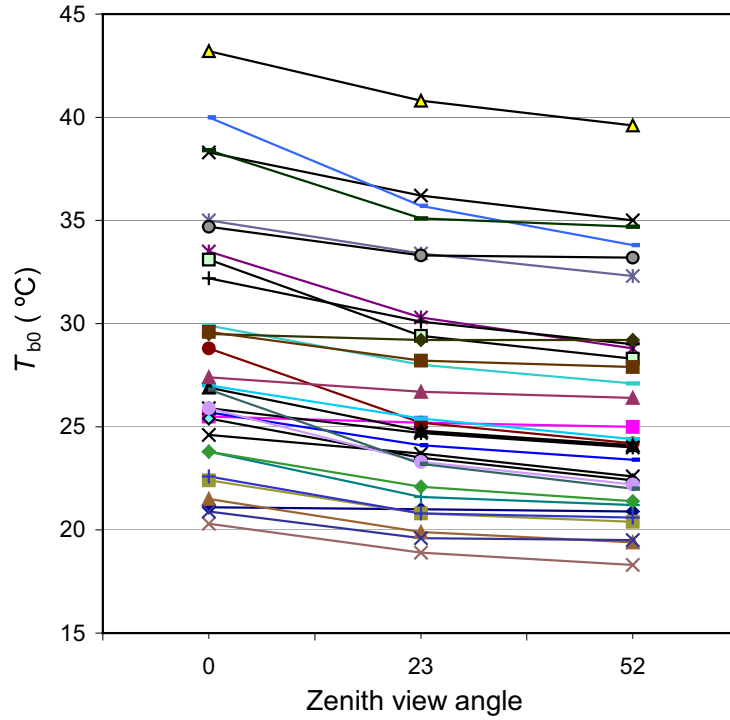
Figure 6.1 Variation of $T_{b0}(\theta_v, \varphi_v)$ with θ_v over the grassland surface at IMGRASS site 4. Each sequence of three data points was measured at different times during 26 - 31 July 1998.

QRSLSP case study

The directional T_{b0} measurements were carried out during the QRSLSP experimental period from the beginning of April to the middle of May. The measurements made in the first few days of April failed due to the unstable set-up of the goniometer. The data from these days have been taken out. Moreover, rapid changes in cloud cover will bring uncertainties in T_{b0} measurements. Measurements under such weather conditions have not been used in our analysis. After a preliminary screening of the data in relation with quality and weather conditions, measurements on 11 April and 21 April 2001 were used for the analysis of the angular variability of brightness temperature, and thereafter used for the validation of the inversion of the linear mixture model.

Fig 6.2 shows the change in T_{b0} from nadir to off-nadir view zenith angles at each view azimuth angle at different hours during the two selected days: (a) 11 April and (b) 21 April. Only the measurements across two perpendicular planes are shown: one in the N – S direction along the canopy rows and one in the E – W direction across the row

At each azimuth direction, measurements were made twice, e.g. at both 0° and 90° azimuth the first observation started from $\theta_v = +60$ º through nadir to $\theta_v = -60$ º (denoted as

'go' in Fig.6.2) and the second observation went back from view zenith $\theta_v = -60°$ through nadir to $\theta_v = +60°$ (denoted as 'back' in Fig.6.2).

All the measurements shown in Fig.6.2 have been corrected for temporal change taking into account the measurements provided by the second nadir looking radiometer.

Changes in T_{b0} with θ_v are significant and show different trends at different hours during a day. Around noon, the observed near-nadir T_{b0} is always higher than that at off-nadir positions. On the contrary, in the early morning and the late afternoon, near-nadir T_{b0} tends to be lower than the off-nadir values. Maximum difference between near-nadir T_{b0} and those at off-nadir is about 2.8 °C on 11 April, while 4.4°C is observed on 21 April, both around noon time.

It would be interesting to investigate the 'hot spot' effect in the angular change of T_{b0} by plotting T_{b0} in the principal and normal planes of the sun. Unfortunately, the measurements at these specific positions were not made during the QRSLSP experimental period. However, the 'hot spot' is evident if one takes into account the sun position (Fig. 6.3) to interpret the observations. The maximum T_{b0} (shown as the minimum difference in T_{b0} between near-nadir and off-nadir) often appears close to the position where the sun was located which was close to the 90° plane in the morning and close to the 270° plane in the afternoon. Such 'hot spot' effect was particularly obvious during some morning hours, for instance, at 9:00, 9:30 and 10:00 on 21 April 2001 when the sun was located at . This indicates that the difference between sunlit and shaded leaves and between soil sunlit and shaded leaves affect the directional variations in T_{b0}, in addition to the difference of temperatures between the soil and the leaves. Around local solar noon time (at 13:00 on 11 April and at 12:00 on 21 April), the 'hot spot' is not obvious any longer.

The row structure of the winter wheat also plays an important role in determining the angular change of T_{b0}. Such structure effects are evident when comparing the shape of the curves in the along-row direction (the plane from 0° to 180°) and the curves in the across-row direction (the plane from 90° to 270°) in Fig. 6.2. The latter shows deeper slope, particularly in the position opposite to the sun, e.g. at 270° plane (negative zenith view angle) at 10:30, 11:00 and 11:30 on 11 April 2001 when the sun was located between 90° and 180° planes, and asymmetric than the former.

For the proper interpretation of multi-angular measurements the geometry of observations needs to be described in more details. Fig 6.4 shows schematically the changes in the diameters of the radiometer footprint when the radiometer observes the target at

different zenith view angles, while the position of the major axis of the radiometer footprint within the circle observable by the goniometer is given in Fig.6.5.

(a)
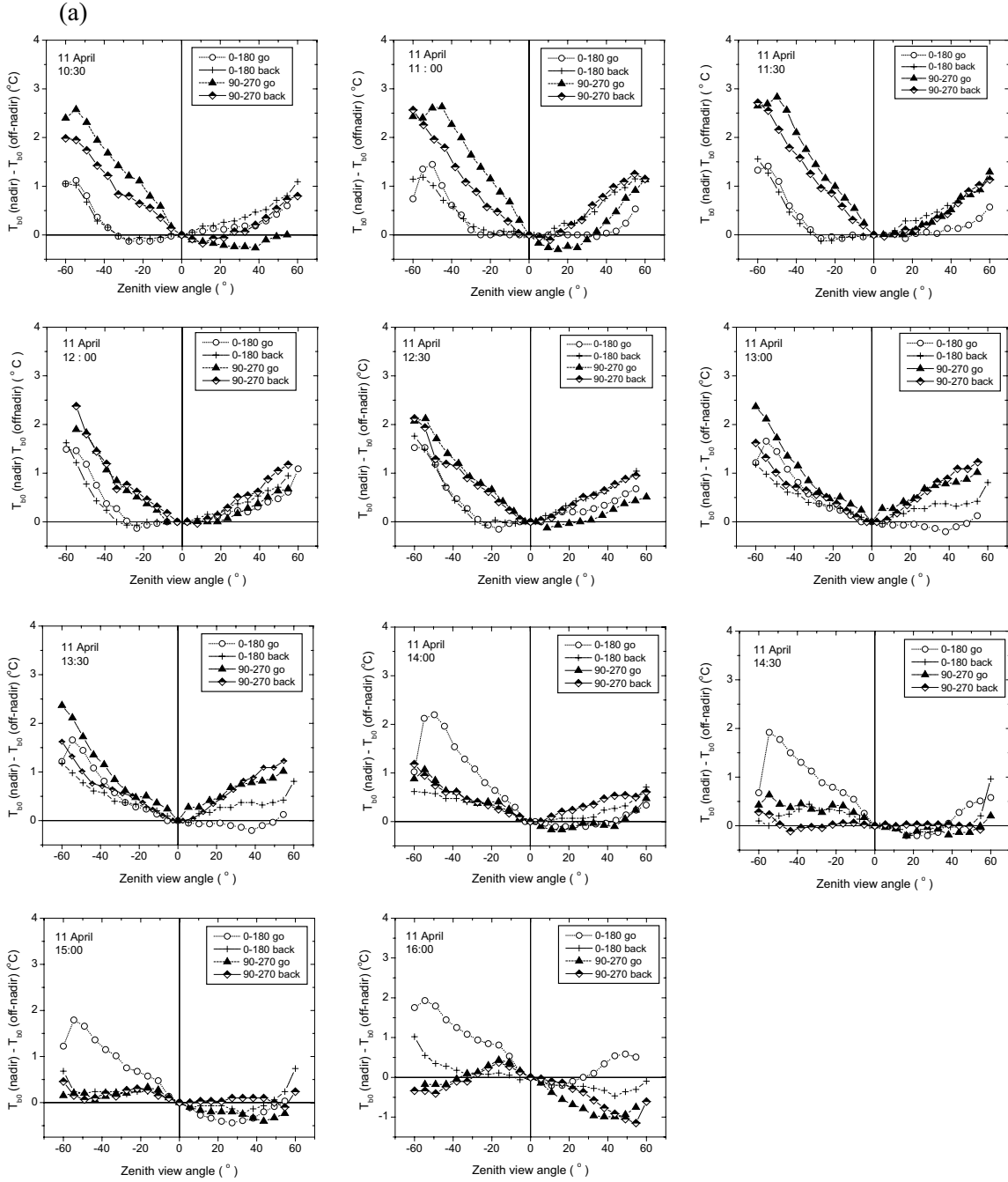
Figure 6.2 Measurements of the directional variation of TOC brightness temperature difference $T_{b0}(nadir) - T_{b0}(off-nadir)$ with zenith view angle: (a) on 11 April and (b) on 21 April at different times of the day at the QRSLSP site. $T_{b0}(nadir)$ is T_{b0} at $\theta_v = 0^\circ$, $T_{b0}(off-nadir)$ is T_{b0} measured at $\theta_v \neq 0^\circ$. The positive zenith view angle correspond to the azimuth 0° and 90° planes, the negative zenith view angle correspond to the 180° and 270° azimuth planes.

(b)

(Continued **Fig.6.2**)

0°

270° ———————— 90°

16:00
15:00
14:30
14:0
13:30
13:00   11:00
12:30 12:00 11:30   10:30

180°

11 April 2001

0°

17: 00
16: 30   270° ———————— 90°
16: 00
15:30   8: 00
15:00   8: 30
14:30   9: 00
14:00   9: 30
                         10: 00
                   10:30
12:00 11:30

180°
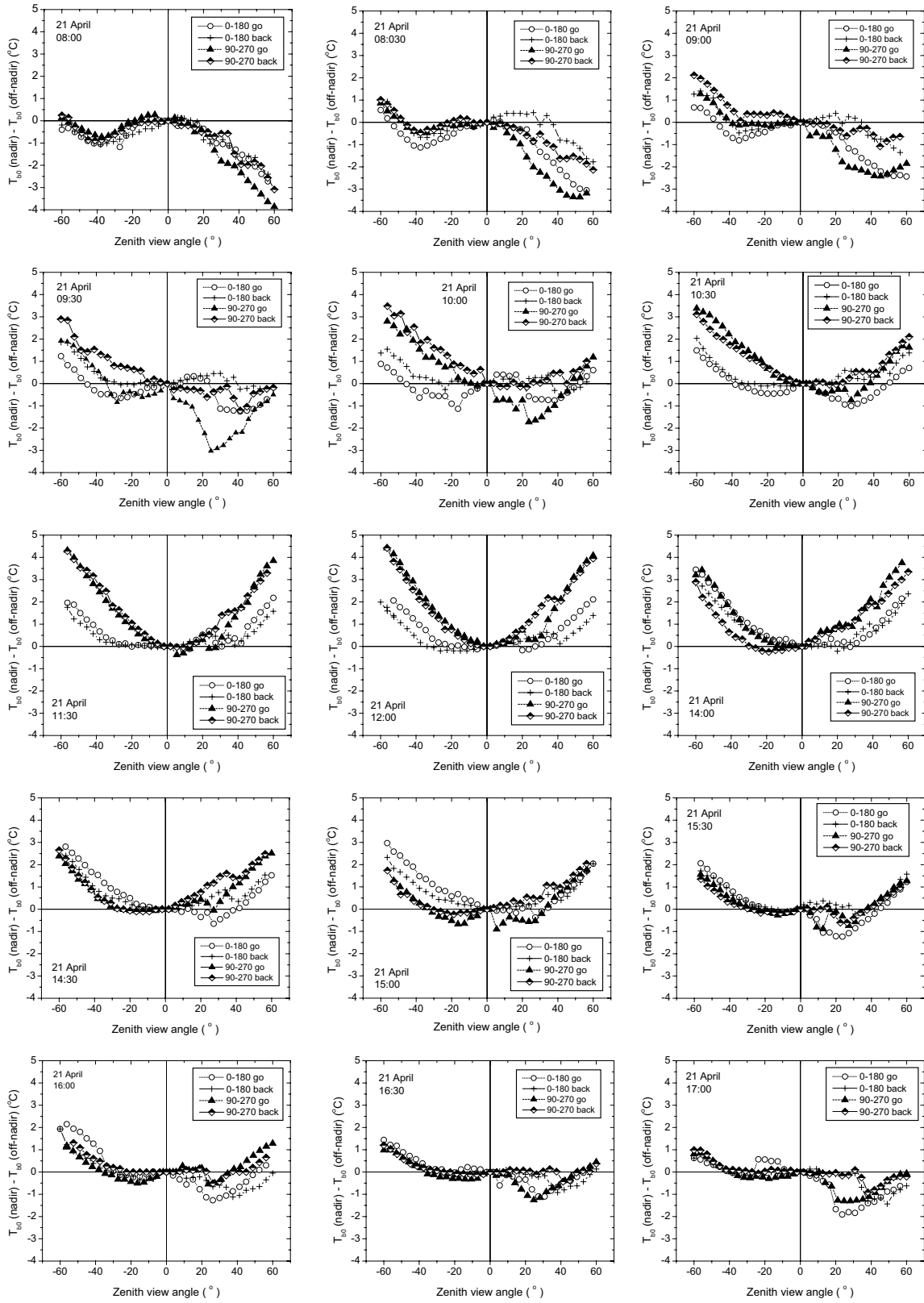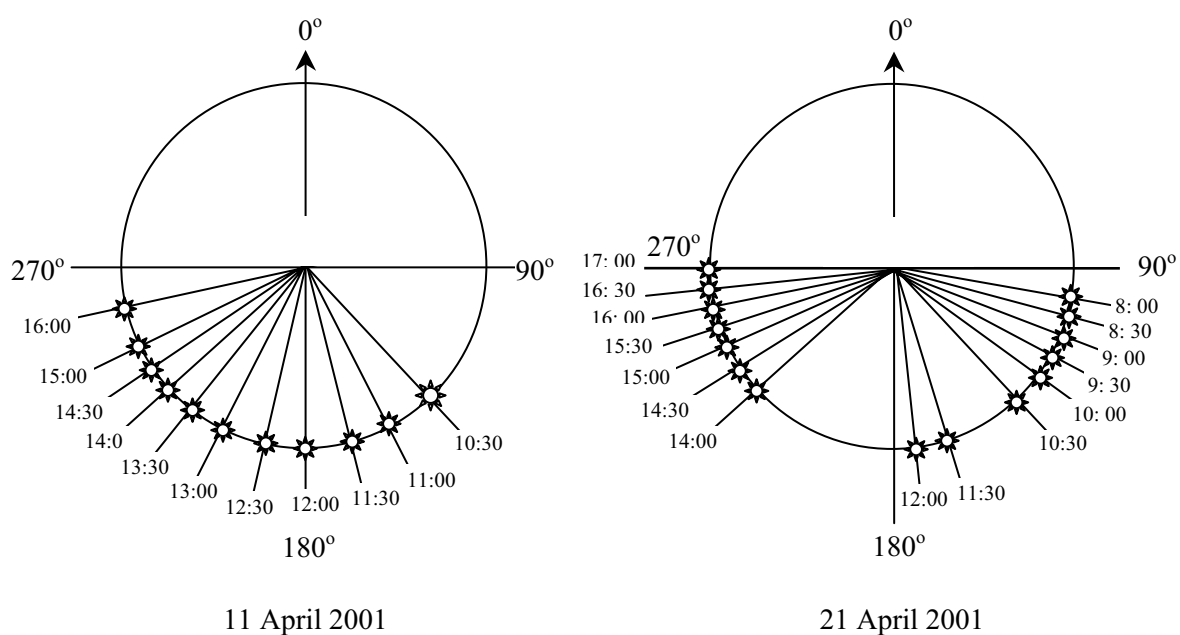
21 April 2001

Figure 6.3 Solar position during the selected observation periods on 11 (left) and 21 (right) April 2001 at the QRSLSP site.

Nadir

30°

FOV

60°

D0
D30
D60

Figure 6.4 The schematic illustration of the diameter of radiometer footprint at different zenith view angles. D0, D30 and D60 represents the diameter at nadir view angle, 30° and 60° zenith view angle. The symbol ⊗ denotes the central position of the radiometer footprint.
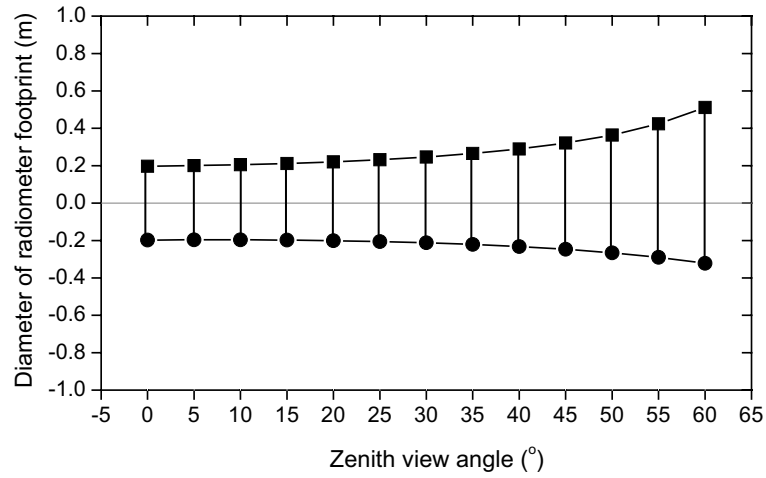
Figure 6.5 Length of the major axis of the radiometer footprint. The full scale of y-axis is the diameter (2 m) of the base of the goniometer with center at 0 m; distance of observation 1.5 m from target.

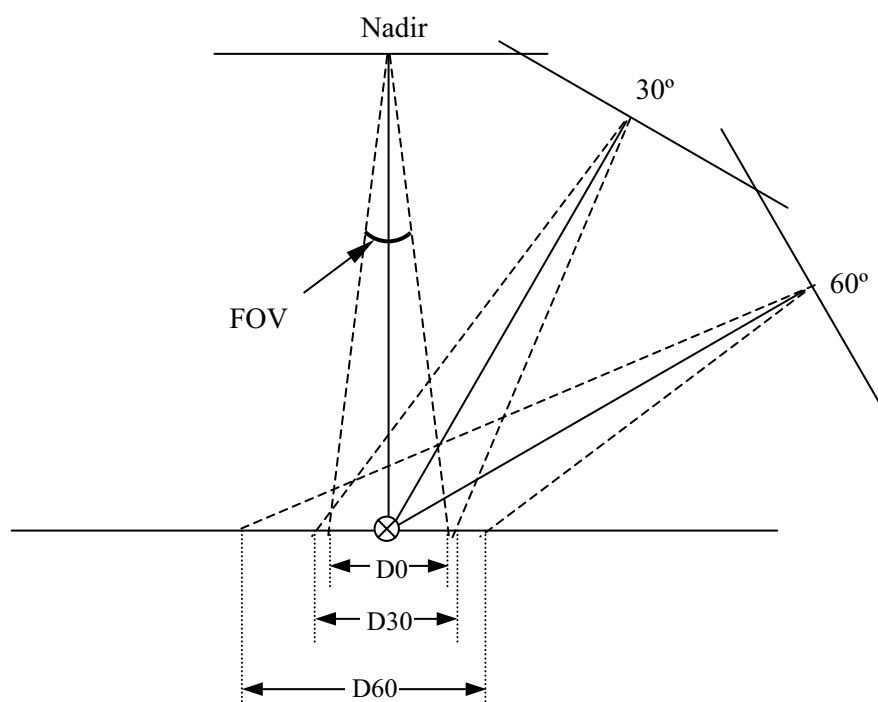To understand better the impact of the canopy structure on the directional T_{b0} measurements, a schematic illustration of changes in canopy proportions seen by the radiometer at different observation angles is shown in Fig 6.6. The angular change of T_{b0} in the along-row direction can be related to the fraction of soil and the leaves in the IFOV of the radiometer (Fig 6.6b): No matter at which zenith angle θ_v observation is done, the fractional area of rows is the same. In this case, the canopy structure has less impact in the angular change in T_{b0}. However, in the across-row direction, the situation is more complicated due to the row structure effect. At larger zenith view angle the side-wall of the canopy contributes as well to the radiance observed by the radiometer (Fig 6.6c) while it does not contribute when view zenith angle changes in the along row direction. Particularly, when the sun is located in the opposite position of the radiometer (e.g. at the left side of Fig 6.6c), cooler leaves of the canopy side-wall will be the main contributor to the radiance in the IFOV at large θ_v and this leads to larger differences between the near-nadir T_{b0} and the one at this position. Such situations correspond to the cases with steeper slope in the change of T_{b0} with θ_v as shown in Fig.6.2, particularly on 11 April when the LAI is smaller and the canopy structure has an important impact (e.g. in 270° plane in the morning hours).

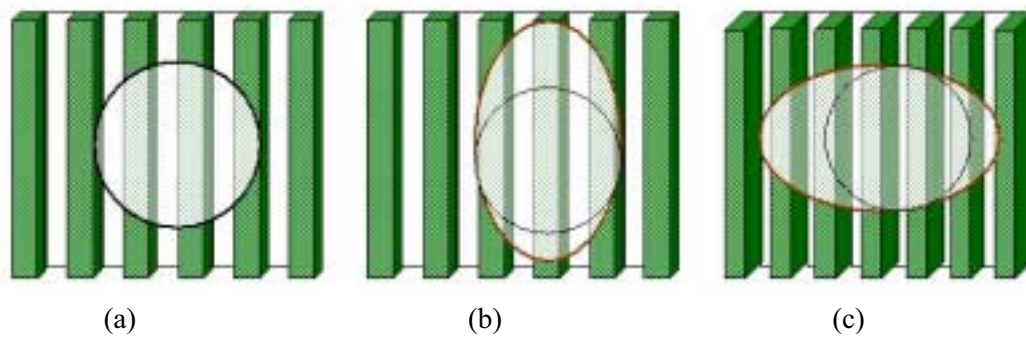**Figure 6.6** The proportion of canopy components in the IFOV of the radiometer changes with observation angles in the along- and across-row direction: (a) at nadir-view; (b) at off-nadir view 50º along the row direction; (c) at 50º off-nadir view across the row direction.

6.2.2 Observations of component temperatures

The soil and leaf temperatures were measured during the experimental period using the contact thermometer described in Chapter 5. On 11 April, the temperatures of three components (sunlit soil, shaded soil and leaf) were measured (Fig.6.7a) while the temperatures of the four components, i.e. sunlit and shaded soil, sunlit and shaded foliage, were measured on 21 April (Fig.6.7b). In general, both the mean soil and the mean foliage temperature are higher on 21 April than on 11 April as shown in Fig 6.7c. The difference between the soil and the foliage temperature is much larger on 21 April than on 11 April.

Significant temperature differences between the sunlit soil and the shaded soil, $T_s(sunlit)-T_s(shaded)$, are observed even in the early morning hours. On 11 April, $T_s(sunlit)-T_s(shaded)$ can reach as much as 6 °C while a value of 3.7 °C was observed on 21 April. On the contrary, the temperature difference between the sunlit foliage and the shaded foliage, $T_f(sunlit)-T_f(shaded)$, is relatively small (Fig.6.7b) with the maximum value about 1.5 °C and within 0.5 °C in most of the cases during the day on 21 April. Table 6.1 gives the summary of the maximum, minimum and the mean values of the temperature difference between the sunlit and shaded foliage and between the sunlit and the shaded soil, in which the mean values are the average over a day cycle. It should be noted that the temperature of shaded soil was close to foliage temperature most of the time.

Table 6.1 The maximum, minimum and mean values of the temperature difference between sunlit leaf $T_f(sunlit)$ and shaded leaf $T_f(shaded)$ and between sunlit soil $T_s(sunlit)$ and shaded soil $T_s(shaded)$ during the diurnal cycle on two different days in April 2001.

Date	$T_f(sunlit) - T_f(shaded)$			$T_s(sunlit) - T_s(shaded)$		
	Minimum	Maximum	Mean value	Minimum	Maximum	Mean value
11 April 2001	-	-	-	2.7	6.2	3.9
21 April 2001	-0.5	1.5	0.3	0.3	3.7	2.25

(a)

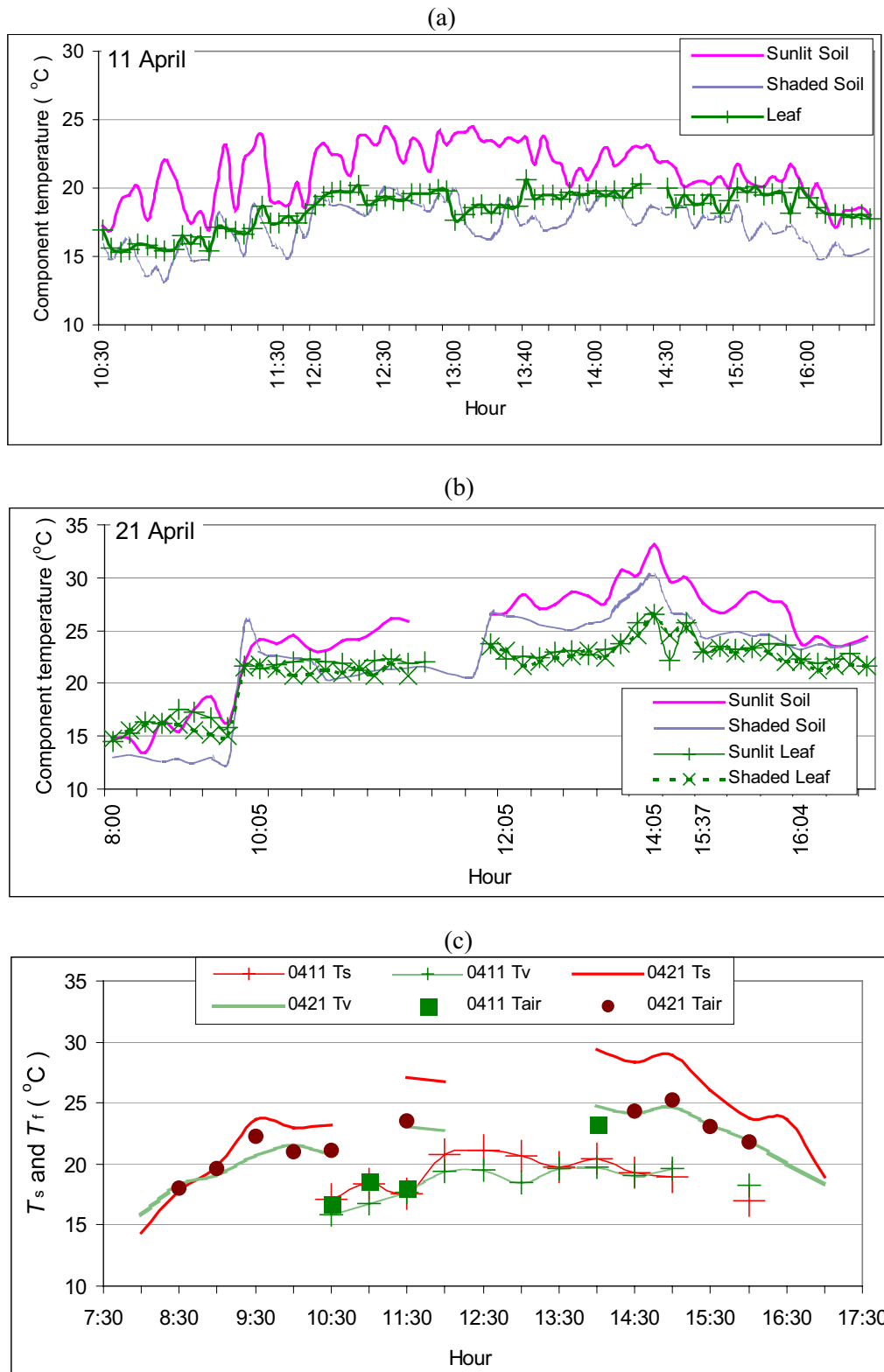(b)

(c)

Figure 6.7 The diurnal patterns of (a) (sunlit/shaded) T_s and T_f on 11 April, (b) (sunlit/shaded) T_s and (sunlit/shaded) T_f on 21 April 2001, and (c) the mean values of T_s and T_f on these two days at QRSLSP site.

Measurements of canopy temperature were also made using a thermal camera at different zenith view angles in along-row and in across-row plane on 11 April 2001 in the QRSLSP field experiment. Data analysis shows that it is challenging, at least for the studied canopy, to measure explicitly the four component temperatures, i.e. the sunlit and the shaded leaf and the sunlit and the shaded soil, although the thermal camera has the ability to capture the details of the thermal heterogeneity of the canopy elements. Some selected examples of images measured by the thermal camera are shown in Fig. 6.8 together with the histograms describing the range of temperatures of the canopy elements. Both the color scaled and gray density images are shown to document the variability of canopy component temperatures.

Fig. 6.8a: The observations were done at θ_v = 30º looking to the south at 13h. Two distinct peaks are observable in the histogram which are dominated by leaves and soil corresponding to the blue and sea-green colors and to the yellow/coral/brown/red colors respectively in the image. The sunlit/shaded leaf, especially the sunlit and the shaded soil may still be recognized if one looks at the image although they are not distinguishable from the histogram.

Fig. 6.8b: The measurements were done at θ_v = 50º looking to the south at 13h. Two peaks in the histogram, one is for the leaves and the other is for the sunlit soil, are still observable. Compared to Fig.6.8a, a range of dispersion exists in between the two peaks corresponding to some (sunlit) leaves and shaded soil. However, it is difficult to distinguish these two components in the image because they have quite similar temperatures.

Fig.6.8c: The measurements were done at θ_v = 50º looking to the south at 10:30h on 11 April. The patches of sunlit/shaded leaves and soil seem clear in the image, however, there is only one peak in the histogram with a large dispersion with the temperature increasing. Except the sunlit soil with relatively high temperature, it is actually quite difficult to distinguish the other three component temperatures – they are mixed together.

Fig. 6.8d: The measurements were at θ_v = 20º looking to the east at 13h. Smaller fraction of canopy is viewed in the IFOV of the thermal camera due to a smaller zenith view angle. Only one peak with narrow dispersion can be observed in the histogram. This peak seems to correspond to the shaded leaves and soil. The sunlit leaves are explicitly observable while the other components are mixed together. The sunlit soil is probably not seen within the IFOV.
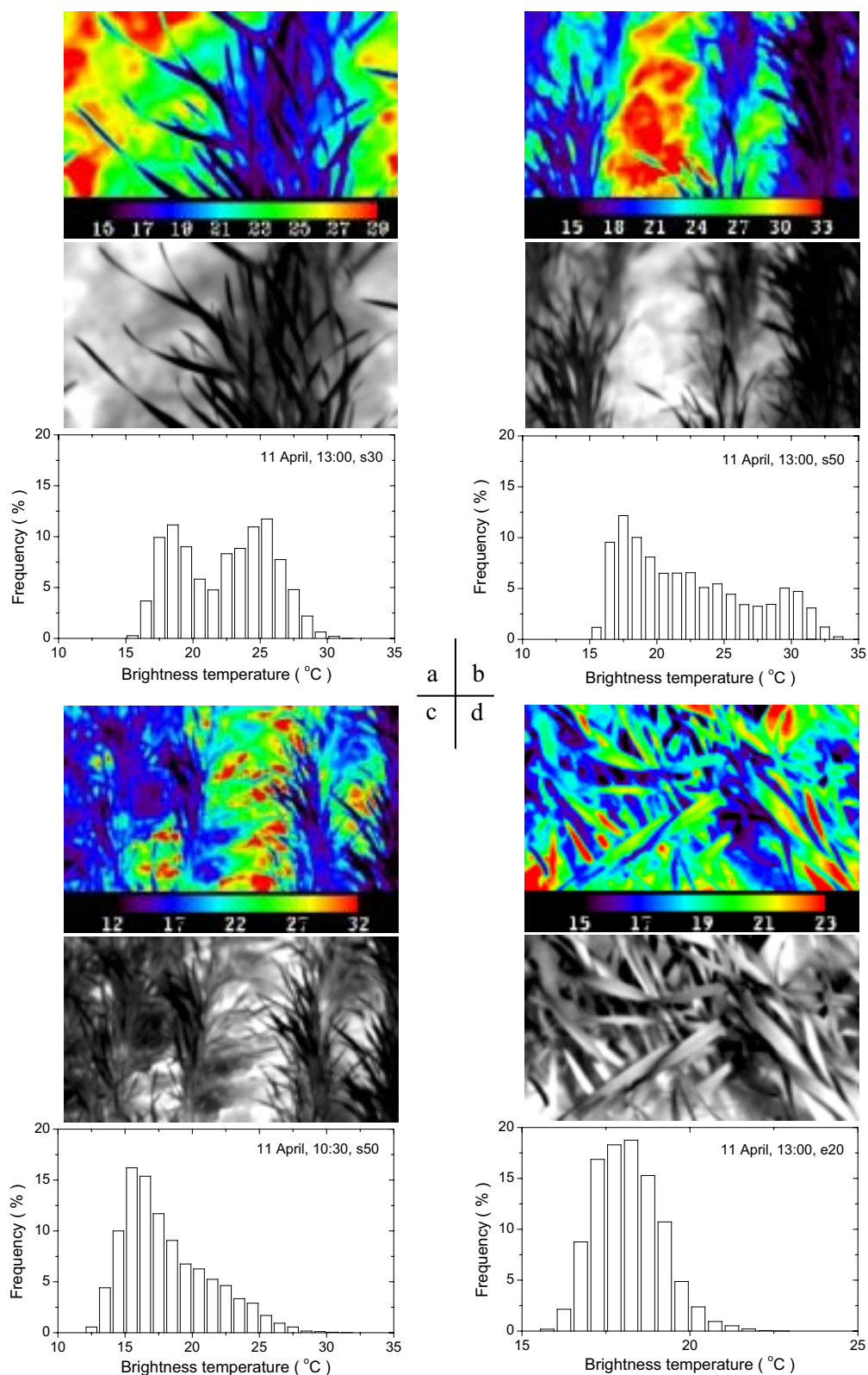
Fig. 6.8 Images of brightness temperature measured by the thermal camera showing the range of temperatures in the winter wheat canopy on 11 April 2001at QRSLSP site. s30 (or s50): looking from the south at 30º (or 50º) zenith view angle; e20: looking from the east at 20º zenith view angle.

6.2.3 Sensitivity of directional thermal infrared emittance to canopy conditions

As shown in the previous section, the observed directional T_{b0} and the component temperatures showed different features on the two selected days 11 and 21 April 2001, i.e. a larger difference of T_{b0} between nadir and off-nadir zenith view angles as well as a stronger contrast between foliage and soil temperature are clearer on 21 April than those on 11 April. A higher LAI value 2.5 was observed on 21 April compared with 1.7 on 11 April. Larger differences between near-nadir and off-nadir T_{b0} are expected on 11 April with lower LAI than on 21 April when LAI is higher, because smaller LAI allows more radiation penetrating to the soil surface through the canopy, hence the soil is warmer than at larger LAI. However, with LAI increasing to 2.5 (21 April), the directional variability in T_{b0} becomes significant and the maximum differences between soil and leaves can reach up to 4.6 °C (Fig. 6.7c). Moreover, net radiation on 11 April is slightly higher than on 21 April (Fig. 6.9) which should lead to the soil surface on 11 April being warmer than on 21 April. Nevertheless, such inconsistency is reasonable if one compares the soil water content between these two days (Fig. 6.10). Although on both days the surface was drier than the deeper soil layers, the soil surface on 21 April was drier than on 11 April. On 11 April, part of the radiation was absorbed by the soil moisture.
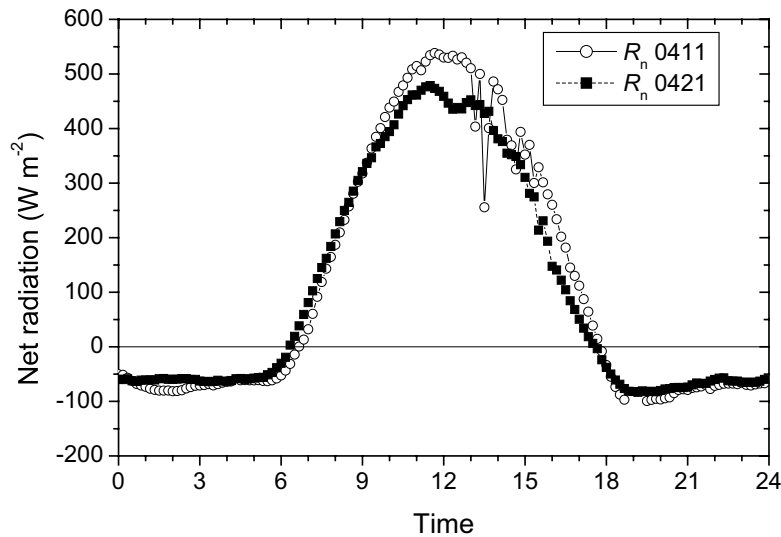
Figure 6.9 Diurnal change in net radiation flux density R_n observed on 11 April respectively on 21 April 2001at QRSLSP site.
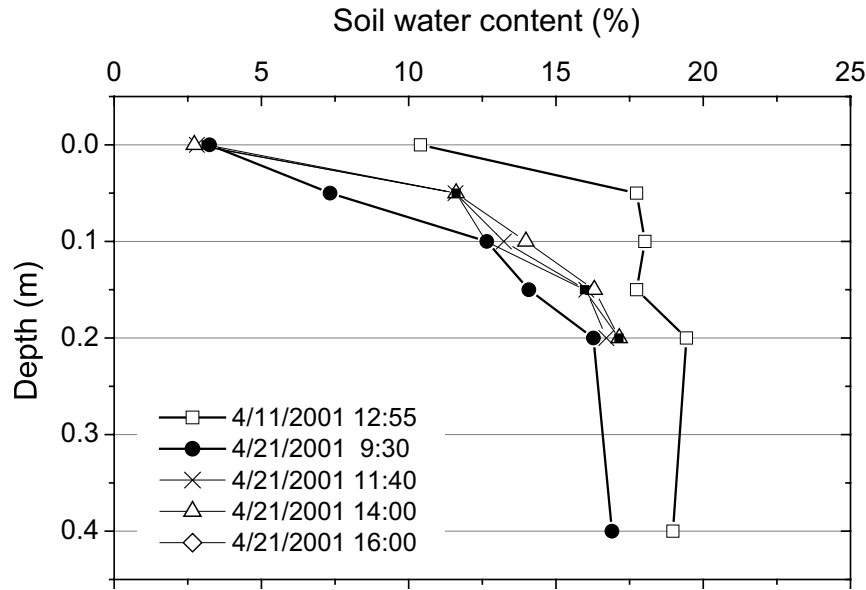
Figure 6.10 The volumetric soil water content w at different soil depths measured on 11 April and on 21 April 2001 at QRSLSP site.

As a conclusion from the discussions above, the canopy structure and the soil water content are two major factors affecting the angular variation of T_{b0}. The canopy structure determines the radiation field and heat exchange within the canopy, while the soil moisture determines the partitioning of absorbed energy by the canopy, hereafter controls the soil and foliage temperature. Exchanges of energy within the soil-vegetation system are intimately linked. Many processes occurring at the same time make it difficult to distinguish the importance of each factor. For further investigation of the sensitivity of the directionality of T_{b0} to the canopy structure and the soil water content, as well as to evaluate the inversion of the linear mixture model to retrieve component temperatures (see section 6.3), a modeling study of all these impacts is therefore necessary.

In this section, the 1D version of the complete model described in Chapter 2, i.e. the soil-plant-atmosphere model CUPID (Norman 1979, 1981, Norman et al. 1990, 1992; Wilson et al, 2003) was used to generate synthetic data sets over a wide range of LAI and soil water content conditions. These data sets were used to evaluate the sensitivity of anisotropy in brightness temperature to Leaf Area Index (LAI) and to soil water content.

Setup of the sensitivity study

A set of inputs to the complete model CUPID has been generated on the basis of the measurements during the QRSLSP field experiment. Meteorological variables (wind speed, air temperature, humidity, solar radiation), canopy properties such as the leaf inclination

100

angle distributions, the optical spectrum of the soil (reflectance r_s and emissivity ε_s) and that of leaves (reflectance r_f /transmittance τ_f /emissivity ε_f) have been taken directly from the QRSLSP measurements. A clumping factor is introduced to take into account the row structure effect.

The soil water content profiles have been taken from the measurements made on 11 and 21 April (Fig.6.10). The former one is referred to as 'wet' condition, while the latter is referred to as 'dry' condition. The values of LAI were: 0.5, 1.5, 2.5, 3.5, and 4.5.

Influence of soil water content and LAI on the anisotropy of thermal emittance

Fig.6.11 gives the simulation results at 10:30 hour in the sun principal plane showing the dependence of the angular $T_{b0}(\theta_v, \varphi_v)$ on the soil moisture content and the changes in LAI.

The soil moisture content exerts an important role in determining the shape and the magnitude of directional TIR signature when comparing Fig.6.11a ('wet' condition) and Fig.6.11b ('dry' condition). Under the 'dry' condition, the angular variation in T_{b0} is obvious and the maximum change with zenith view angle reaches up to 3.4 °C. The T_{b0} observed at nadir is larger than those at off-nadir angles even when the LAI is as high as 4.5. Contrariwise, under 'wet' condition, nadir and off-nadir surface temperature differences are generally negligible under smaller LAI conditions and negative values are observed when LAI ≥ 2.5.

When the surface is dry, the directional TIR signature is rather significant under low LAI (Fig. 6.11a). The directional TIR signature decreases when LAI increases. At very high LAI (i.e. 4.5 in this study), the directional signature is weak and difficult to interpret.
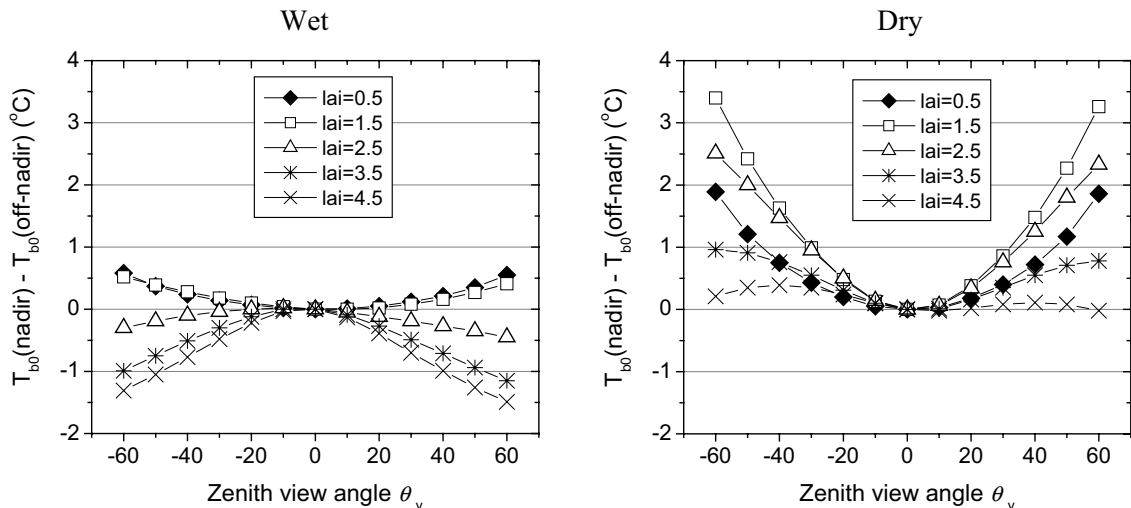
Figure 6.11 Variation of brightness temperature T_{b0} due to the changes of LAI and soil water content w: under 'wet' and under 'dry' soil moisture conditions.

It is interesting to see that smallest LAI (0.5) didn't give the largest difference of T_{b0} between nadir and off-nadir view angle when the soil is dry. Instead, the maximum difference between nadir T_{b0} and off-nadir T_{b0} appears when LAI is moderate (1.5), i.e. for the environment and canopy conditions of the QRSLSP experiment.

Evaluation of the simulated component temperatures under the same conditions leads to similar conclusions (Fig.6.12). At lower LAI values the fractional vegetation cover is also small, the soil in the soil-vegetation system can receive higher solar radiation than in the case when LAI is large. In the 'wet' case (irrigated canopy for instance), it is quite interesting to see that the soil is rather cooler than the soil in the 'dry-surface' case, even cooler than foliage even though LAI is rather low allowing more radiation to arrive at the soil surface (Fig.6.12b). This is because most radiation absorbed by soil is used for evaporation rather than to heat the soil surface. This agrees well with measurements shown in §6.2.2.
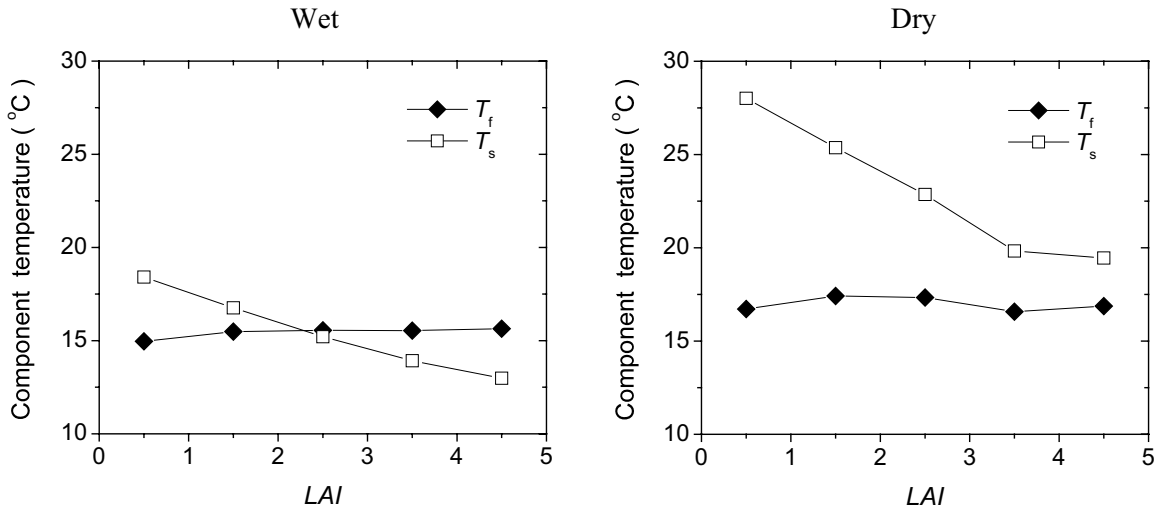
Figure 6.12 Component temperatures under various LAI and soil water content conditions under 'wet' and under 'dry' soil moisture conditions.

6.2.4   Sensitivity of the simple linear mixture model

The sensitivity of the directional brightness temperature to the canopy conditions has been analyzed by means of model simulations, which can help to understand the anisotropy of TIR radiance from a canopy. However, the crucial aspect in the inversion of Eq. 3.19 is to investigate the sensitivity of the retrieval of T_f and T_s to errors in $T_{b0}(\theta_v, \varphi_v)$ measurements and errors in the estimation of $f_f(\theta_v)$. We considered a simple case like Eq.3.19, neglecting the interaction between the soil and foliage in the canopy. Rewriting Eq.3.19 explicitly for

the radiance from foliage, R_f, and the radiance from the soil, R_s, we have the following expressions:

$$R_f = R_{fw} - \frac{1-f_{fw}}{f_{fw}-f_{nd}}(R_{nd}-R_{fw}) - \left[R_{atm}^{fw} - \frac{1-f_{fw}}{f_{fw}-f_{nd}}\left(R_{atm}^{nd}-R_{atm}^{fw}\right) \right] \tag{6.1}$$

$$R_s = R_{nd} + \frac{f_{nd}}{f_{fw}-f_{nd}}(R_{nd}-R_{fw}) - \left[R_{atm}^{nd} + \frac{f_{nd}}{f_{fw}-f_{nd}}\left(R_{atm}^{nd}-R_{atm}^{fw}\right) \right] \tag{6.2}$$

where the subscripts 'nd' and 'fw' denote any pair of zenith view angles at so-called 'nadir' (relative to 'forward', not necessary 0 zenith angle) under which the brightness temperature in terms of radiance is measured. The two terms on the right-hand side of Eqs 6.1 and 6.2, R_{atm}^{nd} and R_{atm}^{fw}, are related to the reflection of the down-welling atmospheric radiance by the foliage and the soil components respectively:

$$R_{atm}^{nd} = (1-\varepsilon_f)f_{nd}R_{atm}^{\downarrow} + (1-\varepsilon_s)(1-f_{nd})R_{atm}^{\downarrow} \tag{6.3}$$

$$R_{atm}^{fw} = (1-\varepsilon_f)f_{fw}R_{atm}^{\downarrow} + (1-\varepsilon_s)(1-f_{fw})R_{atm}^{\downarrow} \tag{6.4}$$

Following the definition that the sensitivity of a dependent variable y ($y = R_f$ or R_s) to the independent variable x ($x = R_{nd}$, R_{fw}, f_{nd} and f_{fw}) is equal to its partial differential, $\partial y/\partial x$, one can get the sensitivity of R_f to R_{nd}, R_{fw}, f_{nd} and f_{fw} as

$$\frac{\partial R_f}{\partial R_{nd}} = -\frac{1-f_{fw}}{f_{fw}-f_{nd}} < 0 \tag{6.5a}$$

$$\frac{\partial R_f}{\partial R_{fw}} = \frac{1-f_{nd}}{f_{fw}-f_{nd}} > 0 \tag{6.5b}$$

$$\frac{\partial R_f}{\partial f_{nd}} = -(R_s-R_f)\frac{1-f_{fw}}{f_{fw}-f_{nd}} + R_{atm}^{\downarrow}(\varepsilon_f-\varepsilon_s)\frac{1-f_{fw}}{f_{fw}-f_{nd}} < 0 \tag{6.5c}$$

$$\frac{\partial R_f}{\partial f_{fw}} = (R_s-R_f)\frac{1-f_{nd}}{f_{fw}-f_{nd}} - R_{atm}^{\downarrow}(\varepsilon_f-\varepsilon_s)\frac{1-f_{nd}}{f_{fw}-f_{nd}} > 0 \tag{6.5d}$$

and the sensitivity of R_s to R_{nd}, R_{fw}, f_{nd} and f_{fw} as

$$\frac{\partial R_s}{\partial R_{nd}} = \frac{f_{fw}}{f_{fw}-f_{nd}} > 0 \tag{6.6a}$$

$$\frac{\partial R_s}{\partial R_{fw}} = -\frac{f_{nd}}{f_{fw}-f_{nd}} < 0 \tag{6.6b}$$

$$\frac{\partial R_{\mathrm{s}}}{\partial f_{\mathrm{nd}}} = (R_{\mathrm{s}} - R_{\mathrm{f}})\frac{f_{\mathrm{fw}}}{f_{\mathrm{fw}} - f_{\mathrm{nd}}} - R_{\mathrm{atm}}^{\downarrow}(\varepsilon_{\mathrm{f}} - \varepsilon_{\mathrm{s}})\frac{f_{\mathrm{fw}}}{f_{\mathrm{fw}} - f_{\mathrm{nd}}} > 0 \qquad (6.6c)$$

$$\frac{\partial R_{\mathrm{s}}}{\partial f_{\mathrm{fw}}} = -(R_{\mathrm{s}} - R_{\mathrm{f}})\frac{f_{\mathrm{nd}}}{f_{\mathrm{fw}} - f_{\mathrm{nd}}} + R_{\mathrm{atm}}^{\downarrow}(\varepsilon_{\mathrm{f}} - \varepsilon_{\mathrm{s}})\frac{f_{\mathrm{nd}}}{f_{\mathrm{fw}} - f_{\mathrm{nd}}} < 0 \qquad (6.6d)$$

The general conclusions from Eqs.6.5 and 6.6 are the following:

- The sensitivities of R_{f} (or R_{s}) to the measurements of R_{nd} (or R_{fw}) depend only on the fractional cover of foliage and soil (f_{nd} and f_{fw}) and their difference (f_{fw} - f_{nd}). R_{f} decreases with increasing R_{nd}, while R_{s} increases with increasing R_{nd}. On the contrary, R_{f} increases with increasing R_{nd} and R_{s} decreases with increasing R_{s}.

- The sensitivities of R_{f} (or R_{s}) to f_{nd} and f_{fw} depend not only on f_{nd} and f_{fw}, but also on the contrast between the soil and foliage temperature (in terms of R_{f} and R_{s}). The stronger the contrast between R_{f} and R_{s}, the more significant the sensitivities of R_{f} (or R_{s}) to f_{nd} and f_{fw} are.

- For a given f_{fw} (or f_{nd}) value, the smaller the difference between f_{fw} and f_{nd}, the larger the sensitivities of R_{f} (or R_{s}) to R_{nd} (or R_{fw}) are. For a given f_{fw} (or f_{nd}) and a given difference between T_{f} and T_{s}, the same rule applies to the sensitivity of R_{f} (or R_{s}) to f_{nd} (or f_{fw}). This implies that the measurements of T_{b0} made at two zenith view angles very close to each other, would probably give a small value of (f_{fw} - f_{nd}), and should not be used in the inversion of T_{s} and T_{f}. The threshold of the zenith angle difference at which the expected changes become significant, depends on the canopy structure in terms of LIDF. For a given pair of zenith view angles, the difference of fractional cover of foliage between these two angles can be significantly larger in the vertical LIDF case than in the spherical LIDF case (Fig. 6.19).

To investigate the magnitude of the errors in the retrieval of T_{f} and T_{s} caused by the errors in the estimation of f_{nd} (f_{fw}) and by the errors in the measurements of T_{nd} (T_{fw}), we consider a few specific cases with different contrast of T_{f} and T_{s} under various f_{nd} and different difference between f_{fw} and f_{nd} as shown in Figs. 6.13, 6.14, 6.15 and 6.16 where the radiance R_{nd} (or R_{fw}) is converted to the equivalent T_{b0} values T_{nd} (or T_{fw}).

Sensitivity of the retrieved T_f to T_{nd} and T_{fw}

It is apparent from Fig. 6.13 that a small difference between f_{fw} and f_{nd} leads to quite large errors in the retrievals of T_f. For instance, when $f_{nd} = 0.6$ which is the smaller sensitivity case as compared to other cases with lower f_{nd}, the errors in the retrieved T_f can reach -0.28K and 0.38K for a 0.1K errors on T_{nd} and T_{fw} (-1.4K and 1.9K in T_f per 0.5K error in T_{nd} and T_{fw}) respectively when the difference between f_{fw} and f_{nd} is as small as 0.1. However, with the difference between f_{fw} and f_{nd} increasing, the error in the retrieval of T_f decreases rapidly. At ($f_{fw} - f_{nd}$) = 0.4, all the cases give an error smaller than 0.2K in the retrieved T_f for 0.1K error in T_{nd} and T_{fw} (1 K error in T_f per 0.5K error in T_{nd} and T_{fw}).

Figure 6.13 Sensitivities of the retrieved foliage temperature T_f to (a) the errors in nadir brightness temperature T_{nd}, and (b) the errors in off-nadir brightness temperature T_{fw}.

Sensitivity of the retrieved T_f to f_{nd} and f_{fw}

The larger contrast between T_f and T_s results in significant errors in the retrieved T_f with 0.1 error both in f_{nd} and in f_{fw}, particularly when the nadir fractional cover is small and difference between f_{fw} and f_{nd} is also small (Fig. 6.14). However, when the contrast between T_f and T_s is reduced to a value smaller than 5K and the nadir fractional cover is as large as 0.2, no matter how small the difference between f_{fw} and f_{nd} is, the error in the retrieved T_f caused by the error in either f_{fw} or in f_{nd} is acceptable. For instance, when ($T_s - T_f$) = 5K, f_{nd}=0.25, and ($f_{fw} - f_{nd}$) = 0.3, the error in T_f due to 0.1 change in f_{fw} and in f_{nd} is -0.5K and 0.9K respectively.

Figure 6.14 Sensitivities of the retrieved foliage temperature T_f to (a) the errors in nadir fractional cover of foliage f_{nd}, and (b) the errors in forward fractional cover of foliage f_{fw}.

Sensitivity of the retrieved T_s to T_{nd} and T_{fw}

At a given difference between f_{fw} and f_{nd}, the retrieved T_s is more sensitive to T_{nd} and T_{fw} when f_{nd} is larger (Fig.6.15). The error will decrease with the (f_{fw} - f_{nd}) increasing. When (f_{fw} - f_{nd}) reach some level, i.e. around 0.4, all the cases can give an acceptable accuracy in the retrieved T_s, that is the error on T_s is smaller than 1 K.
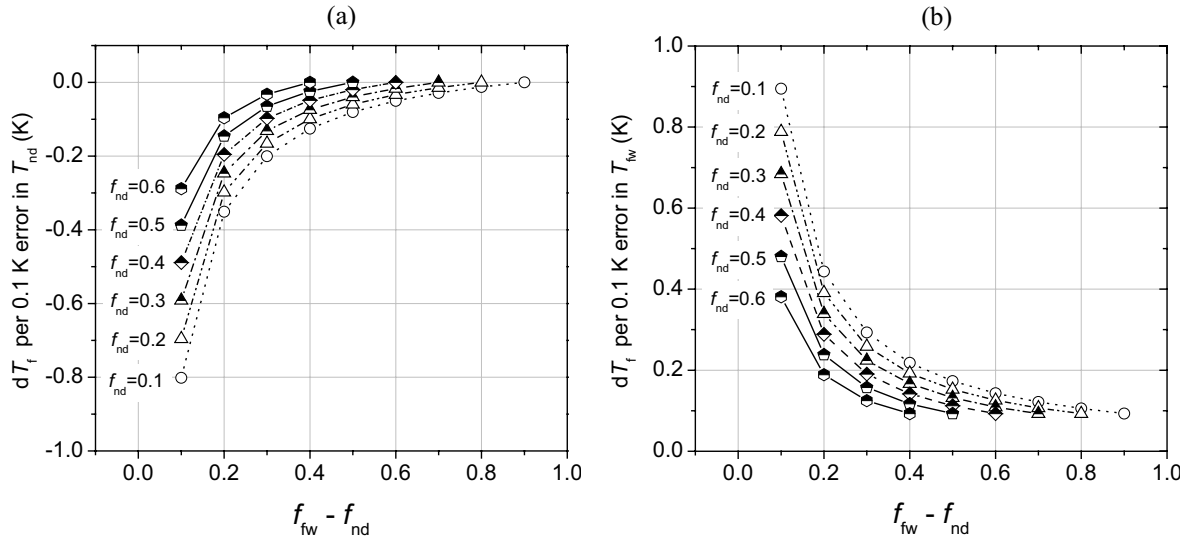

Figure 6.15 The sensitivities of the retrieved soil temperature T_s to (a) the errors in nadir brightness temperature T_{nd}, and (b) the errors in forward brightness temperature T_{fw}.

106

Sensitivity of the retrieved T_s to f_{nd} and f_{fw}

For a given difference between T_f and T_s, the retrieval of T_s is more sensitive to both f_{nd} and f_{fw} when f_{nd} is higher and (f_{fw} - f_{nd}) is small (Fig.6.16). At a given f_{nd}, a smaller difference between T_f and T_s results in less sensitivity of T_s both to f_{nd} and f_{fw}. As an example, 0.1 error in f_{nd} and f_{fw} brings an error less than 0.5K in T_s retrieval when (T_s - T_f) is 5K no matter what the values of f_{nd} and (f_{fw} - f_{nd}) are.
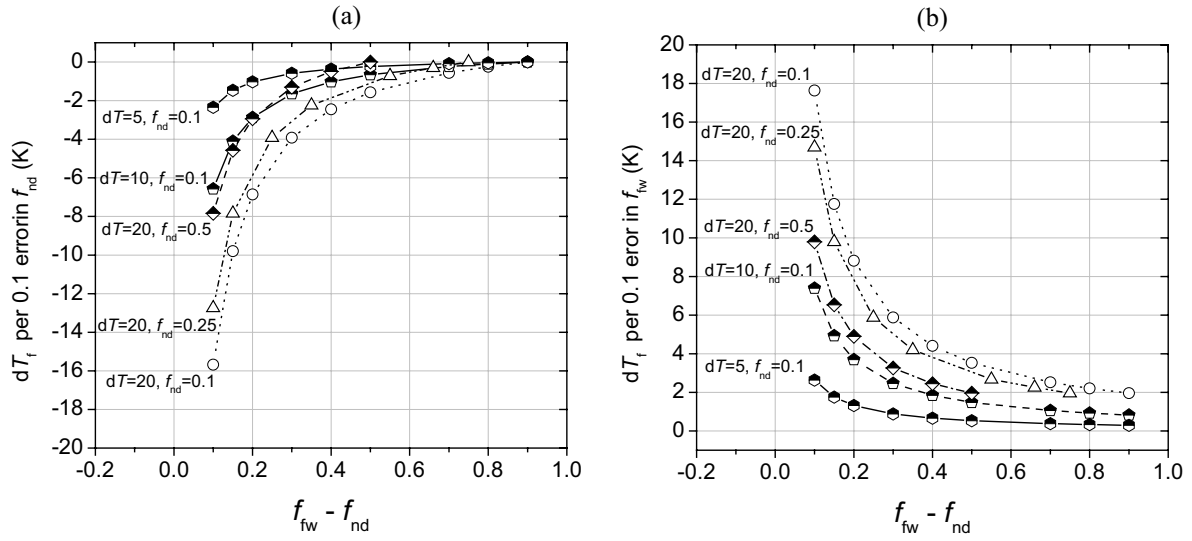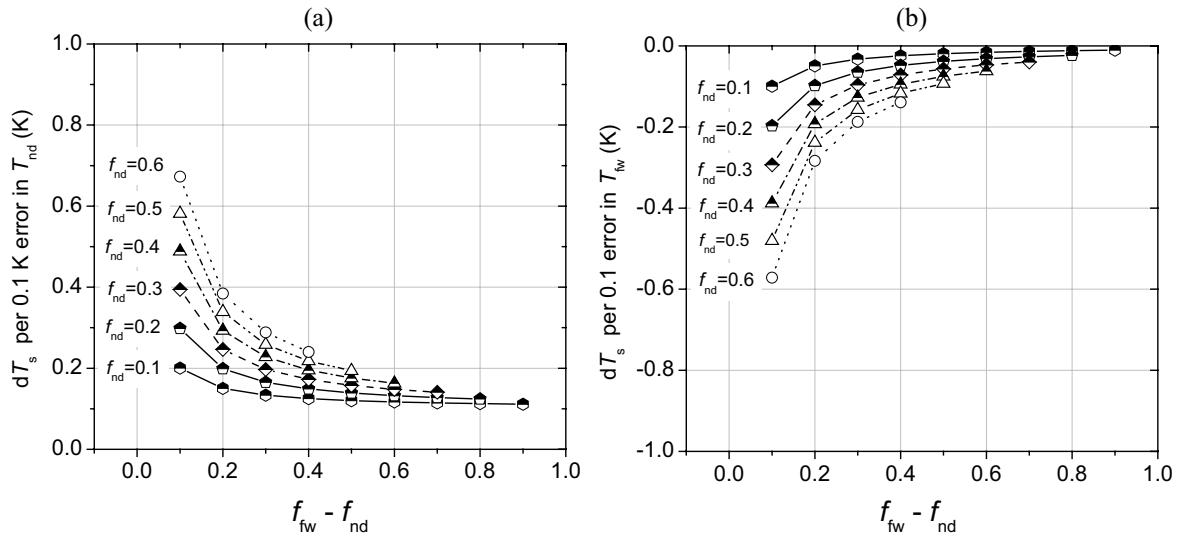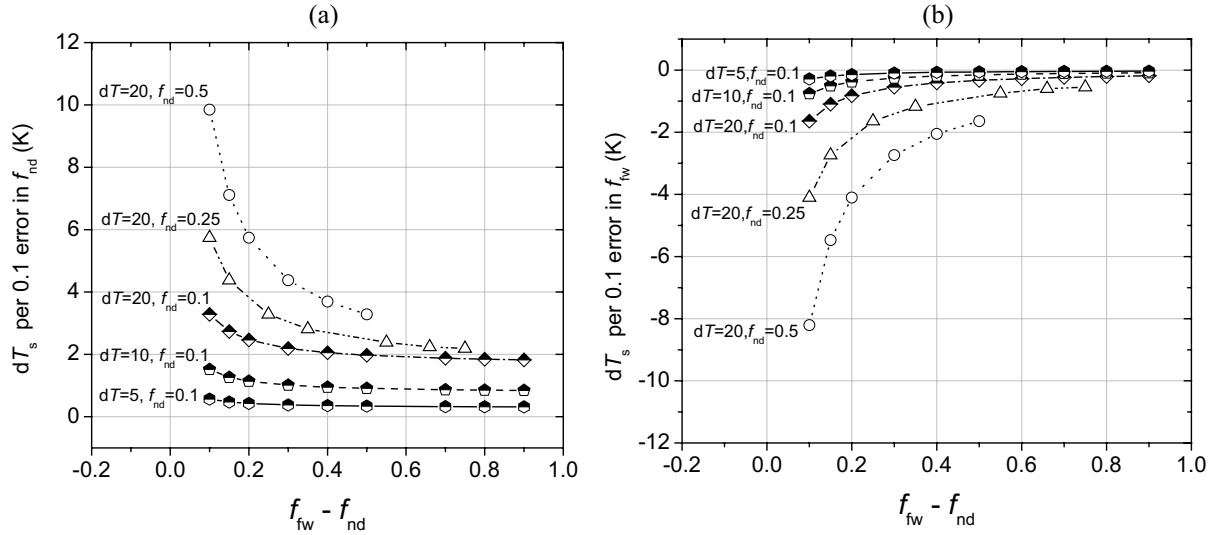

Figure 6.16 Sensitivities of the retrieved soil temperature T_s to (a) the errors in nadir fractional cover of foliage f_{nd}, and (b) the errors in forward fractional cover of foliage f_{fw}.

Summarizing the analysis given above, larger differences between f_{nd} and f_{fw} are expected to allow more accurate retrieval of T_f and T_s. This can be achieved partly by taking T_{b0} measurements at two zenith view angles far from each other. Moreover, the retrieval of T_f and T_s for a canopy with near vertical leaves may always be promising because a larger difference between f_{fw} and f_{nd} is easily obtained even when the two zenith angles are close to each other. Under moderate contrast between T_f and T_s, the errors in the retrieval of T_f and T_s caused either by the errors in T_{nd} and T_{fw} measurements or by the errors in the estimation of f_{nd} and f_{fw} are in an acceptable range, i.e. smaller than 1 K. In the cases when the contrast between T_f and T_s is very large (>20K) and when the fractional cover is very small (<0.2), careful attention must be paid to ensure accurate measurements of T_{nd} (and T_{fw}) and the estimation of fractional cover. It should be noted, however, that larger errors on T_f and T_s are still acceptable, given the larger value of (T_s - T_f).

6.3   Validation of the simple linear mixture model

To invert Eq.3.19 to determine the two component temperatures T_f and T_s, one has to know the fractional cover of the vegetation and the soil. If leaves can be treated as randomly distributed in the canopy space, the fractional cover of foliage is related to *LAI* (Fig.6.17) by Beer's law as:

$$f_f(\theta_v) = 1 - \exp[-k_\alpha LAI] \tag{6.7}$$

where k_α is the extinction coefficient of a ray penetrating the canopy which is related to the non-interception probability (Chapter 2) and a function of LIDF of the canopy (Rose, 1981; Norman, 1979). Note that the subscript for azimuth angle φ_v is neglected in Eq.6.7 and in the text, since we assume here that $f_f(\theta_v)$ only changes with θ_v. The value of k_α depends on the canopy structure and the zenith view angle and its general expression is:

$k_\alpha = \dfrac{2\tan\theta}{\pi}$, for an erectophile leaf distribution;

$k_\alpha = \dfrac{1}{2\cos\theta}$, for a spherical leaf distribution;

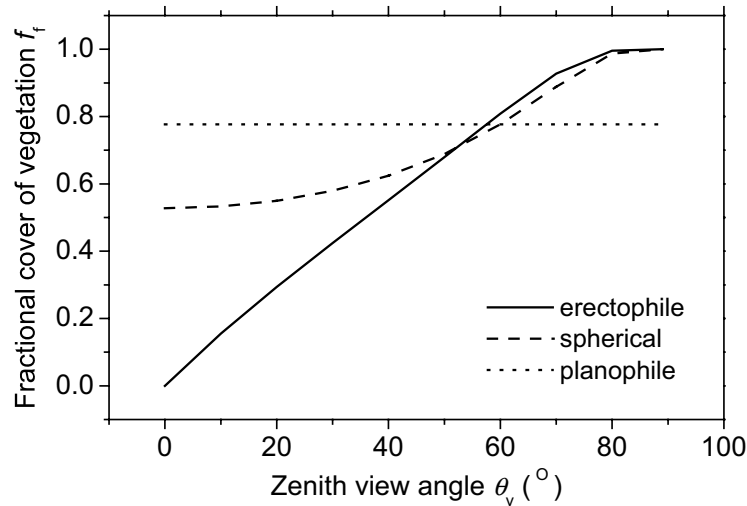$k_\alpha = 1$, for a planophile leaf distribution.

Figure 6.17 Fractional vegetation cover of a canopy as a function of zenith view angle and leaf inclination angles: erectophile, spherical and planophile (*LAI* = 1.5).

IMGRASS case study

A spherical leaf distribution is considered as an adequate approximation for the mixture of grasses at the IMGRASS site 4 (see also §5.2.1). The measured *LAI* was 0.5, corresponding with $f_f \approx 0.30$ according to Eq. 6.7.

Theoretically, T_f and T_s can be derived using measurements of T_{b0} at any pair of view angles, such as $[T_{b0}(0), T_{b0}(23)]$, $[T_{b0}(0), T_{b0}(52)]$, and $[T_{b0}(23), T_{b0}(52)]$. However, in our study, due to the small IFOV of the radiometer used, only bare soil was seen in the IFOV for measurements done at nadir, so that $T_{b0}(0)$ is the soil brightness temperature. To obtain T_s from $T_{b0}(0)$, $\varepsilon_s = 0.95$ was used. The observed T_s was taken as the reference to evaluate the T_s retrieval from $T_{b0}(23)$ and $T_{b0}(52)$. Agreement of T_s between retrievals and measurements was good, with a root mean square error (RMSE) of 0.8 K (Fig. 6.18a). Fig. 6.19 shows the retrieved T_s and T_f together with the net radiation flux density at different time of a day during the measurements period (26 - 31 July 1998). Foliage emissivity was assumed $\varepsilon_f = 0.98$. The same trends are observed, i.e. higher T_s and T_f are accompanied by a higher net radiation.
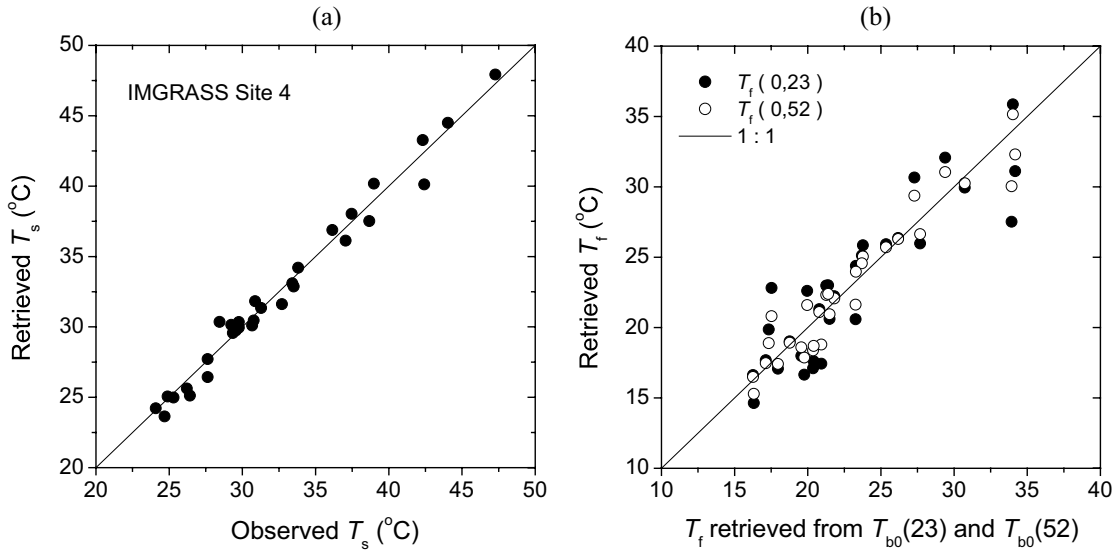
Figure 6.18 (a) Comparison of the observed soil surface temperature T_s with estimates obtained by solving Eqs. 3.19a and 3.19b with T_{b0} measurements at 23° and 52° view angles at site 4 of the IMGRASS in July 1998. The RMSE is 0.8K. (b) Comparison of foliage temperature T_f retrieved from T_{b0} measured at different pairs of θ_v: $[T_{b0}(0), T_{b0}(23)]$, $[T_{b0}(0), T_{b0}(52)]$ against $[T_{b0}(23), T_{b0}(52)]$, at site 4 of the IMGRASS in July 1998.
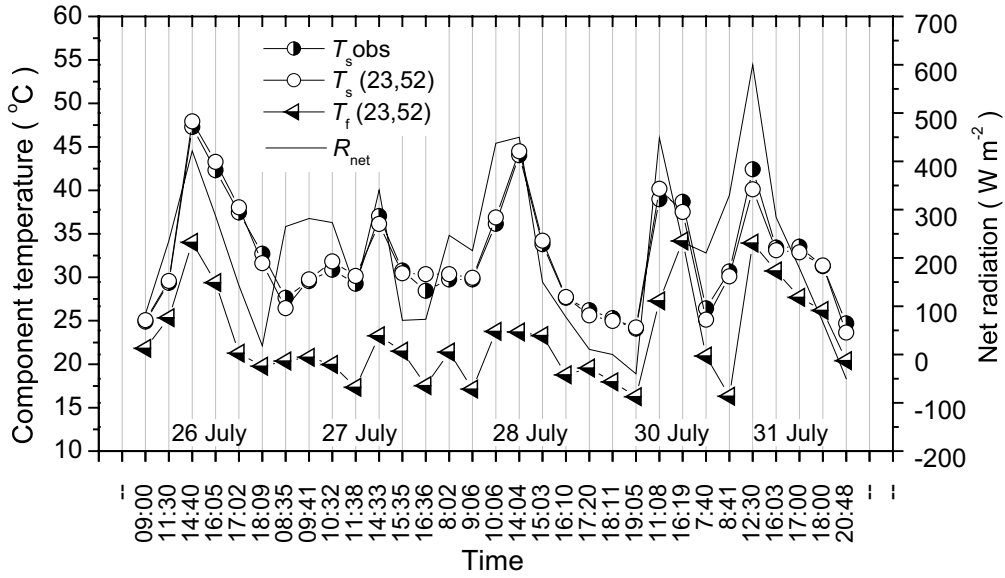
Figure 6.19 Component temperatures and net radiation flux density R_n at site 4 of the IMGRASS in July 1998.

The same measurements of $T_{b0}(23)$ and $T_{b0}(52)$ give T_f, as well as the measurements of $[T_{b0}(0),\ T_{b0}(23)]$ and $[T_{b0}(0),\ T_{b0}(52)]$. Since no observations of T_f in the IMGRASS experiment were available, we compared the retrieved T_f using T_{b0} measurements at different pairs of θ_v, i.e. between (0º, 23º), (23º, 52º) and (0º, 52º) as shown in Fig.6.18b – the RMSE of retrieved T_f using the measurements of $[T_{b0}(23),\ T_{b0}(52)]$ and using $[T_{b0}(0),\ T_{b0}(23)]$ is 2.5 K, while the RMSE is 1.5 K when using $[T_{b0}(23),\ T_{b0}(52)]$ and $[T_{b0}(0),\ T_{b0}(52)]$. Since the spherical LIDF is taken in the estimation of $f_f(\theta_v)$, the smaller estimated difference in $f_f(\theta_v)$ when observation angles are closer, i.e. $[T_{b0}(0),\ T_{b0}(23)]$, tends to bring larger errors in the retrieved T_f as discussed in 6.2.4. The RMSE was 1.5K when comparing $T_f[T_{b0}(0),\ T_{b0}(23)]$ with $T_f[T_{b0}(23),\ T_{b0}(52)]$.

QRSLSP case study

The canopy conditions was different in terms of LAI and of the spacing between wheat rows on the two selected days 11 and 21 April 2001 due to the growth of the crop (Table 6.2). For the present study, only LAI is relevant, because the row structure is not explicitly treated in the inverse model.

110

Table 6.2 Measured canopy parameters on 11 and 21 April 2001 at the two field sites of the Quantitative Remote Sensing theory and application for Land Surface Parameters (QRSLSP) experiment.

Date	Site	Breed	LAI	Canopy Height (cm)	Distance Between row (cm)	Width of the wheat (cm)	Interval within wheat row (cm)
April, 11	C5	9210	1.7	9.5	15	7	8
April, 21	NW3	Jing 411	2.5	29	15	10.7	4.3

The leaf angle distributions were measured in the four selected fields (NW1, NW4, C3 and C4) on three dates: 14 April, 24 April and 3 May 2001. The site NW3, where measurements of directional brightness temperature were made, was sowed with the same wheat breed (Jing 411) as the site NW4. Fig. 6.20 shows the measurements of the leaf angle distribution for the Jing 411 wheat, together with three typical distribution functions of leaf angle, i.e. erectophile, spherical and planophile. The shape of the observed LIDF is close to the erectophile type. Both LIDF, the erectophile and spherical ones, will be used in the validation of the inverse model and the results will be compared.
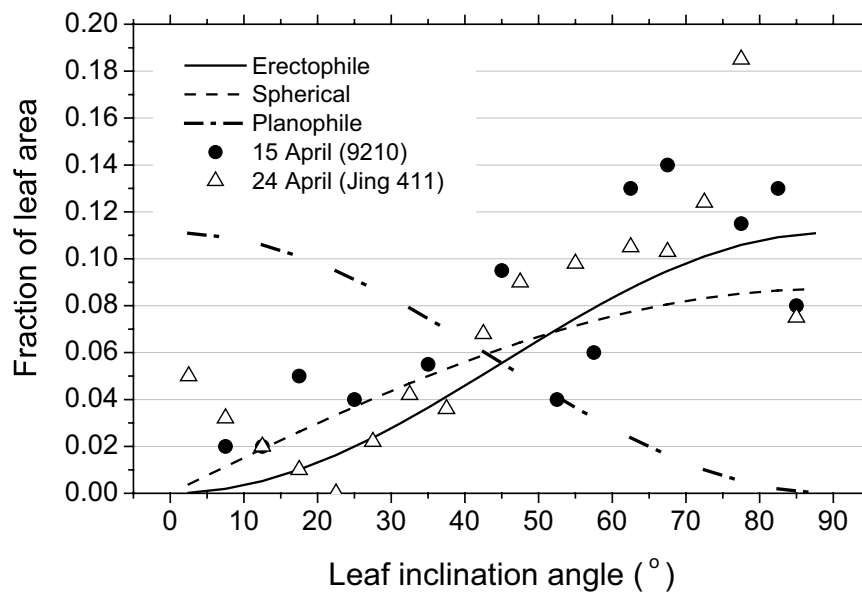
Figure 6.20 The leaf inclination function distribution LIDF as measured in the field at the QRSLSP experimental site and two standard ones, the erectophile and the spherical.

Since observations were done at 5 $^{\circ}$ intervals in θ_v, many different pairs of θ_v can be used to retrieve T_f and T_s. A smaller θ_v interval may not be sufficient, however, to have a difference in T_{b0} larger than the errors on T_{b0} as discussed in the sensitivity study (§6.2.4).

Therefore, T_f and T_s are inverted using the $T_{b0}(\theta_v, \varphi_v)$ when the difference in zenith view angles is larger than 10˚ and when the difference in $T_{b0}(\theta_v, \varphi_v)$ between two observing angles is larger than 0.5K (accuracy of the radiometer).

The emissivities for leaves and for soil are taken as 0.98 and 0.96 respectively. The downward atmospheric radiation $R_{atm}^{\downarrow}$ is calculated from the effective sky temperature measured in situ.

The foliage and soil component temperatures were calculated by inverting Eq.3.19 after determining $f_f(\theta_v)$ from Eq. 6.7. Both erectophile and spherical leaf angle are considered in the calculation of $f_f(\theta_v)$.

Figs. 6.21 shows the comparison between the observed component temperatures and retrieved ones on 11 and 21 April when erectophile LIDF is used in calculating $f_f(\theta_v)$. At each azimuth plane (0º, 180º, 90º and 270º), T_f and T_s are inverted using possible pairs of brightness temperature measurements, $T_{b0}(\theta_{v1}, \varphi_v)$ and $T_{b0}(\theta_{v2}, \varphi_v)$, where θ_{v1} and θ_{v2} are the two zenith view angles in the same azimuth plane.
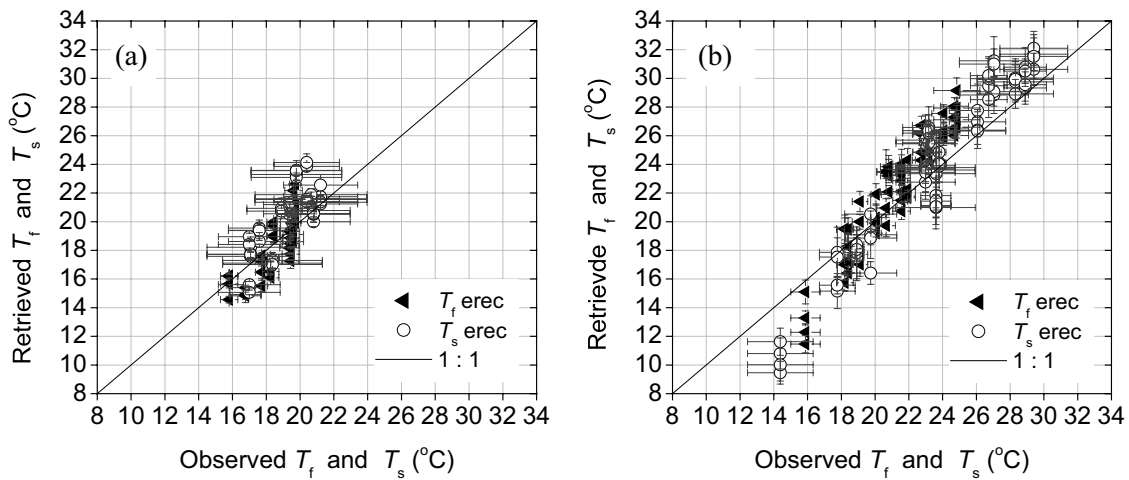
Figure 6.21 The comparison between observations and the soil and foliage component temperatures retrieved from paired measurements of [$T_{b0}(\theta_{v1}, \varphi_v)$, $T_{b0}(\theta_{v2}, \varphi_v)$] at the QRSLSP site. The results are the mean values of all inversion results over each plane at each hour on (a) 11 April 2001 with *LAI* as 1.7 and (b) 21 April 2001 with *LAI* as 2.5. The error bars for the observations are the standard deviation of the measurements taken during each run of goniometer observations (see §5.2.2). The error bars for the retrieved values are the standard deviations of T_f and T_s values using all pairs of [$T_{b0}(\theta_{v1}, \varphi_v)$, $T_{b0}(\theta_{v2}, \varphi_v)$] in each azimuth plane.

At first look, one gets the impression that in some cases the agreement between the inversion and the observation was not achieved while most of them compared well.

When we look at the details of the inversion by plotting results for each azimuth plane versus time (Fig. 6.22), it is interesting to see that the row structure and the sun have a combined impact on the retrieval, which is indicated by the regular shape of the inverted foliage temperature both in the early morning and in the late afternoon hours. As illustrated in Fig.6.22, the combined influence of the sun position and of the row structure lead to the steeper slope of the change in T_{b0} with the observation angle. More shaded leaves may be seen at larger θ_v, i.e. opposite to the sun position, for instance in the 270º azimuth plane in the morning hours, which in turn leads to underestimate foliage temperatures.

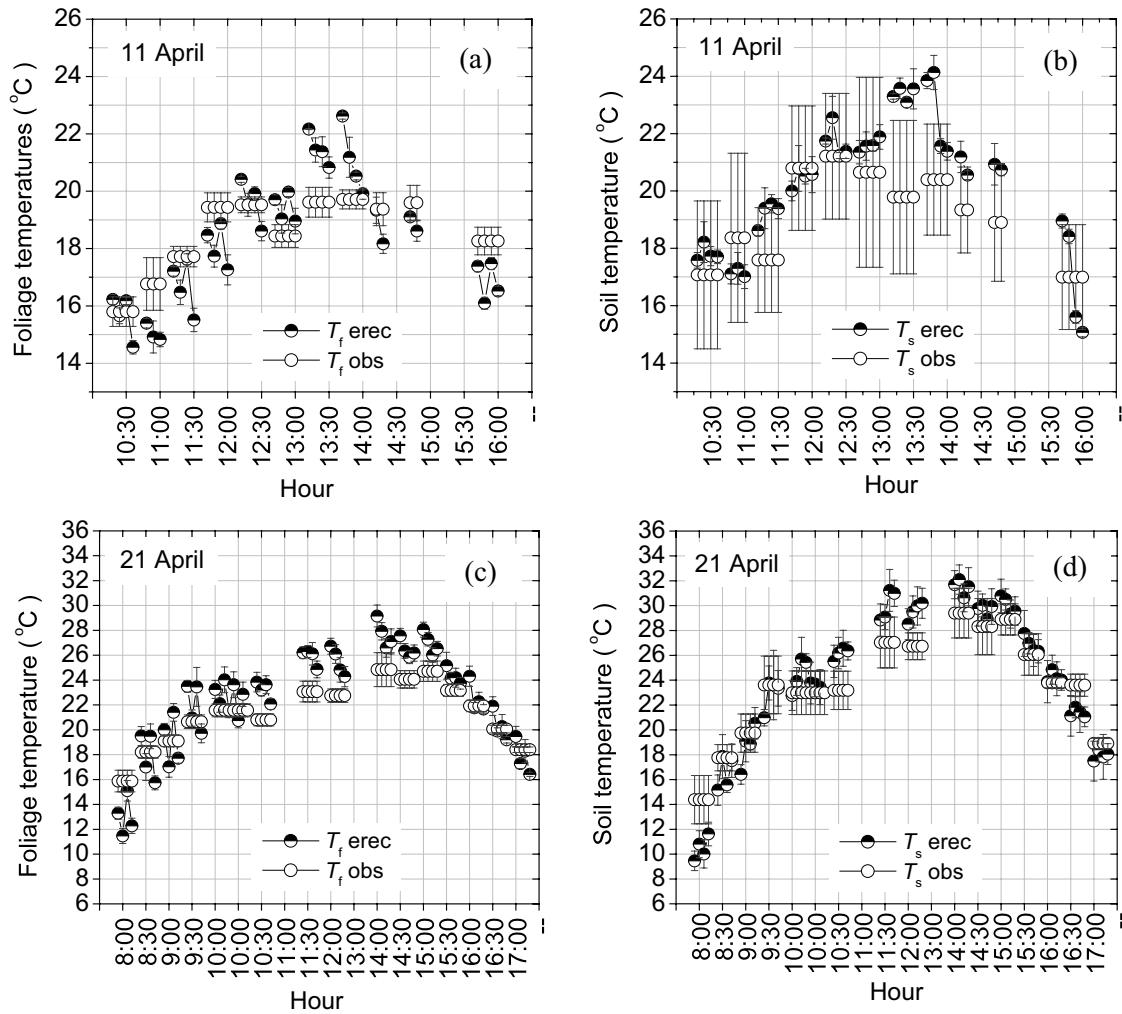**Figure 6.22** The comparison between observations and the inversions of foliage temperature T_f and soil temperature T_s (a) (b) on 11 April 2001 with LAI 1.7 and (c) (d) on 21 April 2001 with LAI 2.5 at the QRSLSP site. The results in each plane, in the sequence of 0º, 180º, 90º and 270º for each hour are plotted together with the observations. The error bars are the same as in Fig. 6.21.

When a spherical LIDF is assumed in the calculation of $f_f(\theta_v)$, larger errors appear between the observations and the retrievals as shown in Fig.6.23a. The inversion of Eq.3.19 gives smaller T_f and larger T_s on 11 April in general. The deviations both in the inverted T_f and in the inverted T_s are much larger compared with those when the erectophile LIDF is used to calculate $f_f(\theta_v)$ and in turn to retrieve T_f and T_s. The results are even worse for the inversion of T_s on 21 April while the comparison of T_f has a good agreement (Fig.6.23b). If the LIDF is not predicted correctly for the canopy under consideration, the weight of foliage and soil emittance in Eq.3.19 are not correct and inversion of the linear mixture model results in inaccurate estimates of T_f and T_s. As discussed in the §6.2.3, the retrieval of T_f and T_s are sensitive to errors in $f_f(\theta_v)$, in particular when the difference of fractional cover between nadir and off-nadir is small. The LIDF of the studied canopy may be closer to the erectophile one so that the assumption of spherical LIDF is not adequate. Actually, the shapes of these two LIDF are quite different (Fig.6.17) especially when the fractional cover is small which is consistent with the analysis in §6.2.3.
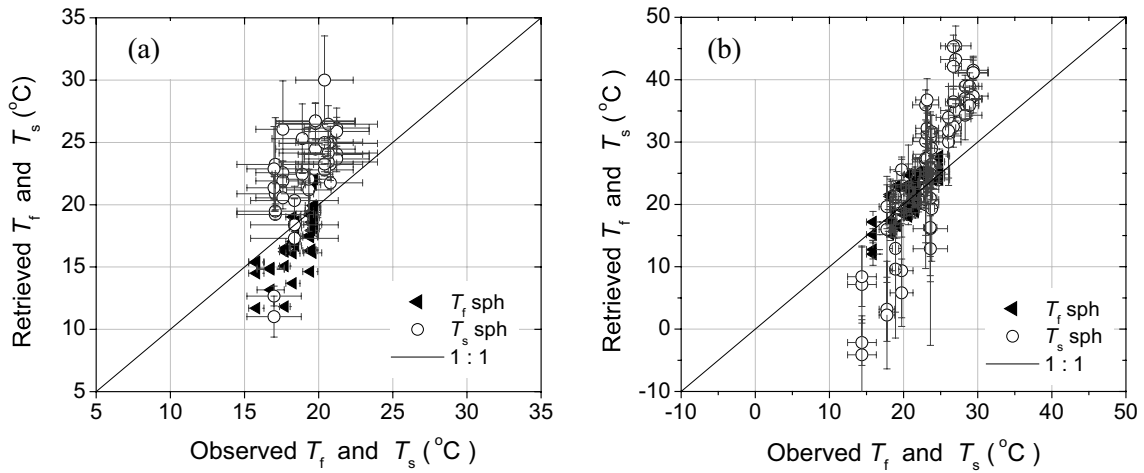
Figure 6.23 The same as Fig 6.21 but spherical LIDF is used to calculate $f_f(\theta_v)$ when inverting T_f and T_s.

Considering the deviation in the observations of T_f and T_s, particularly in T_s, the overall agreement as shown in Table 6.3 is good with RMSE 1.1 ºC and 1.4 ºC for T_f and T_s on 11 April, and 1.9 ºC and 2.0 ºC for T_f and T_s on 21 April. As one can see from Fig. 6.22, except for a few extreme cases, the retrievals of T_f and T_s fall into the range of the standard deviation of the observations. The inversion of Eq.3.19 has a better performance on 11 April than on 21 April. This is partly because that on 11 April lower LAI results in smaller impact

of the row structure so that the canopy can be considered as homogeneous, which is the assumption used in the linear mixture model.

Table 6.3 Summary of the comparison between the retrieval and the observation of T_f and T_s as expressed by RMSE when a different LIDF is assumed to calculate $f_f(\theta_v)$ at the QRSLSP site. 'Plane' indicates that RMSE is calculated using the retrieved T_f and T_s in each individual azimuth plane, while 'mean' represents the mean values of T_f and T_s over the four planes (0°, 180°, 90° and 270°) at each hour was calculated first, hereafter used to calculate the RMSE.

Date	RMSE of T_f (K)				RMSE of T_s (K)			
	Erectophile		Spherical		Erectophile		Spherical	
	Plane	Mean	Plane	Mean	Plane	Mean	Plane	Mean
11 April 2001	1.2	1.1	1.5	1.4	1.9	1.4	2.1	2.1
21 April 2001	3.4	1.9	3.4	0.7	3.6	2.0	9.5	9.1

6.4   Summary and conclusions

In this chapter, the anisotropy of $T_{b0}(\theta_v, \varphi_v)$ was evaluated using data collected during two field experiments (see Chapter 5) with different land surface types: mixture of short grasses in IMGRASS and winter wheat in QRSLSP, which leads to the following conclusions:

- Significant changes in T_{b0} with θ_v are observable with magnitudes larger than the measurements errors for the two land surface types (IMGRASS and QRSLSP).

- The structure of the canopy has an important impact on the angular change in T_{b0} when the measurements of T_{b0} at different φ_v in combination with the row direction and the sun position are analyzed.

- With the row structure canopy at the QRSLSP site, the field observations and the model simulations bring to the consistent conclusion that the LAI and soil water content are the two main factors determining the magnitude and the shape of $T_{b0}(\theta_v, \varphi_v)$. The LAI together with the canopy structure determines the radiation field and heat exchange within the canopy, while the soil water content determines the partitioning of the absorbed energy by the canopy, hereafter controlling the foliage and soil temperatures and therefore the angular change in T_{b0}.

Second, the sensitivity of the simple linear mixture model (Eq.3.19) to the measurements of T_{b0} and the estimation of fractional cover of vegetation $f_f(\theta_v)$ was investigated. The

results show that retrievals of T_f and T_s by inverting Eq.3.19 are quite sensitive to both T_{b0} and to $f_f(\theta_v)$ when the difference of $f_f(\theta_v)$ between nadir and off-nadir is small, which can arise from either the two angles being too close or from the canopy LIDF, e.g. the planophile type of LIDF leads to a small change in $f_f(\theta_v)$ with θ_v. However, a larger difference of $f_f(\theta_v)$ between nadir and off-nadir zenith view angle leads to less sensitivity of the retrieved T_f and T_s both to T_{b0} and to $f_f(\theta_v)$. This implies that measurements of T_{b0} at two very different θ_v are preferred to obtain more accurate retrievals of T_f and T_s.

The retrievals of T_f and T_s were evaluated using the same datasets from IMGRASS and QRSLSP field experiments. The canopy structure had a large impact on the retrieval. The retrievals of T_f and T_s using the directional measurements of T_{b0} along the row direction were in good agreement with the measurements than when using measurements of T_{b0} across the row direction. Besides, using different LIDF types to estimate $f_f(\theta_v)$ had a significant impact on the retrievals of T_f and T_s. Inadequate choice of the LIDF caused larger errors on the retrievals of T_f and T_s. This is consistent with the conclusion from the sensitivity study. In general, the retrieved T_f and T_s were in very goo agreement with the measurements: RMSE = 1.1 K for T_f and 1.4 K for T_s on 11 April. Slightly larger RMSE was found on 21 April: 1.9 K for T_f and 2.0 K for T_s.

Chapter 7

Retrieval of soil and foliage temperatures using bi-angular TIR measurements from space

7.1 Outline of the algorithm

A linear mixture model of a foliage-soil system and its inversion to determine the foliage and soil component temperatures was described in Chapter 3 and the validation of this method using field measurements of $T_{b0}(\theta_v, \varphi_v)$ made in two experiments with different land surface types was illustrated in Chapter 6. Agreement of retrieved T_f and T_s with observations was good. To apply this inversion model to multi-spectral and bi-angular Top-Of-Atmosphere (TOA) measurements by space-borne instruments such as ATSR-2, several pre-processing steps are needed to obtain the TOC variables required in Eq. 3.19. The ATSR-2 measures TOA radiance, atmospheric corrections are therefore needed to obtain the TOC radiance for each spectral channel. Moreover, theoretical or empirical algorithms are needed to retrieve fractional vegetation cover using ATSR-2 observations. Besides, the footprints of ATSR-2 measurements at nadir and off-nadir view angles are significantly different and both are much larger than the footprint of the radiometer used in the field measurements. This implies that different targets may be seen by the sensor in nadir and forward view and this will add noise to the observed angular change in $T_{b0}(\theta_v, \varphi_v)$. The latter leads to the problem that radiance from a ATSR-2 pixel is originated by a mixture of elements with different thermal properties due to the heterogeneity within a pixel.

To cope with all these potential problems, a general scheme of inverting component temperatures using ATSR-2 measurements was constructed as shown in Fig. 7.1, containing the following procedures:

(1) *Atmospheric correction*, which includes the retrieval of water vapor and of aerosol optical depth of the atmospheric column between the satellite and the land surface. Atmospheric correction needs to be applied in the VIS, NIR, SWIR and TIR domains to obtain the reflectances and brightness temperature at TOC.

(2) *Estimation of fractional cover of vegetation* using ATSR-2 measurements in VIS, NIR and SWIR channels.

(3) *Spatial Smoothing* will resample $f_f(\theta_v)$ and $T_{b0}(\theta_v)$ to remove the effect due to the different footprint between nadir and forward views.

(4) *Separation of soil and foliage component temperatures* by inverting Eq. 3.19.

The detailed description of these five procedures is given in the following sections. The characteristics of ATSR-2 instruments were given in §5.3.3.
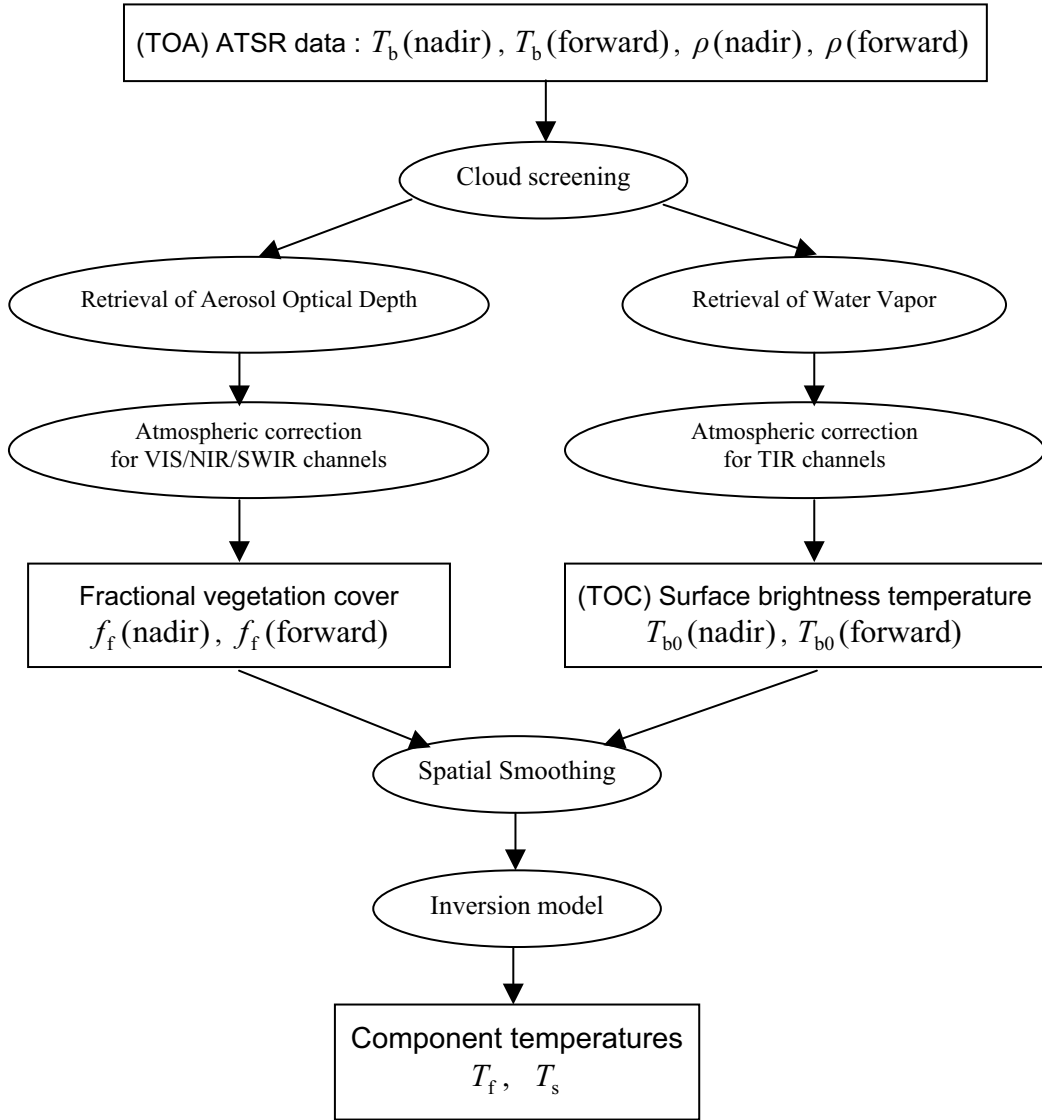
Figure 7.1 Scheme of the operational algorithm for retrieval of T_f and T_s from ATSR multi-spectral and dual-angular measurements. T_b is the brightness surface temperature at TOA measured by TIR channels of ATSR-2; ρ is reflectance at TOA measured by the VIS/NIR/SWIR channels of ATSR-2.

7.2   Cloud screening

The cloud-screening algorithm is based on the threshold method proposed by Saunders and Kriebel (1988) and is adapted to ATSR-2. Threshold values are subjectively determined for each image based on ATSR-2 visible and infrared data. Moreover, pixels in which the TIR detectors of ATSR-2 are saturated (approximately > 319 K) are screened out. Finally

118

water pixels are screened out, since the separation of soil and foliage temperatures is not relevant in these cases.

7.3 Atmospheric corrections of ATSR-2 observations

7.3.1 Column water vapor determination

Column water vapor content in the atmosphere, W, plays an important role in the atmospheric corrections in the visible, near infrared and thermal infrared channels. The knowledge of water vapor in the atmosphere allows to improve the accuracy of the remotely sensed surface variables (Sobrino et al. 1994, Francois and Ottle 1996). Because water vapor varies rapidly in time and space, the radiosoundings made at one place and at one time are generally not representative for the entire image. It is therefore desirable to retrieve water vapor content directly from satellite data.

A new approach was developed to retrieve water vapor content using the two split-window measurements of ATSR-2 at the two view zenith angles. A brief description about the methods is given here (see details in Li et al., 2003).

Principle of the Method

On the basis of radiative transfer theory, for a cloud-free atmosphere under local thermodynamic equilibrium, the radiance R_i measured from space in channel i at the zenith view angle θ_v may be written with good approximation as (Becker and Li, 1990)

$$R_i(\theta_v) = B_i\big(T_{bi}(\theta_v)\big) = \varepsilon_i(\theta_v)B_i(T_0)\tau_i(\theta_v) + R^{\uparrow}_{atm,i}(\theta_v) + \big(1-\varepsilon_i(\theta_v)\big)R^{\downarrow}_{atm,i}\tau_i(\theta_v) \qquad (7.1)$$

where $T_{bi}(\theta_v)$ is the brightness temperature in channel i at TOA and at θ_v, $\varepsilon_i(\theta_v)$ and $\tau_i(\theta_v)$ are the directional surface emissivity and total atmospheric transmittance in channel i at θ_v, T_0 is the TOC temperature, $R^{\uparrow}_{atm,i}(\theta_v)$ is the atmospheric upwelling radiance at θ_v and $R^{\downarrow}_{atm,i}$ is the downwelling hemispheric atmospheric radiance in channel i divided by π.

Under the condition that the $\tau_i(\theta_v)$ and $\varepsilon_i(\theta_v)$ are constant in space or that the effects of their spatial variation are not larger than the combined effects of instrument noise over the N neighboring pixels and of the linear approximation Eq. 7.1, the spatial variation of radiance measured from space in channel i at θ_v due to the spatial variation of surface temperature can be expressed as

$$B_i\big(T_{bi,k}(\theta_v)\big) - B_i\big(\overline{T_{bi}}(\theta_v)\big) = \varepsilon_i(\theta_v)\tau_i(\theta_v)\big(B_i(T_{0,k}) - B_i(\overline{T_0})\big) \qquad (7.2)$$

where the subscript k denotes pixel k and $\overline{T_{bi}}$ and $\overline{T_0}$ are the mean (or the median) TOA brightness temperature and the mean (or the median) TOC temperature over N neighboring pixels of pixel k, respectively. Since the total number of lines (m) and columns (n) constituting N pixels ($N = m \times n$) is generally small ($n, m \leq 50$), the variation $\Delta\theta_v$ of θ_v is very small over the N pixels ($\Delta\theta_v \leq 4°$ for AVHRR and ATSR-2). Thus, the view angle θ_v can be considered as constant over the N neighboring pixels; for simplicity, the dependence on view angle in Eq. 7.2 will be omitted in the text below.

Considering the first-order Taylor series of the Planck function $B_i(T)$ around some mean temperature $\overline{T}$ in the form

$$B_i(T) \cong B_i(\overline{T}) + \frac{\partial B_i(\overline{T})}{\partial T}(T - \overline{T}) \tag{7.3}$$

Eq. 7.2 can be linearized and expressed in terms of temperature differences as:

$$\left(T_{bi,\,k} - \overline{T_{bi}}\right) = \varepsilon_i \tau_i \left(T_{0,\,k} - \overline{T_0}\right) \tag{7.4}$$

By analogy, for measurements in channel j, one has

$$\left(T_{bj,\,k} - \overline{T_{bj}}\right) = \varepsilon_j \tau_j \left(T_{0,\,k} - \overline{T_0}\right) \tag{7.5}$$

Dividing Eq. 7.5 by Eq. 7.4 gives

$$\left(T_{bi,\,k} - \overline{T_{bi}}\right)\frac{\tau_j}{\tau_i}\frac{\varepsilon_j}{\varepsilon_i} - \left(T_{bj,\,k} - \overline{T_{bj}}\right) = 0 \tag{7.6}$$

or

$$\left(T_{bj,\,k} - \overline{T_{bj}}\right)\frac{\tau_i}{\tau_j}\frac{\varepsilon_i}{\varepsilon_j} - \left(T_{bi,\,k} - \overline{T_{bi}}\right) = 0 \tag{7.7}$$

If the assumption made above holds for N neighboring pixels, then by least-squares analysis of Eqs.7.6 and 7.7, the transmittance ratios in two channels, τ_j/τ_i, and its reciprocal τ_i/τ_j, can be respectively derived from

$$\frac{\tau_j}{\tau_i} = \frac{\varepsilon_i}{\varepsilon_j} R_{ji} \quad \text{with} \quad R_{ji} = \frac{\sum\limits_{k=1}^{N}\left(T_{bi,\,k} - \overline{T_{bi}}\right)\left(T_{bj,\,k} - \overline{T_{bj}}\right)}{\sum\limits_{k=1}^{N}\left(T_{bi,\,k} - \overline{T_{bi}}\right)^2} \tag{7.8}$$

and

$$\frac{\tau_i}{\tau_j} = \frac{\varepsilon_j}{\varepsilon_i} R_{ij} \quad \text{with} \quad R_{ij} = \frac{\sum\limits_{k=1}^{N}\left(T_{bi,\,k} - \overline{T_{bi}}\right)\left(T_{bj,\,k} - \overline{T_{bj}}\right)}{\sum\limits_{k=1}^{N}\left(T_{bj,\,k} - \overline{T_{bj}}\right)^2} \tag{7.9}$$

It is worth to note that:

(1) The numerator and denominator at the right-hand side of these equations represent the covariance and the variance of the brightness temperature directly measured by the satellite. The transmittance ratios can be derived directly from satellite data provided that the emissivity ratio of two channels are known.

(2) Eq. 7.8 has the same form as the SWCVR method developed by Sobrino et al. (1994), however, operational use of this equation is different as shown below.

(3) Let r denote the linear correlation coefficient of two measurements T_{bi} and T_{bj}. From Eqs 7.8 and 7.9 the square of this linear correlation coefficient, r^2, is just the product of R_{ji} and R_{ij}, namely,

$$r^2 = \frac{\left(\sum\limits_{k=1}^{N}(T_{bi,\,k} - \overline{T_{bi}})(T_{bj,\,k} - \overline{T_{bj}})\right)^2}{\sum\limits_{k=1}^{N}\left(T_{bi,\,k} - \overline{T_{bi}}\right)^2 \sum\limits_{k=1}^{N}\left(T_{bj,\,k} - \overline{T_{bj}}\right)^2} = R_{ji} \times R_{ij} \tag{7.10}$$

and

$$r^2 = R_{ji} \times R_{ij} = \frac{\varepsilon_j \tau_j}{\varepsilon_i \tau_i} \times \frac{\varepsilon_i \tau_i}{\varepsilon_j \tau_j} = 1 \tag{7.11}$$

This indicates that the transmittance ratio can be derived from Eq. 7.8 or Eq. 7.9 only if the brightness temperatures T_{bi} and T_{bj} in the two split-window channels i and j over N pixels are perfectly correlated ($r = 1$) or almost perfectly correlated ($r \cong 1$). This constraint can be used to check whether the assumptions made in the derivation of Eq. 7.8 and Eq. 7.9 are fulfilled.

(4) With the aid of the hemispheric spectral reflectance measured in the laboratory (Salisbury and D'Aria 1992), emissivity ratios of channels 11μm and 12μm ($\varepsilon_{11}/\varepsilon_{12}$) are calculated using the channel filter functions of ATSR-2 for different types of natural surface materials including rocks, soils, vegetation, snow and water. The results show that $\varepsilon_{11}/\varepsilon_{12}$ is between 0.98 and 1.01 for soils, vegetation, snow and water. Because pixels at the scale of $1\,\text{km} \times 1\,\text{km}$ (like ATSR2 and AVHRR) are generally mixtures of different types of surfaces, in practice, this emissivity ratio is

assumed to be unity at this scale (which might be a good approximation for most surfaces), leading to

$$\frac{\tau_j}{\tau_i} \cong R_{ji}.$$ (7.12)

Emissivity ratios of channels 11 μm and 12 μm are far from unity for igneous and minerals rocks. For these types of surfaces, emissivity ratio correction in Eqs. 7.8 and 7.9 should be performed to get correctly the transmittance ratio. However, for meteorite and most of metamorphic and sedimentary rocks, emissivity ratios of channels 11μm and 12μm are between 0.98 and 1.01, therefore, Eq. 7.12 might be also a good approximation for these types of surfaces at a scale of $1\,km \times 1\,km$.

Relationship between transmittance ratio and water vapor content

The transmittance ratio, either simulated or estimated, provides a relative measure of water vapor content in the atmosphere. Thus the spatial distribution of the split-window channel covariance and variance ratio (SWCVR) gives an estimate of the relative horizontal variability in water vapor content in the atmosphere. In order to quantify this variability, it is necessary to establish a relationship between total column water vapor W and the transmittance ratio (τ_j/τ_i). If we take the channel 11 μm of ATSR2 as channel i and the channel 12 μm as channel j, the transmittance ratio is always less than unity, since the effect of water vapor in channel 12 μm is larger than that in channel 11 μm. The larger the water vapor content in the atmosphere, the smaller the transmittance ratio. Therefore, an inverse relationship exists between W and τ_j/τ_i.

Since the atmospheric absorption in the atmospheric window (10-12μm) is principally due to the water vapor continuum and its absorption coefficient generally depends on temperature and pressure, and particularly on the water vapor partial pressure (Clough et al. 1989, Theriaut et al. 1994; Ma and Tipping 1994, Clough 1995), it is difficult or plainly impossible to express explicitly these dependences in a simple form. Thus, at present, the relationship between the transmittance ratio and water vapor content is determined by regression analysis of simulated data. Channel transmittances are simulated using the widely used atmospheric transmittance/radiance computer code MODTRAN 4.0 (Beck et al. 1999) with ATSR2 filter response functions for each of 1761 atmospheric profiles covering a wide range of atmospheric conditions. These atmospheric profiles were carefully selected from a global radiosounding dataset and were initially used to provide initial guess for atmospheric profiles retrievals from satellite sounders (Chedin et al. 1985). These atmospheric profiles represent a worldwide set of atmospheric situations and can be used to derive the relationship

between W and τ_{12}/τ_{11} (subscripts 11, 12 denote channel 11μm and 12μm, respectively). The transmittance ratio τ_{12}/τ_{11} is then regressed against the total column water vapor content W for each one of the 1761 atmospheric profiles. Scatter diagrams and regression coefficients for ATSR2 at nadir view are shown in Fig. 7.2, which shows that for a given zenith view angle θ_v, total water vapor content in the atmosphere W is essentially linearly related to the ratio of the two split-window channel transmittances τ_{12}/τ_{11}. Quadratic and logarithmic fits were also tried, but they did not give better results.

Nadir View

slope=-13.662, offset=13.73
r^2=0.987,   Std dev=0.13
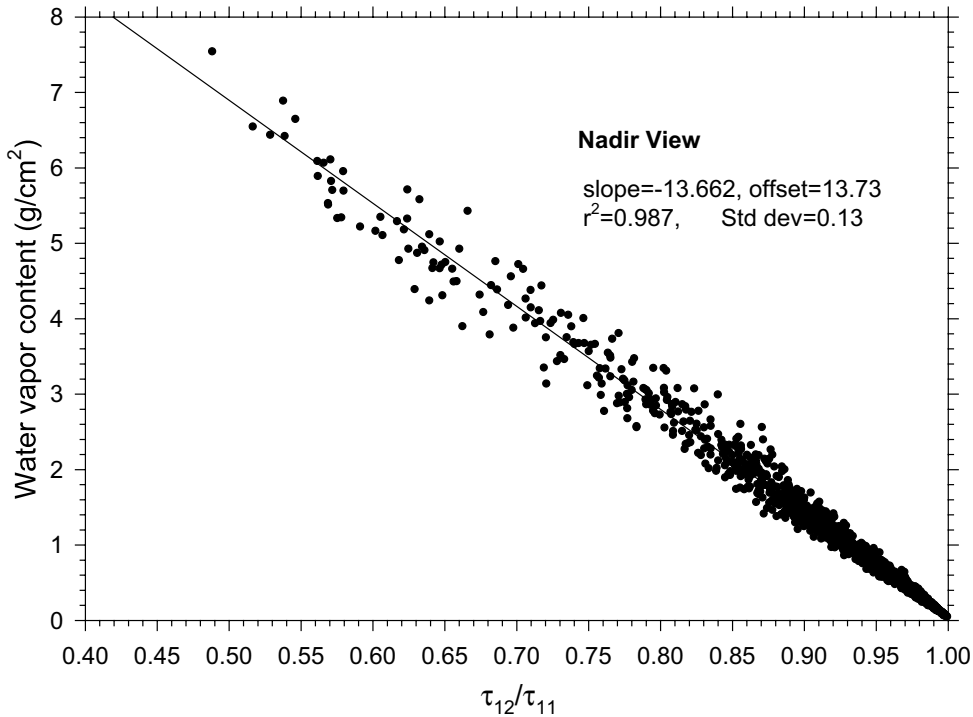
Figure 7.2 Water vapor content W plotted as a function of the transmittance ratio, τ_{12}/τ_{11}, for ATSR2 at near nadir view ($\theta_v \cong 10°$).

However, in this database, the majority of atmospheric profiles are very cold and dry and the statistics shown in Fig. 7.2 are dominated by the cases containing little water vapor. In order to check how accurate the linear regression given in Fig. 7.2, more moderate and moist atmospheric profiles should be added. Because there are no more atmospheric profiles available in the library used here, instead of including more moderate and moist atmospheres in the statistics, the dry atmospheres with water vapor content less than 10 kg/m^2 are excluded.

The variations of θ_v at the surface for both ATSR2 nadir and forward views are limited. The variation of θ_v over possible viewing geometries ranges from 0 ° to 22 ° for nadir view and from 52 ° to 55 ° for forward view of ATSR-2; while the range is from 0 ° to 69 ° for AVHRR and MODIS. The mean zenith view angle is used in our simulations: $\theta_v \cong 10°$ and $\theta_v \cong 53°$ for ATSR-2 nadir and forward views, respectively. From the linear regression analysis on the simulated data, for ATSR-2 near nadir view ($\theta_v \cong 10°$), we get

$$W = 13.85 - 13.48\, \tau_{12}/\tau_{11} \qquad (7.13)$$

with a correlation coefficient of 0.987 and a standard deviation error of estimate of 1.3 kg/m^2.

By analogy, for ATSR2 forward view ($\theta \cong 53°$), we get

$$W = 10.02 - 9.971\tau_{12}/\tau_{11} \qquad (7.14)$$

with a correlation coefficient of 0.986 and a standard deviation error of estimate of 1.3 kg/m^2.

It should be noted that

(1) The linear relationship (Eqs. 7.13 and 7.14) is only a first-order approximation of the relationship between W and τ_{12}/τ_{11}.

(2) The discrepancy between the water vapor predicted by the linear regression and the actual water vapor in Fig. 7.2 might result from the non-linear effect of the air temperature profile. This effect has been pointed out and discussed by Iwasaki (1994, 1999). Thus, to get more accurate water vapor content from the ratio of the two split window channel transmittances, the non-linear effect of air temperature profile must be taken into account (Iwasaki 1994).

Eqs. 7.13 and 7.14 are obtained and applied under the conditions that τ_{12}/τ_{11} ranges from 1.0 to 0.55 which correspond roughly to W from 0 to 60 kg/m^2, errors in W varies from – 0.7 to 0.7 kg/m^2 which is negligible compared with the other errors in the development and application of the method.

7.3.2 Retrieval of aerosol optical depth

Methods of atmospheric correction in the VIS through SWIR regions are generally concerned with the estimation of atmospheric effects associated with molecular absorption, molecular and aerosol scattering. Current methods for the estimation of atmospheric effects employ a radiative transfer model (Vermote et al. 1997, Beck et al. 1999) whose inputs are generally the vertically integrated gaseous contents, aerosol optical properties and geometric conditions.

Principle of the Method

If ρ_i^* is the reflectance measured in channel i at TOA, from radiative transfer theory the surface reflectance in channel i, ρ_i, can be expressed as (Rahman and Dedieu 1994, Vermote et al. 1997):

$$\rho_i(\theta_{s0},\theta_v,\Delta\varphi) = \frac{\rho_i^{ac}(\theta_{s0},\theta_v,\Delta\varphi)}{1+S_i\,\rho_i^{ac}(\theta_{s0},\theta_v,\Delta\varphi)} \tag{7.15}$$

with

$$\rho_i^{ac} = \frac{\rho_i^*(\theta_{s0},\theta_v,\Delta\varphi)\big/tg_i(\theta_{s0},\theta_v)-\rho_i^a(\theta_{s0},\theta_v,\Delta\varphi)}{\tau_i(\theta_{s0})\tau_i(\theta_v)} \tag{7.16}$$

where θ_{s0} is solar zenith angle, $\Delta\varphi$ is the relative azimuth angle between the sun and satellite direction, S_i is the spherical albedo of atmosphere in channel i, tg_i is the total gaseous transmittance in channel i associated with gaseous absorption along the sun-target-sensor atmospheric path, $\rho_i^a(\theta_{s0},\theta_v,\Delta\varphi)$ is the atmospheric reflectance, $\tau_i(\theta_{s0})$ and $\tau_i(\theta_v)$ are the total atmospheric transmittance along the sun-target and target-sensor atmospheric paths, respectively.

In general, independent measurements of atmospheric composition and aerosol optical properties are not available. It is therefore desirable to derive them directly from satellite data. The most important gases for atmospheric corrections in the VIS/NIR channels are water vapor and ozone. Water vapor content W in the atmosphere can be derived from the two split-window channel measurements as shown in §7.3.1, and ozone content is taken from climatological data. As for the determination of the aerosol optical properties, if the surface may be considered isotropic, then the difference in surface reflectance retrieved from multi-angle directions using Eq. 7.15 may be used to derive the atmospheric optical thickness if aerosol type is assumed. However, most land surfaces are far from Lambertian (Hapke, 1981). With multi-angle measurements, it is imperative to consider non-Lambertian reflectances. Several aerosol retrieval schemes for ATSR-2 have been proposed (Flowerdew and Haigh, 1997; Mackay and Steven, 1998; North et al, 1999). The iteration of a two step-process proposed by North et al., (1999) has been used in this study. The first step is to derive using Eq. 7.15 eight land surface reflectances $\rho_i(\theta_{s0},\theta_v,\Delta\varphi)$ from ATSR observations of TOA reflectance $\rho_i^*(\theta_{s0},\theta_v,\Delta\varphi)$ at four channels (0.55 μm, 0.65 μm, 0.87 μm, 1.60 μm) and two view angles (nadir and forward views), given an initial estimate of the atmospheric aerosol optical depth at 550nm τ_{550}^a. The second step is to fit a parametric bi-directional

reflectance model to the eight retrieved surface reflectances by minimization of the error metric function

$$E = \sum_{\theta_v=1}^{2} \sum_{i=1}^{4} \left[\rho_i(\theta_{s0}, \theta_v, \Delta\varphi) - \rho_i^m(\theta_{s0}, \theta_v, \Delta\varphi) \right]^2 \qquad (7.17)$$

where $\rho_i^m(\theta_{s0}, \theta_v, \Delta\varphi)$ is the land reflectance in channel i predicted by the parametric reflectance model.

Since there are at maximum eight land surface reflectance measurements, the land surface bi-directional model must have maximum seven model parameters so that there is at least one degree of freedom available for atmospheric parameter retrieval, for instance, the aerosol optical depth at 550 nm, τ_{550}^a. Assuming that the land surface is composed of opaque facets, each with Lambertian reflectance ω_i, and that separate parameters are required to describe the wavelength invariant three-dimensional structure of the surface and the spectral dependence of component spectra, North et al. (1999) developed a seven free parameters model: P nadir, P forward, γ and ω_i (i = 1, 2, 3 and 4):

$$\rho_i^m(\theta_{s0}, \theta_v, \Delta\varphi) = (1-D_i) P(\theta_{s0}, \theta_v, \Delta\varphi)\omega_i + \frac{\gamma\omega_i}{1-(1-\gamma)\omega_i}\left[D_i + (1-\gamma)\omega_i(1-D_i)\right] \qquad (7.18)$$

where D_i is the incident diffuse fraction of irradiance, which excludes the radiation scattered close to the solar beam direction. D_i can be estimated by means of a radiative transfer model for different combinations of sun position and aerosol optical depth. $P(\theta_{s0}, \theta_v, \Delta\varphi)$ is the geometric parameter dependent only on view and illumination directions. γ denotes the mean hemispherically integrated probability of escape of light without further interaction, after a scattering event at the land surface.

If there are no fewer than four channels available, an alternative scheme can be used to retrieve the aerosol optical depth by assuming that the functional shape of the bidirectional effects is invariant with respect to the wavelength within the visible and near-infrared region (Flowerdew and Haigh 1997; Mackay and Steven 1998):

$$\frac{\rho_i(\theta_{s0}, \theta_{v1}, \Delta\varphi)}{\rho_i(\theta_{s0}, \theta_{v2}, \Delta\varphi)} = \frac{\rho_j(\theta_{s0}, \theta_{v1}, \Delta\varphi)}{\rho_j(\theta_{s0}, \theta_{v2}, \Delta\varphi)} \qquad (7.19)$$

This relationship gives a constraint for atmospheric correction by forcing the retrieved bidirectional reflectance to have a consistent angular variation, even though the magnitude of the reflectance may vary greatly.

The aerosol optical thickness is therefore obtained through the minimization of the error metric function

126

$$E = \sum_{i=1}^{n} \sum_{j>i}^{n-1} \left[\frac{\rho_i(\theta_{s0}, \theta_{v1}, \Delta\varphi)}{\rho_i(\theta_{s0}, \theta_{v2}, \Delta\varphi)} - \frac{\rho_j(\theta_{s0}, \theta_{v1}, \Delta\varphi)}{\rho_j(\theta_{s0}, \theta_{v2}, \Delta\varphi)} \right]^2 \tag{7.20}$$

where n is the total number of channels available, i and j are channel numbers.

Implementation of the method

Retrieval of the aerosol optical depth is performed by averaging the TOA data for a box of 10×10 pixels to minimize noise and the effect of misregistration between the two views and to reduce the computing time. Given an initial estimate of aerosol optical depth at 550 nm (or aerosol loading), τ_{550}^a, the water vapor content W retrieved as described in 7.3.1 and the climatological ozone content, initial estimates of land surface reflectances are obtained by the inversion of the atmospheric model 6S (Second Simulation of the Satellite Signal in the Solar Spectrum, Vermote et al. 1997) for each set of ATSR-2 observations. The degree of fit of this set of reflectances to the land surface bi-directional reflectance model (Eq. 7.18) gives an error matrix as shown in Eq. 7.17, which is minimized using the Levenberg-Marquardt algorithm (Press et al. 1989) with simple bounds on variables ($0.1 \leq \tau_{550}^a \leq 0.7$, $0 \leq \rho_i \leq 1.0$).

7.3.3 Atmospheric corrections in the visible and near infrared channels

Knowing W and τ_{550}^a, the atmospheric correction is performed on a pixel by pixel basis to get the land surface reflectances for all visible and near infrared channels and for all viewing angles. It should be noted that for pixels which are assessed as cloud – free, but where water vapor and aerosol loading cannot be retrieved, atmospheric correction is performed with the mean water vapor content and mean aerosol loading over the whole image.

7.3.4 Atmospheric corrections in the TIR channels using the Split Window method

If the TOC brightness temperature T_{b0} is, or can be assumed, independent of the channels used to measure it, the Split Window (SW) method [e.g. Sobrino et al., 1994 among others] can be used to obtain T_{b0}. Following the procedure developed by Becker and Li [1995], a general SW algorithm is derived for ATSR-2 nadir and forward views using the simulation data from MODTRAN 4.0,

$$\begin{aligned} T_{b0}(\theta_v) = &\left[a(\theta_v) + b(\theta_v)W \right] + \left[c(\theta_v) + d(\theta_v)W \right] T_{11}(\theta_v) \\ &+ \left[e(\theta_v) + f(\theta_v)W \right] \left[T_{11}(\theta_v) - T_{12}(\theta_v) \right] \end{aligned} \tag{7.21}$$

First a large range of surface and atmospheric conditions is taken as a reference scenario: $W \leq 45$ kg/m^2, 272K $\leq T_a \leq 311$K and -5 K $\leq T_{b0} - T_a \leq 15$K. Next the T_{11} and T_{12} at TOA are computed using the radiative transfer model MODTRAN 4 for each combination of these variables, obtaining a synthetic data set. Finally the coefficients $a \sim f$ in Eq. 7.21 are determined by a multi – linear regression analysis. This was done separately for the ATSR-2 nadir and forward views (see Table 7.1).

Table 7.1 The coefficients of the Split-Window method (Eq. 7.21) to determine $T_{b0}(\theta_v)$ from ATSR-2 thermal infrared channels at nadir and forward view angles. σ is the root mean square (RMS) residual of $T_{b0}(\theta_v)$ retrieval.

	a	b	c	d	e	f	σ (K)
Nadir	-4.89	3.74	1.0205	-0.0151	0.916	0.509	0.10
Forward	-14.41	8.51	1.0582	-0.0343	0.565	0.857	0.24

Given the water vapor content in the atmosphere, $T_{b0}(\theta_v)$ is directly derived on a pixel-by-pixel basis with Eq. 7.21 for both nadir and forward views. As in 7.3.2, for clear pixels in a 10×10 box in which water vapor content is not available, the mean water vapor content in the whole image is used in Eq. 7.21.

7.4   Estimation of fractional vegetation cover

As described in chapter 6 fractional vegetation cover can be estimated by means of Beer's law (Eq. 6.7) knowing *LAI* and *LIDF*. On the one hand, information for a specific *LIDF* may not be findable in the ATSR-2 spatial resolution of 1 km since it is quite possible to have different vegetation types in an ATSR pixel. On the other hand, multi-angular and hyperspectral information may needed to retrieve simultaneously all the relevant canopy variables, which unfortunately is not available yet from current space sensors. A stepwise multiple linear regression was therefore proposed in this study to estimate the fractional vegetation cover $f_f(\theta_v)$ using TOC reflectances $\rho_i(\theta_s, \theta_v, \Delta\varphi)$. The stepwise multiple linear regression is written

$$f_f(\theta_v) = a_0(\theta_{s0}, \theta_v) + \sum_{i=1}^{n} a_i(\theta_{s0}, \theta_v) \rho_i(\theta_{s0}, \theta_v, \Delta\varphi) \qquad (7.22)$$

where *n* is the number of channels used. The model OSCAR (Verhoef 1998) has been applied to generate TOC reflectances for an ensemble of canopy and atmospheric conditions and for the viewing and illumination conditions applying to the ATSR-2 observations used in this study. OSCAR stands for Optical Soil-Canopy-Atmosphere Radiance and is a coupled model

based on four-stream radiative transfer theory. It includes the model SAILH (i.e. the SAIL model with the hot spot effect modeled according to Kuusk 1985) and a simple model of atmospheric bi-directional scattering. The OSCAR model includes the atmospheric adjacency effect and therefore the properties of the surroundings of the target pixel need to be specified. Strictly speaking OSCAR is a turbid medium model, as in SAILH the hot spot effect related to the finite leaf size is parameterized.

Reflectances at TOC in the three optical bands (green, red and NIR) have been simulated for nadir view and for $\theta_v = 53°$. The relative azimuth angle was estimated to be 120°.

The reflectance data base constructed in this way is used to determine the coefficients a_i in Eq. 7.22, which apply to the ensemble of conditions simulated with OSCAR. These conditions comprise the variation over ten LAI values, three leaf inclination distribution function (LIDF), four hot spot parameters, four types of leaf (leaf spectral reflectance), four types of soil, four surroundings which consist of a simple description of the terrain surrounding the target, three atmospheric visibilities and five solar zenith angles (see Table 7.2). The LAI values range from 0 to 6. The three LIDFs are representative for moderately planophile (most leaves having 25° inclination), plagiophile (most leaves having 45° inclination) and moderately erectophile (most of leaves having 65° inclination) canopies, respectively. The hot spot size parameter q is the ratio of the horizontal correlation length of leaf projection and the height of the canopy layer. The q values are taken as 0.05, 0.10, 0.20 and 0.50. Spectrally different leaf types were taken from the literature (Gausman et al., 1978). Spectral reflectance data of four soil types were taken from atmospherically corrected Landsat Thematic Mapper images of the Netherlands (1986), supplemented with data for the spectral band at 1250 nm. The three atmospheric visibility conditions were taken as 5, 10, and 40 km (see Verhoef 1998, Verhoef and Menenti 1998, Verhoef 2001 for the details).

For all combinations of the above conditions (115 200 cases in total) the reflectance was computed in the three ATSR-2 bands centered at 0.55 μm, 0.65 μm and 0.87 μm in the two directions at TOC. Table 7.2 gives the values of regression coefficients between TOC $\rho_i(\theta_{s0}, \theta_v, \Delta\varphi)$ and $f_f(\theta_v)$ (see Eq. 7.22) at the selected θ_{s0} values and the correlation coefficients R^2 for the three ATSR-2 channels in the two directions. The coefficients for each ATSR-2 pixel are then obtained by interpolating the values in Table 7.2 according to θ_s for each pixel. Estimation of $f_f(\theta_v)$ is then performed on a pixel-by-pixel basis using Eq. 7.22.

Table 7.2 The regression coefficients in the stepwise multiple linear regression (Eq. 7.22) at different solar zenith angle θ_{s0}. The subscripts '1, 2, 3' in the coefficient a_i correspond to the three ATSR-2 channels centered at 0.55 μm, 0.65 μm and 0.87 μm at 0° and 53° zenith view angles. R^2 is the square of the correlation coefficient.

$\theta_s(°)$	$f_f(0)$					$f_f(53)$				
	a_0	a_1	a_2	a_3	R^2	a_0	a_1	a_2	a_3	R^2
15	0.1684	0.94	-3.79	1.46	92.0	0.2213	1.05	-4.26	1.50	90.3
30	0.1550	0.92	-3.84	1.51	92.3	0.2045	1.02	-4.21	1.54	91.2
45	0.1239	0.90	-3.79	1.58	92.7	0.1660	0.98	-4.05	1.59	92.6
60	0.0762	0.69	-3.53	1.67	93.0	0.1066	0.80	-3.67	1.65	93.7
75	0.0388	0.19	-3.12	1.75	92.6	0.0447	0.38	-3.14	1.71	93.9

7.5 Smoothing

The bi-angular ATSR-2 observations may be affected by co-registration errors and by the different footprint between nadir and forward views (Fig.7.3). To reduce the impact on the soil and foliage temperature separation, a local moving window filter of 5×5 pixels for the nadir image and of 3×3 pixels for the forward view image were applied over the whole image. The window size was chosen taking into account the different spatial resolution of nadir and forward views ($1\,\text{km}\times1\,\text{km}$ for nadir view, $1.5\,\text{km}\times2\,\text{km}$ for forward view).
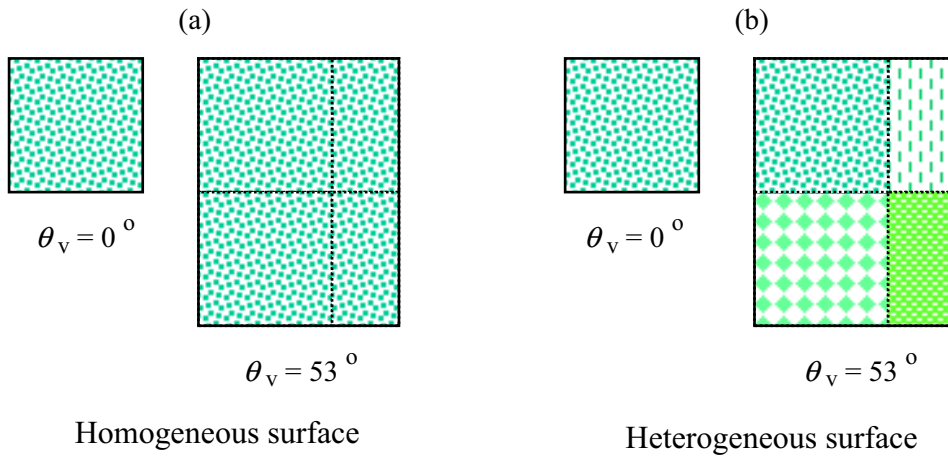

Figure 7.3 Spatial sampling effect due to the different footprint of pixel: (a) in nadir and (b) in forward view of ATSR-2.

7.6 Retrieval of soil and foliage component temperatures

Component temperatures of soil T_s and foliage T_f are derived from measurements at two zenith view angles, i.e. $T_{b0}(0)$ and $T_{b0}(53)$ of ATSR-2 using Eq. 3.19 by means of the Levenberg-Marquardt algorithm (Press et al. 1989) with simple bounds on variables. Cases with full vegetation cover and bare soil are treated separately.

Retrieval of T_s and T_f is not performed in the following abnormal situations: a) the difference of T_{b0} for nadir and forward view, $T_{b0}(0) - T_{b0}(53)$ is too large (>7.5K for instance) or b) the difference of T_{b0} is inconsistent with the difference of fractional vegetation cover.

Initial values of T_s and T_f are taken from the approximate solution of Eq. 3.19 with $B(T) \cong \sigma T^4$, the lower and upper bounds for T_s and T_f are their initial values minus and plus 5K, respectively. Eq. 3.19 is then solved to obtain T_s and T_f.

7.7 Results and discussions

7.7.1 Estimation of fractional vegetation cover

Fractional vegetation cover, $f_f(\theta_v)$, is derived by Eq. 7.22 using TOC reflectances $\rho_i(\theta_{s0}, \theta_v, \Delta\varphi)$ at i = 0.55μm, 0.65μm, and 0.87μm. Fig. 7.4 gives the histograms of $f_f(\theta_v)$ for several days over the study areas. In general, the surface over the EWBMS study area in Spain is characterized by relatively low $f_f(\theta_v)$ values compared with the SGP'97 area. Apparently, $f_f(\theta_v)$ in the forward view is generally larger than the one observed at nadir.

At the current stage, it is difficult to evaluate the accuracy of fractional vegetation cover estimated by Eq. 7.22 at the ATSR-2 pixel scale due to lack of detailed measurements of vegetation properties at such scale. An alternative way to evaluate the method was by utilizing a set of synthetic images (see §5.4) at relatively small pixel size such as the ones generated in the preparation of the SPECTRA mission (Menenti et al., 2003). In the preparatory study, a set of multi-angular hyperspectral imagery was generated over the area of Barrax in Spain. The simulation procedures were discussed by Verhoef and Bach (2003) for VIS/NIR/SWIR region and by Jia et al. (2001) for TIR region.

The TOC spectral reflectance was averaged over the (10, 11, 12), (20, 21, 22) and (41, 42, 43) channels of SPECTRA respectively to match the spectral bands of the ATSR-2 centered at 0.55 μm, 0.65 μm and 0.87 μm as indicated in Table 7.3.
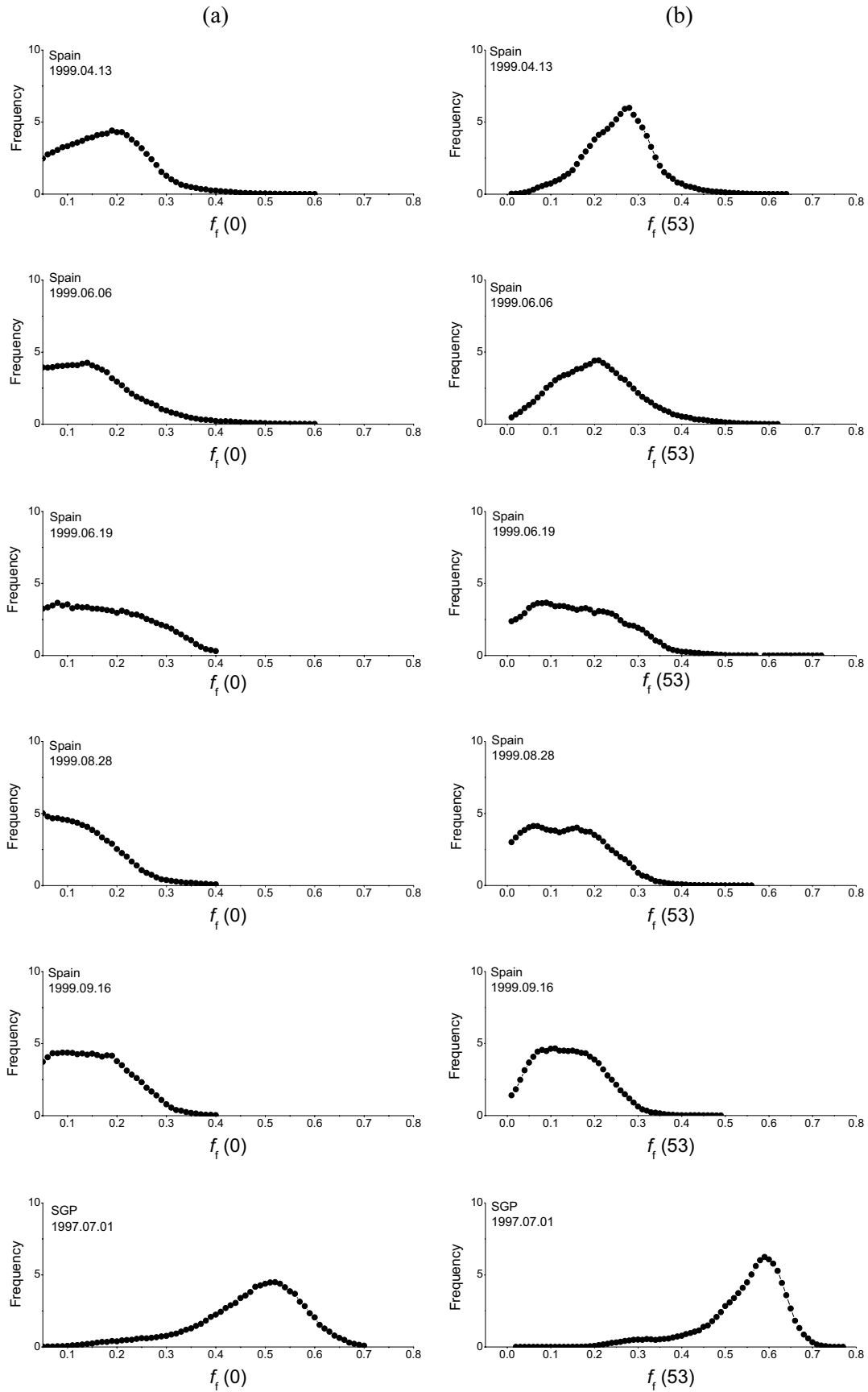
Figure 7.4 Histograms of fractional vegetation cover $f_f(\theta_v)$ estimated using the linear regression equation (Eq.7.22) for six studied images over EWBMS area (Spain) and SGP'97 area: (a) at nadir view; (b) at forward view.

Table 7.3 The spectral data of ATSR-2 visible and near infrared channels and the equivalent SPECTRA channels.

ATSR-2		SPECTRA	
Central wave-length (μm)	Full width at half maximum (μm)	Channel No.	Spectral range (μm)
0.55	0.543 - 0.565	10	0.54 - 0.55
		11	0.55 - 0.56
		12	0.56 - 0.57
0.65	0.647 - 0.669	20	0.64 - 0.65
		21	0.65 - 0.66
		22	0.66 - 0.67
0.87	0.853 - 0.875	41	0.85 - 0.86
		42	0.86 - 0.87
		43	0.87 - 0.88

The land use in the Barrax site was grouped into 5 vegetation types, i.e. corn, barley, alfalfa, dry crops and forest. Dry crops were almost dominated by brown leaves and do not contribute to the green fractional cover, it is therefore not taken into account in this validation. The 'forest ' type of vegetation is present in a very small fraction of the area and mostly as windbreak, which will not be considered as well. Consequently, three vegetation types with erectophile and uniform leaf inclination distribution as represented by their a and b parameters as used in SAIL (Verhoef, 1997) were retained in the validation of green fractional vegetation cover. Table 7.4 gives the values of a and b parameters for each of the three LID types. These LIDF parameters are used together with the LAI map over the Barrax site to produce maps of $f_f(\theta_v)$ at $\theta_v = 0°$ and 53° zenith angles based on Beer's law as given by Eq. 6.7 at each θ_v. The maps of $f_f(0)$ and $f_f(53)$ will be taken as a reference for the validation and is referred to as 'reference fractional vegetation cover', or 'reference $f_f(0)$' and 'reference $f_f(53)$'.

Table 7.4 The vegetation parameters used to simulate multi-angular TIR images.

		Corn $h_c = 0.9$ m	Barley $h_c = 0.8$ m	Alfalfa $h_c = 0.5$ m
LIDF	a	-0.65	-0.85	0.00
	b	-0.15	-0.15	-0.15
Average leaf angle (°)		68.7	76.0	45.0
Standard leaf angle (°)		18.5	13.7	23.6

By applying the regression equation for $f_f(\theta_v)$ (Eq. 7.22) to the TOC reflectances in the three equivalent ATSR-2 bands groups (Table 1) at $\theta_v = 0°$, 45° and 60 ° (the mean reflectance of the latter two view angles was taken as the reflectance at $\theta_v = 53°$ of ATSR-2), the fractional vegetation cover $f_f(\theta_v)$ at $\theta_v = 0°$ and 53° were calculated and compared with the reference ones in Fig. 7.5. The regression Eq.7.22 works rather well when vegetation is green, i.e. corn and alfalfa, while slightly larger errors appear for vegetation with some fraction of brown leaves, like barley at this time of the year (DOY = 179). Table 7.5 gives the summary of the model performance represented by RMSE and Absolute Difference (AD) for each case and for the total dataset.

As a summary, if the regression coefficients determined with the OSCAR model (Eq.7.22) could be produced from a specific database designed to be closer to the actual situation of the area concerned, one can expect that Eq.7.22 would give a reliable estimation of $f_f(\theta_v)$.
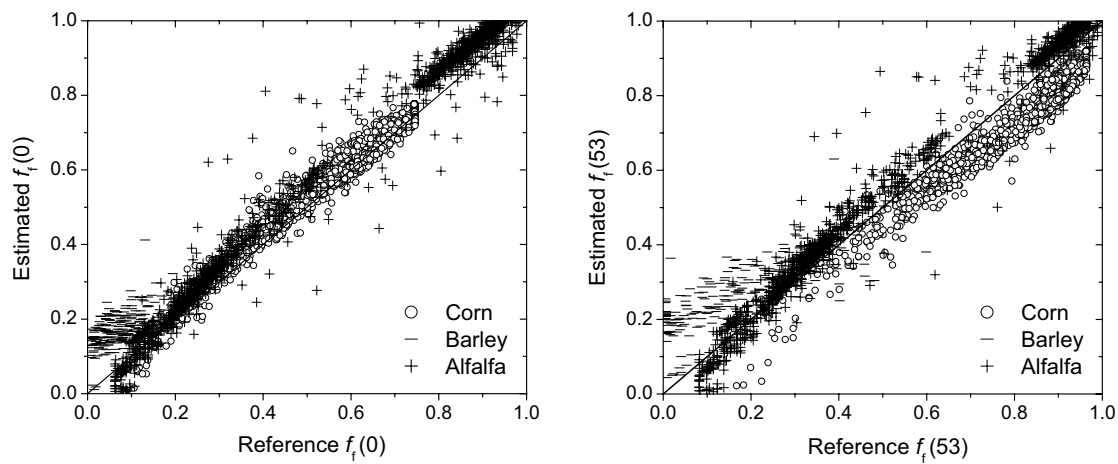
Figure 7.5 The comparison of fractional vegetation cover as estimated by the regression equation Eq. 7.22 with the reference values at (a) nadir zenith view and (b) forward 53° over Barrax simulation site.

Table 7.5 Performance of the regression equation for estimating fractional vegetation cover (Eq. 7.22): as Root Mean Square Error (RMSE) and Absolute Difference (AD) at nadir and forward 53° for each vegetation type. 'Total' indicates the overall performance over the entire simulation dataset.

Vegetation	$\theta_v = 0°$		$\theta_v = 53°$	
	RMSE	AD	RMSE	AD
Corn	0.0339	0.025	0.1038	0.103
Barley	0.1086	0.109	0.0745	0.073
Alfalfa	0.0327	0.030	0.0515	0.049
Total	0.0456	0.046	0.0785	0.076

7.7.2 Retrieval of soil and foliage temperatures

Soil and foliage component temperatures are derived from Eq.3.19 with vegetation cover, $f_f(\theta_v)$, estimated using Eq. 7.22. Soil and foliage emissivities are needed to solve T_f and T_s from Eq.3.19. These values are simply taken as $\varepsilon_s = 0.95$ and $\varepsilon_f = 0.98$. Variability of ε_f in the ATSR spectral bands used in this study is very limited and our assumption does not lead to large errors. Changes in ε_s are somewhat larger, although still rather small and different values might be used if available. Fig. 7.6 shows the histograms of the retrieved T_f and T_s over EWBMS (Spain) and SGP'97 study areas.

Over the Spain area $f_f(\theta_v)$ is relatively small with a peak value smaller than 0.2, mostly smaller than 0.1. As discussed in the sensitivity study in Chapter 6, the retrieval of T_f is more sensitive to $f_f(\theta_v)$ both in nadir and forward zenith view angles when $f_f(\theta_v)$ is relatively small and the difference between T_s and T_f is large. As shown in Fig. 7.7, the peak of (T_s - T_f) in the histogram appears around 20 degrees for most of the cases which is the most sensitive case as illustrated in Fig. 6.14 ($dT = 20K$, $f_{nd} = 0.1$) and 0.05 errors in the estimation of $f_f(\theta_v)$ will bring about 8 K errors in T_f if the difference between nadir $f_f(\theta_v)$ and the forward $f_f(\theta_v)$ is as small as 0.1. On the other hand, the retrieval of T_s is much less sensitive to the errors in $f_f(\theta_v)$ under the same condition as illustrated in Fig. 6.16, about 1 K errors in T_s with 0.05 errors in the estimation of $f_f(\theta_v)$. In the SGP'97 area, $f_f(\theta_v)$ is relatively large with a peak at about 0.4 - 0.5 for nadir and 0.5 - 0.6 for forward angle. Under such surface cover condition, the sensitivity of T_f to $f_f(\theta_v)$ is moderate and the sensitivity of T_s to $f_f(\theta_v)$ is the largest case as shown in Figs. 6.14 and 6.16.

Summarizing the discussions above, under the surface conditions of the Spain area with smaller fractional cover of vegetation, the retrieval of T_s is less sensitive to the estimation of $f_f(\theta_v)$, while the different methods for estimating $f_f(\theta_v)$ result in a large bias in the retrieval of T_f.
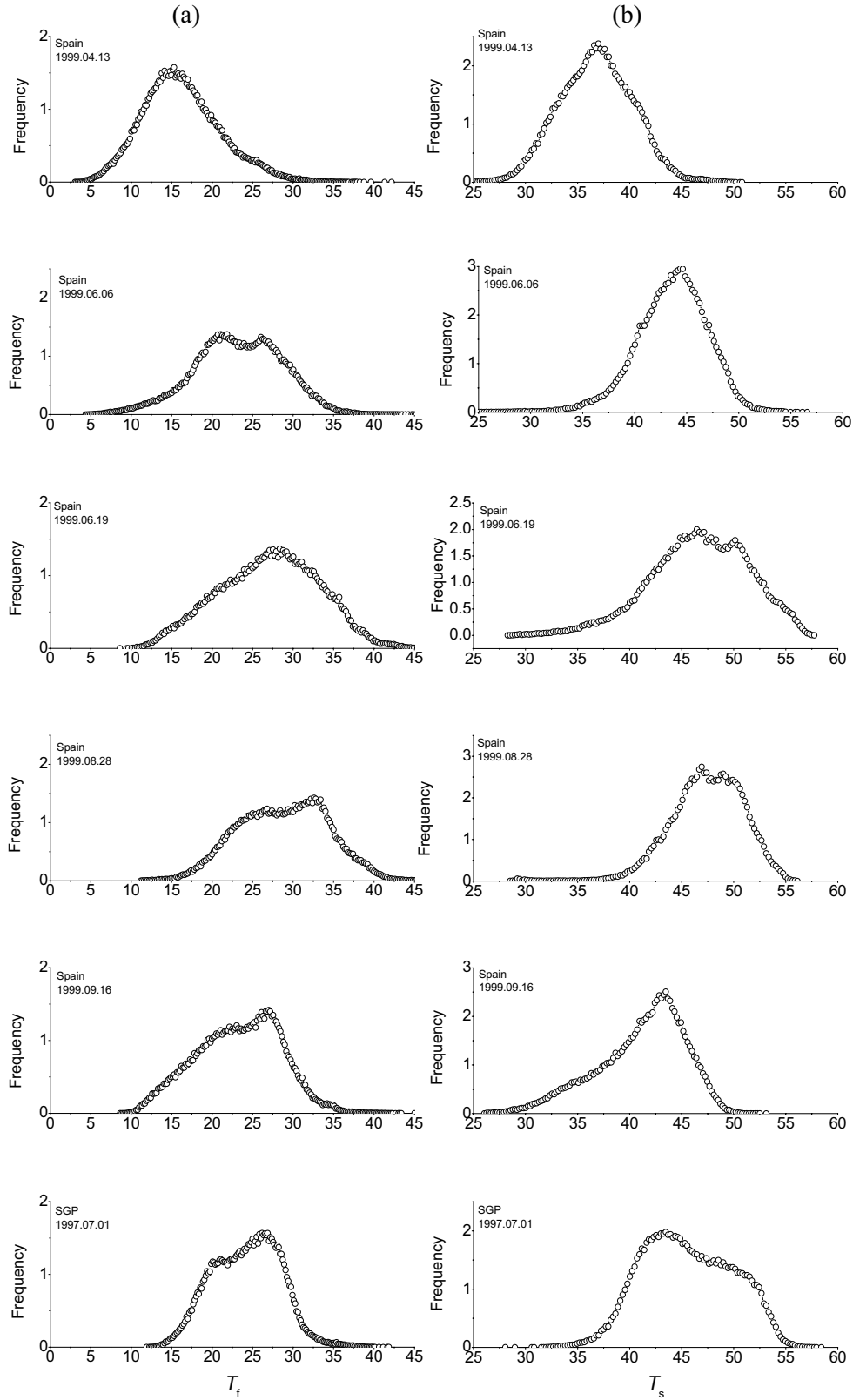
Figure 7.6 Histograms of retrieved (a) T_f and (b) T_s over the EWBMS area (Spain) and SGP'97 area.
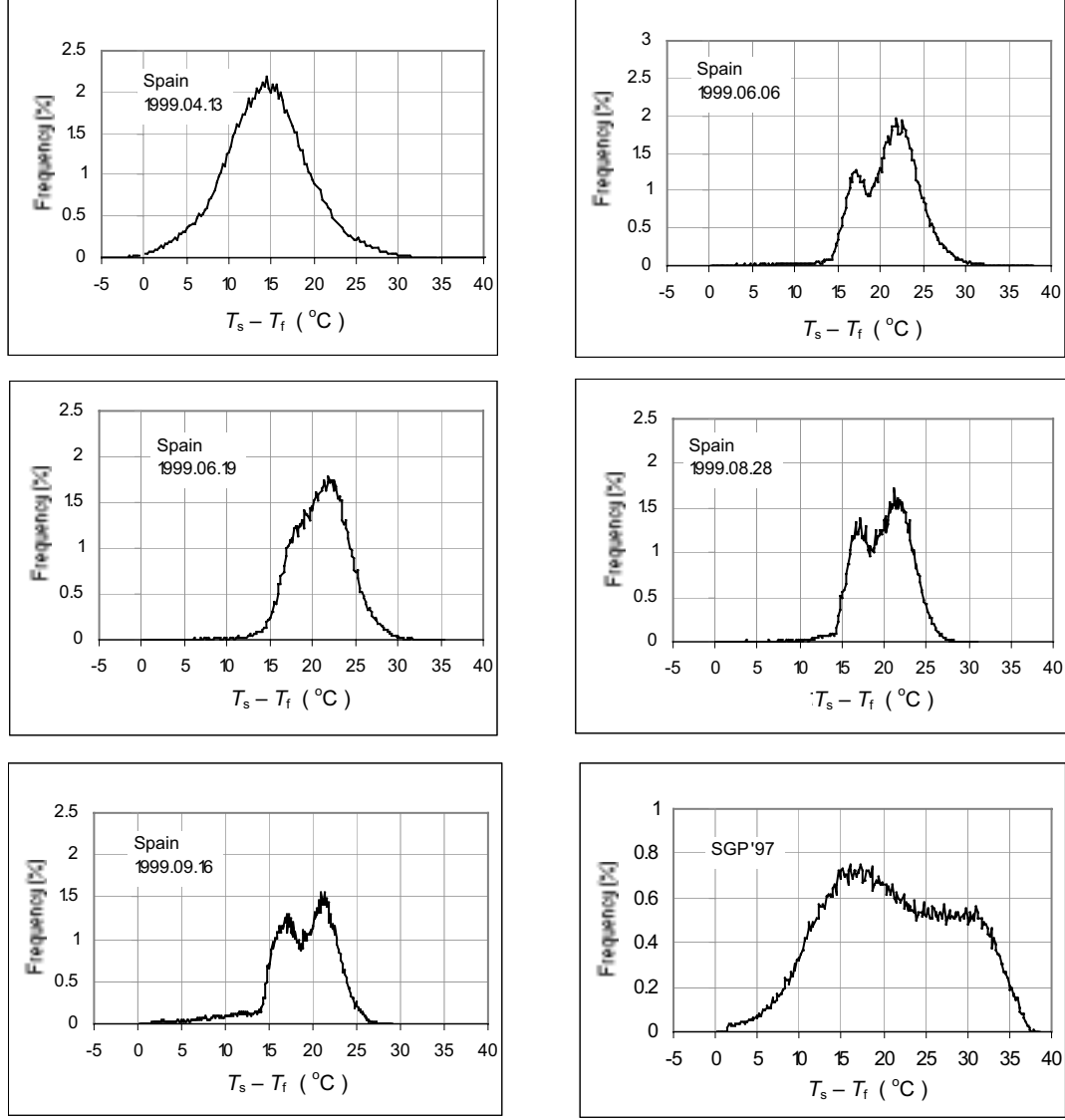
Figure 7.7 The difference between soil and foliage temperature retrieved by Eq. 3.19 over EWBMS area (Spain) and SGP'97 area.

7.7.3 Validation

The direct validation of the retrieved component temperatures using ATSR-2 bi-angular measurements is challenging due to the difficulty of obtaining observations of temperatures of soil and foliage in situ at the ATSR-2 spatial resolution.

As done for evaluation the algorithm for $f_f(\theta_v)$, a similar method can be used to evaluate the retrievals of T_f and T_s using the same simulation dataset over Barrax site (see §5.4). The reference T_f and T_s were simulated using the complete model described in Chapter 2. Simultaneously, $T_{b0}(\theta_v, \varphi_v)$ at $\theta_v = 0°$ and $\theta_v = 53°$ were obtained from the

synthetic data and used in Eq.3.19 to retrieve T_f and T_s. For the purpose of checking the assumption of the linear mixture model – that is the 3D-canopy properties can be represented by the simple linear mixture expression of radiative contribution from foliage and soil components - the reference values of $f_f(\theta_v)$ are used (see §7.7.1). The comparisons between the retrievals and the simulations of T_f and T_s for the three crops are encouraging (Fig. 7.8). The corresponding RMSE for each case is given in Table 7.6.
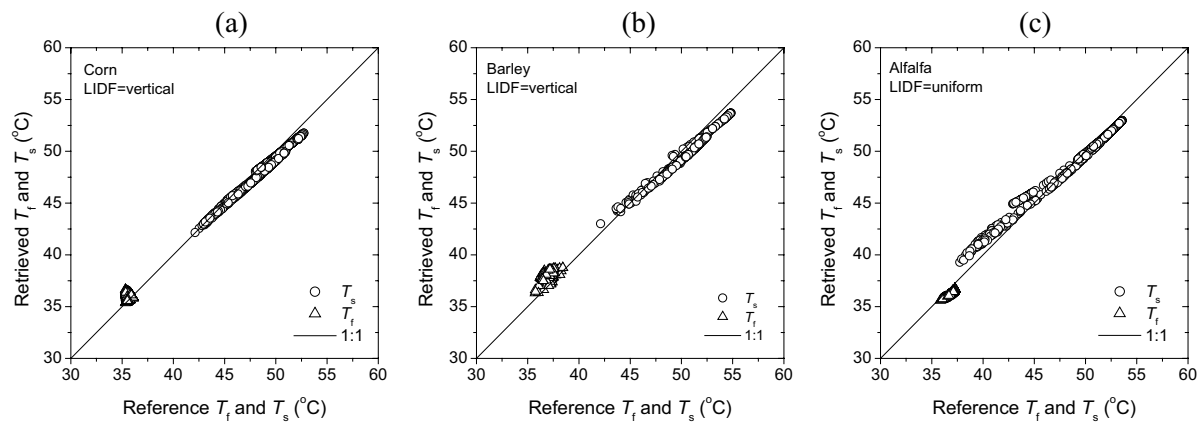
Figure 7.8 The comparison between the retrieved T_f (T_s) and the reference T_f (T_s) for (a) corn; (b) barley; and (c) alfalfa.

Table 7.6 Performance of the retrieval of T_f and T_s for corn, barley and alfalfa crops; RMSE = Root Mean Square Error.

RMSE	Corn (K)	Barley (K)	Alfalfa (K)
T_f	0.381905	1.164064	0.590805
T_s	0.669429	0.867213	0.772624

Another way to evaluate the retrieval of T_f and T_s using ATSR-2 bi-angular measurements is by comparing the foliage temperature T_f and the air temperature T_a. Some authors have found from experiments that leaf temperature of most crops was close to air temperature (Miller and Saunder 1923, Ehrler 1973, Fig.6.7 of this thesis). Following these conclusions, the results are roughly validated by comparing the derived T_f with the air temperature in our study (Fig. 7.9). In Spain area, several meteorological stations of World Meteorological Organization (WMO) network which are located in the images are selected as reference sites. In the SGP'97 area, two sites (CF01 and CF02) are chosen as the reference sites. The air temperatures at meteorological stations were measured at 2 meters height, while at the two SGP'97 experimental sites air temperature was measured at 0.96 and 1.96 meters

height at site CF01 and at 3 meters height at site CF02, respectively. The reference air temperature for SGP'97 area is taken as the mean between two measurements before and after ATSR-2 passing time over the two reference sites. In Fig. 7.9, the values of retrieved T_f and T_s are the average over 5×5 pixels around each reference site. The error bars indicate the standard deviations of T_f averaged over 5×5 pixels.

As shown Fig. 7.9, the values of the retrieved T_f are in better agreement with the air temperatures at most of the reference sites. Discrepancy is larger at a few sites. It is not surprising to observe some differences between T_f and air temperature. Several environmental factors, such as radiation, convection and transpiration, and soil moisture content in the root zone, affect T_f. Larger differences between foliage and air temperature were noted both from measurements and modeling results (see Jackson, 1982). Measurements of directional TIR and component temperatures at higher spatial resolution are needed to accomplish more accurate validation of the retrieved component temperatures.
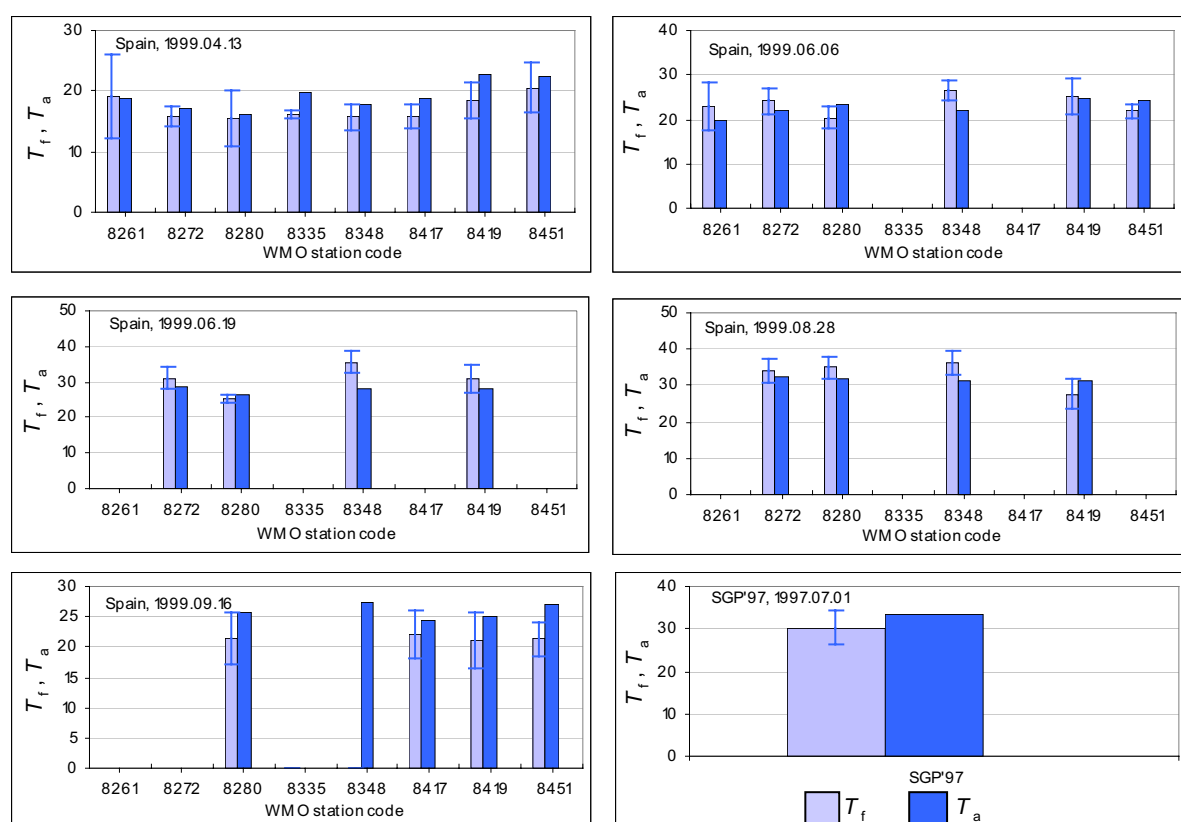

Figure 7.9 Comparison between foliage temperatures and air temperatures at reference sites 18 over EWBMS area (Spain) and SGP'97 area. The numbers at the X-axis the WMO meteorology station numbers. The error bars indicate the standard deviations of T_f 5×5 pixels.

Although the accuracy of the retrieved T_f and T_s still need to be investigated, the use of the component temperatures in NWP model is quite promising. A preliminary case study has been done by employing these two component temperatures in a newly developed multi-component land surface parameterization scheme (van den Hurk et al. 2001), in which improvements in the estimation of surface energy balance have been obtained.

7.8   Summary and conclusions

In this chapter a practical algorithm was developed to derive component temperatures of soil and foliage using multi-spectral and dual-view angle measurements made by ATSR-2 on the basis of the proposed linear mixture model described in Chapter 4 and evaluated using field measurements in Chapter 6. The algorithm includes the following steps:

- The raw ATSR-2 TOA data were screened for cloud-contaminated observations, observations not valid because of detectors saturation and observations of water targets; these observations were not considered when retrieving component temperatures.

- Algorithms to determine atmospheric column water vapor and aerosol optical depth from the multi-spectral, bi-angular radiometric data provided by the ATSR-2 sensor have been developed. The former gave column water vapor in good agreement with the measurements obtained by radiosoundings, while the validation of the algorithm to estimate aerosol optical depth is still necessary.

- Atmospheric correction of the TOA radiance measurements in the VIS – SWIR channels of ATSR-2 was done using both atmospheric column water vapor and aerosol optical depth retrieved with the new algorithms.

- The atmospheric correction for TIR channels was done with a general SW algorithm derived for ATSR-2 nadir and forward views using the simulation data from MODTRAN 4.0 considering a wide range of atmospheric and surface conditions.

- Smoothing: the different spatial sampling resolutions of ATSR-2 at nadir and forward observations must be taken into account to reduce the effect of heterogeneity of the land surface on the angular change in TOC brightness temperature.

- The fractional vegetation cover $f_f(\theta_v)$ is a crucial parameter in the retrieval of soil and foliage component temperatures. The retrieved $f_f(\theta_v)$ values were in good agreement with reference values. As discussed in Chapter 6 about the impact of errors on fractional cover, when the contrast between T_f and T_s is reduced to a value smaller than 5K and the nadir fractional cover is as large as 0.2, no matter how small the difference between f_{fw} and f_{nd} is, the errors in the retrieved T_f caused by the

error in either f_{fw} or in f_{nd} are acceptable. Under the surface conditions of the Spain case study, the retrieval of T_s is less sensitive to errors in the estimation of the fractional vegetation cover. However, the retrieval of T_f is more sensitive to the fractional vegetation cover.

- Simulated high resolution hyper-spectral synthetic images in the VIR/NIR to TIR domain were used to evaluate the algorithms to retrieve fractional cover and the soil and foliage component temperatures. The results showed that the inversion of the simple linear mixture model (Eq.3.19) gave foliage and soil component temperatures in good agreement with the reference values. This is consistent with the validation results showed in Chapter 6. The retrievals of T_f and T_s were also evaluated by comparing the retrieved T_f with air temperature. The retrieved T_f was in good agreement with the air temperature. This implies that our simple linear inversion model can be applied to separate the two components temperatures based on the use of bi-angular TIR measurements.

Chapter 8

Heat transfer between land surface and the atmosphere: application of single- and dual-source models

8.1   Introduction

Estimates of the component temperatures of foliage and soil within a heterogeneous target can be used to improve the parameterization of heat transfer at heterogeneous land surfaces (van den Hurk et al, 2002). A mixture of foliage and soil is characterized by large temperature differences within the canopy space. Under these conditions heat transfer between foliage and air and between soil and air should be described separately (so-called dual-source model, Chapter 4). We have shown elsewhere [Jia et al., 2001] that estimates of foliage and soil temperatures obtained with the method described here can be used to model heat transfer in this way. On the other hand, one has to expect that estimates of heat exchange by a single-source model may still be accurate if the resistance for heat transfer can be parameterized in a proper way by analyzing the thermal anisotropy of a vegetation canopy. In this chapter, the dual-source and the single-source heat transfer model developed in Chapter 4 will be used to estimate sensible heat flux density. The model performance will be validated locally and regionally using measurements made in the field and by satellite.

8.2   Model validation using field measurements

Measurements of $T_{b0}(\theta_v, \varphi_v)$ describe the thermal anisotropy of vegetation canopies and hereafter provide access to foliage and soil component temperatures. The latter was discussed in detail in Chapters 3, 6 and 7 and the retrieved component temperatures T_f and T_s on the basis of field observations and of ATSR-2 observations will be applied with the dual-source model (Chapter 4) to estimate sensible heat flux density H.

8.2.1   Parameterization of resistance in the single-source model

It was concluded in Chapters 1 and 4 that the adequacy of the parameterization of aerodynamic resistance r_{ah} determines the accuracy of the H estimates when using a single-source model. Two different types of parameterization for r_{ah} were described in Chapter 4: one accounts for the aerodynamics of vegetation in relation with canopy geometry (Eq.4.66), the other one accounts also for the thermodynamic anisotropy of a vegetation canopy by introducing $T_{rad}(\theta_v, \varphi_v)$ or T_f and T_s (Eqs. 4.68 and 4.69).

To establish a parameterization of r_{ah} using multi-angular measurements of $T_{rad}(\theta_v, \varphi_v)$, a data set was generated by a radiative transfer model. The one-dimensional version of the complete model as described in Chapter 2 was used to simulate radiative, heat and water vapor transfer within and above the vegetation canopy. The simulation was done for the following controlled conditions:

- LAI from 0.5 to 6 in steps of 0.5;
- Three types of LIDFs are considered: erectophile, uniform and spherical;
- Two soil water conditions:

  (a) upper soil layer is drier than root zone (named 'dry-surface');

  (b) upper soil layer is wetter than root zone (named 'wet-surface').

The simulation was done during one day cycle, i.e. from 8:00 to 17:00 hours, using actual meteorological observations for each hour, thus simulating changes in the intensity and location of heat sources with time when foliage and soil receive different solar irradiance.

Leaf area index LAI has a significant influence on kB^{-1} (see also §1.2.2), as also observed by Prévot et al. (1994) who took into account LAI in their parameterization of kB^{-1}. Simulations show that the relation between $T_{rad}(\theta_v, \varphi_v)$ and LAI is dependent on the canopy structure in terms of LIDF (Fig.8.1) at each hour which is plotted as different lines. A linear relation between kB^{-1} and nadir fractional vegetation cover $f_f(0)$ was found (Fig8.2), with similar slope but different offset for each hour. The latter implies that kB^{-1} does also depend on mean temperature of the canopy space.
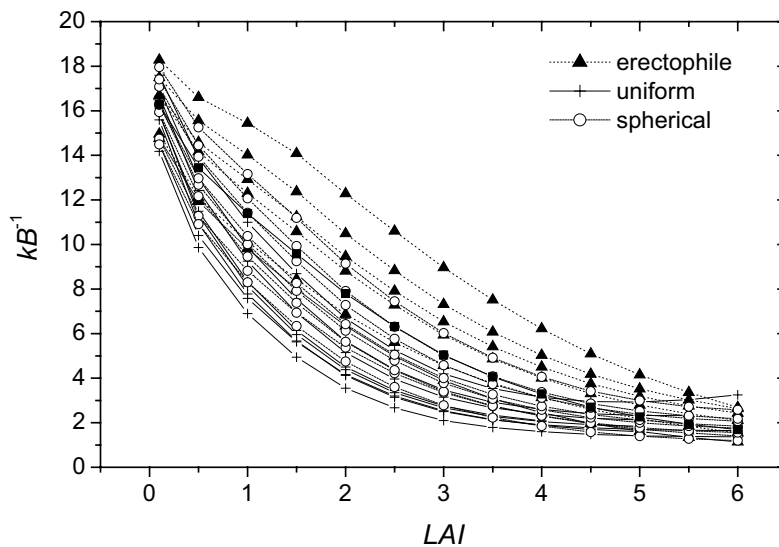

Figure 8.1 The relationship between kB^{-1} and LAI for different LIDFs. The different lines show the variations with time of the day.
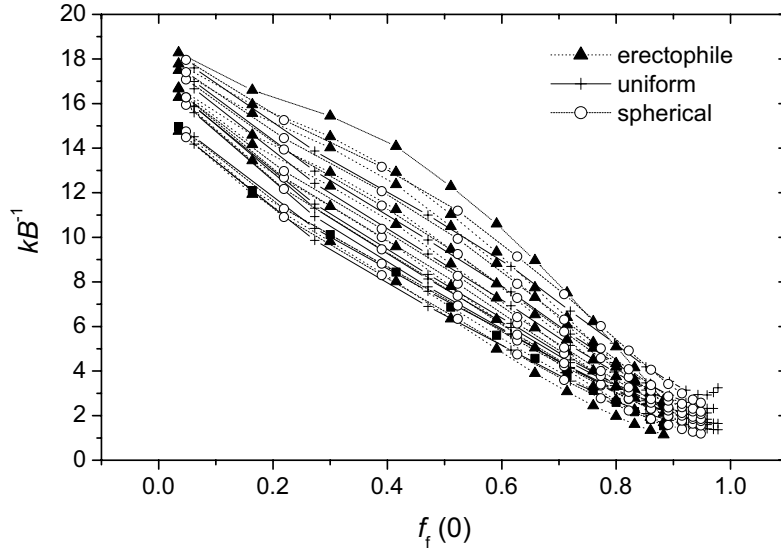
Figure 8.2 The relationship between kB^{-1} and $f_f(0)$ for different LIDFs. The different lines show the variations with time of the day.

The simulation study showed that kB^{-1} has a strong dependence on the difference of $T_{rad}(\theta_v, \varphi_v)$ at two zenith view angles (i.e. $\theta_v = 0^\circ$ and $\theta_v = 53^\circ$ in the case of this study), $\Delta T_{rad} = T_{rad}(0) - T_{rad}(53)$, and on the difference of $f_f(\theta_v)$ between the two angles, $\Delta f = f_f(53) - f_f(0)$ (Fig.8.3a,b). The shapes of the two curves leads one to link kB^{-1} to the ratio $\Delta T_{rad}/\Delta f$, this gives a near linear relation between kB^{-1} and $\Delta T_{rad}/\Delta f$ (Fig.8.3c).

The shift in the relationships between kB^{-1} and $f_f(0)$ and $\Delta T_{rad}/\Delta f$ with time (different lines in Figs. 8.1, 8.2 and 8.3) implies the dependence on time due to irradiance change with time. This therefore leads to include some variables reflecting the influence due to the variation of the absorbed radiation by the foliage-soil system. Soil temperature T_s, usually changes rapidly with the absorbed radiation by the canopy system, may be considered as a adequate variable to normalize the dependence of the relationship between kB^{-1} and the impact variables as described above. For the purpose of using directly multi-angular measurements of radiometric temperature, however, radiometric temperature observed at nadir, to which soil has more contribution than foliage, is more practical to be used.
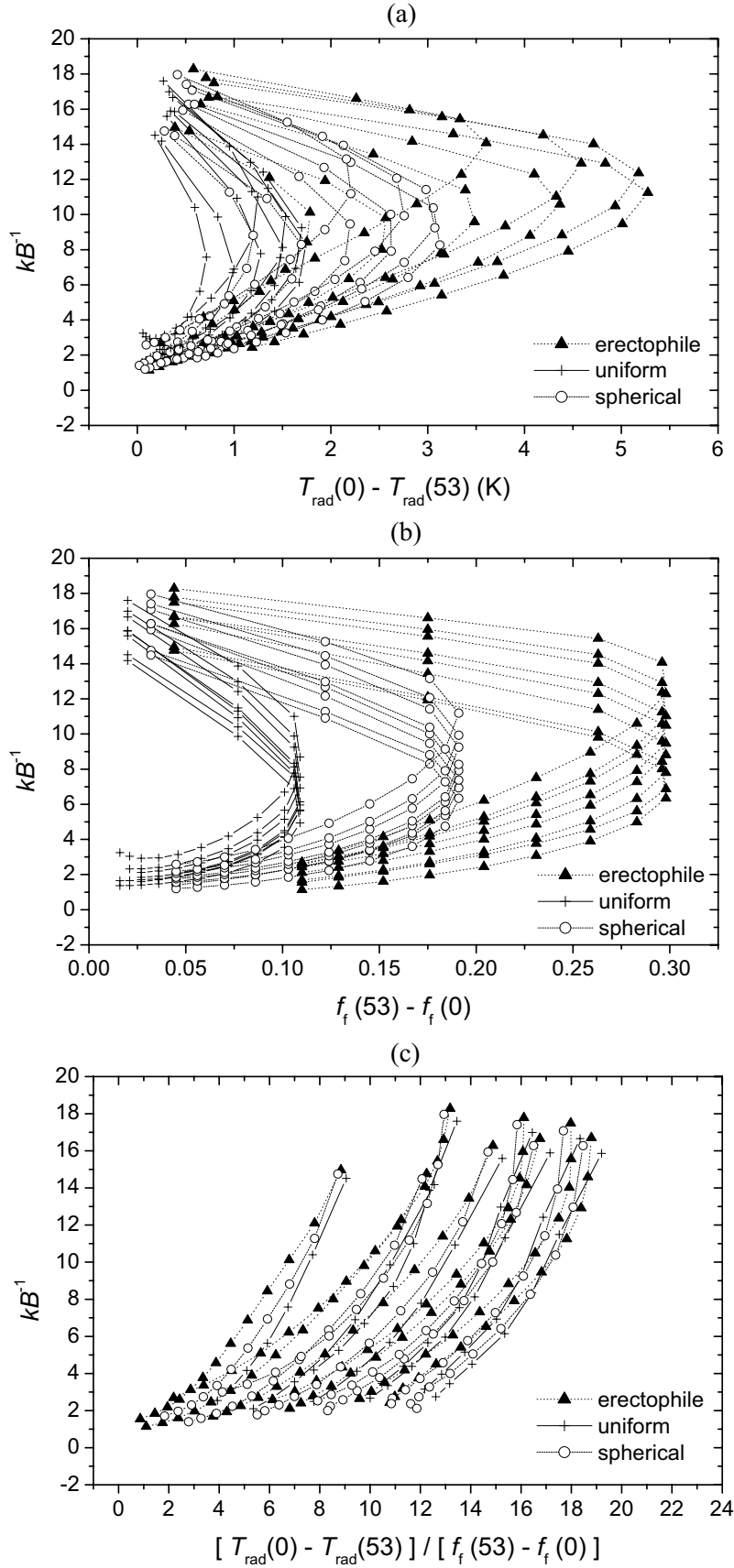
Figure 8.3 The dependence of kB^{-1} on (a) thermal anisotropy of a canopy represented by $\Delta T_{\mathrm{rad}} = T_{\mathrm{rad}}(0) - T_{\mathrm{rad}}(53)$, (b) the change of vegetation cover with view angle: $\Delta f = f_{\mathrm{f}}(53) - f_{\mathrm{f}}(0)$ and (c) the ratio $\Delta T_{\mathrm{rad}} / \Delta f = [T_{\mathrm{rad}}(0) - T_{\mathrm{rad}}(53)] / [f_{\mathrm{f}}(53) - f_{\mathrm{f}}(0)]$.

146

Summarizing the discussion above, a multiple linear regression is proposed based on the simulated dataset which reads as:

$$kB^{-1} = b_1 \frac{T_{rad}(0) - T_{rad}(53)}{f(0) - f(53)} + b_2 T_{rad}(0) + b_3 f(0) + b_0 \qquad (8.1)$$

where b_1, b_2 and b_3 are the regression coefficients, b_0 is the intercept. The simulation data yield: $b_1 = -0.07913$, $b_2 = 0.23193$, $b_3 = -13.07048$, $b_0 = 6.79439$ with $R^2 = 0.984$. Eq.8.1 relates kB^{-1} to the anisotropy of a canopy by means of bi-angular observations of $T_{rad}(\theta_v, \varphi_v)$ and $f_f(\theta_v)$.

8.2.2   Validation of the single-source and the dual-source model

The single-source model was first evaluated using the field measurements collected at the IMGRASS site, where dominant land cover was mixed grasses with fractional vegetation cover $LAI = 0.5$ and at the QRSLSP site, where land cover was a row crop with $LAI = 2.3$. Both Eq. 4.64 and the improved parameterization of kB^{-1} (Eq. 8.1) were tested. To illustrate the importance of kB^{-1} in the parameterization of resistance for heat transfer, two simplified cases are also given which have been often used in many studies of land surface processes. One is $kB^{-1} = 2.3$ which implies $z_{0h} = z_{0m}$, the other case is that no additional resistance is considered in the resistance parameterization, i.e. $kB^{-1} = 0$.

Fig. 8.4 and Fig. 8.5 show the comparison between model results and measurements of H at the two experimental sites. At both sites, the parameterization of kB^{-1} (Eq. 8.1) using bi-angular measurements of $T_{rad}(\theta_v, \varphi_v)$ gives the best agreement of the estimated sensible heat flux density H as compared with the results obtained by using Eq.4.64 in which thermal anisotropy is not taken into account. The sensible heat flux H is slightly overestimated when Eq. 4.64 is used in the parameterization of resistance, which implies that kB^{-1} is underestimated by Eq. 4.64.

When kB^{-1} is taken as a constant value of 2.3, the single-source model gives systematically higher estimates of H. The worst case is when no additional resistance is considered, i.e. the case when $kB^{-1} = 0$ (Fig. 8.4d and Fig. 8.5d). Hence the single-source model leads to very large errors in the estimation of H.

The kB^{-1} values as estimated by Eq. 4.64 and Eq. 8.1 were plotted against time on the two selected days each for IMGRASS site and QRSLSP site when measurements of directional brightness temperature were available during a day cycle (Fig. 8.6). The kB^{-1} values estimated by Eq. 8.1 show clearly diurnal variation at both sites and are twice the

kB^{-1} values estimated by Eq. 4.46. This can explain the overestimates of H when using Eq. 4.64 in the single-source model. The diurnal variation has also been reported by other researchers, e.g. Blyth and Dolman (1995) and Verhoef et al (1997), by using both modelling and measurements. Such variation is attributed to the change in the absorbed radiation which hereafter affects the heat and water distribution in a foliage and soil system.
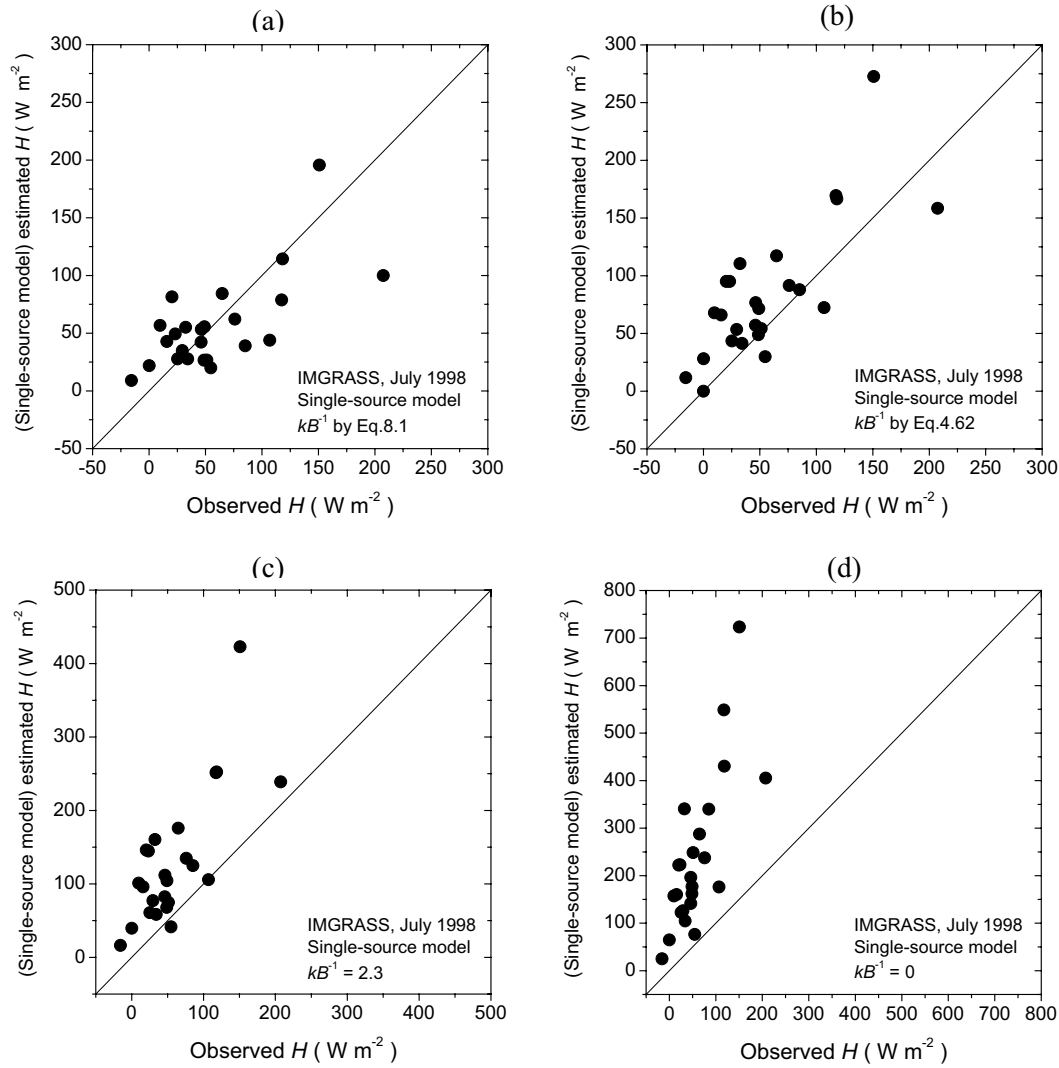
Figure 8.4 Sensible heat flux density H estimated by the single-source model vs. the measurements at the IMGRASS site in July 1998: (a) kB^{-1} as estimated by Eq.8.1 using bi-angular $T_{\mathrm{rad}}(\theta_{\mathrm{v}}, \varphi_{\mathrm{v}})$ measurements; (b) kB^{-1} as estimated by Eq. 4.64; (c) $kB^{-1} = 2.3$; and (d) kB^{-1} not being considered in the parameterization of resistance r_{ah}. The RMSE is given in Table 8.1.

148
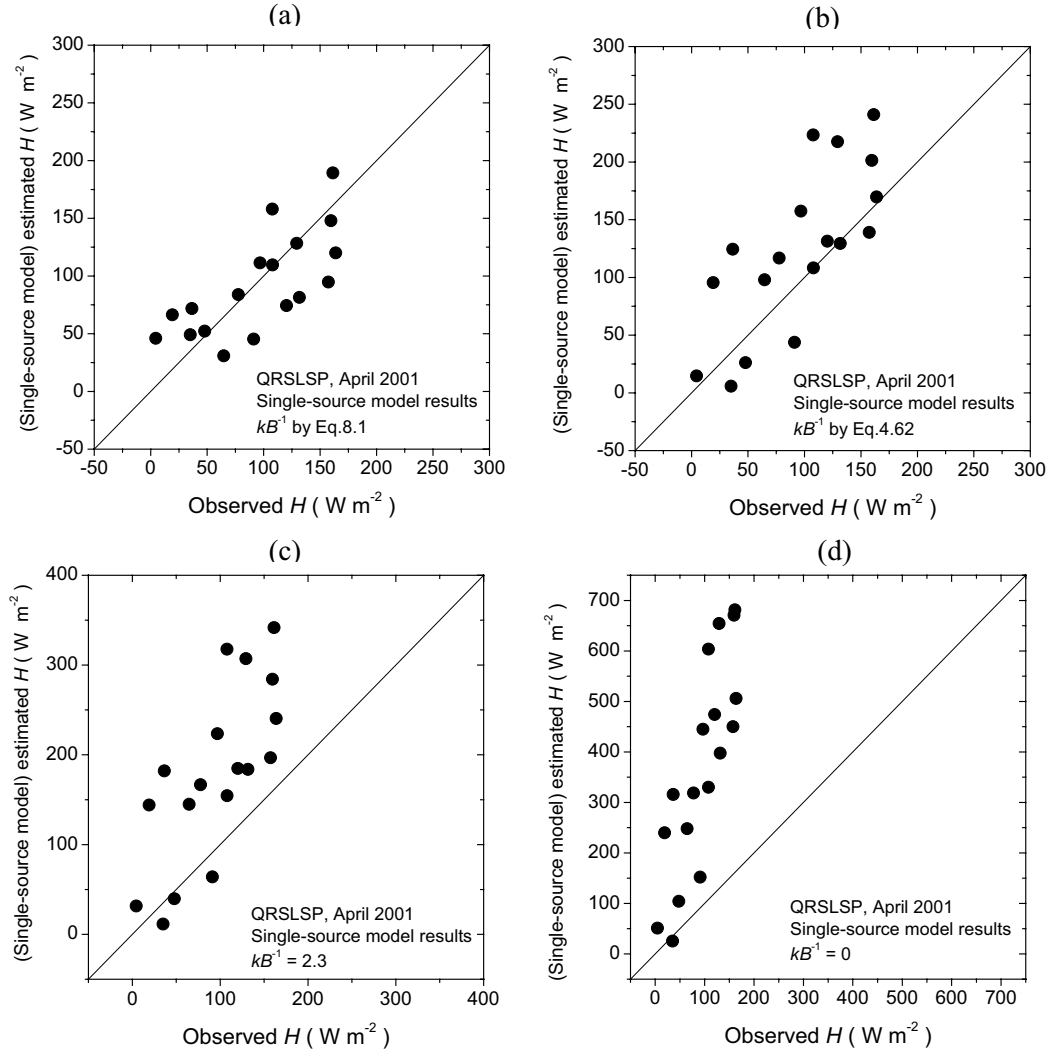
Figure 8.5 Sensible heat flux density H estimated by the single-source model vs. the measurements at the QRSLSP site in April 2001: (a) kB^{-1} as estimated by Eq.8.1 using bi-angular $T_{rad}(\theta_v, \varphi_v)$ measurements; (b) kB^{-1} as estimated by Eq. 4.64; (c) $kB^{-1} = 2.3$; and (d) kB^{-1} not being considered in the parameterization of resistance r_{ah}. The RMSE is given in Table 8.1.
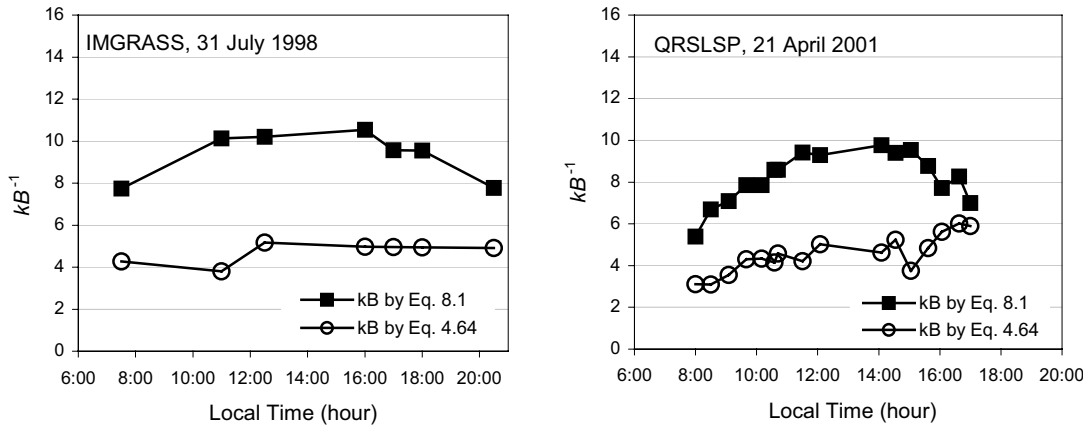
Figure 8.6 Diurnal variation of the kB^{-1} values estimated by Eq. 8.1 using bi-angular measurements and by Eq. 4.64 at the IMGRASS (31 July 1998) and QRSLSP sites (21 April 2001).

The dual-source model described in Chapter 4 was applied to estimate sensible heat flux density H using component temperatures T_f and T_s retrieved from field measurements of $T_{b0}(\theta_v, \varphi_v)$ at the two experimental sites. The agreement between the model estimation and the measurements was good for both sites (Fig.8.7).
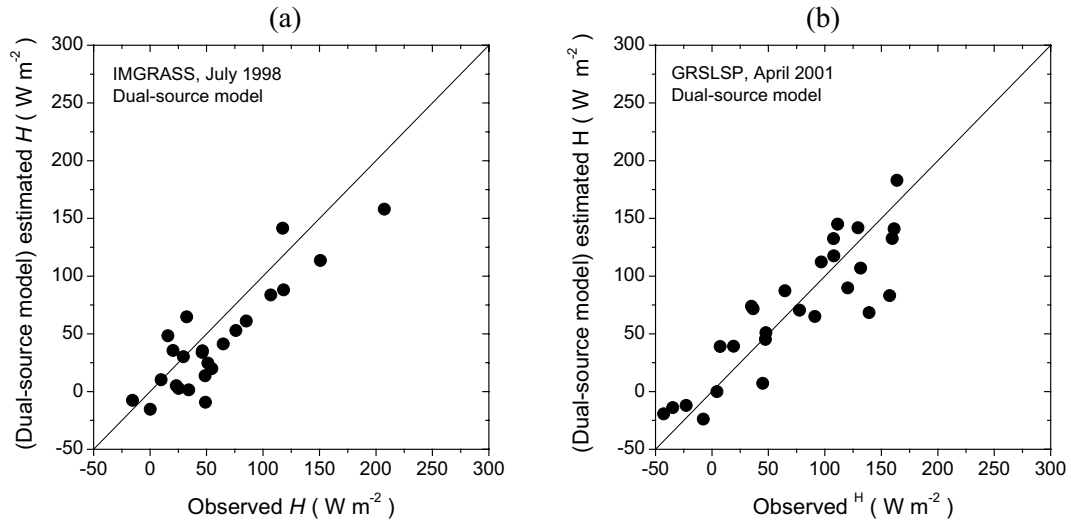
Figure 8.7 Comparison of sensible heat flux density H estimated by the dual-source model with the measurements (a) at the IMGRASS site in 1998, and (b) at the QRSLSP site in April 2001.

As a summary of model performance, the RMSE of all estimates of H presented here is given in Table 8.1. It appears that the dual-source model gave he best estimates of H. The single-source model also gave good estimates of H when the two new parameterizations of

150

kB^{-1} are used, particularly Eq. 8.1, but the results from the single-source model show slightly larger dispersion as compared to the results from the dual-source model. This confirms that the dual-source model has a better physical basis than the single-source and is able to account for the thermal heterogeneity of a foliage-soil canopy.

Table 8.1 The Root Mean Square Error (RMSE) of estimates of H using both the dual-source model and the single-source model at the two experimental sites IMGRASS and QRSLSP.

Site	RMSE (W m^{-2}) for dual-source model	RMSE (W m^{-2}) for single-source model			
		SM_1	SM_2	SM_3	SM_4
IMGRASS	28.0	37.2	47.4	92.8	218.4
QRSLSP	30.4	47.1	54.5	107.9	320.6

Note: SM_1: kB^{-1} was parameterized by bi-angular $T_{b0}(\theta_v, \varphi_v)$ measurements;

SM_2: kB^{-1} was estimated by Eq.4.64;

SM_3: kB^{-1} = 2.3 was assumed;

SM_4: no kB^{-1} was considered in the resistance r_{ah}, i.e. $z_{0h} = z_{0m}$.

8.3 Regional scale applications of the single/dual-source models

8.3.1 Introduction

In § 8.2, both the dual-source model and the single-source model developed in Chapter 4 were evaluated at the field scale over two different land surface types, i.e. relatively homogeneously mixed grassland and a row-crop canopy (winter wheat). These two models will now be applied to estimate the sensible heat flux density H at the regional scale by using satellite observations of TOC albedo α, fractional vegetation cover $f_f(\theta_v)$, LAI, TOC radiometric temperature T_{rad} and component temperatures of foliage T_f and soil T_s. Moreover, meteorological variables at a reference height in the atmosphere are also needed.

8.3.2 Determination of surface variables

TOC variables α***, LAI and*** $f_f(\theta_v)$

TOC albedo α, *LAI* and fractional vegetation cover $f_f(\theta_v)$ have been derived from TOC reflectances $\rho_i(\theta_{s0}, \theta_v, \Delta\varphi)$ using stepwise multiple linear regressions. The multiple linear regression for albedo α is:

$$\alpha = a_0(\theta_{s0}, \theta_v) + \sum_{i=1}^{n}\left[a_i(\theta_{s0}, nadir)\rho_i(\theta_{s0}, nadir, \Delta\varphi)\right] + \sum_{i=1}^{n}\left[a_i(\theta_{s0}, forward)\rho_i(\theta_{s0}, forward, \Delta\varphi)\right]$$

(8.2)

where n is the number of channels used in the VIS/SWIR channels of 0.55 μm, 0.65 μm, 0.87 μm and 1.6 μm as measured by ATSR-2, θ_{s0} and $\Delta\varphi$ was defined befor. A similar regression for the transformed LAI was obtained:

$$e^{-LAI} = A_0(\theta_{s0}, \theta_v) + \sum_{i=1}^{n}\left[A_i(\theta_{s0}, nadir)\rho_i(\theta_{s0}, nadir, \Delta\varphi)\right]$$

$$+ \sum_{i=1}^{n}\left[A_i(\theta_{s0}, forward)\rho_i(\theta_{s0}, forward, \Delta\varphi)\right]$$

(8.3)

The regression for $f_f(\theta_v)$ was given in chapter 7 (Eq. 7.22).

The coefficients a_i and A_i in Eq. 8.2 and Eq. 8.3 were derived with the same procedures as for the regression coefficients in Eq. 7.22 (see Chapter 7) by using a radiance data base generated by OSCAR model simulations of an ensemble of canopy and atmospheric conditions (Verhoef, 1998; Verhoef, 2001). The reflectances observed in the four channels of ATSR-2 at the two view angles, however, were combined in one regression either for LAI or for α compared to the regression for $f_f(\theta_v)$ (Eq. 7.22), where the reflectance measurements at the two view angles were applied independently to estimate $f_f(\theta_v)$ at the respective zenith view angle θ_v. Also, information obtained in the SWIR channel (1.6 μm) were also used to better account for the absorption due to plant water. In the simulations, the TOC reflectances in the four optical channels were calculated for the nadir and forward view angles of ATSR-2 observations. The relative azimuth angle was roughly estimated to be equal to 120 degrees. The atmospheric correction procedures described in Chapter 7 were applied to obtain reflectances at TOC from the TOA radiance measured by ATSR-2 in VIS/SWIR channels (see also Jia, et al., 2003).

The algorithms were derived by stepwise regression analysis with the TOC simulated bi-angular reflectances $\rho_i(\theta_{s0}, \theta_v, \Delta\varphi)$ as predictive variables and the surface albedo, i.e. the hemispherical spectrally integrated reflectances, or LAI or $f_f(\theta_v)$, as the predicted variable. This algorithm is generic in the sense that the coefficients in Eq. 8.2 and Eq. 8.3 are determined over an ensemble of situations, i.e. the range of target characteristics (e.g. fractional vegetation cover, leaf and soil reflectances) considered to compute the reflectances $\rho_i(\theta_{s0}, \theta_v, \Delta\varphi)$ in Eq. 8.2 and Eq. 8.3. The forward calculation of reflectance was done at the ATSR-2 wavelengths and view-angles for different solar zenith angles θ_{s0}. Table 8.2 and Table 8.3 give the values of the regression coefficients at different solar zenith angles θ_{s0}. To

obtain a measure of the accuracy of the algorithm the correlation coefficients of determination R^2 were calculated (Table 8.2 and Table 8.3) (note that R^2 doesn't include the effect of other factors, i.e. the accuracy of atmospheric correction for VIS/NIR channels). It was obtained by comparing the values of albedo α and LAI obtained by using the coefficients in Table 8.2 and Table 8.3 with the values of albedo α and LAI known a-priori for all cases considered in the forward radiative transfer simulation. The coefficients in Table 8.2 and Table 8.3 were then interpolated to each ATSR-2 pixel according to the solar zenith angle for each pixel.

Table 8.2 The regression coefficients in the stepwise multiple linear regression for albedo α (Eq. 8.2) for different solar zenith angle θ_{s0}. R^2 is the square of correlation coefficients. Symbol 'n' and 'f' denote nadir and forward zenith view angles respectively.

θ_{s0} (°)	a_0	a_1 (n)	a_2 (n)	a_3 (n)	a_4 (n)	a_1 (f)	a_2 (f)	a_3 (f)	a_4 (f)	R^2
15	0.0074	-0.16	-0.07	0.03	0.28	0.31	0.23	0.37	-0.09	0.998
30	0.0144	0.09	-0.25	-0.13	0.59	0.04	0.44	0.55	-0.45	0.997
45	0.0169	0.15	0.07	-0.24	0.69	-0.03	0.12	0.68	-0.57	0.996
60	0.0096	0.01	0.74	-0.14	0.40	0.11	-0.63	0.57	-0.20	0.994
75	-0.0030	-0.10	1.19	0.12	-0.05	0.23	-1.18	0.29	0.36	0.994

Table 8.3 The regression coefficients in the stepwise multiple linear regression for LAI (Eq. 8.3) at different solar zenith angle θ_{s0}. The subscripts '1, 2, 3, 4' in the coefficient a_i correspond to the three ATSR-2 channels centered at 0.55 μm, 0.65 μm, 0.87 μm and 1.6 μm at 0º and 53º zenith view angles. R^2 is the square of the correlation coefficient.

θ_{s0} (°)	A_0	A_1 (n)	A_2 (n)	A_3 (n)	A_4 (n)	A_1 (f)	A_2 (f)	A_3 (f)	A_4 (f)	R^2
15	0.6423	-0.24	-2.38	2.46	-3.00	-0.50	4.72	-4.38	4.70	0.927
30	0.6516	1.49	3.08	2.18	2.29	0.62	5.70	-4.05	3.81	0.926
45	0.6547	-1.15	4.06	2.00	2.55	0.16	6.71	-3.86	4.11	0.928
60	0.7057	1.35	3.76	1.15	1.13	0.25	6.67	-3.00	2.42	0.935
75	0.7742	-4.81	3.61	0.09	0.71	3.59	-0.42	-1.95	0.27	0.947

Radiometric temperature T_{rad}

The brightness temperature at TOC, $T_{b0}(\theta_v)$, was obtained by Eq. 7.21 from observation of TOA brightness temperature $T_b(\theta_v)$ made by ATSR-2 at the two zenith view angles. To convert $T_{b0}(\theta_v)$ to radiometric temperature T_{rad} by using Eq. 3.21, the directional TOC emissivity $\varepsilon_c(\theta_v)$ was needed which is calculated as a weighted average of emissivities of soil ε_s and vegetation ε_f according to proportion occupied in the IFOV considering single scattering only:

$$\varepsilon_c(\theta_v) = f_f \varepsilon_f + (1-f_f)\varepsilon_s + \frac{f_f(1-f_f)[1-\varepsilon_s][\varepsilon_f + \varepsilon_s - \varepsilon_f \varepsilon_s]}{1-f_f[1-\varepsilon_f - \varepsilon_s + \varepsilon_f \varepsilon_s]} \qquad (8.4)$$

The emissivities of soil ε_s and vegetation ε_f can be taken from literature or from experiment for different vegetation types. Since the vegetation type was not known for each pixel of ATSR-2 observations, ε_s and ε_f were simply taken as 0.95 and 0.98 respectively which are considered as reasonable approximations in the spectral channels of ATSR-2. The third term in Eq. 8.4 accounts for single scattering between foliage and the soil.

Roughness length for momentum z_{0m} and zero-plane placement d

The roughness length for momentum transfer, z_{0m}, is a crucial parameter in any land surface process model, which determines the source/sink height of momentum and therefore the source/sink of heat. Moreover, heat exchange height in a canopy as used in the dual-source model is also related to the roughness length (i.e. $d + z_{0m}$, see Chapter 4). Several models have been developed to estimate roughness length for momentum with consideration of canopy structure (Raupach, 1992, 1994; Massman, 1997). When applying these physically detailed models to regional scale, difficulties are encountered due to lack of the information needed by the models. Remote sensing technique, e.g. laser altimeter, was also used to estimate effective roughness length of a heterogeneity land surface (Menenti and Ritchie, (1994). Such measurements, however, are not available over the experimental sites used in this thesis. Alternatively, empirical relationships can be used to determine z_{0m} from the heights of vegetation for given land use types (e.g. Brutsaert, 1982). More recently an objective, physically-based model for estimation of effective z_{0m} was developed (Hasager and Jensen, 1999). The model uses a high resolution land use map to provide initial estimates of z_{0m} and takes the turbulent response of the atmospheric flow into account for every roughness step change in the terrain. No further investigations have been carried out on this aspect in this thesis.

Based on studies from different researchers (Hatfield, 1988; Asrar et al., 1992), a relationship between z_{0m} and *NDVI* may be expected so that measurements made by satellites can be used for regional estimation of z_{0m}. An empirical relationship between z_{0m} and *NDVI* was derived in the Tomelloso area (seed Chapter 5) by Bastiaanssen (1995):

$$z_{0m} = \exp(C_1 + C_2\ NDVI) \qquad (8.5)$$

where C_1 and C_2 are empirical coefficients which are study area dependent. Following Bastiaanssen (1995), $C_1 = -5.5$ and $C_2 = 5.8$ for the Tomelloso area with mixture of crops and vineyard.

Eq. 8.5 can be easily used with satellite measurements in the VIS/NIR bands. Such parameterization, however, may also easily bring problems: land surface with high *NDVI* values does not necessarily correspond to large roughness. An alternative method is to estimate effective roughness length by combining a suitable land cover classification. In this thesis, the Corine land cover database (CEC, 1993) was used and the roughness length classification proposed by Wieringa (1993) was assigned to each land cover. Both methods, i.e. the empirical relation Eq. 8.5 referred to as 'NDVI method' and the land cover method will be tested in the validation of the single/dual-source model.

It seems that the roughness length z_{0m} as estimated by Eq. 8.5 is too low particularly for vineyard, even a bit low for crops. On the contrary, the land cover method tends to give too high values of z_{0m} for crops, while it can provide reasonable values for vineyards in Tomelloso site. Although the coefficients in Eq. 8.5 were obtained based on the in-situ measurements in Tomelloso, it includes also crops where the samples were made. Along the line of sight of the LAS in Tomelloso (see Chapter 5), however, probably the ATSR-pixels only covered vineyard. Thus, the land cover method was considered to give better estimates for the Tomelloso test site. As regards to the values of z_{0m} for crops, there is up to an order of magnitude difference between the two method.

The zero-plane displacement d was determined following the work by Shaw and Pereira (1982):

$$\frac{d}{h_c} = 1.1 \times \ln\left[1 + \left(c_{df} \times LAI\right)^{0.25}\right] \tag{8.6}$$

The symbols used in Eq. 8.6 were defined in the previous chapters.

8.3.3   Determination of CBL meteorological variables

At large spatial scales, both the single-source model and the dual-source model require reference potential temperature T_{ap} and humidity q_a of the air at an appropriate height above heterogeneous land. The height of the Convective Boundary Layer (CBL) is considered as a suitable reference level (Brutsaert and Sugita, 1992; Brutsaert 1999) to estimate the regional heat flux density. The interdependence of horizontal and vertical length scales in relation with the CBL fluxes was addressed by e.g. Finnigan et al. (1990) who related horizontal, *X*, to vertical length scales as:

$$X = \frac{u}{u_*} h_{\mathrm{b}} \qquad\qquad (8.7)$$

where h_{b} is the blending height of the boundary layer under neutral conditions. With the magnitude of $\frac{u}{u_*} \sim 10\text{-}100$, the ratio of vertical scale to horizontal scale is about the order of magnitude of $\frac{1}{100} \sim \frac{1}{10}$. This implies that the land - atmosphere exchange of energy and vapor within a rather large land area will contribute to air potential temperature T_{ap} observed at the top of the CBL. We have chosen the height of the CBL as the reference height to determine H both in the dual-source model and in the single-source model.

The most direct observations of the potential temperature T_{ap} and humidity q_{a} at the CBL height is by using detailed vertical soundings of the atmosphere. However, the number of meteorological stations within the area of interest is usually not sufficient to obtain the required meteorological variables at a spatial resolution consistent with land observations from space. Moreover, the coarse vertical resolution of standard atmospheric soundings may lead to inaccurate estimates of the CBL height, as well as of potential temperature T_{ap} and humidity q_{a} at this height. We have used spatial fields of atmospheric variables (at the lowest model level) generated with the advanced Numerical Weather Prediction (NWP) model, i.e. Regional Atmospheric Climate Model (RACMO) (Christensen et al. 1996), which includes a detailed description of land - atmosphere interactions. The spatial resolution of the model fields is $25\,\mathrm{km} \times 25\,\mathrm{km}$. This spatial resolution is consistent with the relation between horizontal and vertical length - scales (Eq. 8.7) in the sense that a single value of both potential air temperature and air humidity at CBL height for a $25\,\mathrm{km} \times 25\,\mathrm{km}$ grid-box is indeed representative of the overall effect of land – atmosphere exchanges of energy and vapor within the entire grid-box. This implies that a single value of the reference potential temperature and humidity q_{a} of air is used for each RACMO model grid including a number of ATSR-2 pixels with a resolution of $1\,\mathrm{km} \times 1\,\mathrm{km}$. The latter applies to the observations of vegetation properties and accounts for sub-grid variability of land cover, thermodynamic and hydrological conditions.

8.3.4 Estimates of sensible heat flux density using the dual-source model

The dual-source model proposed in Chapter 4 was applied to estimate H at the regional scale over Spain during the EWBMS experiment in 1999. The component temperatures T_{f} and T_{s} were retrieved using the ATSR-2 bi-angular measurements over the study area

(Chapter 7) and were used in the dual-source model. The data used for the validation were the measurements of sensible heat flux density H by means of the LAS system as described between the transmitter and the receiver at distances of 1070 m, 4690 m and 5250 m for Tomelloso, Lleida and Badajoz respectively. This implies that the line of sight spans about 2, 5, and 6 pixels of ATSR-2 for the three sites, respectively (Fig. 8.8).

When comparing the estimated H with the measurements, one should notice the following: first, the footprints in LAS measurements and in the SEBS estimates are different. For instance, H measured by a LAS is a line-averaged value along the line of sight even though it may capture the contributions of turbulence from upwind direction over the observation period but not those from downwind direction. However, the estimates of H by the dual-source model using the surface variables determined with ATSR-2 data and NWP model derived CBL variables are the average over a larger area, at least at ATSR pixel scale. Although the dominant landuse types along the line of sight at each site were dry vineyard (Tomelloso), irrigated crops with fruit trees (Lleida) and irrigated crops only (Badajoz) (in Chapter 5), in fact the land surface in the ATSR-2 pixels covering the sites also included different land surface types beyond the line of sight due to low spatial resolution (Table 8.4). If the surface shows a large degree of heterogeneity, the selection of adequate pixels for comparison with the LAS measurements of H should be dealt with carefully (see Meijninger et al. 2002).

Second, a dissimilar temporal scale can also have effects on the agreement between the observed and estimated fluxes. Measurements of H by LAS provide H values averaged over some 10 minutes which integrate the mixed turbulent characteristics and heat exchange processes over the integration time, while satellites can only provide instantaneous observations of surface variables at overpass time.

Table 8.4 Landuse classifications in the surrounding of the three EWBMS experimental sites.

Code	Description
1	Continuous urban fabric
7	Mineral extraction sites
12	Non-irrigated arable land
13	Permanently irrigated land
14	Rice field
15	Vineyards
16	Fruit trees and berry plantation
17	Olive trees
20	Complex cultivation patterns
26	Natural grasslands
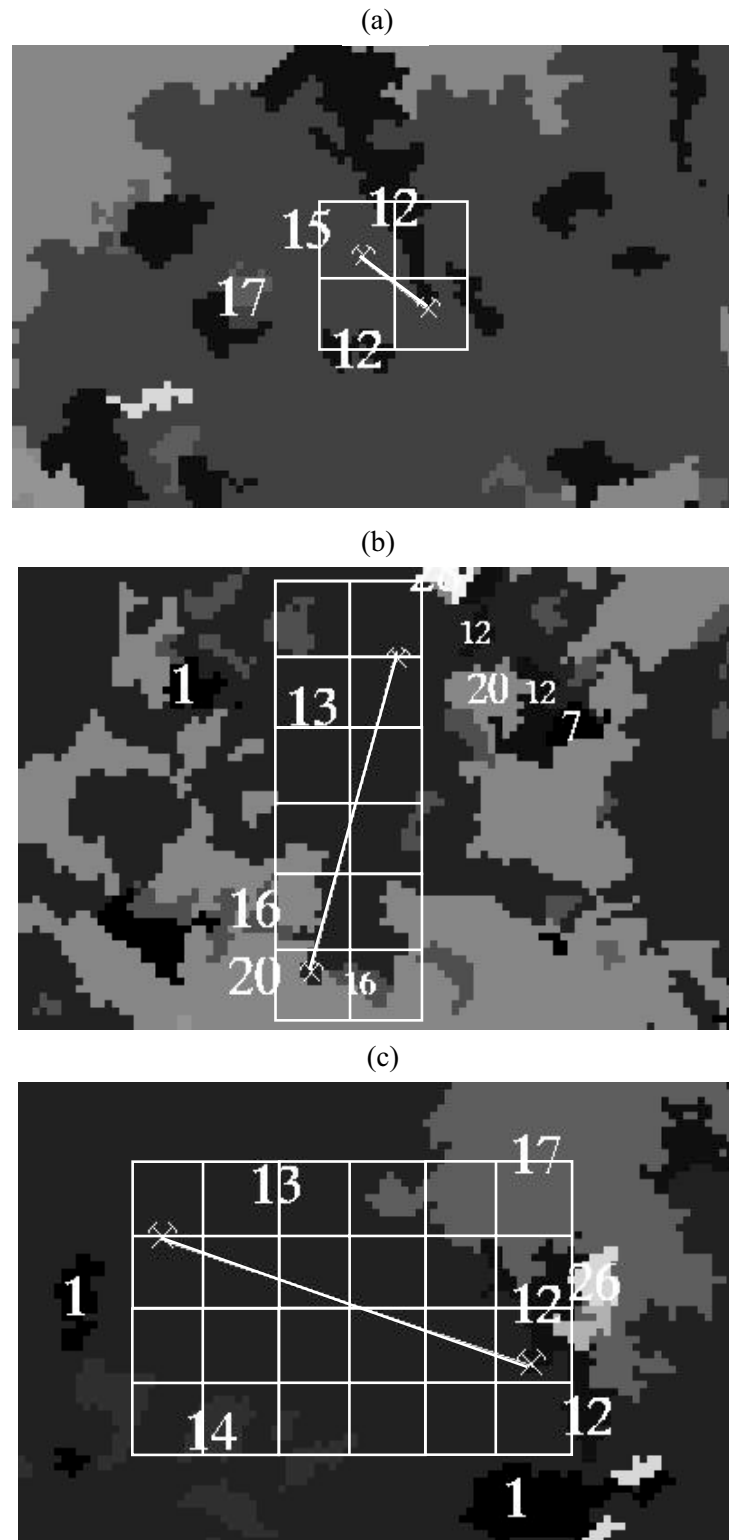
Figure 8.8 The line of sight of the Large Aperture Scintillometer (LAS) used for sensible heat flux density measurements at the three EWBMS sites in Spain: (a) Tomelloso, (b) Lleida, and (c) Badajoz. The land use is represented by gray level together with numbers indicating the landuse codes given in Table 8.4. The grids show the ATSR-2 pixels.

Sensible heat flux density H was calculated for each ATSR-2 overpass time at each experimental site. Since that the land cover at the three validation sites was different, analyses were carried out individually for each site. At Tomelloso, the accuracy of the dual-source model was very good: RMSE 37.1 when Eq. 8.5 was used for z_{0m} and 42 Wm^{-2} when land cover method was used to estimate z_{0m} (Fig. 8.9). Apparently, the dual-source model is not sensitive to the values of z_{0m}.
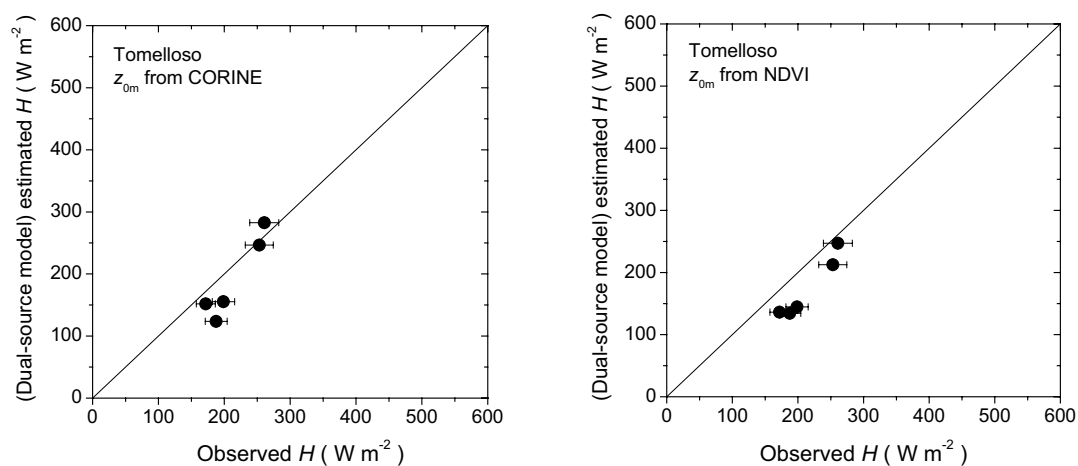
Figure 8.9 Comparison of the sensible heat flux density H values estimated by the dual-source model and obtained from the Large Aperture Scintillometer (LAS) at Tomelloso: (a) when z_{0m} was from Eq. 8.5 and (b) when z_{0m} was from the land cover method. The vertical error bars give the standard deviation over the pixels along the line of sight of the LAS, while the horizontal error bars give the accuracy of the LAS measurements.
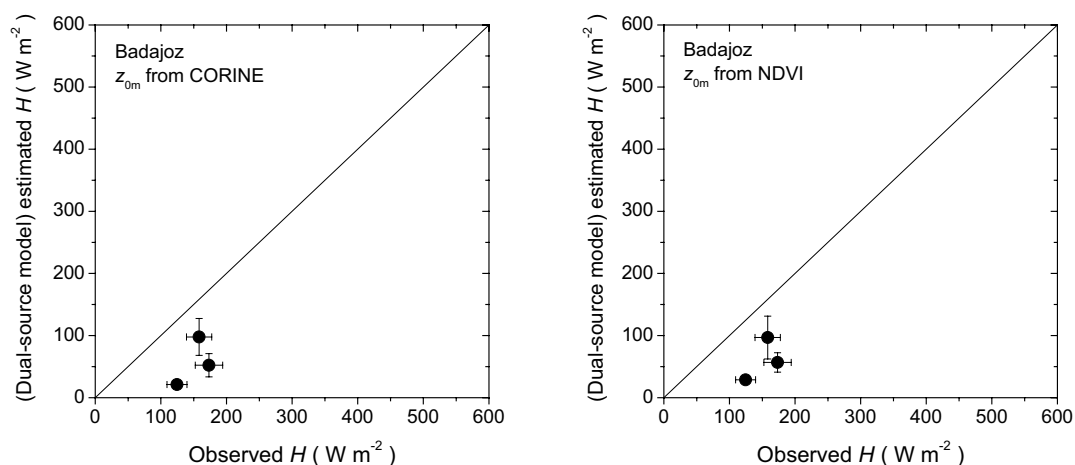
Figure 8.10 The same as Fig. 8.9, but for Badajoz.
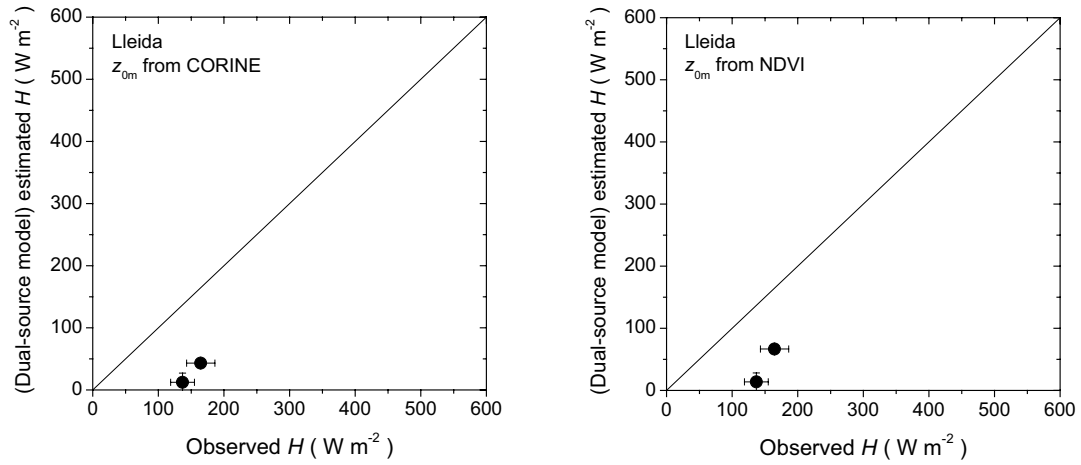
Figure 8.11 The same as Fig. 8.9, but for Lleida site.

The dual-source model underestimated H at Badajoz with large RMSE (Fig. 8.10, Table 8.5). However, the worst cases for the estimated H by the dual-source model are those at Lleida (Fig. 8.11). The large bias in the estimation of H at Badajoz and Lleida sites is probably due to the errors in inverted foliage and soil component temperatures T_f and T_s.

At these two sites, the land surface were relatively homogeneous so that less anisotropy in both the TIR radiance and in the VIS/NIR reflectance were observed, which caused inaccurate retrieval of T_f and T_s. Actually, only very few pixels provided valid observations of T_f and T_s, since several constrains were applied in the inversion of the linear mixture model (see Chapter 7) in addition to the homogeneity of the land surface.

One should notice that these comparisons (Figs. 8.9 - 8.11) involve both the spatial variability along the LAS path length and the accuracy of LAS (for more detailed discussion about the accuracy of LAS measurements see Moene, 2001; Moene and De Bruin, 2001).

8.3.5   Estimates of sensible heat flux density using the single-source model

The single-source model SEBS described in Chapter 4 was evaluated using TOC radiometric temperature T_{rad}, surface albedo α and surface fractional vegetation cover $f_f(\theta_v)$ estimated from ATSR-2 observations over a large area in Spain. The same data of LAS measurements as used in the evaluation of the dual-source model (§8.3.4) were also used in this section.

160

The most crucial variable in the single-source model is the excess resistance in terms of kB^{-1} as described in Chapter 1 and Chapter 4. Two parameterizations of kB^{-1} (Eq. 4.64 and Eq. 8.1) were evaluated by comparing the sensible heat flux density H as estimated by the single-source model with the LAS measurements. The mean values of H estimated by the single-source model along with the standard deviation (the vertical error bars) over the pixels along the path for each site versus measured values by LAS (the horizontal error bars give the accuracy of LAS measurements) are shown in Fig. 8.12. The single-source model with the parameterization Eq. 8.1 did a better job at Tomelloso, implying that the single-source model can provide acceptable estimates of sensible heat flux (Table 8.5) when the anisotropy properties of the land surface was taken into account in the parameterization of resistance for heat transfer. However, the RMSE is larger than the results of the dual-source model which proved the solid physical basis of the dual-source model. At Lleida and Badajoz, H was underestimated which implies that the correction to the resistance by Eq. 8.1 was overestimated over homogeneous land surface where the anisotropy is not significant.

Fig. 8.13 gives the histograms of kB^{-1} values over $50\text{km} \times 50\text{km}$ area surrounding Tomelloso on the five overpass days of ATSR-2. Large variation in kB^{-1} is observed over the area and one most days the peak is located at around 10. The similar order of magnitude of kB^{-1} was found using assimilation study by coupling the foliage and soil component temperatures in an advanced NWP model over the same area to give the prediction of air temperature and humidity (van den Hurk, 2002). The used of foliage and soil component temperatures did improve the NWP model prediction.
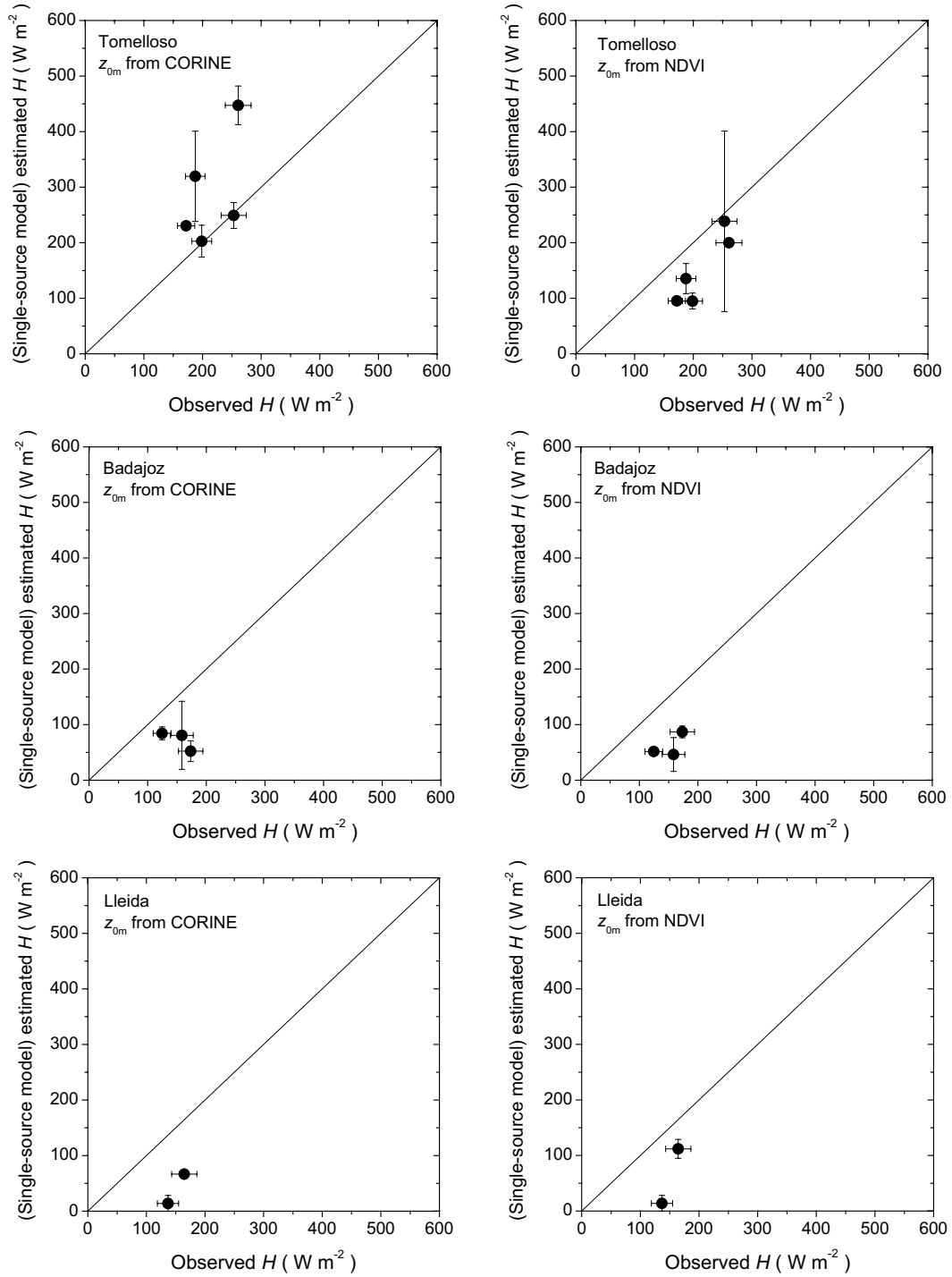
Figure 8.12 Comparison of the sensible heat flux density H values estimated by the single-source model with measurements by the Large Aperture Scintillometer (LAS) at Tomelloso, Badajoz and Lleida sites on the corresponding days listed in Table 5.8: (Left) when z_{0m} was from Eq. 8.5 and (Right) when z_{0m} was from the land cover method. Eq. 8.1 was used to estimate kB^{-1}. The vertical error bars give the standard deviation over the pixels along the line of sight of the LAS, while the horizontal error bars give the accuracy of the LAS measurements.

162
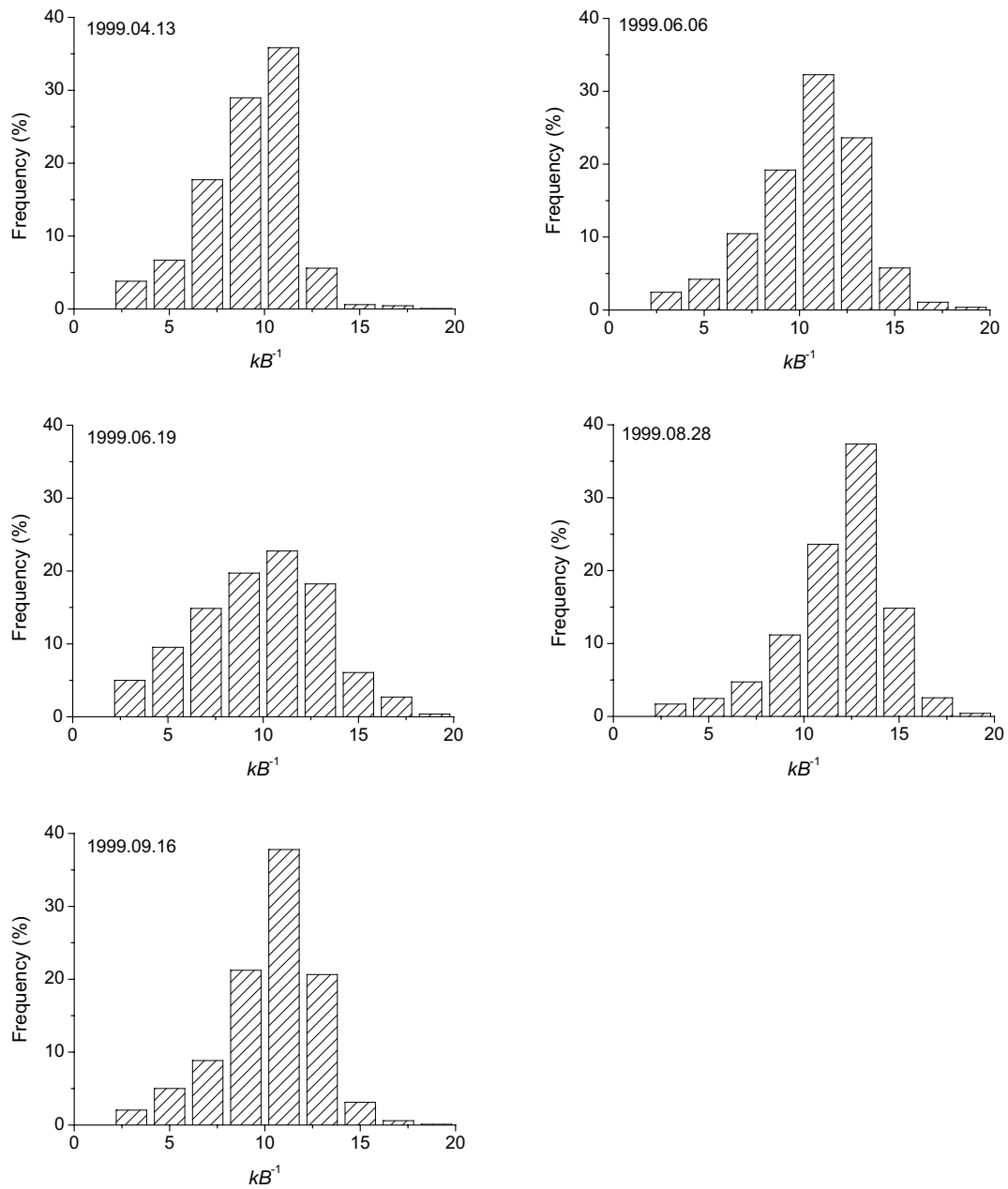
Figure 8.13 Histograms of kB^{-1} estimated by Eq. 8.1 over 50km x 50km area surrounding Tomelloso site of EWBMS in Spain.

The Eq. 4.64, in which the anisotropy in the canopy radiance was not considered, was also used in the single-source model to estimate H (Fig. 8.14). Comparing Fig. 8.12 and Fig. 8.14, it is interesting to see that Eq. 4.64 is applied better to a relatively homogenous land

surface. For instance, at Badajoz, the single-source model combining Eq. 4.64 gave a good agreement between the estimate and the measurements of H with RMSE about 50 W m^{-2}.
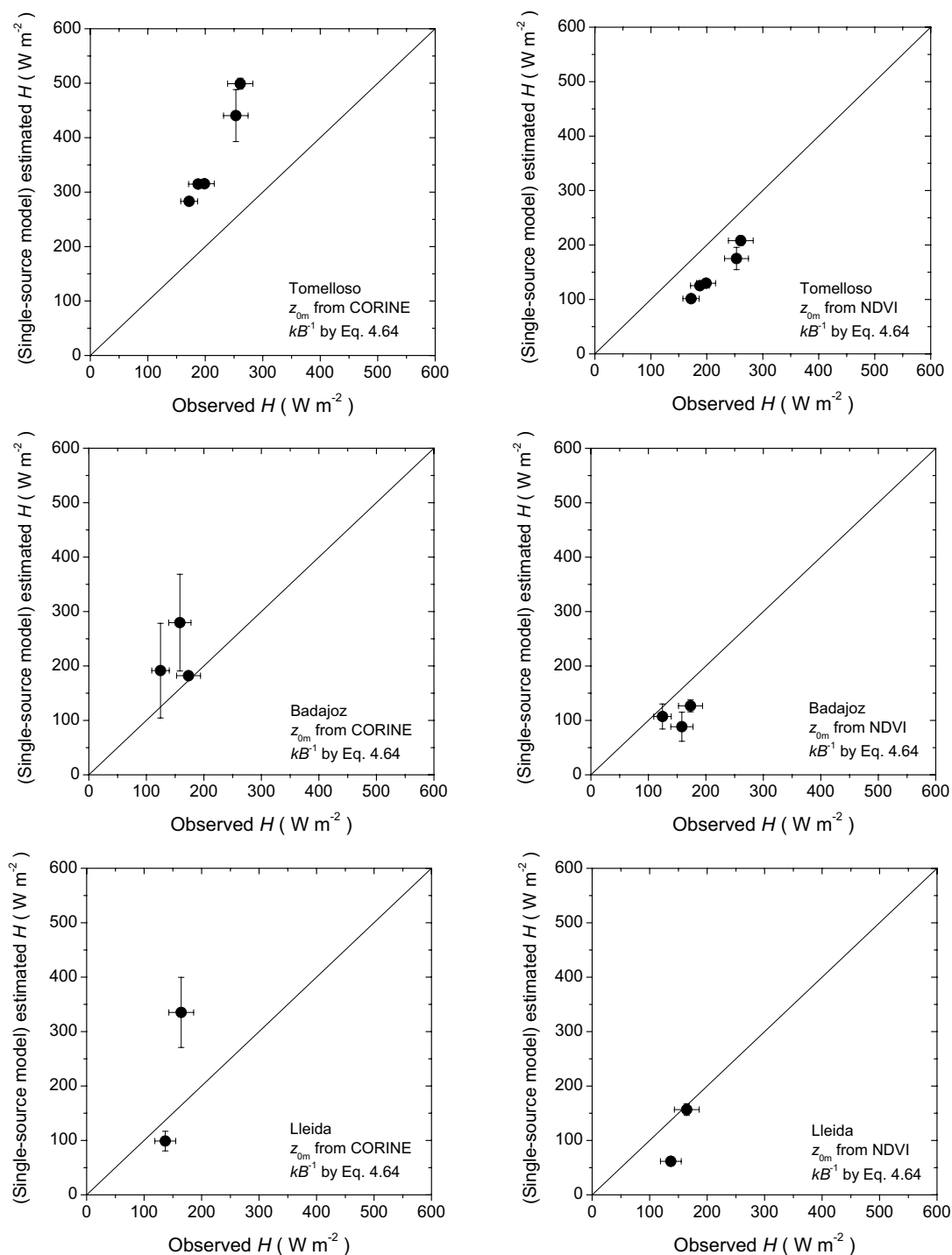
Figure 8.14 The same as Fig. 8.12, but Eq. 4.64 was used instead of Eq. 8.1.

Table 8.5 The Root Mean Square Error (RMSE) of estimates of H using both the dual-source model and the single-source model at the three experimental sites Tomelloso, Lleida and Badajoz using ATSR-2 bi-angular measurements.

Model	Tomelloso	Lleida	Badajoz
DM_1 : z_{0m} from land cover	**37.1**	122.9	98.3
DM_2 : z_{0m} from Eq. 8.5	**42.1**	111.2	93.9
SM_1 : z_{0m} from land cover kB^{-1} from Eq. 8.1	105.5	111.2	86.1
SM_2 : z_{0m} from Eq. 8.5 kB^{-1} from Eq. 8.1	68.2	94.6	91.9
SM_5 : z_{0m} from land cover kB^{-1} from Eq. 4.64	163.8	123.6	80.1
SM_4 : z_{0m} from Eq. 8.5 kB^{-1} from Eq. 4.64	67.0	**53.4**	**49.6**

8.4   Summary and conclusions

In this chapter, the proposed dual-source model and the single-source model were validated first by comparing the model estimates of sensible heat flux density H with ground measurements. The two models were then applied at the regional scale using surface variables determined with satellite radiometric data.

Validation with ground measurements showed that the dual-source model gives the best estimates of sensible heat flux density H in comparison with the single-source model with different parameterizations of resistance for heat transfer. The dual-source model avoids assumptions on the vertical and horizontal structure of the surface layer by dealing separately with heat transfer in the canopy air space and in the surface layer above the canopy. The single-source model treats the surface as an effective source for heat and water vapor transfer which extremely simplifies the 3D nature of the soil-vegetation system. However, the results from the single-source model were still acceptable if the resistance for heat transfer was estimated using an advanced parameterization of resistance derived from bi-angular measurements of $T_{b0}(\theta_v, \varphi_v)$.

The single-source and the dual-source model were then applied to estimate H over a larger area by combining the foliage and soil component temperatures retrieved from ATSR-2 bi-angular and multi-spectral measurements of radiance. The results from both models were compared with the LAS measurements over the three experimental sites with lines of sights of 1 km, 4.4km and 5km respectively and covering dry vineyard to irrigated area respectively. The dual-source model gave a good agreement over the vineyard land surface

where anisotropy in the exitance and heat exchange is significant due to the canopy structure. On the contrary, the dual-source model underestimated sensible heat flux which is probably partly due to the inaccurate retrieval of foliage and soil component temperatures.

The new parameterization of excess resistance in terms of kB^{-1} by the use of angular measurements of TOC brightness temperature also showed acceptable agreement with the measurements of sensible heat flux over vineyard area, but not for relatively homogeneous land surface such as the irrigated crops area. An aerodynamic based parameterization of kB^{-1}, however, gave a better agreement between the estimates and the measurements of H, while it gave overestimates of H over land characterized by large anisotropy.

As a conclusion, both the single-source model and the dual-source model are able to model the heterogeneity of heat exchange over the line of sight of the LAS due to the variation of surface conditions characterized by surface temperature, albedo and fractional vegetation cover as long as the anisotropy of the canopy exitance is taken into account properly in the parameterization.

For land targets characterized by large anisotropy, particularly large difference between foliage and soil component temperatures (see Fig 6.7), the dual-source model provides the best estimates of H.

Summary and conclusions

The land surface is often characterized by sparse or partial vegetation cover, e.g. in most of semi-arid area and also in agricultural land due to seasonality. Multi-spectral and bi-angular measurements of radiance from satellites have been used to study land-atmosphere interaction. Observations in the thermal infrared region provide information on exchange of energy and water between vegetation and atmosphere. Over sparse vegetation, significant anisotropy of emitted radiance is observed over vegetation canopies due to large differences in soil and foliage temperatures. It is problematic to define a 'surface' for a thermally heterogeneous canopy, in particular, when radiometric temperature as measured by a radiometer is used. A radiometer captures different contributions from soil and foliage when looking at the canopy at different zenith and azimuth viewing angles (Fig. 1.2), thus adding complexity to observation and modeling of surface temperature and heat exchange when using the radiometric temperature. This leads to inaccurate estimation of sensible and latent heat flux over partially covered land when using the classical single-source model of land – atmosphere heat transfer, which relates the surface heat flux to the temperature gradient between surface and air by an aerodynamic resistance (Fig. 1.3). Knowledge of thermal heterogeneity is therefore of relevance towards understanding and modelling land – atmosphere exchanges of energy and water.

In this thesis, the three-dimensional (3D) nature of radiative, heat and water vapor transfer within a soil-foliage system was investigated in detail (Chapter 2) by establishing a complete model to describe the radiative and convective processes in the canopy (Fig. 2.1). The complete model provides the physical basis to understand the relation of thermal heterogeneity of the land surface with the dependence of exitance on view angle. The *complete model*, however, *cannot be easily applied* to determine properties of heterogeneous land targets in practice, *because too many variables and unknowns are involved in the complete model*. Simplified models of radiative and heat transfer were therefore developed.

As the first step of simplification of the complete model, a *four-source model of heat transfer* (Eqs. 4.9 and 4.10), considering four components, i.e. sunlit foliage, shadowed foliage, sunlit soil and shadowed soil, was developed. The model assumes that each of the four components exchanges heat and water vapor with the atmosphere independently. The interaction between the four components are taken into account by introducing a reference height in the canopy which links the four components to the air within the canopy boundary layer resistances r_{ah, s_f}, r_{ah, sh_f}, r_{ah, s_s}, and r_{ah, s_sh}, and the canopy space to he atmosphere just above the canopy by an aerodynamic resistance r_{ah}. Such a four-component model of heat transfer requires the four component temperature. Thus, a simplified radiative model

was developed to consider the emissions from the *four components* (Eq. 3.13) by assuming that each component type has a mean temperature and the canopy geometry is characterized by the fractional area occupied by each component in the IFOV - the component fractional cover which changes only with zenith view angle. Such equations system is invertible to obtain the component temperatures when measurements of the thermal infrared (TIR) exitance are made at least at four zenith view angles, provided that the component emissivities are known and the component fractional covers can be derived based on e.g. multi-angular visible/near-infrared (VIS/NIR) radiance measurements.

Because of shadows, to retrieve the fractional cover of each component one needs to know the ratio of the height of the canopy and the distance between plants, besides leaf area index (LAI) and leaf area density. Multi-angular radiance measurements (at least at four view angles) are also needed which is not available from current space- and airborne observations. Moreover, the parameterization of resistances in the four-component model of heat transfer may need more information on canopy properties which may not be easy to derived using current remote sensing observations (see Chapter 3). As a consequence, an even simpler case - a *dual-source model of heat transfer* (Eqs. 4.10 – 4.13) was developed considering the interactions between foliage-atmosphere and soil-atmosphere. Foliage and the soil in the dual-source model, as in the four-source model, are linked by a reference height z_0 in the canopy. Three resistance, leaf boundary resistance, $r_{\mathrm{ah,\,f}}$, soil surface boundary resistance $r_{\mathrm{ah,\,s}}$, and the aerodynamic resistance between z_0 and overlying atmosphere, control the interactions of the foliage-soil system with the atmosphere.

A *linear mixture radiative model* (Eq. 3.19) accounting for the exitance from a mixture of foliage and soil components weighted by their respective fractional covers, was derived. In this two components radiance model, the vegetation forms a uniform layer covering the soil surface with fractional cover, this vegetation layer has an effective foliage temperature T_{f} and the underlying soil has effective soil temperature T_{s}, which both can be easily retrieved by inverting the linear mixture radiative model. The component fractional covers were determined either directly (Eq. 7.22) or via relationship with LAI (Eq. 6.7) using radiance measurements in the VIS-NIR-SWIR spectral regions.

The most simplified way to model heat exchange between the canopy and the atmosphere is a *single-source model* in which only a single TOC radiometric temperature is considered. An adequate parameterization of resistance is necessary to take into account for the substitution of aerodynamic temperature with radiometric temperature. An *aerodynamic-radiometric excess resistance* in terms of an *aerodynamic-radiometric non-dimensional parameter* kB^{-1} was introduced to adjust for the difference between the aerodynamic temperature and the radiometric temperature observed at nadir view angle (Eqs. 1.5 and 1.6).

A new parameterization of aerodynamic-radiometric parameter kB^{-1} (Eq. 8.1) was proposed based on bi-angular measurements of TOC radiometric temperature $T_{rad}(\theta_v)$ to characterize the thermal anisotropy of the foliage-soil system. The thermal heterogeneity of a partial canopy can be taken into account in a single-source model by using this new parameterization of kB^{-1} (Chapter 4 and Chapter 8).

The validation of the retrieved foliage and soil component temperatures using both field measurements (Chapter 6) and simulation data (Chapter 7) showed that the simple two components linear mixture model reproduced with satisfactory accuracy the three dimensional foliage-soil system for the canopies studied. The inversion of this model gave a good agreement of foliage and soil temperature with the measurements at the two experimental sites (Fig. 6.18 and Fig. 6.21): the root mean square error (RMSE) was 0.8K for soil temperature retrieval at the mixed grass land site (IMGRASS). At the winter wheat site (QRSLSP), the RMSE was 1.1 K for foliage temperature and 1.4 K for soil temperature in the early stage of crop growth. When fractional vegetation cover $f_f(\theta_v)$ was increasing with crop growth, a slightly larger RMSE of 1.9 K for foliage temperature and 2.0K for soil temperature was found for winter wheat.

The sensitivity study on the inversion of the simple linear mixture model (Eq.3.19) showed that retrievals of T_f and T_s by inverting Eq.3.19 are quite sensitive to the accuracy of both T_{b0} and to $f_f(\theta_v)$ when the difference of $f_f(\theta_v)$ between nadir and off-nadir is small due to either the two angles being too close or to the leaf inclination distribution function (LIDF) type, e.g. the planophile type of LIDF leads to a small change in $f_f(\theta_v)$ with θ_v. However, a larger difference of $f_f(\theta_v)$ between nadir and off-nadir zenith view angle leads to less sensitivity of the retrieved T_f and T_s to the accuracy of both T_{b0} and $f_f(\theta_v)$. This implies that measurements of T_{b0} at two very different θ_v are preferred to obtain more accurate retrievals of T_f and T_s. Besides, the use of different LIDF types to estimate $f_f(\theta_v)$ had a significant impact on the retrievals of T_f and T_s.

Estimates of the component temperatures of foliage T_f and soil T_s within a heterogeneous target were used to improve the parameterization of heat transfer at heterogeneous land surfaces. The performance of the proposed dual-source model and the improved single-source model have been evaluated using bi-angular measurements of brightness temperature T_{b0} and of sensible heat flux density H obtained in the field at the two experimental sites with different vegetation types (Chapter 8). The estimated H was compared with measurements done by eddy correlation and Bowen ratio systems. This local scale validation showed that the dual-source model gave the best estimates of H, better than

the single-source model including an advanced parameterization of resistance for heat transfer (Figs. 8.4, 8.5 and 8.7). This is attributed to the fact that the *dual-source model avoids assumptions on the vertical and horizontal structure of the surface layer by dealing separately with heat transfer in the canopy air space and in the surface layer above the canopy*. On the other hand the single-source model treats the surface as an effective source for heat and water vapor transfer which extremely simplifies the 3D nature of foliages-oil system. However, *the results from the single-source model were still acceptable if the resistance for heat transfer was parameterized taking into account canopy architecture and canopy thermal anisotropy through bi-angular observation of TOC radiometric temperature.*

To apply the linear mixture model at a larger spatial scale, multi-spectral and bi-angular measurements by space-borne instruments such as Along-Track Scanning Radiometer (ATSR)-2 were used. A new scheme of inverting component temperatures (Fig.7.1) was constructed including the following steps (Chapter 7):

- *Atmospheric correction.* Algorithms to determine atmospheric column water vapor and aerosol optical depth from the multi-spectral, bi-angular radiometric data provided by the ATSR-2 sensor have been developed. Atmospheric correction for the measurements in the VIS – SWIR channels of ATSR-2 was done using both atmospheric column water vapour and aerosol optical depth retrieved with the new algorithms. The atmospheric correction for TIR channels was done with a general Split Window (SW) algorithm derived for ATSR-2 nadir and forward views using the simulation data from MODTRAN 4.0 considering a range of atmospheric and surface conditions.

- *Estimation of fractional vegetation cover* $f_f(\theta_v)$. A stepwise multiple regression algorithm was derived to estimate fractional vegetation cover using ATSR-2 measurements in VIS, NIR and SWIR channels. Evaluation of the regression equation for $f_f(\theta_v)$ using synthetic images showed good agreement between the estimated and the reference values of $f_f(\theta_v)$.

The retrievals of T_f and T_s using ATSR-2 bi-angular and multi-spectral measurements of radiance were evaluated preliminarily by comparing the retrieved T_f with air temperature T_a. The retrieval of T_f shows good agreement with T_a. However, multi-angular measurements of exitance and of component temperatures at higher spatial resolution are still needed to accomplish more accurate validation of the retrieved component temperatures. As an alternative, simulated high resolution synthetic images from VIR/NIR to TIR domain were used to evaluate first the algorithm for $f_f(\theta_v)$ (Fig. 7.5 and Table 7.5) and then the retrieval of T_f and T_s because such high resolution synthetic images can provide more detailed information on the observed targets. The results (Fig. 7.8 and Table 7.6) showed that the

inversion of the simple linear mixture model (Eq.3.19) gives T_f and T_s values closed to the reference values.

The single-source and the dual-source model were applied to estimate sensible heat flux density H over a larger area by combining T_f and T_s retrieved from ATSR-2 bi-angular and multi-spectral measurements of radiance. The results from the dual-source compared well with the H measurements made by LAS over sparse canopy, i.e. at Tomelloso with vineyard land cover, while is underestimated H over relatively homogeneous area, i.e. at irrigated vegetation area, where the anisotropy of the foliage-soil system is not significant (Figs. 8.9 – 8.11 and Table 8.5). The single-source model with the new parameterization of resistance also gave acceptable results over vineyards (Fig. 8.12). However, without considering the anisotropy in the parameterization of resistance for heat transfer the single-source model only works well with relatively homogeneous land surface (Fig. 8.14). Both the dual-source model and the single-source model with the new parameterization for resistance using bi-angular measurements of TIR exitance are able to model the heterogeneity of heat exchange over the line of sight characterized by directional TOC radiometric temperature, albedo and fractional vegetation cover.

Perspectives for future research

The following issues were addressed for the further study with respect to modeling heat exchanges between land surface and the atmosphere using multi-angular and multi-spectral measurements:

- The accuracy in estimation of fractional vegetation cover is a crucial issue to retrieve accurately foliage and soil component temperatures using the linear mixture exitance model. Multi-angular and hyper-spectral observations at higher spatial resolution are expected to provide simultaneous multi-variables retrieval.
- The dual-source model was evaluated only based on limited vegetation type and canopy conditions, further studies over various sparse canopies are therefore necessary to access and to improve the model performance. The same task should also be accomplished for the single-source model with the new parameterization of resistance for heat transfer considering the anisotropy of foliage-soil system.
- Further effort will also be to estimate evaporation and transpiration separately by extending the dual-source model, which will benefit to the study of carbon cycle in a complex ecosystem, because foliage and soil often play different roles in CO_2 exchange in a ecosystem.

Samenvatting en conclusies

Het landoppervlak wordt vaak gekenmerkt door gedeeltelijke bodembedekking zoals in aride en semi-aride gebieden en als gevolg van de seizoenale processen (bijvoorbeeld landbouw). Om landoppervlak – atmosfeer uitwisselingsprocessen te kwantificeren is gebruik gemaakt van multi-spectrale en multi-angulaire radiometrische satellietwaarnemingen in het zichtbare en thermisch-infrarode bereik. Bij een gedeeltelijke bodembedekking is de variatie van de waargenomen radiantie met de kijkrichting aanzienlijk als gevolg van het grote temperatuursverschil tussen bladeren en bodem. Onder dergelijke omstandigheden is het niet mogelijk om eenduidig een oppervlak te identificeren en de temperatuur daarvan te meten, vooral wanneer gebruik wordt gemaakt van een stralingsmeter. Een stralingsmeter neemt de gesommeerde bijdragen van bladeren en bodem waar, terwijl de relatieve gewichten van bladeren en bodem op de waargenomen straling met de kijkrichting veranderen (Figuur 1.2). Dit laatste maakt het waarnemen van de gewastemperatuur en het modelleren van warmteuitwisseling aanzienlijk moeilijker. In het bijzonder kan de zogenaamde *single-source* warmteuitwisseling modelbenadering onnauwkeurige schattingen van voelbare en latente warmtestroom opleveren, omdat er uit wordt gegaan van een enkele oppervlaktetemperatuur (Figuur 1.3). Het kwantificeren van de thermische heterogeniteit van het gewas is dus een vereiste om landoppervlak – atmosfeer uitwisselingsprocessen te kunnen begrijpen en kwantificeren.

In dit proefschrift zijn de driedimensionale kenmerken van straling, warmte en waterdamp stromingsprocessen binnen een heterogeen bodem-bladeren systeem beschreven en geanalyseerd (Hoofdstuk 2). Dit is uitgevoerd door het uitwerken van een gedetailleerd model van stralings- en convectieve processen binnen een bodem-bladeren systeem (Figuur 2.1). Dit volledige model bevat de belangrijkste processen die nodig zijn om het verband tussen de thermische heterogeniteit van het systeem en de kijkrichtingafhankelijkheid van de waargenomen straling te kunnen begrijpen. Het grote aantal onbekende variabelen van het volledige model maakt het model moeilijk toepasbaar om eigenschappen van het landoppervlak te bepalen met behulp van stralingsmetingen. Daarom zijn vereenvoudigde modellen van stralings- en convectieve processen uitgewerkt.

Een belangrijke vereenvoudiging is gemaakt door aan te nemen dat er slechts vier componenten zijn, namelijk a) blad in het zonlicht en b) blad in de schaduw, c) bodem in het zonlicht en d) bodem in de schaduw, dit is de zogenaamde *four-source benadering* (Vergelijkingen 4.9 en 4.10). Er wordt vanuit gegaan dat warmteuitwisseling door elke component zonder directe interacties met de overige componenten kan plaatsvinden. Alle componenten wisselen warmte uit met de lucht. Er wordt een referentiehoogte genomen

binnen het systeem en vier grenslaagweerstanden toegepast: $r_{ah,\,s\_f}$, $r_{ah,\,sh\_f}$, $r_{ah,\,s\_s}$, en $r_{ah,\,s\_sh}$, terwijl warmteoverdracht met de lucht boven het bladerdak door een aërodynamische weerstand (r_{ah}) wordt bepaald. Om een dergelijk model toe te kunnen passen, moeten de bijbehorende temperaturen bepaald worden. Om dit te bewerkstelligen is er een vereenvoudigd stralingsuitwisselingsmodel uitgewerkt dat stralingsemissie door de vier componenten beschrijft (Vergelijking 3.13). Er wordt aangenomen dat elke component door een afzonderlijke temperatuur wordt gekenmerkt, terwijl met de structuur rekening wordt gehouden m.b.v. de binnen de kijkhoek waargenomen fractie van elke component, die van de kijkrichting afhankelijk is. De beoogde componenttemperaturen kunnen door het oplossen van de op deze wijze uitgewerkte vergelijkingen bepaald worden, indien straling bij vier verschillende kijkrichtingen gemeten kan worden. Daarnaast moeten de vier emissiviteiten van de vier componenten bepaald worden, m.b.v. multi-angulaire stralingsmetingen in het VIS/NIR bereik. Om de fractie bladeren en bodem te bepalen die in zich in het zonlicht dan wel schaduw bevinden, moet ook de planthoogte en de afstand tussen de planten bekend zijn. Uiteindelijk moeten ook de *leaf area index* en het specifieke bladoppervlak bepaald worden om het stelsel van vergelijkingen op te kunnen lossen. Vanuit het oogpunt van toepasbaarheid in relatie tot aardobservatie zijn deze beperkingen ongewenst.

Om deze reden is er een nog eenvoudiger warmteuitwisselingsmodel uitgewerkt, de zogenaamde *dual-source benadering* (Vergelijkingen 4.10 – 4.13), welke slechts een tweetal componenten in beschouwing neemt: bladeren en bodem. In overeenstemming met de *four-source benadering* wordt er een tweetal grenslaagweerstanden toegepast, $r_{ah,\,f}$ (blad), $r_{ah,\,s}$ (bodem) en een aërodynamische weerstand, r_{ah}. Stralingsoverdracht wordt door een *linear mixture* model (Vergelijking 3.19) beschreven, waar een bladtemperatuur, T_f, een bodemtemperatuur, T_s en een bodembedekkingsgraad worden toegepast. Door het inverteren van het model, kunnen beide temperaturen bepaald worden. De bodembedekkingsgraad wordt verkregen m.b.v. stralingsmetingen in het visuele, nabij-infrarode en thermische bereik (Vergelijking 6.7; Vergelijking 7.22).

Het eenvoudigste warmteuitwisselingsmodel is de zogenaamde *single-source benadering* waarbij slechts één radiometrisch temperatuur wordt toegepast, daardoor wordt een nauwkeurige parameterisatie van de aërodynamische weerstand van groot belang. Om het verschil tussen de aërodynamische en de radiometrische temperatuur te kwantificeren is er een zogenaamde *aerodynamic-radiometric excess* weerstand toegepast (Vergelijkingen 1.5 en 1.6). Daarnaast is een nieuwe parametrisatie van r_{ah} (Vergelijking 8.1) toegepast welke direct is afgeleid van multi-angulaire stralingsmeting in het thermisch infrarode bereik $T_{rad}(\theta_v)$, zie hoofdstukken 4 en 8.

Vergelijking van de door inversie van het zogenaamde *linear mixture* model verkregen blad temperaturen (T_f) en bodem temperaturen (T_s), heeft bewezen dat deze temperatuurschattingen nauwkeurig zijn. Hiervoor zijn zowel veldmetingen (Figuur 6.18, Figuur 6.21; Hoofdstuk 6) als synthetische gegevens (Hoofdstuk 7) toegepast. Vervolgens is de nauwkeurigheid van de *dual-source benadering* geëvalueerd, eerst met locale veldmetingen, daarna met satellietwaarnemingen en scintillometer schattingen op grotere lengteschaal. De beste resultaten zijn met de *dual-source benadering* verkregen, ook wanneer de *single-source* benadering met een verbeterde parameterisatie van r_{ah} toegepast werd (Figuren 8.4, 8.5 en 8.7), hoewel het gebruik van de parameterisatie gebaseerd op bi-angulaire metingen van $T_{rad}(\theta_v)$ de nauwkeurigheid van de *single-source benadering* sterk verbeterde.

Zowel de *linear mixture benadering* als het *dual-source benadering* zijn ook op grotere schaal toegepast m.b.v. de door de Along-Track Scanning Radiometer (ATSR)-2 verkregen multi-spectrale, bi-angulaire metingen. Om de blad- en bodemtemperaturen met satellietwaarnemingen te kunnen bepalen is een nieuwe procedure ontwikkeld (Hoofdstuk 7) en de nauwkeurigheid daarvan is geëvalueerd zowel met veldmetingen, als met synthetische gegevens. Dit laatste is stapsgewijs uitgevoerd: als eerste het algoritme om de bodembedekking te bepalen (Figuur 7.5 en Tabel 7.5), daarna T_f en T_s (Figuur 7.8 en Tabel 7.6) met goede resultaten.

Zowel de *single-source* als de *dual-source benadering* zijn toegepast om de voelbare warmtestroom H over een groter gebied te bepalen, waarbij scintillometer schattingen als referentie beschouwd werden. De nauwkeurigheid van de *dual-source benadering* bleek goed voor een heterogeen gebied, zoals Tomelloso, terwijl afwijkingen ten opzichte van de scintillometer schattingen groter waren voor een homogeen gebied met irrigatie (Figuren 8.9, 8.10 en 8.11 en Tabel 8.5).

Aanbevelingen voor nader onderzoek

Uit het uitgevoerde onderzoek en de bereikte resultaten kunnen enkele aanbevelingen ten behoeve toekomstige ontwikkelingen worden geformuleerd:

- De bodembedekkingsgraad moet met hoge nauwkeurigheid bepaald worden, om het *linear mixture* model op betrouwbare wijze te inverteren. Multi-angulaire, hyper-spectrale metingen met een hoge ruimtelijke resolutie kunnen in de toekomst gebruikt worden om de stelsels van vergelijking op te lossen en de variabelen in het *linear mixture model* simultaan te schatten.

- Het model werd geëvalueerd voor slechts enkele vegetatietypen. Dit moet in de toekomst verbeterd worden, ook wat betreft de *single-source benadering* om de nieuwe parameterisatie beter te kunnen evalueren.
- Een nadere gewenste ontwikkeling is het uitbreiden en verbeteren van de *dual-source benadering* om evaporatie en transpiratie apart te schatten, ook t.b.v. studies van CO_2 uitwisseling.

References

Albertson, J.D., Katul, G.G., and Wiberg, P., 2001, Relative importance of local and regional controls on coupled water, carbon, and energy fluxes, *Advances in Water Resources*, 24: 1103-1118.

Anderson, M.C., Norman, J.M., Diak, G.R., Kustas, W.P., and Mecikalski, J.R., 1997, A two-source time-integrated model for estimating surface fluxes using thermal infrared remote sensing, *Remote Sens. Environ.*, 60: 195-216.

Asrar, G., Myneni, R.B. and Choudhury, B.J., 1992, Spatial heterogeneity in vegetation canopies and remote sensing of absorbed photosynthetically active radiation: a modeling study*, Remote Sens. Environ.*, 41: 85-103.

Bailey, P., 1995, *SADIST-2 v100 products*, ER-TN-RAL-AT-2164, Space Science Department, Rutherford Appleton Laboratory (http://www.atsr.rl.ac.uk/software.html).

Balick, L. K., Hutchison, B. A., Smith, J. A., and McGuire, M. J., 1987, Directional thermal exitance distributions of a deciduous forest in summer, *IEEE Trans. Geosci. Remote Sensing,* 25: 410-412.

Bastiaanssen, W. G. M., 1995, *Regionalization of surface flux densities and moisture indicators in composite terrain*, Ph.D thesis, Wageningen Agriculture University.

Beck, A., Anderson, G.P., Acharya, P.K. et al., 1999, MODTRAN4 User's Manual, Air Force Research Laboratory, Hanscom AFB, MA.

Becker, F., Li, Z.-L., 1995, Surface temperature and emissivity at various scales: definition, measurement and related problems, *Remote Sensing Reviews*, 12: 225-253.

Beljaars, A.C.M., and Holtslag, A.A.M., 1991, Flux parameterization over land surface for atmospheric models, *J. Appl. Meteorol.*, 30: 327-341.

Blad, B.L., and Rosenberg, N.J., 1976, Evaluation of resistance and mass transport evapotranspiration models requiring canopy temperature data, *Agronomy Journal*, 68: 764-769.

Blümel, K., 1999, A simple formulation for estimation of the roughness length for heat transfer over partly vegetated surfaces, *J. Appl. Meteorol.*, 38: 814-829.

Blyth, E.M. and Dolman, A. J., 1995, The roughness length for heat of sparse vegetation, *J. Appl. Meteorol.*, 34: 583-585.

Bowen, I.S., 1926, The ratio of heat losses by conduction and by evaporation from any water surface, *Physics Review*, 27: 779-787.

Brutsaert, W.H., 1982, *Evaporation into the Atmosphere*, Reidel, Dordrecht, The Netherlands.

Brutsaert,W.H., and M. Sugita, 1992, Regional surface fluxes from satellite-derived surface temperatures (AVHRR) and radiosonde profiles, *Boundary-Layer Meteorol.*, 58:355-366.

Brutsaert, W.H., 1999, Aspects of bulk atmospheric boundary layer similarity under free-convective conditions, *Rev. Geophy.,* 37: 439-451.

Businger, J.A., J.C. Wyngaard, I. Izumi, and E.F. Bradley, 1971, Flux profile relationships in the atmospheric surface layer. *J. Atmos. Sci.*, 28: 181-189.

Campbell, G.S., and Norman, J.M., 1988, The description and measurement of plant canopy structure. In G. Russell et al. (ed.) Plant canopies: Their growth, form and function, *Soc. Exp. Biol.*, Seminar Series 31, Cambridge University Press, New York, 1-19.

Carlson, T. N., R. R. Gillies, and E. M. Perry, 1994. A method to make use of thermal infrared temperature and NDVI measurements to infer soil water content and fractional vegetation cover, *Remote Sens. Rev*., 52: 45-59.

Caselles, V., Sobrino, J. A., and Coll, C., 1992, A physical model for interpreting the land surface temperature obtained by remote sensors over incomplete canopies, *Remote Sens. Environ.*, 39: 203-211.

CEC, 1993, CORINE Land Cover technical guide, European Union, Directorate-General Environment, Nuclear Safety and Civil Protection, Luxemburg, ISBN 92-826-2578-8.

Chamberlain, A.C., 1968, Transport of gases to and from surfaces with bluff and wave-like roughness elements, *Quart. J. Roy. Meteorol. Soc.*, 94: 318-332.

Chedin, A., Scott, N. A., Wahiche, C., and Moulinier, P. 1985, The Improved Initialization Inversion Method: A High resolution Physical Method for Temperature Retrievals from Satellites of the TIROS-N Series. *J. Clim. Appl. Meteorol.*, 24:124 -143.

Chehbouni, A., Lo Seen, D., Njoku, E.G., and Monteny, B.M., 1996, Examination of the difference between radiative and aerodynamic surface temperatures over sparsely vegetated surfaces, *Remote Sens. Environ.*, 58: 177-186.

Choudhury, B.J., and Monteith, J.L., 1988, A four-layer model for the heat budget of homogeneous land surfaces, *Quart. J. Roy. Meteorol. Soc.*, 114: 373-398.

Choudhury, B.J., Idso, S.B., and Reginato, R.J., Analysis of an empirical model for soil heat flux under a growing wheat crop for estimating evaporation by an infrared-temperature based energy balance equation, *Agric. For. Meteorol.*, 39: 283-297, 1987.

Choudhury, B.J., Reginato, R.J. and Idso, S.B., 1986, An analysis of infrared temperature observations over wheat and calculation of the latent heat flux, *Agric. For. Meteorol.*, 37: 75-88.

Clothier, B.E., Clawson, K.L., Pinter, P.J., J.R., Moran, M.S., Reginato, R.J., and Jackson, R.D., Estimation of soil heat flux from net radiation during the growth of alfalfa, *Agric. For. Meteorol.*, 37: 319-329, 1986.

Clough, S. A., 1995, The water vapor continuum and its role in remote sensing, Optical Remote Sensing of the Atmosphere - OSA Technical Digest Series 2, 76-78.

Clough, S. A., Kneizys, F. X., and Davies, R. W., 1989, Line shape and the water vapor continuum, *Atmospheric Research*, 23: 229–241.

Colton, A. L., 1996, Effective thermal parameters for a heterogeneous land surface, *Remote Sens. Environ.*, 57: 143-160.

De Bruin, H.A.R., 2002, Renaissance of scintillometry, *Boundary-Layer Meteorol.*, 105: 1-4.

De Bruin, H.A.R., and Jacobs, C.M.J., 1989, Forest and regional scale processes, Phil; *Trans. R. Met Soc.*, B 324: 393-406.

De Bruin, H.A.R., B.J.J.M. van den Hurk and W. Kohsiek, 1995, The scintillation method tested over a dry vineyard area, *Boundary-Layer Meteorol.*, 76: 25-40.

Deanmead, O. T., and Bradley, E. F., 1985, Flux-gradient relationships in a forest canopy, in: B. A., Hutchinson and B. B. Hicks (Eds.), *The Forest-Atmosphere Interaction*, D. Reidel Publishing Company, Dordrecht, 421-442.

Deanmead, O. T., and Bradley, E. F., 1987, On scalar transport in plant canopies, *Irrigation Science*, 8: 13-149.

Feddes, R.A., 1971, *Water, heat and crop growth*, PhD. Thesis, Wageningen, Agricultral University, The Netherlands.

Finnigan, J. J., and Raupach, M.R., 1987, Transfer processes in plant canopies in relation to stomatal characteristics, in: Stomatal Function, E. Zeiger, G. Farquhar and I. Cowan, Stanford University Press, Stanford, CA, U.S.A., 385-429.

Finnigan,J.J., M.R.Raupach, E.F,Bradley, and G.K.Aldis, 1990, A wind tunnel study of turbulent flow over a two-dimensional ridge, *Boundary-Layer Meteorol.*, 50: 277-317.

Flowerdew, R.J. and Haigh, J.D., 1997, Retrieving land surface reflectances using the ATSR-2: A theoretical study, *J. Geophys. Res.,* 102(D14): 17163-17171.

François C., C. Ottlé, and L. Prévot, 1997, Analytical parameterization of canopy directional emissivity and directional radiance in the thermal infrared; Application on the retrieval of soil and foliage temperatures using two directional measurements, *Int. J. Remote Sensing*, 18(12): 2587-2621.

Francois, C., 2002, The potential of directional radiometric temperatures for monitoring soil and leaf temperature and soil moisture status, *Remote Sens. Environ.*, 80: 122– 133.

François, C., and C. Ottlé, 1994, Estimation of the angular variation of the sea surface emissivity with the ATSR/ERS-1 data, *Remote Sens. Environ.*, 48: 302-308.

Garratt, J.R., 1978, Transfer characteristics for a heterogeneous surface of large aerodynamic roughness, *Quart. J. Roy. Met. Soc.*, 104: 491-502.

Gausman, H.W., Escobar, D.E., Everitt, J.H., Richardson A.J. and Rodriquez, R.R., 1978, The leaf mesophylls of twenty crops, their light spectra, and geometrical parameters. SWC Research Report 423, Rio Grande Soil and Water Research Center, Weslaco, Texas, 88pp.

Goudriaan, J., 1977, Crop micrometeorology: a simulation study, Centre for Agricultural Publishing and Documentation, Wageningen, The Netherlands.

Hall, A.E., Canell, G.H., and Lawton, H.W., 1979, Agriculture in semi-arid environments, Springer-Verlag Berlin Heidelberg New York, 340pp.

Ham, J. M., and Heilman, J.L., 1991, Aerodynamic and surface resistances affecting energy transport in a sparse crop, *Agric. For. Meteorol.*, 53: 267-284.

Hapke, B., 1981, Bidirectional reflectance spectroscopy. 1. Theory, *J. Geophys. Res.,* 86: 3039-3054.

Hasager, C.B. and Jensen, N.O., 1999, Surface-flux aggregation in heterogeneous terrain, *Quart. J. Roy. Met. Soc.*, 125: 2075-2102.

Hatfield, J. L., Reginato, R.J. and Idso, S. B., 1984, Evaluation of canopy temperature – evapotranspiration models over various crops, *Agric. Meteorol.*, 32: 41-53.

Hatfield, J. L., 1988, Large scale evapotranspiration from remotely sensed surface temperature, Proc. on planning, now for irrigation and drainage Ir. Div. ASCE, Lincoln, NE, July 18-21, 502-509.Hollinger, S. E., and Daughtry, C. S. T. 1999, Southern Great Plains 1997 Hydrological Experiment: Vegetation Sampling and Data Documentation, Report to United States Department of Agriculture, Agricultural Research Service, on Contract nr. AG-58-1270-7-043.

Huband, N.D.S., and Monteith, J.L., 1986, Radiative surface temperature and energy balance of a wheat canopy, *Boundary-Layer Meteorol.*, 36: 1-17.

Idso, S. B., Aase, J.K., and Jackson, R. D., Net radiation-soil heat flux relations as influenced by soil water content variations, *Boundary-Layer Meteorol.*, 9: 113-122, 1975.

Iwasaki, H., 1994, Estimation of precipitable water over land using the split-window data from the NOAA satellite, *Journal of the Meteorological Society of Japan*, 72(2): 223–233.

Iwasaki, H., 1999, Case study on the distribution of precipitable water associated with local circulation using the split-window data of a NOAA satellite, *Journal of the Meteorological Society of Japan*, 77(3): 711–719.

Jackson, R.D. and Idso, S. B., 1975, Surface albedo and desertification, *Science*, 189: 1012-1013.

Jackson, R.D., 1982, Canopy temperature and crop water stress, *Advances in Irrigation*, 1: 43-85.

Jackson, R.D., 1985, Evaluating evapotranspiration at local and regional scales; *Proc. IEEE*, 73: 1086-1095.

Jackson, R.D., Idso, S.B., Reginato, R.J., and Pinter, P.J., 1981, Canopy temperature as a Crop Water Stress Indicator, *Water Resources Research*, 17(4): 1133-1138.

Jackson, R.D., Moran, M.S., Gay, L.W., and Raymond, L.H., 1987, Evaluating evaporation from field crop using airborne radiometry and ground-based meteorological data, *Irrig. Sci.*, 8: 81-90.

Jacobs, A.F.G., van Boxel, J.H., and El-Kilani, R.M.M., 1995, Vertical and horizontal distribution of wind speed and air temperature in a dense vegetation canopy, *J. Hydrol.*, 166: 313-326.

Jia, L., M. Menenti and Z.-L. Li, 2002, Sensitivity study of TIR directional emittance to soil water content and LAI in the soil-vegetation-atmosphere system, *Proc. 1ˢᵗ Int. Symp. on Recent Advances in Quantitative Remote Sensing* (ed. J.A. Sobrino), Universitat de Valencia, Spain, 686-691.

Jia, L., Menenti, M., Su, Z. B., Djepa, V., Li, Z.-L. and Wang, J., 2001, Modeling sensible heat flux using estimates of soil and foliage temperatures: the HEIFE and IMGRASS experiments, in "Remote sensing and climate modeling: Synergies and Limitations", M. Beniston and M. Verstraete (Eds.) Kluwer, Dordrecht, 23-49.

Jia, L., Su, Z., van den Hurk, B. J.J.M., Menenti, M., et al, 2003a, Estimation of sensible heat flux using the Surface Energy Balance System (SEBS) and ATSR measurements, *Journal of Physics and Chemistry of the Earth*, 8: 75-88.

Jia, L., Wang, J., and Hu, Z., 2000, The characteristics of roughness length for heat and its influence on determination of sensible heat flux in HEIFE area, *Plateau Meteorology*, (in Chinese), 19(4): 495-503.

Jia, L., Z.-L. Li, M. Menenti, Z. Su, W. Verhoef and Z. Wan, 2003b, A practical algorithm to infer soil and foliage component temperatures from bi-angular ATSR-2 data, *Int. J. Remote Sensing*, 24(23): 4739–4760.

Jia, L., Z.-L., Li and M., Menenti, 2001, Simulation of hyperspectral and directional radiance images using coupled biophysical and atmospheric RT-models: TIR region. In: Data Assimilation And Scaling for the Candidate Earth Explorer core SPECTRA (DAASCEES) (Contract nr. 15164/01/NL/SF), M. Menenti (Editor), 1st Progress Report, 35-48.

Kalma, J.D., and Jupp D.L.B., 1990, Estimating evaporation from pasture using infrared thermometry: evaluation of a one-layer resistance model, *Agric. For. Meteorol.*, 51: 223-246.

Kimes, D. S., 1980, Effects of vegetation canopy structure on remotely sensed canopy temperatures, *Remote Sens. Environ.*, 10: 165-174.

Kimes, D. S., 1981, Remote sensing of temperature profiles in vegetation canopies using multiple view angles and inversion techniques, *IEEE Trans. Geosci. Remote Sensing,* 19(2): 85-90.

Kimes, D. S., Smith, J. A., and Link, L. E., 1981, Thermal IR exitance model of a plant canopy, *Applied Optics*, 20(4): 623-632.

Kimes, D.S. and Kirchner, J. A., 1983, Directional radiometric measurements of row-crop temperatures, *Int. J. Remote Sensing*, 4: 299-311.

Kimes, D.S., 1983, Remote sensing of row crop structure and component temperatures using directional radiometric temperatures and inversion techniques, *Remote Sens. Environ.*, 3: 33-55.

Kimes, D.S., and Kirchner, J.A., 1983, Directional radiometric measurements of row-crop temperatures, *Int. J. Remote Sensing*, 4(2): 299-311.

Kustas, W. P., and Daughtry, C. S. T., 1990, Estimation of the soil heat flux/net radiation ratio from spectral data, *Agric. For. Meteorol.*, 49: 205-223.

Kustas, W.P., 1990, Estimates of evapotranspiration with a one- and two-layer model of heat transfer over partial canopy cover, *J. Appl. Meteorol.*, 29: 704-715.

Kustas, W.P., B.J. Choudhury, K.E. Kunkel, and L.W. Gay. 1989, Estimate of the aerodynamic roughness parameters over an incomplete canopy cover of cotton. *Agric. For. Meteorol.*, 46: 91–105.

Kustas, W.P., Choudhury, B.J., Reginato, M.S., Jackson, R.D., Gay, L.W., and Weaver, H.L., 1989, Determination of sensible heat flux over sparse canopy using thermal infrared data, *Agric. For. Meteorol.*, 44:197-216.

Kustas, W.P., Moran, M.S., Humes, K.S., Stannard, D.I., Pinter Jr., P.J., Hipps, L.E., Swiatek, E., and Goodrich, D.C., 1994, Surface energy balance estimates at local and regional scales using optical remote sensing from an aircraft platform and atmospheric data collected over semiarid rangelands, *Water Resource Research*, 30: 1241-1259.

Kustas, W.P., Stannard, D.I., and Allaine, K.J., 1996, Variability in surface energy flux partitioning during Washita '92: Resuting effects on Penman-Monteith and Priestly-Taylor parameters, *Agric. For. Meteorol.*, 82: 171-193.

Kuusk, A., 1985, The hot spot effect of a uniform vegetative cover. *Sov. J. Rem. Sens.*, 3: 645-658.

Lagouarde, J. P., Kerr, Y., and Brunet, Y., 1995, An experimental study of angular effects on surface temperature for various plant canopies and bare soils, *Agric. For. Meteorol.*, 77: 167-190.

Legg, B.J., and Monteith, J.L., 1975, Heat and mass transfer in plant canopies, in D.A. Devries and N.H. Afgan (Eds.), *Heat and Mass Transfer in the Biosphere*, Scripta Books, Washinton D.C., 167-186.

Lhomme, J.P., Monteny, B., Amadou, M., 1994a, Estimating sensible heat flux from radiometric temperature over sparse millet, *Agric. For. Meteorol.*, 68: 77-91.

Lhomme, J.-P., Monteny, B., Chehbouni, A., Troufleau, D., 1994b, Determination of sensible heat flux over Sahelian fallow savannah using infra-red thermometry, *Agric. For. Meteorol.*, 68: 93-105.

Lhomme, J.-P., Troufleau, D., Monteny, B., Chebhouni, A., and Bauduin, S., 1997, Sensible heat flux and radiometric surface temperatures over sparse Sahelian vegetation, II: A model for the kB^{-1} parameter, *J. Hydrol.*, 188-189: 839-854.

Li, Z.-L., Jia, L., Su, Z., Wan, Z., and Zhang, R., 2003, A New Approach for Retrieving Precipitable Water From ATSR2 Split-Window Channel Data Over Land Area, *Int. J. Remote Sensing*, 24: 5059-5117.

Li, Z.-L., Stoll, M.P., Zhang, R.H., Jia, L., and Su, Z., 2001, On the separate retrieval of soil and vegetation temperatures from ATSR2 data, *Science in China, series D*, 44: 97-111.

Liu, Q.-H., Li, X., and Chen, L.-F., 2002, Field Campaign for Quantitative Remote Sensing In Beijing, In *Final Proceedings: IGARSS'02 Symposiu*m, June 24-28 2002, Toronto, Canada, VI: 3133-3135.

Lu, D.R., 1997, Inner Mongolia Semi-Arid Grassland Soil Vegetation-Atmosphere Interaction (IMGRASS), *Global Change News Letter*, 31: 4-5.

Ma, Q., and Tipping, R., 1994, The detailed balance requirement and general empirical formalisms for continuum absorption, *Journal of Quantitative Spectroscopy Radiation Transfer*, 51: 751–757.

Mackay, G. and Steven, M.D., 1998, An atmospheric correction procedure for the ATSR-2 visible and near infrared land surface data, *Int. J. remote Sensing*, 19(15): 2949-2968.

Massman, W.J., 1997, An analytical one-dimensional model of momentum transfer by vegetation of arbitrary structure, *Boundary-Layer Meteorol.,* 83: 407-421.

Massman, W.J., 1999: A model study of kB_H^{-1} for vegetated surfaces using 'localized near-field' Lagrangian theory, *J. Hydrol.,* 223: 27-43.

Matsushima, D., and Kondo, J., 1997, A proper method for estimating sensible heat flux above a horizontal-homogeneous vegetation canopy using radiometric surface observations, *J. Appl. Meteorol.*, 36: 1696-711.

McGuire, M.J., Smith, J.A., Balick, L.K., and Hutchison, B.A., 1989, Modeling directional thermal radiance from a forest canopy, *Remote Sens. Environ.*, 27: 169-186.

McNaughton, K.G., and Van den Hurk, B.J.J.M., 1995, A 'Lagrangian' revision of the resistors in the two-layer model for calculating the energy budget of a plant canopy, *Boundary-Layer Meteorol.,* 74: 261-288.

Meijninger, W.M.L., Hartogensis, O.K., Kohsiek, W., Hoedjes, J.C.B., Zuurbier, R.M., De Bruin, H.A.R., 2002, Determination of area averaged sensible heat fluxes with a large aperture scintillometer over a heterogeneous surface - Flevoland field experiment, *Boundary-Layer Meteorol.*, 105: 63-83.

Menenti, M., Rast, M., Baret, F., Van den Hurk, B.J.J.M., Knorr, W., Mauser, W., Miller, J., Moreno, J., Schaepman, M., and Verstraete, M., 2003, Understanding vegetation response to climate variability from space: recent advances towards the SPECTRA Mission, In: R. Meynart et al. (Eds), *Sensors, Systems and Next Generation Satellites*, Proceedings Series, SPIE, Bellingham, USA, 5234: 76-85.

Menenti, M. and B. J. Choudhury, 1993, Parameterization of land surface evapotranspiration using a location- dependent potential evapotranspiration and surface temperature range. In: H.J. Bolle et al. (Eds.). *Exchange processes at the land surface for a range of space and time scales*, IAHS Publ. 212: 561-568.

Menenti, M., 1984, *Physical aspects and determination of evaporation in deserts – applying remote sensing techniques*, Ph.D. Thesis, Wageningen Agricultural University, Wageningen, The Netherlands.

Menenti, M., Jia, L., Li, Z.-L., Djepa,, V., Wang, J., Stoll, M.P., Su, Z.B., and Rast, M., 2001, Estimation of soil and vegetation temperatures with directional thermal infrared observations: the IMGRASS, HEIFE and SGP'97 experiments, *J. Geophys. Res.,* 106(D11): 11,997-12,010.

Menenti, M., Ritchie, J.C, 1994, Estimation of effective aerodynamic roughness length of Walnut Gulch watershed with laser altimeter measurements, *Water Resources Research*, 30: 1329-1337.

Miller, E.C., and Saunders, A.R., 1923, Some observations on the temperature of the leaves of crop plants, *J. Agric. Res.*, 26: 15-43.

Moene, A.F., 2001, Description of field experiments, in: Su, Z. and Jacobs, C. (Eds.), *Advanced Earth Observation - land surface climate*, Final Report, USP-2 Report 01-02, 183pp.

Moene, A.F., and De Bruin, H.A.R., 2001, Sensible heat flux data derived from the scintillometers, in: Su, Z. and Jacobs, C. (Eds.), *Advanced Earth Observation - land surface climate*, Final Report, USP-2 Report 01-02, 183pp.

Monteith, J. L., 1965, Evaporation and environment, In*: The State and Movement of Water in Living Organisms*, G.E. Fogg (ed.), *Sympos. Soc. Exper. Biol.*, Academic Press, N.Y., 19: 205-234.

Monteith, J. L., *Principles of Environmental Physics*, Elsevier, New York, 241pp, 1973.

Mutlow, C., Murray, J., Bailey, P., Birks A., and Smith, D., 1999, *ATSR-1/2 User Guide*, http://www.atsr.rl.ac.uk/documentation/docs/userguide/atsr_user_guide_rev_3.pdf.

Nielsen, D.C., Clawson, K. L., and Blad, B. L., 1984, Effect of solar azimuth and infrared thermometer view direction on measured soybean canopy temperature, *Agronomy Journal*, 76: 607-610.

Nilson, T., 1971, A theoretical analysis of the frequency of gaps in plant stands, *Agric. Meteorol.*, 8: 25-38.

Norman, J. M., Kustas, W. P., Humes, K. S., 1995, A tow source approach for estimating soil and vegetation energy fluxes in observations of directional radiometric surface temperature, *Agric. For. Meteorol.*, 77: 263-293.

Norman, J.M., 1975, Radiative transfer in vegetation, In: deVries, D.A and Afgan, N.H. (Eds.), *Heat and Mass Transfer in The Biosphere. Part 1 Transfer Processes in The Plant Environment*, John Wiley & Sons, New York, U.S.A.

Norman, J.M., 1979, Modeling the complete crop canopy, In: Barfield B.J and Gerbert J.F. (Eds.), *Modification of the Aerial Environment of Plants*, ASAE, Monogr. Am. Soc. Agric. Eng., St. Joseph, MI, 249-277.

Norman, J.M., and Campbell, G., 1983, Application of a plant-environment model to problems in irrigation, In: D. Hillel (Editor), *Advanced in irrigation*, 2, Academic Press, New York, 155-188.

Norman, J.M., and Chen, J. L., 1990, Thermal emissivity and infrared temperatures dependence on plant canopy architecture and view angle, in *Proceedings of the International Geoscience and Remote Sensing Symposium (IGARSS'90)*, pp. 1747-1750, IEEE Geoscience and Remote Sensing Society, New York, NY, USA.

Norman, J.M., and Jarvis, P.G., 1975, Photosynthesis of Sitka Spruce (*Picea Sitchensis* (Bong.) Carr.). V. Radiation penetration theory and a test case, *J. Appl. Ecol.*, 12: 839-878.

Norman, J.M., and Welles J.M., 1983, Radiative transfer in an array of canopies*, Agronomy Journal*, 75: 481-488.

Norman, J.M., Goel, N.S., Chen, J.-L., and Sun, S.F., 1992, Relating directional infrared canopy temperatures to plant water stress, *Proc. 12th Ann. Inter., Geoscience Remote Sensing Symp.*, Vol. I, pp. 755-756, IEEE, 445 Hoes Lane, Piscataway, NJ 08854.

North, P.R.J., Briggs, S.A., Plummer, S.E. and Settle, J.J., 1999, Retrieval of land surface bi-directional reflectance and aerosol opacity from ATSR-2 multiangle imagery, *IEEE Trans. Geosci. Remote Sensing,* 37(1): 526-537.

Otterman, J., Brakke, T.W., and Susskind, J., 1992, A model for inferring canopy and underlying soil temperatures from multi-directional measurements*, Boundary-Layer Meteorol.*, 61: 81-97.

Ottermann, J., J. Susskind, T. W. Brakke, D. S. Kimes, R. Pielke, and T. J. Lee, 1995, Inferring the thermal-infrared hemispheric emission from a sparsely vegetated surface by directional measurements, *Boundary- Layer Meteorol.*, 74: 163-180.

Ottermann, J., T. W. Brakke, M. Fuchs, V. Lakshmi, and M. Cadeddu, 1999, Longwave emission from a plant/soil surface as a function of the view direction; Dependence on the canopy architecture, *Int. J. Remote Sensing*, 20 (11): 2195-2201.

Owen, P.R., and W.R. Thomson, 1963, Heat transfer across rough surface, *J. Fluid Mech.*, 15: 321-334.

Paw U, K. T., 1991, Anisotropy of thermal infrared exitance above and within plant canopies, in: *Physical Measurements and Signatures in Remote Sensing*, *ESA,* SP-319: 369-374.

Paw U, K.T., 1992, Development of models for thermal infrared radiation above and within plant canopies, *ISPRS Journal of Photogrammetry and Remote Sensing*, 47: 189-203.

Penman, H.L., 1948, Natural evaporation from open water, bare soil, and grass, *Pro. Roy. Soc.*, London, A193: 120-146.

Press, W.H., Flannery, B.P., Teukolsky, S.A. and Vetterling, W.T., 1989, *Numerical recipes*, Cambridge, U.K., Cambridge Univ. Press.

Prévot, L., Brunet, Y., Paw U, K. T., and Seguin, B., 1994, Canopy modelling for estimating sensible heat flux from thermal infrared measurements, in: *Proc. Workshop on Thermal Remote Sensing of The Energy And Water Balance Over Vegetation in Conjunction With Other Sensors* (La Londe), 17-22.

Price, J.C., 1982, On the use of satellite data to infer surface fluxes at meteorological scales*, J. Appl. Meteorol.*, 21: 1111-1122.

Priestley, C.H.B., and Taylor, R.J., 1972, On the assessment of surface heat flux and evaporation using large-scale parameters, *Mon. Weather Rev.*, 100: 81-92.

Rahman, H. and Dedieu, G., 1994, SMAC: a simplified method for the atmospheric correction of satellite measurements in the solar spectrum. *Int. J. Remote Sensing*, 15: 123-143.

Raupach, M.R., 1988, Canopy transport processes, in: Steffen, W. L. and Denmead, O. T. (Eds.), *The Natural Environment: Advances and Applications*, Spring-Verlag, Berlin, 95-127.

Raupach, M.R., 1989, A practical Lagrangian method for relating scalar concentrations to source distributions in vegetation canopies, *Quart. J. Roy. Meteorol. Soc.*, 115: 609-632.

Ross, J., 1981, *The radiation regime and architecture of plant stands*, Dr. W. Junk Publishers, The Hague, 391pp.

Raupach, M.R., 1992, Drag and Drag partition on rough surfaces, *Boundary-Layer Meterol.*, 60: 375-395.

Salisbury, J.W., and D'Aria, D.M., 1992, Emissivity of terrestrial materials in the 8-14mm atmospheric window, *Remote Sens. Environ.*, 42: 83-106.

Sauer, T.J., and Norman, J.M., 1995, Simulated canopy microclimate using estimated below-canopy soil surface transfer coefficients, *Agric. For. Meteorol.*, 75: 135-160.

Saunders, R.W. and Kriebel, K.T, 1988, An improved method for detecting clear sky and cloudy radiances from AVHRR data, *Int. J. Remote Sensing,* 9: 123-150.

Schmugge, T.J., W.B. Kustas, K.S. Humes, 1998, Monitoring of Land Surface Fluxes Using ASTER Observations, *IEEE Trans. Geosci. Remote Sensing*, 36: 1421 - 1430.

Seguin, B., Assad, E., Freteaud, J. P., Imbernon, J., Kerr, Y. H., and Lagouarde, J. P., 1989, Use of meteorological satellite for water balance monitoring in Sahelian regions, *Int. J. Remote Sens.*, 10: 1001-1017.

Shuttleworth, W.J., and Wallace, J.S., 1985, Evaporation from sparse crops – an energy combination theory, *Quart. J. Roy. Meteorol. Soc.*, 111: 839-855.

Smith, D.L., Read, P.D. and Mutlow, C.T., 1997, The Calibration of the Visible/Near Infra-Red Channels of the Along-Track Scanning Radiometer-2 (ATSR-2), in: *Sensors, Systems and Next-Generation Satellites*, Hiroyuki Fujisadsa (Editor), *Proceedings of SPIE*, 3221: 53-62.

Smith, J. A., Ranson, K. J., Nguyen, D., Balick, L., Link, L. E., Fritschen, L., and Hutchison, B. A., 1981, Thermal vegetation canopy model studies, *Remote Sens. Environ.*, 11: 311-326.

Smith, J.A., and S. M. Goltz, 1995, A thermal exitance and energy balance model for forest canopies, *IEEE Trans. Geosci. Remote Sensing,* 32(5): 1060-1066.

Smith, J.A., Chauchan, N. S., and Ballard, J., 1996, Remote sensing of land surface temperature: the directional viewing effect, *IEEE Trans. Geosci. Remote Sensing*, 13(4): 2146-2148.

Smith. R.C.G., Barrs, H.D., and Fisher, R.A., 1988, Inferring stomatal resistance of sparse crops from infrared measurements of foliage temperature, *Agric. For. Meteorol.*, 7: 183-189.

Sobrino, J., Li. Z.-L., Stoll, M. P. and Becker, F., 1994, Improvements in the split-window technique for land surface temperature determination, *IEEE Trans. Geosci. Remote Sensing*, 32(2): 243-253.

Sobrino, J.A., and Caselles, V., 1990, Thermal Infrared radiance model for interpreting the directional radiometric temperature of a vegetative surface, *Remote Sens. Environ.*, 33: 193-199.

Sobrino, J.A., Caselles, V. and Becker, F., 1990, Significance of the remote sensed thermal infrared measurements obtained over a citrus orchard, *ISPRS Journal Photogramm and Remote Sensing*, 44: 343-354.

Stanghellini, C., 1987, *Transpiration of greenhouse crops – an aid to climate management*, Ph.D thesis, Agriculture University, Wageningen, The Netherlands.

Stewart, J.B., Kustas, W.P., Humes, K.S., Nichols, W.D., Moran, M.S., and de Bruin, A.A.R., 1994, Sensible heat flux-radiometric surface temperature relationship for eight semiarid areas*, Agric. For. Meteorol.*, 33: 1110-1117.

Stoll, M. P., Z.-L. Li, and J. Labed, 1998, Sensitivity study in directional TIR radiance measurements: Atmospheric corrections and heterogeneity, in *Spatial and Spectral Scales of Spaceborne Imaging Spectro-radiometers (SASSSIS)*, W. Verhoef and M.Menenti (Eds.), *NLR Cont. Rep.* CR – 98424, National Aerospace Laboratory, Amsterdam, The Netherlands, 212-219.

Su, Z., 2002, The Surface Energy Balance System (SEBS) for estimation of turbulent heat fluxes, *Hydrology and Earth System Sciences*, 6(1): 85-99.

Su, Z., Wang, J., Wen, J., Jia, L., Menenti, M., 1999, Field observations during IMGRASS - An examination on possibilities of using AATSR data to estimate soil and vegetation temperature, *Proc. Int. Geosci. And Remote Sens. Symp.*, 1999, 634-645. Also in: Su, Z. and Menenti, M. (Eds.), Mesoscale climate hydrology: the contribution of the new observing systems, Report USP-2, Winand Staring Centre, Wageningen UR, The Netherlands, pp141.

Su, Z.B., Schmugge, T., Kustas, W. P., and Massman, W. J., 2001, An Evaluation of Two Models for Estimation of the Roughness Height for Heat Transfer between the Land Surface and the Atmosphere, *J. Appl. Meteorol.*, 40: 1933-1951.

Sutherland, R.A. and Bartholic, J.F., 1977, Significance of vegetation in interpreting thermal radiation from a terrestrial surface, *J. Appl. Meteorol.*, 18: 759-763.

Theriault, J-M., Roney, P. L., St.-Germain, D., Revercomb, H. E., Knuteson, R. O., and Smith, W. L., 1994, Analysis of the FASCODE model and its H2O continuum based on long-path atmospheric transmission measurements in the 4.5–11.5 micron region, *Applied Optics*, 33(3): 323–333.

Thom, A.S., 1972, Momentum, mass, and heat exchange in vegetation, *Quart. J. Roy. Meteorol. Soc.*, 98: 124-134.

Troufleau, D, Lhomme, J.-P., Monteny, B., Vidal, A., and Moran, M.S., 1995, Using thermal infrared temperature over sparse semi-arid vegetation for sensible heat flux estimation, *Proc. IGARSS'95*, Firenze, July 10-14, 1995, 2227-2229.

Troufleou, D., Lhomme, J.P., Monteny, B., and Vidal, A., 1997, Sensible heat flux and radiometric surface temperature over sparse Sahelian vegetation. I. An experimental analysis of the kB^{-1} parameter, *J. Hydrol.*, 188-189: 815-838.

Van den Hurk, B.J.J.M. and McNaughton, K.G., 1995, Implementation of near-field dispersion in a simple two-layer surface resistance model, *J. Hydrol.*, 166: 293-311.

Van den Hurk, B.J.J.M., Jia, L., Jacobs, C., Menenti, M., and Li, Z.-L., 2002, Assimilation of land surface temperature data from ATSR in an NWP environment – a case study, *Int. J. Remote Sensing*, 23(24): 5193-5210.

Verhoef, A., De Bruin, H.A.R., and Van Den Hurk, B.J.J.M., 1997, Some practical notes on the parameter kB^{-1} for sparse vegetation, *J. Appl. Meteorol.*, 36: 560-572.

Verhoef, W. and Bach, H., 2003, Simulation of hyperspectral and directional radiance images using coupled biophysical and atmospheric radiative transfer models, *Remote Sens. Environ.*, 87: 23–41.

Verhoef, W. and Menenti, M, 1998, Spatial and Spectral Scales of Spaceborne Imaging Spectro-radiometers (SASSSIS), Final Report, NLR-CR-98213, National Aerospace Lab. (NLR), Amsterdam, the Netherlands.

Verhoef, W., 1998, Theory of radiative transfer models applied in optical remote sensing of vegetation canopies, PhD thesis, Wageningen Agricultural University, 310pp.

Verhoef, W., 2001, Development of algorithms for estimation of atmospheric and surface physical parameters. in Su, Z. and Jacobs, C. (Eds.), *Advanced Earth Observation - land surface climate*, Final Report, USP-2 Report 01-02, 183pp.

Verma, S.B, Rosenberg, N.J., Blad, B.L. and Baradas, N.W., 1976, Resistance-energy balance method for predicting evapotranpiration, determination of boundary layer resistance, and evaluation of error effects, *Agronomy Journal*, 68: 776-782.

Vermote, E.F., Tanre, D., Deuze, J.L., Herman, M. and Morcrette, J.-J., 1997, Second simulation of the satellite signal in the solar spectrum, 6S: An overview, *IEEE Trans. Geosci. Remote Sensing*, 35: 675-686.

Vinning, R.C., and Blad, B.L., 1992, Estimation of sensible heat flux from remotely sensed canopy temperatures, *J. Geophys. Res.,* 97: 18,951-18,954.

Welles, J.M. and Norman, J.M., 1991, Photon Transport in discontinuous canopies: a weighted random approach, In: Myneni, R.B. and Ross, J. (Eds*.), Photon-Vegetation Interactions. Applications in Optical Remote Sensing and Plant Ecology*, Springer-Verlag.

Wilson, T.B., Norman, J.M., Bland, W.L., and Kucharik, C.J., 2002, Evaluation of the importance of Lagrangian canopy turbulence formulations in a soil-plant-atmosphere model, *Agric. For. Meteorol.*, 115: 51-69.

Wieringa, J, 1993, Representative roughness parameters for homogeneous terrain, *Boundary-Layer Meteorol.*, 63: 323-363.

Xue, Y., Llewellyn-Jones, D. T., Lawrence, S. P., and Mutlow, C. T., 2000, On the Earth's surface energy exchange determination from ERS satellite ATSR data: Part 2. Short-wave radiation, *Int. J.Remote Sensing*, 21(18): 3415–3426.

Zhan, X., W.P. Kustas, and K.S. Humes, 1996, An intercomparison study on models of sensible heat flux over partial canopy surfaces with remotely sensed surface temperature, *Remote Sens. Environ.*, 58: 242–256.

Appendix I

Calculation of diffuse radiation flux density $R_{Df}^{uh}(\vec{r})$ and $R_{Df}^{lh}(\vec{r})$ in a 3D canopy

To use the multiple scattering theory for a 1D layered canopy as developed by Norman and Jarvis (1975) in a 3D canopy, *an equivalent 1D canopy* must be defined such that the calculation of $R_{Df}^{uh}(\vec{r})$ and $R_{Df}^{lh}(\vec{r})$ (in Eqs.2.6 and 2.7) can be done with the 1D theory. The equivalent 1D model is described briefly below.

In a 1D canopy, the probability of penetration of diffuse radiation from the upper hemisphere non-intercepted to a point (or a leaf) in the canopy, $P_{D1}(\theta)$, is (Norman, 1975)

$$P_{D1}(\theta) = \frac{\int_0^{2\pi} \int_0^{\pi/2} \Gamma(\theta,\varphi) P_{B1}(\theta)\,\sin\theta\,\cos\theta\,d\theta\,d\varphi}{\pi} \tag{A1.1}$$

where $\Gamma(\theta,\varphi)$ is the intensity distribution. The probability of penetration of direct radiation, $P_{B1}(\theta)$, in Eq. (A1.1) is

$$P_{B1}(\theta) = \exp(-k_\alpha \rho_f D(\theta,\varphi)) \tag{A1.2}$$

where ρ_f is the total foliage area density in the 1D canopy, D is the total path length through the canopy and usually expressed as $\rho_f D = \dfrac{LAI}{\cos\theta}$. The parameter k_α was defined before (Chapter 6).

According to Norman and Welles (1983), such theory can be extended to array canopies provided that:

a) The foliage area density ρ_f of the 1D canopy equals the leaf density of the sub-canopies in the 3D canopy.

b) The orientation distribution of foliage in the sub-canopy is the same as that in the 1D horizontal canopy.

c) The soil surface has the same physical and optical properties both in 1D and 3D canopies.

d) The diffuse penetration probability $P_{Df}(\vec{r})$ for the grid point $\vec{r}$ for the upper (lower) hemisphere $P_{Df}(\vec{r}) = P_{Df,U}$ ($P_{Df}(\vec{r}) = P_{Df,L}$) can be duplicated at point H in the 1D canopy.

The diffuse fluxes at grid point $\vec{r}$ in the sub-canopy in an array canopy are obtained by calculating the diffuse fluxes at point H in the equivalent 1D canopy following the procedures below (see Fig. A1 for the illustration):

1. Compute the $P_{Df,U}$ and $P_{Df,L}$ at grid point $\vec{r}$ in the sub-canopy in an array canopy (Fig. A1(a));

2. Divide the equivalent 1D canopy in a number of horizontal layers and compute $P_{D1}(Z)$ for these layers (Fig. A1(b));

3. Look for point Z_1 in the equivalent 1D canopy such that $P_{D1,U}(Z_1) = P_{Df,U}$, and Z_2 such that $P_{D1,L}(Z_2) = P_{Df,L}$ (Fig. A1(c));

4. The multiple scattering model derived by Norman and Jarvis (1975) is applied to compute the downward diffuse flux above layer Z_1 and the upward diffuse flux below layer Z_2 (see Norman and Jarvis (1975) for the details of the model);

5. These diffuse fluxes then are applied to the grid-point $\vec{r}$ in the sub-canopy in an array canopy.
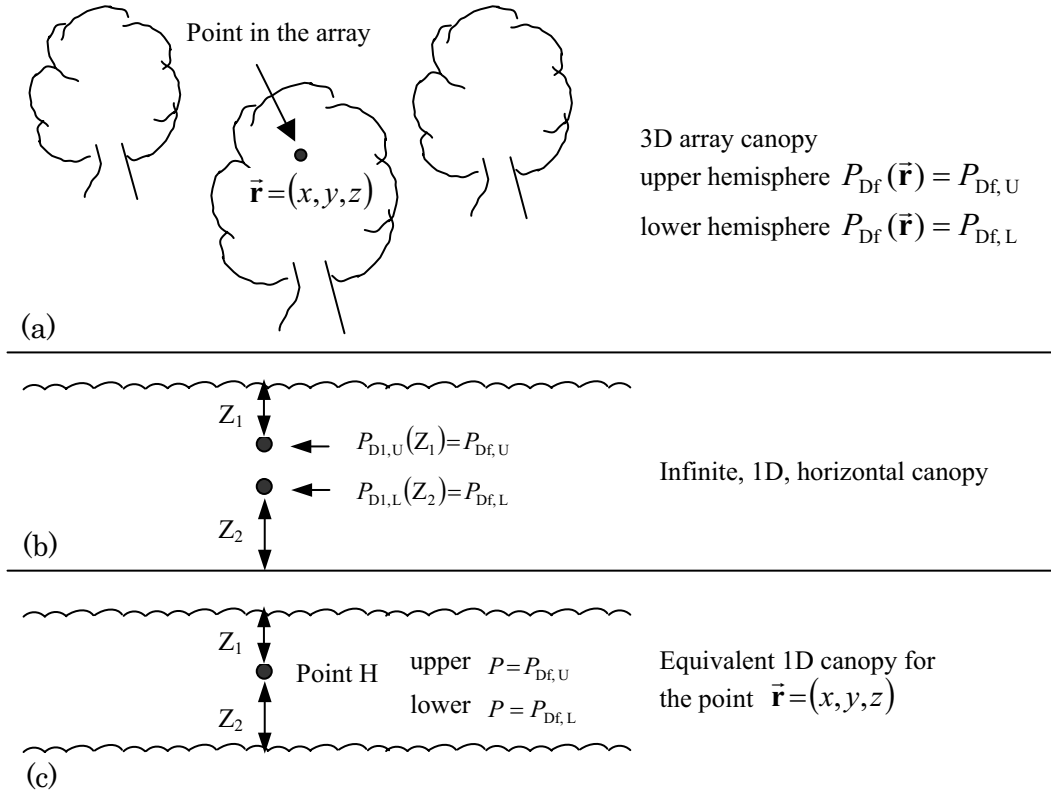

Figure A1 Illustration of the procedure used to find a point H in an infinite horizontal canopy such that the scattered radiative flux density computed for point H is applicable to the point $\vec{r} = (x, y, z)$ in an array canopy (reproduced from Norman and Welles, 1983).

188

Appendix II

Calculation of thermal infrared radiation flux density $R_{\text{TIR}}^{\text{U}}(\vec{\mathbf{r}}, \mathbf{\Omega_L})$ in a 3D canopy

The calculation of $R_{\text{TIR}}^{\text{U}}(\vec{\mathbf{r}}, \mathbf{\Omega_L})$ is done as follows.

Assuming leaves in the canopy in all grid-points emit thermal radiation in an isotropic manner and each grid-point has a constant emissivity ε and a mean temperature $T(\vec{\mathbf{r}})$, the emitted radiance Rad (W m^{-2}sr^{-1}) from the point $\vec{\mathbf{r}}$ is

$$Rad = \frac{\varepsilon\sigma T(\vec{\mathbf{r}})^4}{\pi} \tag{A2.1}$$

This emitted radiance Rad by a leaf in the grid-point $\vec{\mathbf{r}}$ is identical in all directions; however the irradiance on the leaf surface in each grid-point $\vec{\mathbf{r}}$ depends on the possibility of $\vec{\mathbf{r}}$ being able to see the source grid-point. This is determined by a so-called *hit-probability*, $Phit_{\text{ij}}(\vec{\mathbf{r}})$, of a ray originating from point $\vec{\mathbf{r}}$ in the direction of the midvector of the sector i in the hemispherical band j. The value of $Phit_{\text{ij}}(\vec{\mathbf{r}})$ is 1 if the ray hits a neighboring grid-point and this point is considered as the only contributor emitting to the point $\vec{\mathbf{r}}$ in the associated direction. If no grid-point either containing foliage or soil is hit, the atmosphere is the thermal emitter to this point.

The irradiance on the small plane normal to the midvector of sector i in the hemispherical band j at grid-point $\vec{\mathbf{r}}$, $Irrad_{\text{ij}}$, then is calculated as

$$Irrad_{\text{ij}} = \frac{\int_{\varphi_{\text{ij1}}}^{\varphi_{\text{ij2}}} \int_{\theta_{\text{ij1}}}^{\theta_{\text{ij2}}} Rad(\theta,\varphi)\, Phit(\theta,\varphi)\, \cos\theta\, \mathrm{d}\theta\, \mathrm{d}\varphi}{\int_{\varphi_{\text{ij1}}}^{\varphi_{\text{ij2}}} \int_{\theta_{\text{ij1}}}^{\theta_{\text{ij2}}} \cos\theta\, \mathrm{d}\theta\, \mathrm{d}\varphi} \tag{A2.2}$$

where $Rad(\theta,\varphi)$ is the radiance from the emitting elements in the direction (θ,φ), θ_{ij1} and θ_{ij2} are the zenith limits of sector i in the hemispherical band j, and φ_{ij1} and φ_{ij2} are the azimuth limits of sector i in the hemispherical band j, $Phit(\theta,\varphi)$ is the hit-probability in the direction (θ,φ).

For leaves in the leaf angle class $\mathbf{\Omega_L}$, the absorbed irradiance from source sector i in the hemispherical band j, $R_{\mathrm{TIR},ij}^{\mathrm{U}}(\vec{\mathbf{r}},\mathbf{\Omega_L})$, is calculated by correcting EqA2.2 with the dot product of source sector i in the hemispherical band j, $\mathbf{V}_{ij}$, and the normal of leaves with leaf angle, $\mathbf{\Omega_L}$,

$$R_{\mathrm{TIR},ij}^{\mathrm{U}}(\vec{\mathbf{r}},\mathbf{\Omega_L}) = \varepsilon\, Irrad_{ij}\, \mathbf{V}_{ij}\cdot\mathbf{\Omega_L} \tag{A2.3}$$

where $\mathbf{V}_{ij}$ and $\mathbf{\Omega_L}$ are expressed in terms of direction cosines as,

$$\mathbf{V}_{ij} = \begin{bmatrix} \sin(\theta_{ij})\,\cos(\varphi_{ij}) \\ \sin(\theta_{ij})\,\sin(\varphi_{ij}) \\ \cos(\theta_{ij}) \end{bmatrix} \tag{A2.4}$$

and

$$\mathbf{\Omega_L} = \begin{bmatrix} \sin(\theta_{L})\,\cos(\varphi_{L}) \\ \sin(\theta_{L})\,\sin(\varphi_{L}) \\ \sin(\theta_{L}) \end{bmatrix} \tag{A2.5}$$

Then the thermal irradiance, $R_{\mathrm{TIR}}^{\mathrm{U}}(\vec{\mathbf{r}},\mathbf{\Omega_L})$, that is emitted by elements in all sectors and all bands in the upper hemisphere and absorbed by the leaves with leaf angle $\mathbf{\Omega_L}$ at grid-point $\vec{\mathbf{r}}$ is

$$R_{\mathrm{TIR}}^{\mathrm{U}}(\vec{\mathbf{r}},\mathbf{\Omega_L}) = \varepsilon\sum_{i=1}^{18}\sum_{j=1}^{9} Irrad_{ij}\, \mathbf{V}_{ij}\cdot\mathbf{\Omega_L} \tag{A2.6}$$

Considering $Phit_{ij}(\vec{\mathbf{r}})$ is constant within sector i in band j and eighteen sectors within j band have equal solid angle, Eq.A2.2 can be written as

$$\begin{aligned} Irrad_{ij} &= Rad_{ij}\, Phit_{ij}(\theta_{ij},\varphi_{ij})\frac{1}{18}\int_{0}^{2\pi}\mathrm{d}\varphi\int_{\theta_{ij_1}}^{\theta_{ij_2}}\cos\theta\,\mathrm{d}\theta \\[2mm] &= Rad_{ij}\, Phit_{ij}(\theta_{ij},\varphi_{ij})\frac{\pi}{9}(\sin\theta_{ij2}-\sin\theta_{ij1}) \\[2mm] &= \varepsilon\sigma T_{ij}^{4}\, Phit_{ij}(\theta_{ij},\varphi_{ij})\frac{(\sin\theta_{ij2}-\sin\theta_{ij1})}{9} \end{aligned} \tag{A2.7}$$

where T_{ij} is the mean temperature of a grid point that is in the sector i in band j.

$R_{TIR}^{U}(\vec{r},\mathbf{\Omega_L})$ is then expressed in terms of temperature of emitting elements by Stefan-Boltzman law after substituting Eq. A2.7 into Eq. A2.6:

$$R_{TIR}^{U}(\vec{r},\mathbf{\Omega_L}) = \varepsilon(\vec{r})\,\sigma\sum_{i=1}^{18}\sum_{j=1}^{9}\varepsilon_{ij}\,T_{ij}^{4}\,Phit_{ij}(\theta_{ij},\varphi_{ij})\frac{(\sin\theta_{ij2}-\sin\theta_{ij1})}{9}\mathbf{V}_{ij}\cdot\mathbf{\Omega_L} \qquad (A2.8)$$

Appendix III

Calculation of BRDF of soil surface

In Campbell and Norman (1988)'s BRDF model the soil is treated as a unit surface partially shaded by a sphere:

$$\rho(\theta_{s0}, \theta_v, \varphi - \varphi_{s0}) = 1 - \frac{E}{\cos\theta_{s0}}\{1 - \exp[-\xi(a\xi + b)]\} - \frac{E}{\cos\theta}\left\{1 - \frac{[\sin\xi + (\pi - \xi)]\cos\xi}{2\pi\cos\theta_{s0}}\right\} \quad \text{(A3.1)}$$

with

$$a = 1.165\kappa^3 - 4.108\kappa^2 + 4.82\kappa - 1.652$$

$$b = 2.666\kappa^3 + 9.588\kappa^2 - 11.749\kappa + 5.51$$

$$\kappa = \frac{\pi}{2} - \theta_{s0}$$

$$\cos\xi = \cos\theta_{s0}\cos\theta_v + \sin\theta_{s0}\sin\theta_v\cos(\varphi_v - \varphi_{s0})$$

where θ_v is view zenith angle, $\varphi_v - \varphi_{s0}$ is the angle between the view azimuth and solar azimuth, E is the sphere area index which is defined as the fraction of the unit area that is covered by the sphere above the soil surface.

Appendix IV

Table A.IV.1 The physical characteristic of air.

T_a (K)	ρ_a (kg m^{-3})	c_p (J kg^{-1} K^{-1})	v ($\times 10^{-6}$ m^2 s^{-1})	λ_a (W m^{-1} K^{-1})
250	1.4119	1003	11.37	22.26
263	1.3421	1003	12.44	23.28
273	1.2930	1004	13.30	24.07
283	1.2473	1004	14.18	24.86
293	1.2047	1004	15.08	25.63
300	1.1766	1005	15.75	26.14
303	1.1650	1005	16.00	26.37
313	1.1277	1005	16.95	27.09
323	1.0928	1006	17.91	27.80
333	1.0600	1007	18.89	28.51
343	1.0291	1008	19.89	29.21
350	1.0085	1008	20.63	29.70

Appendix V

Atmospheric stability functions inside and above a canopy

1. Atmospheric stability functions inside a canopy

According to Businger et al (1971) the function Φ_m inside the canopy expressed as:

$$\Phi_m = 0.74(1-9\zeta)^{-1/2} \qquad \text{unstable } \zeta<0 \qquad \text{(A5.1a)}$$

$$\Phi_m = 0.74+4.7\zeta \qquad \text{stable } \zeta>0 \qquad \text{(A5.1b)}$$

with

$$\zeta = Ri \qquad \text{unstable } \zeta<0 \qquad \text{(A5.2a)}$$

$$\zeta = \frac{0.74(1+8.926Ri)^{1/2}+9.4Ri-0.74}{9.4(1-4.7Ri)} \qquad \text{stable } \zeta>0 \qquad \text{(A5.2b)}$$

where $Ri(z)=\dfrac{g}{T_{abs}}\dfrac{dT}{dz}\left(\dfrac{l_m}{u_{ac}(z)}\right)^2$ is the Richardson's number with T_{abs} (K) the absolute temperature (being equal to the thermal expansion coefficient for ideal gases).

2. Atmospheric stability functions above a canopy

The vertical structure of atmospheric boundary layer (ABL) has distinctive regions: inner layer and outer layer. The inner layer is usually referred to as atmospheric surface layer(ASL), in which the flow is mainly dependent on the surface characteristics. Monin-Obukhov similarity (MOS) theory relates surface fluxes to surface variables and variables in the ASL. On the other hand, the outer layer is commonly referred to as the Ekman layer where the flow has little dependence on the nature of the surface. Under free convective conditions, the outer region of the ABL is well mixed, such that the mean profiles of wind and potential temperature are nearly constant with height. The bulk atmospheric boundary layer (ABL) similarity (BAS) proposed by Brutsaert (1982, 1999) relates surface fluxes to surface variables and the mixed layer atmospheric variables.

For modeling heat exchanges in the ASL, for instance using field measurements performed at a height of a few meters above ground, all calculations use the relevant MOS stability functions given by Brutsaert (1999). By replacing the MOS stability functions with

the BAS functions proposed by Brutsaert (1999), both single and dual-source model can be used to relate surface fluxes to the mixed layer atmospheric variables. For a large scale estimation of heat transfer, the later will be employed, because meteorological variables at mixed layer height either from radiosounding profiles or from numerical model outputs are usually used. Such parameters is representative of the properties of mean flow over relative larger horizontal scale.

(1) The MOS stability correction functions for momentum and sensible heat transfer

The MOS stability correction functions for momentum and sensible heat transfer respectively Ψ_m and Ψ_h are defined in the following integrated form of the corresponding φ_i functions,

$$\Psi_i(y) = \int_0^y [1-\varphi_i(x)]\frac{dx}{x} \tag{A5.3}$$

where $y=-(z-d)/L$. Subscript i denotes m, or h for momentum and sensible heat transfer respectively. The φ_i functions proposed by Brutsaert (1999) are given as

$$\varphi_m(y) = \frac{\left(a+b\,y^{m+1/3}\right)}{a+y^m} \tag{A5.4}$$

$$\varphi_h(y) = \frac{(c+d\,y^n)}{c+y^n} \tag{A5.5}$$

These φ_i functions cover the entire y-range comparing to the some other forms, e.g. from Kader and Yaglom (1990). On the basis of data reported by Högström (1988) and Kader and Yaglom (1990), the constants in Equations A5.4 and A5.5 were assigned by Brutsaert (1999) as $a=0.33$, $b=0.41$, $m=1.0$, $c=0.33$, $d=0.057$, and $n=0.78$.

For free-convective conditions, the MOS stability functions are given

$$\Psi_m(y) = \ln(a+y)-3by^{1/3}+\frac{ba^{1/3}}{2}\ln\left[\frac{(1+x)^2}{(1-x+x^2)}\right]$$

$$+3^{1/2}b\,a^{1/3}\tan^{-1}\left[\frac{(2x-1)}{3^{1/2}}\right]+\Psi_0, \qquad for\ \ y\leq b^{-3} \tag{A5.6a}$$

$$\Psi_m(y) = \Psi_m(b^{-3}), \qquad for\ \ y>b^{-3} \tag{A5.6b}$$

$$\Psi_h(y) = \left[\frac{(1-d)}{n}\right]\ln\left[\frac{(c+y^n)}{c}\right] \tag{A5.7}$$

where $x=(y/a)^{1/3}$, $\Psi_0=(-\ln a+3^{1/2}b\,a^{1/3}\pi/6)$ is an integration constant. Equation A5.6 and A5.7 are extensions of the Businger-Dyer function for unstable conditions (Brutsaert, 1982).

For stable conditions the expressions proposed by Beljaars and Holtslag (1991) and evaluated by Van den Hurk and Holtslag (1995) can be used. These are given in the following:

$$\Psi_m(y_s) = -\left[a_s y_s + b_s\left(y_s - \frac{c_s}{d_s}\right)\exp(-d_s y_s) + \frac{b_s \cdot c_s}{d_s}\right] \tag{A5.8}$$

$$\Psi_h(y_s) = -\left[\left(1+\frac{2a_s}{3}y_s\right)^{1.5} + b_s\left(y_s - \frac{c_s}{d_s}\right)\exp(-d_s y_s) + \left(\frac{b_s c_s}{d_s}-1\right)\right] \tag{A5.9}$$

where $y_s=(z-d)/L$, $a_s=1$, $b_s=0.667$, $c_s=5$ and $d_s=1$.

(2) The BAS stability correction functions for momentum and sensible heat transfer

The bulk stability functions depend on both the surface roughness and the height of the ABL. The height of ASL, h_{st}, can be determined in the following ways

$$h_{st} = \alpha_b\, h_b \tag{A5.10}$$

where h_b is the height of the ABL and α_b is around 0.10-0.15, or

$$h_{st} = \beta_b\, z_0 \tag{A5.11}$$

where β_b is around 100 -150, which ever is larger. Setting typical values of $\beta_b/\alpha_b=10^3$, and $h_b=10^3$ (m), gives $z_{0m}=(\alpha_b/\beta_b)h_b=1$ (m) which separates very rough from moderate rough terrain.

For moderately rough terrain satisfying $z_{0m}<(\alpha_b/\beta_b)h_b$, the bulk stability functions is given as

$$B_w = -\ln(\alpha_h) + \Psi_m(\alpha_h\, h_b/L) - \Psi_m(z_{0m}/L) \tag{A5.12}$$

196

$$C_{\mathrm{w}} = -\ln(\alpha_{\mathrm{h}}) + \varPsi_{\mathrm{h}}(\alpha_{\mathrm{h}}\, h_{\mathrm{b}}/L) - \varPsi_{\mathrm{h}}(z_{0\mathrm{h}}/L) \tag{A5.13}$$

Similarly, for very rough terrain, i.e. $z_0 \geq (\alpha_{\mathrm{b}}/\beta_{\mathrm{b}})h_{\mathrm{b}}$, we obtain

$$B_{\mathrm{w}} = -\ln\!\left(h_{\mathrm{b}}/(\beta_{\mathrm{h}}\, z_{0\mathrm{m}})\right) + \varPsi_{\mathrm{m}}(\beta_{\mathrm{h}} z_{0\mathrm{m}}/L) - \varPsi_{\mathrm{m}}(z_{0\mathrm{m}}/L) \tag{A5.14}$$

$$C_{\mathrm{w}} = -\ln\!\left(h_{\mathrm{b}}/(\beta_{\mathrm{h}}\, z_{0\mathrm{m}})\right) + \varPsi_{\mathrm{h}}(\beta_{\mathrm{h}} z_{0\mathrm{m}}/L) - \varPsi_{\mathrm{h}}(z_{0\mathrm{h}}/L) \tag{A5.15}$$

Finally, for stable conditions, i.e. when $h_{\mathrm{b}}/L > 0$, we use (Brutsaert, 1982, Eq. 4.93, p.84)

$$B_{\mathrm{w}} = -2.2 \ln\left(1 + h_{\mathrm{b}}/L\right) \tag{A5.16}$$

$$C_{\mathrm{w}} = -7.6 \ln\left(1 + h_{\mathrm{b}}/L\right) \tag{A5.17}$$

198

Curriculum Vitae

Li Jia was born in Yingkou of China on 25 May 1965. She completed her primary education in Beijing and attended Middle/High school in Yingkou and obtained later on a Bachelor degree in Dynamic Meteorology in June 1988 at the Beijing College of Meteorology. She began her career as a junior research scientist at the Lanzhou Institute of Plateau Atmospheric Physics (LIPAP) (currently Cold and Arid Regions Environmental and Engineering Research Institute - CAREERI) of the Chinese Academy of Sciences (CAS). She obtained her Master Degree in Atmospheric Physics from the Chinese Academy of Sciences in 1997 at the Postgraduate School of China University of Science and Technology and LIPAP. She became an Associate Research Professor at LIPAP in 1999. She contributed to a number of projects, among which a NSFC (National Natural Science Foundation of China) project 'The Experimental Study of Atmospheric Diffusion at Complex Terrain' (1988), a CAS project 'Study on Background of Atmosphere in Tibet Plateau' (1989-1990), a Sino-Japan cooperative project 'Hei He International Field Experiments (HEIFE)' (1989-1992), a NSFC project 'Regional Energy Balance and Water Cycle in Continental River Basin in Arid Zone', an KNAW/CAS joint project 'Energy and Water Cycle in Arid Zone' (1994-1997), an extension project of HEIFE 'Arid Environment Comprehensive Monitor Plan' (AECMP'95) (1995), a Key NSFC project 'Inner Mongolia Grassland Atmosphere Interaction Study (IMGRASS)' (1997-2000).

Abroad, she has been a visiting scientist at the Winand Staring Centre and later at Alterra Green World Research of the Wageningen University and Research Center in 1996 and 1999. She became a Ph.D. candidate in July 2000 at Wageningen University. Her study for the Ph.D. degree was partly funded by the Space Research Organization Netherlands (SRON) (Nederlands Wetenschappelijke Organisatie - NWO) (2001-2003). At the Alterra, she contributed to many projects, among which 'Land Surface Processes and Interactions Mission (LSPIM)' (1999-2000), DAISEX-99 (1999), a BCRS/LNV project 'Advanced Earth Observation - Land Surface Climate' (1999-2000), a BCRS/ESA/LNV project 'ENVISAT–Land Surface Processes' (1999-2002), preparatory studies of the ESA SPECTRA mission (2000-2004), an EU project 'Exploitation of AnGular effects in Land surfacE observations from satellite' (EAGLE) (2004-2006).

She is currently a post-doc fellow at the Wageningen University and Research Center.